Miniaturized Broadband Vibration Energy Harvesting

Alcala, Lucia R.

Publication date:
2018

Document Version
Publisher's PDF, also known as Version of record

Miniaturized Broadband Vibration Energy Harvesting

Ph.D. Thesis

Lucía R. Alcalá Jiménez

February 2018

Department of Micro and Nanotechnology
Technical University of Denmark

Supervisor: Professor Erik V. Thomsen

Abstract

This thesis is a contribution to the research in piezoelectric-based energy harvesting with a focus in miniaturized devices. The aim of this project is to develop a small scale vibrational energy harvester that shows a broadband piezoelectric response by applying magnetic fields that force the devices to enter into a non-linear regime. The energy harvesters fabricated in this project use AlN as piezoelectric material and are fabricated using micro and nanotechnology processing techniques. They consist of a silicon-based beam on top of which the piezoelectric material and electrodes are implemented through an extensive process development. AlN material with fairly good c-axis orientation was obtained by reactive sputtering techniques. However, the machine was decommissioned and in the end this material together with the electrodes were deposited by PIEMACS Sarl S.A. in Switzerland. The fragility of these beams is high enough to be considered, and an effort was put on improving the harvesters robustness by a two-step lithography-free process which consisted on rounding the anchoring point of the beams. The enhanced devices showed to withstand a mean acceleration of 5.9 g without breaking, which is almost as twice as the non-enhanced ones, which withstood only an average of 3 g. Once this robustness enhancement was achieved, magnets were implemented into the system. In order for the beam to interact with the magnets, ferromagnetic foil was incorporated on either side of the beam's tip. COMSOL multi-physics software was used for simulating the interaction between the beam and the magnets to the end of obtaining the optimal distances between both the beam and the magnets and between the magnets themselves. The results showed that small-scale dimensions were feasible for the set-up considered.

The characterization of the developed harvesters in impedance terms required a new set-up to be developed by which control over the three dimensional coordinates was achieved. Both softening and hardening effects, which were preciously observed when performing the simulation studies, were also obtained in the characterization part. The devices were also characterized in electromechanical terms, for which a more robust set-up was obtained by minimizing mechanical noise both from the deflection control laser sensor and from the shaking device. A maximum output power of $0.32\,\mu$W was obtained under an acceleration of 0.8 g.

Preface

This thesis is submitted as a partial fulfilment of the requirements to obtain the Ph.D. degree at the Technical University of Denmark (DTU). The work has been carried out at the Department of Micro- and Nanotechnology (DTU Nanotech) at DTU from the 1st of December 2014 to the 28th of February 2018 and has been supervised by Professor Erik V. Thomsen. The aim of this work is to develop a miniaturized piezoelectric-based energy harvester using silicon micro- and nanotechnology techniques. The devices must also prove to be capable of harvesting energy from a broad range of frequencies. By achieving this, the devices are thought to replace batteries in wireless sensor systems, allowing for autonomous self powering.

Acknowledgements

The work presented in this thesis was fully carried out at DTU Nanotech under the supervision of professor Erik V. Thomsen. I am imdebted to him for his help throughout the development of this work. I would specially like to thank him for always having a positive approach towards my questions and making constructive comments. I would like to thank in general my research group colleagues for the very useful discussions and friendly and realxed atmosphere. Among them, Anders Lei is specially acknowledged for his simulation contributions in the beginning of the project, when he was a co-supervisor and member of the group.

During the development of the devices, the staff at Danchip facilities made very useful comments that speeded up my processes, I am very grateful for the knowledge they shared with me. Outside the Danchip facilities, Per Thor Jonassen was very helpful during the fabrication of the different supporting structures that were later on used for the characterization of the devices.

Finally, I would also like to thank the different master and bachelor students that contributed to the development of this project in many different ways. These students are: Døgg Durhuus, Mikkel Vilsbøll Larsen, Vicenç Pomar, Nikolai Anker Michaelsen, Lea Sass Berthou, Thomas Passer, Martin Lind Ommen and Daniel Ugochukwu Anyaogu.

Contents

Chapter 1

Introduction

This chapter introduces the concept of energy harvesting, together with the most common methods employed in the field. A motivation to research in this field is also given and the advantages of utilizing micro electromechanical system (MEMS) methods for achieving our goal are explained. Furthermore, the state-of-the-art developments in the field are presented.

1.1 Motivation for Energy Harvesting

The demand for non-contaminating energy sources escalates through the years due to two main factors: population growth keeps steadily rising and greenhouse gases (GHG) emissions remain at high levels as a result of more than 150 years of industrial activity. Different energy harvesting systems are used thoughout the world, a couple of examples are solar panels and windmills. As expected, these systems consume energy as well, often times from batteries. Windmills are many times located in remote places, which must be accessed when, for examples, the batteries used in their wireless sensor systems need to be changed. A way of reducing the number of replacements that must take place and of replacing the batteries with a *green* energy device is by using micro-systems like vibrational ernergy harvesters (VEHs), which harvest mechanical energy form the vibrations of the turbines and translated it to energy in the electrical domain, by which the wireless sensor systems can be powered.

From an economical perspective, the usage of micro-systems had a revenue in 2009 of 25 billions [1]. According to the Global Microsensor Market Forecast and Opportunities, the global market for micro sensors will experience a compound annual growth rate (CAGR) of around 10% during 2014-2019, with accelerometers and gyroscopic MEMS sensors expected to witness remarkable growth as a consequence of their increasing use in smart phones and wearable devices.

Table 1.1: *Acceleration magnitude and fundamental vibration mode frequencies for a range of common vibrations sources in the environment. Data from* [3].

Vibration source	A [$\mathrm{m\,s^{-2}}$]	f_{peak} [Hz]
Car engine compartment	12	200
Base of 3-axis machine tool	12	70
Blender casing	6.4	121
Clothes dryer	3.5	121
Door frame just after door closes	3	125
Small microwave oven	2.5	121
HVAC vents in office building	0.2-1.5	60
Windows next to a busy road	0.7	100
CD on notebook computer	0.6	75
Second story floor of busy office	0.2	100

1.1.1 Wireless sensor systems

A wireless sensor system is an autonomous device that senses external conditions like a mechanical, thermal or optical input and transmits the data to a main location. From its definition it becomes straight forward that one of the main requirements for prototyping a VEH that can power such a sensor is a small volume. The power consumption of such a system has been continuously decreasing, now a wireless sensor system can be powered at less than 100 µW [2]. The aim of this project is to power wireless sensor systems by using small scale devices, which can be obtained by silicon-based MEMS processing techniques.

1.1.2 Vibration energy harvesting

Vibrations as energy sources have been a research topic for around two decades. It consists on transforming energy in the mechanical domain into usable energy in the electric domain. The sources of energy are commonly ambient vibrations with a frequency range from around 60 Hz to about 200 Hz, as shown in Table 1.1. This already sets a constraint on the size of the devices to be developed, which means that in order to harvest energy from this range of frequencies small-scale devices must be used. In the project presented in this work, the target dimensions are 10 mm$x$10 mm. Among all the sources presented in Table 1.1, low level vibrations are present in many environments. This means that low level vibrations have a wider range of application than other sources, therefore they are the focus for scavenging in this work.

In order to set into perspective the role played by VEH's, Figure 1.1 compares solar power, vibration based power generation and commonly used types of batteries. The boxes inside the figure represent the range of solar and vibration generation power. It can be seen from this figure that if the expected usage of a sensor is for only a few years, then batteries are just as a good solution as VEH's. However, for longer sensor lifetimes, and if sufficient light

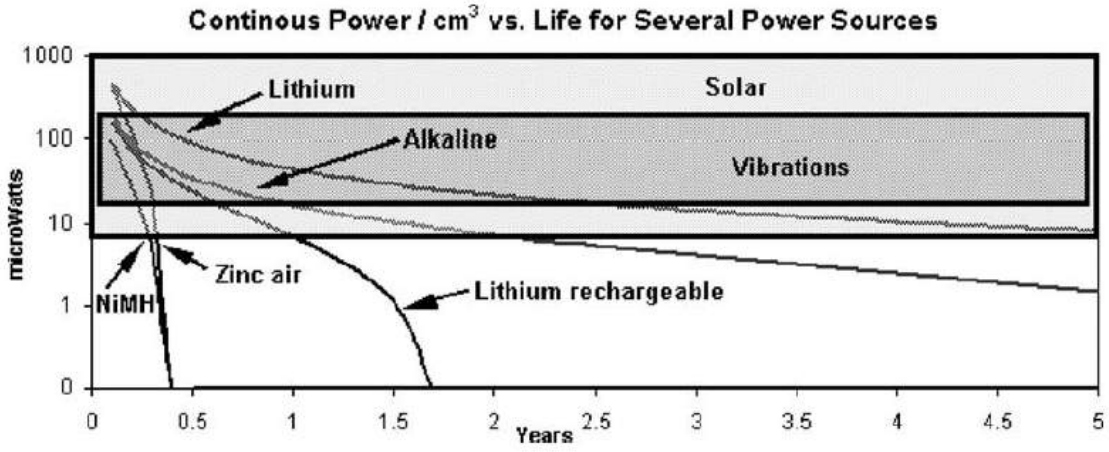

Figure 1.1: *Comparison of power harvested from vibrations, solar exposure and power supplied by different chemistry methods. Figure taken from* [3].

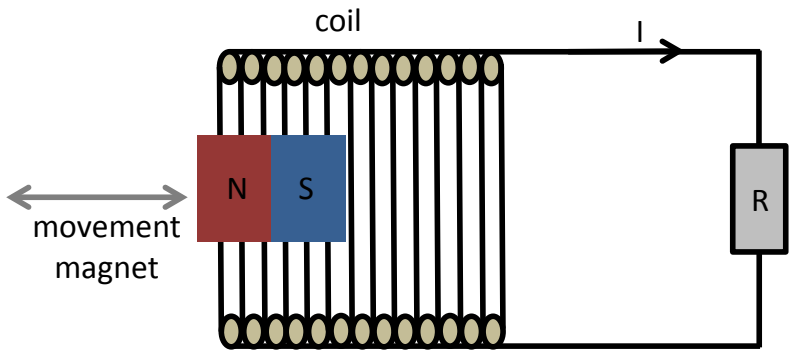

Figure 1.2: *Schematic figure that depicts a magnet moving inside a coil for harvesting energy from vibrations in the horizontal direction.*

energy is not available, VEH's are an attractive solution. Therefore, the aim of this work is not to present VEH's as the best energy harvesting solution, but to study the possibility of applying them where vibrations are present.

There are three basic and most common mechanisms for transducing vibrations, they are electrostatic, electromagnet and piezoelectric, all of which will be shortly described. Undertaking any of these paths for developing this project VEH's depends above all on its application and the possibility of developing them by MEMS silicon processing.

1.1.2.1 Electromagnetic energy harvesting

Electromagnetic energy harvesting is based on the movement of magnets relative to coils [5]. The power generated is directly related to the number of turns of the coil, the strength of the magnets, the magnetic flux gradient and the relative velocity between the magnet and the

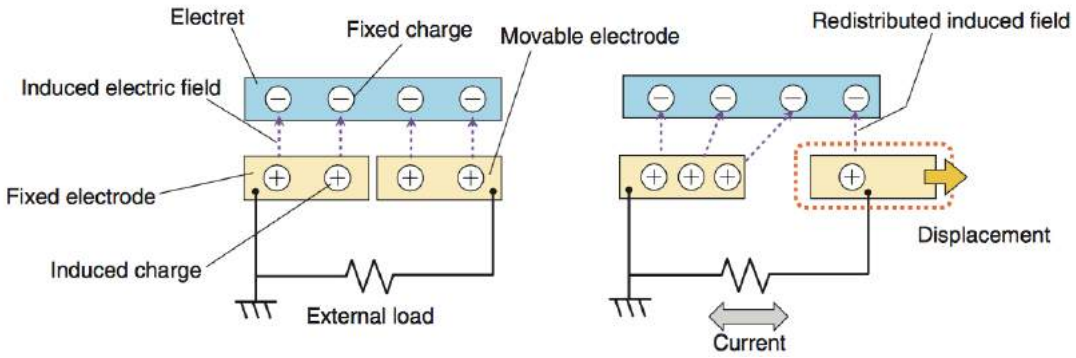

Figure 1.3: *Electrostatic method for harvesting energy from vibrations before (left) and after (right) a vibration displaces the electrode. Figure taken from* [4].

coil. An example of such a system can be seen in Figure 1.2. These kind of VEH's can be very efficient converters of mechanical energy into electrical as long as they are not constrained in size. However, miniaturizing these devices leads to a considerable efficiency reduction. Furthermore, regardless of this power reduction, silicon MEMS processing is restricted to planar structures, leading this to more difficult and costly development of the coil windings.

1.1.2.2 Electrostatic energy harvesting

An electrostatic energy harvester [6,7] can consist of a negatively charged electrode and other two positively charged electrodes, as depicted in Figure 1.3, both of which are connected to the sensor. Negative charges are applied to the top electrode and positive charges are therefore induced on the bottom electrodes, Figure 1.3 left. When an external vibration displaces the movable electrode, Figure 1.3 right, a charge redistribution takes place, generating as a consequence a current on the external load. The same holds for the opposite charges if the top electrode is charged with positive charges. This method is silicon MEMS processing compatible and, compared to its electromagnetic counterpart, does not demand highly complicated and costly procedures. Nevertheless, these devices present a low power density and sometimes require a separate voltage source, depending this on whether a dielectric or an electret material is used.

1.1.2.3 Piezoelectric energy harvesting

A piezoelectric material generates a displacement field when a stress is applied to it, therefore creating an electric potential. This effect is called direct piezoelectric effect. A typical structure that utilises this method consists of a cantilever beam with a mass attached to it. On top of the cantilever a piezoelectric material is sandwiched between two electrodes. The indirect piezoelectric effect consists on applying an electric field on these electrodes, which creates a stress on the piezoelectric film and therefore bends the beam. Piezoelectric energy

harvesting presents two advantages: is silicon MEMS fabrication compatible and has a higher energy density thean the previously introduced types [8].

1.2 Challenges

From the methods presented above the focus of this work is on piezoelectric energy harvesting by using cantilever structures. These structures allow for minuaturization, which is of utmost importance since these beams would substitute low-power batteries. Most MEMS fabrication equipment are located in cleanroom facilities. This presents a constraint regarding the materials that can be used, more specifically, the piezoelectric materials. Another challenge is that different dimensional structures present different optimal frequencies at which they harvest the largest amount of energy, this frequency is what is commonly known as resonant frequency. Furthermore, the bandwidth that they normally present is very small. The greatest challenge arises when aiming at structures whose resonant frequencies lie within the ambient vibration sources, i.e. a couple of hundred Hertz, the structures become very fragile. This section describes these challenges in more detail and presents the methods chosen to overcome them.

1.2.1 Frequency matching

In Table 1.1 a list of ambient sources of vibration with their corresponding peak frequency and acceleration is presented. However, most vibration sources present a shift in their peak frequency over time. Each beam structure is characterized by its resonant frequency according to its dimensions, at which the highest power can be harvested. Therefore, if a vibration source presents a shift in frequencies away from the resonant frequency of the cantilever then the output power will either be decreased or reduced to zero. A solution for this problem was presented by Shahruz [9], where a set of beams of different lengths were fabricated next to the other, each of which as a consequence had a different resonant frequency, covering a spectra of 65 Hz. This solution is not applicable for our purpose since it limits the possibility of the harvester miniaturization. Another approach is to create a beam that itself presents broadband energy harvester properties, this can be achieved by different methods [9–14], the most common is the incorporation of external magnets and implementation of magnetic or ferromagnetic material on the beam's tip [15–18]. The magnetic forces that arise between the magnets and the beam allow for a broadband energy harvester (BEH). This is explained in more detail in Section 1.3.2.

1.2.2 Robustness

In order to tune in to the low ambient frequencies the common approach is to increase the cantilever length and reduce its thickness, which leads to very fragile structures when

Table 1.2: *Material properties of the most commonly used piezoelectric materials. Values taken from* [22].

Material	$d_{31} \cdot 10^{-12}$ $[\mathrm{C\,m^{-2}}]$	ε_{33} $[\epsilon_0]$	$\frac{d_{31}^2}{\varepsilon_{33} \cdot \varepsilon_o}$ $[\frac{N}{m^2}]$
AlN	1.5	10.5	$2.42 \cdot 10^{-14}$
ZnO	2.2	4.6	$1.19 \cdot 10^{-13}$
PZT	88	1000	$8.75 \cdot 10^{-14}$

aiming at small-scale devices. Another method for lowering the frequencies is obtained by a five-step fabrication process which consists of spray coating resist on the backside of the beam after defining the cantilever, then performing a lithography process and finally deep etching holes on the silicon hinge [19]. Nevertheless, the most common approach to lower the resonant frequencies is the former one, which poses a limit on both the handling of it and on the acceleration levels that it can withstand. This challenge can be overcome by reducing the stress concentration at the anchoring point. In pursuance of this reduction in stress concentration, corner rounding techniques can be applied to the anchoring point.

1.2.3 Materials

Among the most common materials used for piezoelectric VEHs are lead zirconate titanate (PZT), aluminum nitride (AlN) and zinc oxide (ZnO). The criteria followed to choose a piezoelectric material extends basically over two parameters: piezoelectric coefficient and dielectric constant. Table 1.2 shows that PZT presents a piezoelectric coefficient an order of magnitude larger than the other two materials. However, a power generation figure of merit (FOM) can be defined as $\frac{d_{31}^2}{\varepsilon_{33} \cdot \varepsilon_o}$ [20]. This means that even though AlN and ZnO present lower piezoelectric coefficients, their figure of merit is comparable to the one for PZT due to their much lower dielectric constants. It is important to know that this power generation FOM was obtained by finding an expression for the input energy from the vibrations and assuming a maximum transmission for a linear transducer relationships [21]. Another important criteria for choosing the material is the feasibility for cleanroom processing since this characteristic will determine its scalability and further processing. In this respect PZT-based materials introduce the problem of lead contamination, which neither AlN nor ZnO present.

1.3 Review of MEMS piezoelectric energy harvesters

Within the past decade some review papers about VEHs have been presented [2, 4, 23–25]. Most VEHs correspond mainly to large structures whose harvesting frequencies are not in the range of ambient vibrations, serving only as a proof of concept and present therefore no possible application for wireless sensor systems [26]. The following review focuses on last decade advancements in miniaturized cantilever based VEH's as well as on developments in

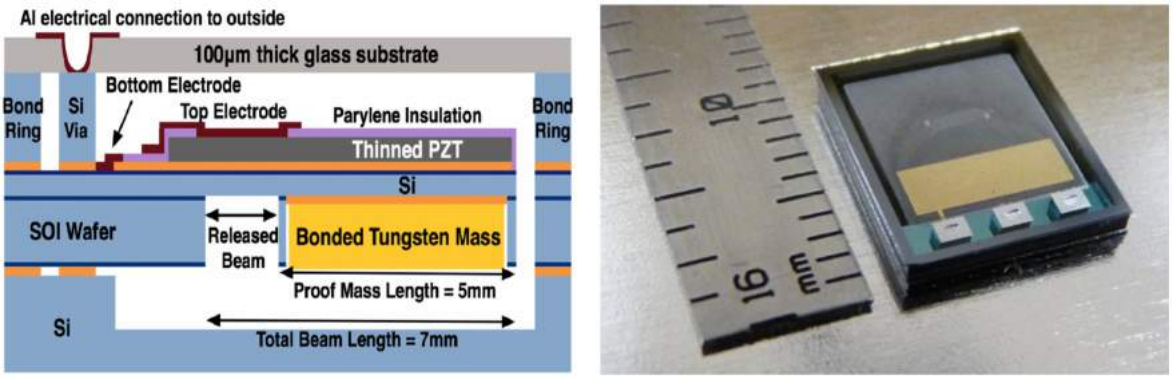

(a) (b)

Figure 1.4: *PZT vibration energy harvester based on a SOI wafer, Aktakka et al. a) Schematic side view. b) Processed device. Both figures from* [27].

broadband VEHs at larger scales.

1.3.1 Miniaturized vibration energy harvesting

1.3.1.1 PZT-based VEHs

Due to its high piezoelectric constant and high coupling coefficient, PZT-based VEHs have occupied large attention. In 2011 a bulk PZT based harvester was presented [27], where a 20 µm thick PZT-5A layer is bonded to a Si wafer using gold indium (AuIn) as eutectic bonding material, as shown in Figure 1.4. At an excitation acceleration of 1.5 g ($(1\ g = 9.81\,\mathrm{m/s^2})$) they obtained 160.8 µW with a resonant frequency of 415 Hz. At the Eliminating Batteries (ELBA) project A. Lei *et al.* [28] developed a 15 µm thick PZT based VEH that used silicon as a supporting structure. A side view sketch of the harvester as well as the processed devices are shown in Figure 1.5. The fabrication process consisted on first screen printing the PZT layer on the silicon wafer, after which the cantilever and its proof mass are defined by a KOH etching. Finally, the cantilever structure is released by dry etching techniques. The structure harvested a maximum power of 36.65 µW at 245.2 Hz at an acceleration of 2 g.

1.3.1.2 AlN-based VEHs

Some studies using AlN as piezoelectric material have taken place [29–32]. Marzencki *et al.* [32] fabricated a cantilever-based VEH for which at 4 g they obtained 1.1 μW from a VEH that had resonant frequency at 1370 Hz. A larger amount of power at a considerably lower base acceleration was obtained by Elfrink *et al.* [29]. The device they developed is shown in Figure 1.6. A silicon wafer is used as substrate where AlN is deposited by reactive sputtering using an Al target. Once the piezoelectric layer is sandwiched between the electrodes the cantilever is defined by KOH etching and afterwards the cantilever is released by etching techniques.

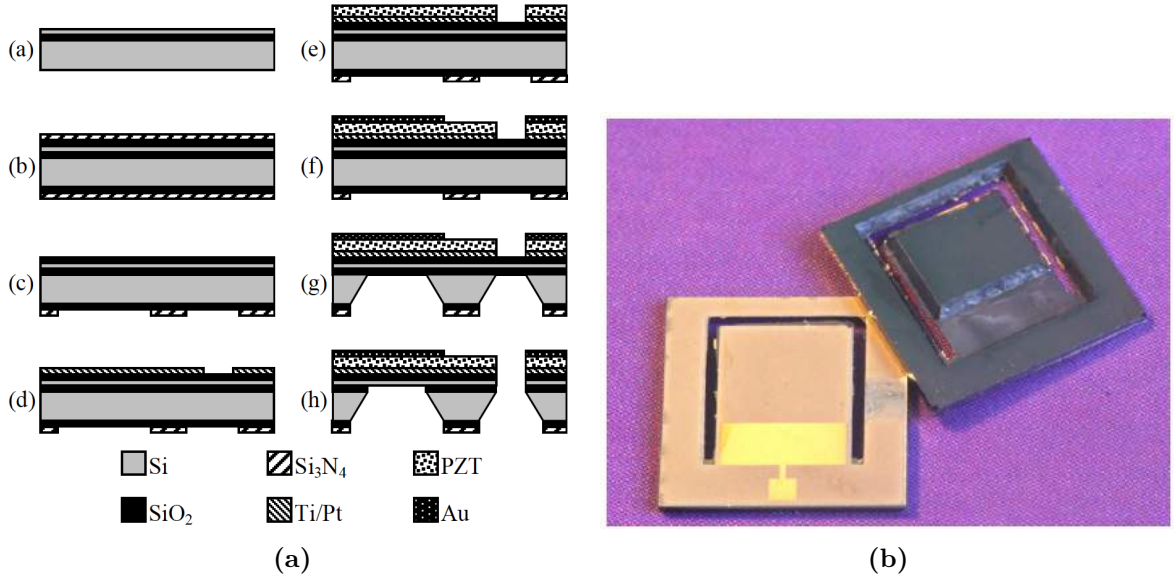

Figure 1.5: *PZT vibration energy harvester, Lei et al. a) Schematic side view where PZT is screen printed (a-c), after which the electrodes are defined (d-f), then the silicon beam is etch defined in a KOH solution (g) and finally the beam is realised by dry etching methods (h). b) Photograph of the devices. Both figures from* [28].

The final thickness of the silicon beam is 45 µm. As a last step, the silicon wafer is vacuum bonded to two glass wafers, which serves a packaging for the VEHs. A maximum power of 60 µW was obtained for an unpackaged device at 2 g input acceleration excited at a frequency of 572 Hz.

1.3.1.3 ZnO-based VEHs

A number of studies of ZnO as piezoelectric material are available [33–35], these studies include optimization of sputtering procedure to obtain right stoichiometry, substrate influence and typical roughness and crystal orientation analysis. However, most literature lacks the implementation of these optimization techniques into an actual VEH. An exception to this is the device developed by Wang et al. [34]. This cantilever had dimensions of 500 µm in width, 1000 µm in length and 10 µm in thickness, with a resonant frequency of about 13 000 Hz and a piezoelectric coefficient of 3.21 pC N^{-1}, Figure 1.7. The maximum power they obtained was 0.98 µW at resonant frequency and an acceleration of 1.02 g.

1.3.1.4 Comparison of the different devices

It is difficult to compare widely differing designs, materials and approaches for vibrational energy harvesting. Therefore, in order to copmpare the different devices that have been presented in this section, the approach of considering the normalized power density (NPD) is

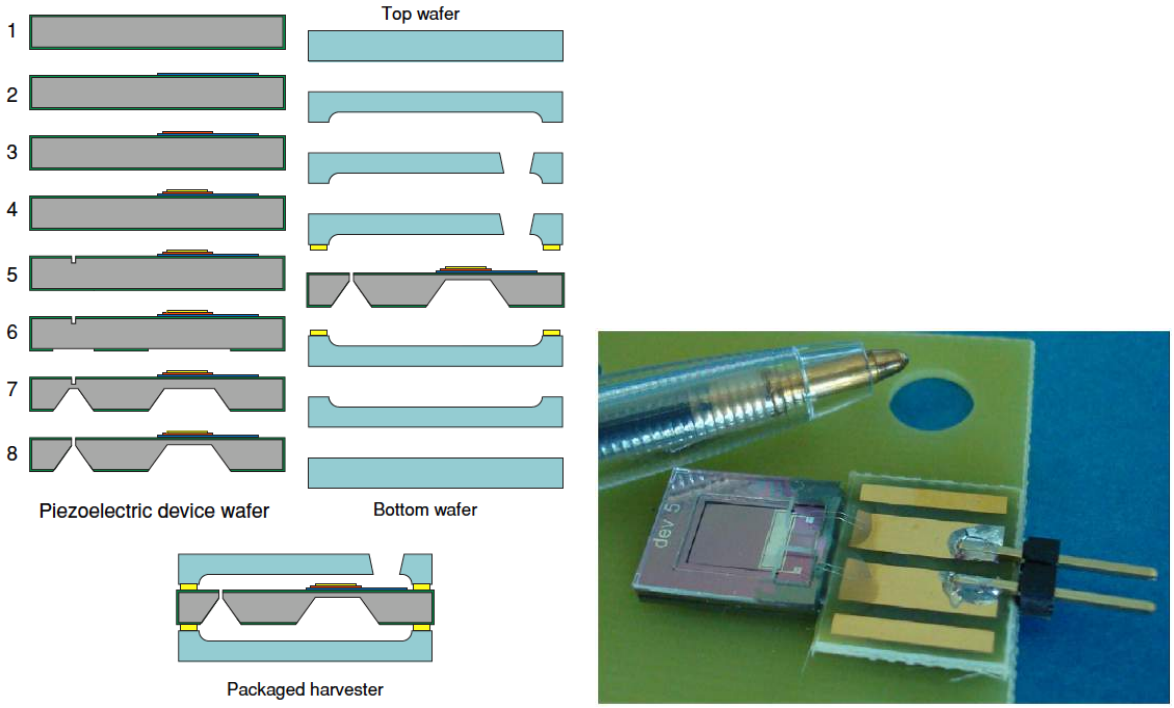

(a) (b)

Figure 1.6: *AlN vibration energy harvester, Elfrink et al. a) Schematic side view where AlN is deposited by reactive sputtering and sandwiched between the eletrodes (1-4), after this the beam is released by a combination of dry and wet etching techniques (5-7) and finally the sislicon wafer is vacuum bonded to two glass wafers. b) Picture of the developed device. Both figures from* [29].

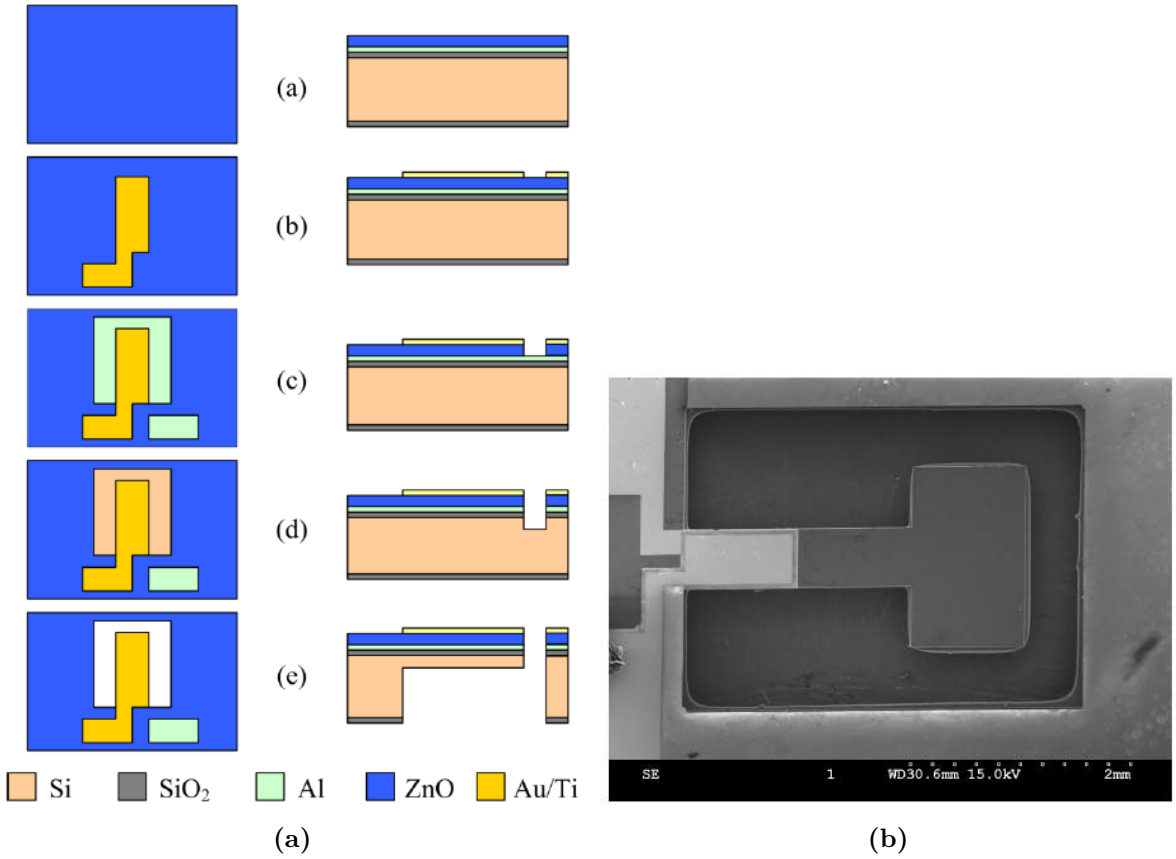

Figure 1.7: *ZnO vibration energy harvester, Wang et al. a) Schematic side view where the first step consists on depositing the piezoelectric material and electrodes (a), the electrodes are afterwards defined (b-c) and finally the beam is defined and released (d-e). b) Scanning electron micrograph of the developed harvester. Both figures from* [34].

Table 1.3: *Comparison of the performance of the VEHs presented in this section. For Wang et al. no proof mass dimensions were given, therefore the NPD could not be calculated.*

Reference	Material	Acc. $[g]$	f_r [Hz]	Power μW	NPD $[\mathrm{mW/cm^3}/g^2]$
Atakka [27]	bulk PZT	1.5	415	160.8	2.65
Lei [28]	thick PZT	2	245.2	36.65	0.51
Marzencki [28]	AlN	4	1370	1.1	0.16
Elfrink [29]	AlN	2	572	60	1.01
Wang [34]	ZnO	1.02	1300	0.98	–

taken. This approach considers the power harvested normalized respect to input acceleration squared and unpackaged device active volume. The resulting comparison is shown in Table 1.3. Bulk PZT shows the highest NPD, as expected. However, the AlN-based energy harvester developed by Elfrink *et al.* [29] presents comparable results. For the energy harvester obtained by Wang *et al.* [34] it is not possible to calculate the NPD since the thickness of the proof mas is lacking in their study.

1.3.2 Broadband energy harvesting

Among BEH's, two basic types can be found: active and passive mechanisms. The active mechanism consists in *continuously* having an external power supply that tunes in the harvesting frequency. Conversely, in the passive mode, power is required only *intermittently*, until the new vibrational frequency is tunned-in. This frequency matching mechanism in either case can be perfomed both manually or in a self-tunning manner. Regardless of whether manual or self tunning takes place, or of whether a passive or active method is employed, a broad range of types of devices have been developed in order to finely tune the vibrational frequency. One possibility is changing the stiffness of the harvester by applying an axial preload [10–12]. Leland *et al.* [10] fabricated a brass center shim sandwiched between two layers of PZT, where a sputtered nickel electrode on the outer surface of each PZT layer allowed for electrical connection. The shim dimensions were 3.17 cm in length by 1.27 cm in width. In their study a reduction in resonant frequency of up to 24% by applying a compressive axial preload was obtained, Figure 1.8a, which resulted in an output power of $300 - 400\,\mu$W over a frequency range of $200 - 250$ Hz under a 1 g excitation acceleration. Another way of adjusting the resonance frequency of the cantilever is by changing the gravity center of the tip mass [36]. In order to do so, the total proof mass is the addition of a fixed part and a movable part, where the movable part can be displaced alongside the longitudinal direction of the cantilever, as depicted in Figure 1.8b, by which a total frequency range of $130 - 180$ Hz was covered.

A passive method for harvesting a broad band of frequencies is by utilizing an array configuration [9, 13, 14, 37] where each cantilever presents its own natural resonant frequency. They

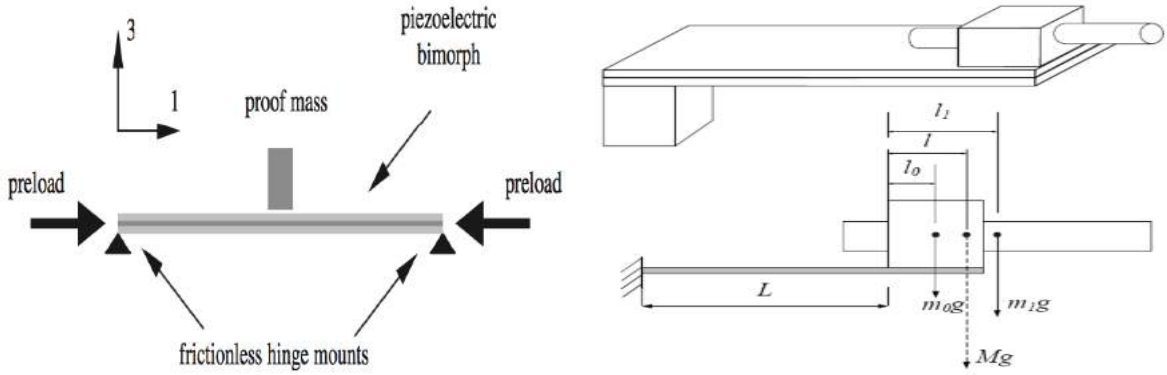

(a) **(b)**

Figure 1.8: *a) Schematic of a clamped-clamped piezoelectric bimorph with a proof mass mounted at the center where a variable compressive axial preload is applied. Figure taken from [10]. b) Schematic of the piezoelectric element where the gravity center is changed longitudinally by displacing the movable mass part. Figure taken from [36].*

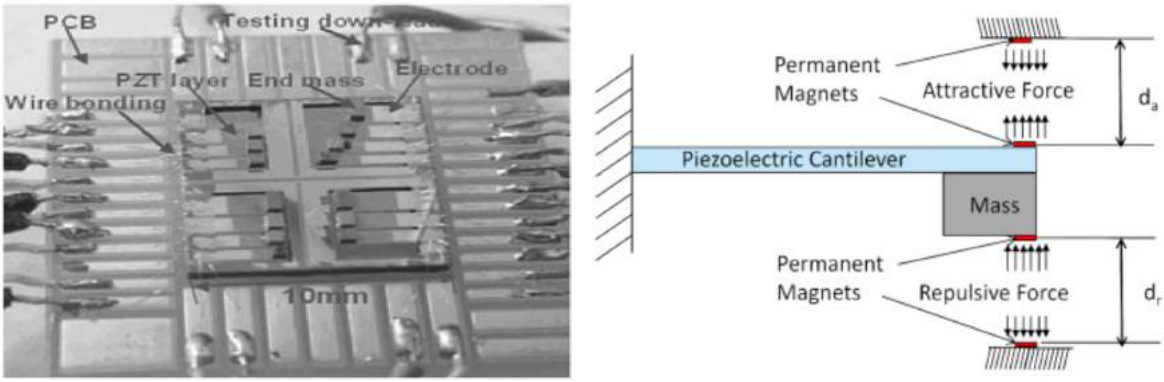

(a) **(b)**

Figure 1.9: *Vibrational energy harvesting mechanisms. a) Array of beams, figure taken from [14]. b) Magnetic system, figure taken form [38].*

might be quasi-uncoupled [13,37], where the coupling takes place through a spring connecting the beams or through a movable mass attached to both of them. Liu *et al.* [14], developed an array of uncoupled beams, see Figure 1.9a, which covered a bandwidth from 226 Hz to 234 Hz, harvesting up to 3.98 μW. However, this kind of device poses the problem of diminishing the harvested power density. Challa *et al.* [38] proposed a manually tunable cantilever harvester where two magnets were located at the end of the beam and other two were fixed at the top and bottom of the beam, as shown in Figure 1.9b. The parameter to be changed was the vertical distance between the magnets, which was manually changed for the different ambient frequencies. The prototype volume was 50 cm^3 and the tunable range was from 22 Hz to 32 Hz, range through which the output power obtained was 240 - 280 μW

Another way of obtaining a BEH is by exploiting non-linearity effects in the stiffness. A number of studies have been developed in that regard [15–18, 39–50]. Among others, they

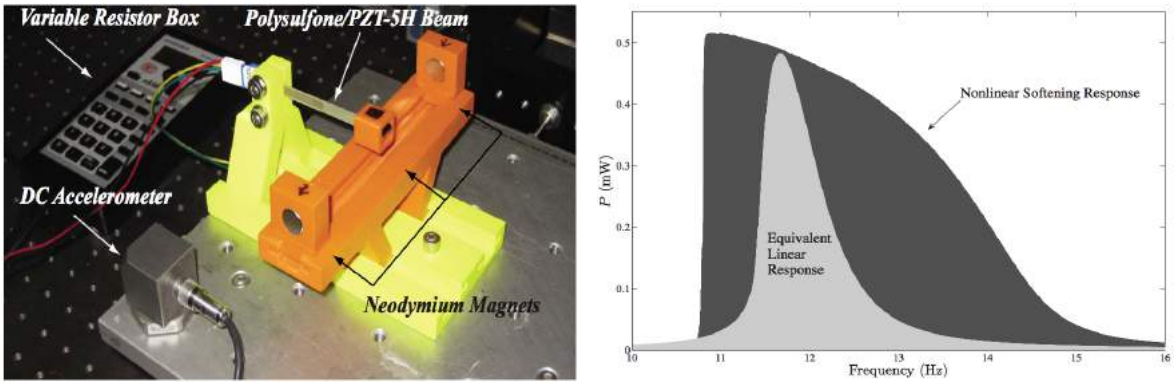

(a) **(b)**

Figure 1.10: *Magnetic system with softening effect, images taken from [15]. a) Set-up b) Power harvested in the linear regime versus the non-linear softening regime.*

comprise the use of stoppers [45, 46], where a piezoelectric beam to which a proof mass is atached is located beneath a metal plate that works as an end stop. The bandwidth of the harvester depends on whether a downsweep or an upsweep in frequencies takes place [51]. Furthermore, the longitudinal position and height of the stopper must be tuned for each given vibrational environment [51].

Non-linear stiffness can lead to both spring softening and spring hardening. The hardening effect increases the bandwidth towards higher frequencies [39] while the softening effect, on the other hand, widens the bandwidth towards lower frequencies [40]. It has been previously outlined that ambient vibrations extend over a low frequency range. For this reason and due as well to the fact that a spring hardening effect limits the displacement of the cantilever, a spring softening effect is preferred.

The focus of this project is on piezoelectric based beams that exploit non-linearity effects by magnetic interaction forces. In this regard, non-linearity effects were studied by different research groups. Stanton *et al.* [15] studied this a system which consisted of a beam 55 mm long, 0.75 mm thick with embedded piezoelectric laminates 26 mm in length and 0.25 mm in thickness, as shown in Figure 1.10a. The beam tip has a neodynium end mass magnet attached to it with a weight of 7.5 g. The linear equivalent system showed a resonant frequency of 12 Hz. At a specific magnets location they achieved a softening regime where a nonlinear frequency of 14.4 Hz was obtained. Contrary to the approach that Challa *et al.* took [38], where the position of the magnets was tunned for each frequency, in this case the distance between magnets was kept constant while a sweep over frequencies was performed. Their results showed that a non-linear beam overperforms the linear one by increasing the bandwidth three times, as shown in Figure 1.10b. A similar set-up to the one of Stanton *et al.* was studied by Lin *et al.* [16]. There, a magnet proof mass was attached to a piezoelectric beam and had a total length of 5 cm. They also reported an increase in the off-resonance output.

Instead of adding a magnet on top of the beam's tip and therefore compromising the minimum

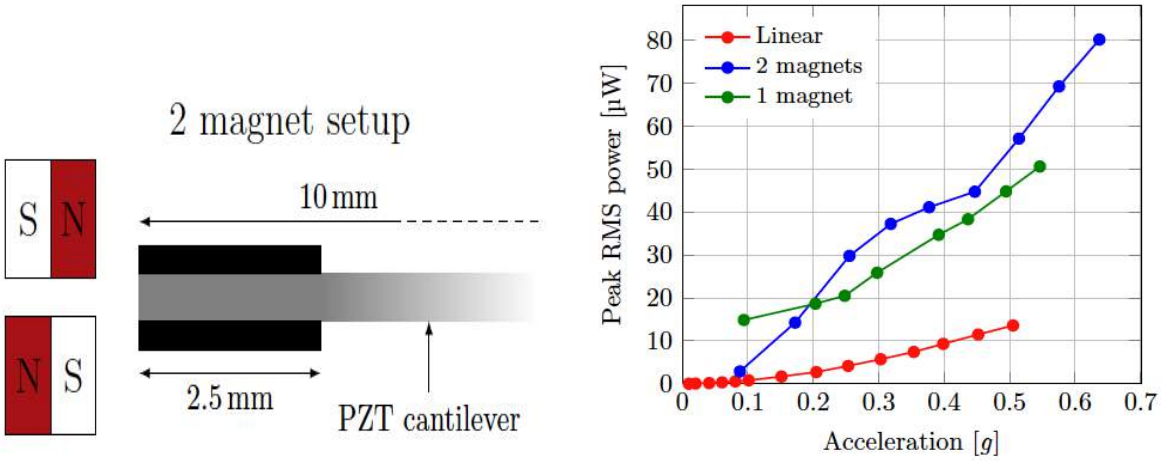

(a) **(b)**

Figure 1.11: *Magnetic system proposed by Lei et al., taken from [17]. a) Set-up b) RMS power harvested in the linear regime versus the non-linear regimes.*

dimensions of the beam, magnetic foil can be implemented on it. This was done by Lei *et al.* [17], where the external magnetic set-up consisted of either one or two magnets. They found that the latter configuration leads to larger output power [17]. Their experimental set-up consisted of, besides the external magnetic setup, a pair of PZT layers with a total thickness of 150 µm and iron foils with dimensions of 100 µm in thickness, 2.5 mm in length and 5.5 mm in width attached to it on both sides, as depicted in Figure 1.11a. The cantilever, presenting a total length of about 10 mm, was anchored to a PCB through soldering. The results showed a clear improvement for the non-linear case respect to the linear one, as seen in Figure 1.11b. In that study, the power harvested showed to be quite sensitive to the vertical positioning of the magnets, i.e. to the distance separating them, claiming that only a range of approx. 30 μm was of interest.

A similar system with the magnetic field incorporated was previously studied by Tam *et al.* [18]. Their focus was on predicting equilibria points and oscillation frequencies of an experimental device by computing the full magnetic field and approximating the forces acting on it. Nevertheless, the dimensional parameters were large compared to a miniaturized deviced, with a beam length as large as 11 cm, Figure1.12a, which is not compatible with the small size requirements for low power batteries. A numerical study of a non-linear oscillator for broadband energy harvesting was also presented [47], which does not include any magnetic set-up and therefore interaction between the beam and the magnets. Hence, it lacks any dimensional analysis.

Recently, Abdelkefi *et al.* [48] developed a model based on Euler-Bernouilli beam theory form which they could calculate the beam's natural frequency, mode shape and displacement. The magentic force expression that they inserted into their equations used a dipole-dipole approximation, accurate enough for long distances between the magnets and the experimental set-up that they used (cantilever with a length of 6.25 cm). However, it was demonstrated

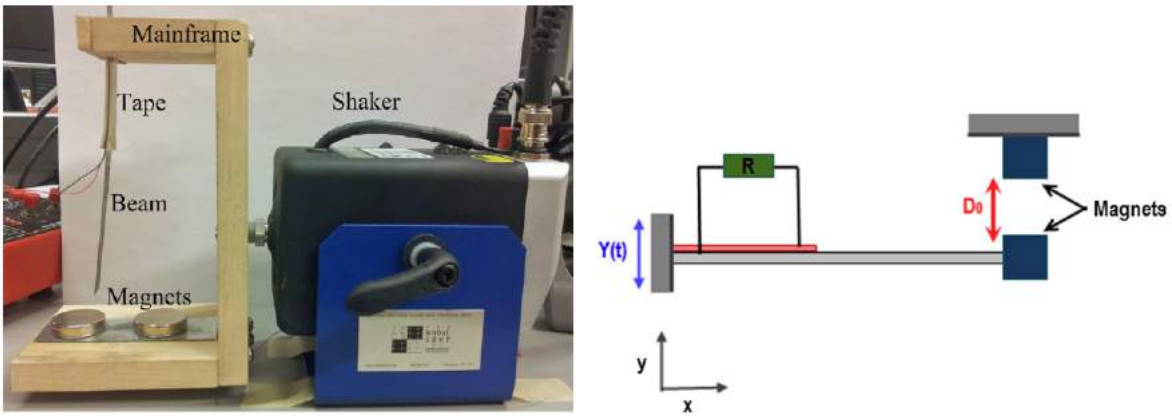

(a) (b)

Figure 1.12: *a) Magnetoelastic VEH developed by Tam et al.. Figure taken from [18]. b) Schematic view of the system implemented by Abdelfeki et al.. Figure taken from [48].*

that this dipole-dipoleapproximation is not valid for distances between magnets smaller than 6.5 mm [52].

Ferrari *et al.* [49] studied the interaction of a ferromagnetic cantilever with a magnet. The cantilever dimensions are not stated in their study, however, the piezoelectric material length is of 4 mm and the magnet thicknesses that they tried were of 2 mm and 6 mm. With these two configurations of thicknesses, bistable behaviour was obtained for distances between cantilever and magnet of up to 4 mm and 8 mm, respectively. These overall dimnesions are, respectively, about four and eight times larger than the dimensions aimed at in this work, threfore exceeding the miniaturization requirements that are held in this thesis. Nevertheless, the magnetic force term used for fitting their simulation results was a third order polynomial function, as is commonly done [18, 50].

1.4 Aimed structures for this thesis

In this thesis the aim can be devided into two main ones: to harvest energy from ambient vibrations and to achieve a broadband response. From the first one and based on what was introduced in this chapter, small-scale devices with a length of the beams considerably larger than the thickness of it must be fabricated. Regarding lateral dimensions, the beam system is constraint to no more than 1 cm to fulfill the small-scale requirements. Hence, silicon micro-technology processing techniques are used to this end and the resulting structure is a cantilever with a built-in silicon proof mass structure. Regarding the second aim, magnets are incorporated into the system and in order for the cantilevers to interact with them another material serving as proof mass must be incorporated. In this case ferromagnetic foil is used on both sides of the beam. This basically means that the resulting structure does not have a built-in proof mass as was the former case but a pair of foils placed on either side of the

cantilever. As a conclusion, it is important to bear in mind that two types of beam structures will be presented throughout this project.

1.5 Summary and overview of the thesis

The thesis is divided into the following chapters

- **Chapter 2 - Piezoelectric Harvesting Theory:** The theory of piezoelectric materials and their implementation into cantilever-based energy harvesting in theoretical terms is presented.
- **Chapter 3 - Broadband Energy Harvesting Theory:** The theoretical background necessary for describing non-linear systems that are used for broadband energy harvesting is explained.
- **Chapter 4 - Deposition of AlN with Piezoelectric Properties:** The basic properties of AlN are presented. Different parameters that play an important role during AlN deposition and the possible substrates that can be used are discussed.
- **Chapter 4 - Process Development:** Major improvements during the fabrication of the devices are addressed and the different solutions are discussed.
- **Chapter 5 - Design and Fabrication:** The design of the devices is given and the final fabrication methods are presented.
- **Chapter 6 - Characterisation:** The different set-ups used for characterizing the beams are presented and the characterization of energy harvesters is performed. The major results are presented.
- **Chapter 8 - Conclusion and Outlook:** The most important results are summarized and an outlook for future work is given.

Chapter 2

Piezoelectric energy harvesting

In this chapter the theoretical background used to model a cantilever-based piezoelectric energy harvester is introduced. The piezoelectric constitutive equations associated are presented, where the piezoelectric material constants are also introduced in matrix form. The system consisting of a beam with piezoelectric material can be treated as a single degree-of-freedom (SDOF) model. These relations, which can be derived from the piezoelectric constitutive equations together with the static Euler Bernoulli beam equation, are presented in this chapter. Regarding the resonant frequency of the beams, it is accurately found by applying the Rayleigh-Ritz energy method. Furthermore, an equivalent electrical circuit model is presented, where parameters in the mechanical domain are translated to the electrical domain by previously finding expressions that relate electrical parameters like current intensity and voltage with mechanical and geometrical ones like moment and deflection slope rate of the cantilever. It is important to note that the starting point of the theory here described is presented in [53, 54], from which modifications to adapt it to the systems presented in this thesis are performed.

2.1 Piezoelectric constitutive equations

Piezoelectric materials couple electrical and mechanical behaviours within themselves and two effects can be distinguished: direct and inverse effects. The former one takes place when the piezoelectric is mechanically strained, this causes an electric polarization that is proportional to the input strain. Conversely, an inverse effect takes place when the piezoelectric material is subjected to an electric polarization, which leads to a strain that is proportional to the polarization. The piezoelectric constitutive equations that describe a piezoelectric material can be deduced by applying the first law of thermodynamics for a linear piezoelectric continuum, enthalpy relations and strain properties. Using Einstein notation, the constitutive equations can be expressed as

$$S_{ij} = d_{ijk}E_k + s^E_{ijkl}T_{kl} \tag{2.1}$$

$$D_i = \epsilon_{ik}^T E_k + d_{ikl} T_{kl}, \tag{2.2}$$

where T_{ij}, S_{ij}, E_i and D_i are, respectively, the stress, the strain, the electric field and electric displacement tensors; s_{ijkl}^E is the elastic compliance at constant electric field, ϵ_{ik}^T the permittivity at constant stress and d_{ijk} the piezoelectric coefficient. Since AlN presents a hexagonal crystal symmetry, the permittivity can be expressed in matrix form as

$$\epsilon^{\mathbf{T}} = \begin{pmatrix} \epsilon_{11}^T & 0 & 0 \\ 0 & \epsilon_{22}^T & 0 \\ 0 & 0 & \epsilon_{33}^T \end{pmatrix}, \tag{2.3}$$

similarly, for the elastic compliance

$$\mathbf{s^E} = \begin{pmatrix} s_{11}^E & -s_{12}^E & -s_{13}^E & 0 & 0 & 0 \\ -s_{12}^E & s_{11}^E & -s_{13}^E & 0 & 0 & 0 \\ -s_{13}^E & -s_{13}^E & s_{33}^E & 0 & 0 & 0 \\ 0 & 0 & 0 & s_{44}^E & 0 & 0 \\ 0 & 0 & 0 & 0 & s_{44}^E & 0 \\ 0 & 0 & 0 & 0 & 0 & 2(s_{11}^E - s_{12}^E) \end{pmatrix}, \tag{2.4}$$

where the double indices (ij) and (kl) have been replaced by a new pair of indices (pq), doing likewise with the piezoelectric coefficient matrix

$$\mathbf{d} = \begin{pmatrix} 0 & 0 & 0 & 0 & d_{15} & 0 \\ 0 & 0 & 0 & d_{15} & 0 & 0 \\ d_{31} & d_{31} & d_{33} & 0 & 0 & 0 \end{pmatrix}. \tag{2.5}$$

2.2 Energy harvester analytic model

As described in Chapter 1, two set of beams were fabricated in this project: one with a built-in silicon proof mass on one side of the beam, whereas for the second one the proof mass is manually incorporated and consists of iron foil on both sides of the beam. In the analytic model described in this chapter whether one or the other case is used will most of the time not affect the modelling. Basically, the proof mass total mass will change together with the location of the neutral axis and center of mass, which does not affect the longitudinal parameters. Nevertheless, both dimensional descriptions are given for the sake of completeness.

The beam with a built-in silicon proof mass can be represented in terms of the parameters shown in Figure 2.1. L is defined as the length of the beam, without including the proof mass longitudinal section, which is defined as L_M and its associated mass is M_1. The thicknesses of the beam are defined as follows, the piezoelectric layer has an associated h_{AlN} thickness, the silicon cantilever thickness is defined as h_{Si} and the silicon proof mass thickness as h_M. As can be seen, the electrodes thickness are neglected in the analysis due to their very small values compared to the silicon beam. The reason for taking into account the AlN layer thickness is that it must be accounted for when the piezoelectric effect takes place. Considering now an

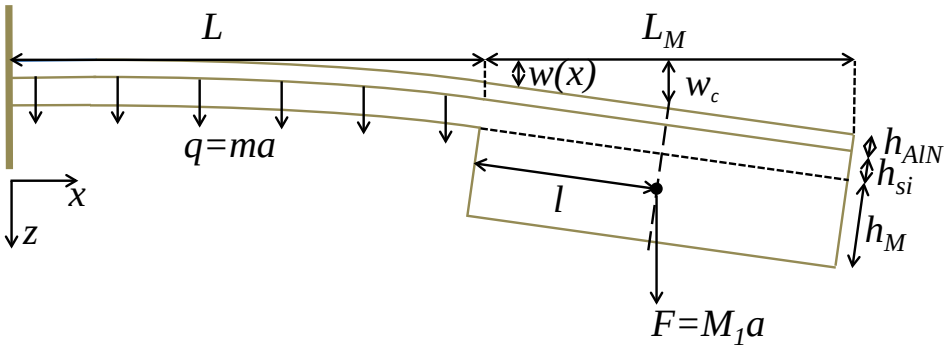

Figure 2.1: *Sketch of the first VEH described in the analysis. It consists of a silicon beam anchored in one end and a built-in proof mass on the other end. Notice the dashed line that separates the thin silicon beam and the silicon proof mass.*

input acceleration that acts on the cantilever, the proof mass creates a force on the cantilever end defined as $F = M_1 a$ at $l = L_M/2$, the latter being vertically and horizontally located at the center of mass. Regarding the cantilever itself, a force per unit length defined as $q = ma$ acts on it, where m is the mass per unit of length. If we define W as the width of the beam, then $m = W(h_{\mathrm{AlN}}\rho_{\mathrm{AlN}} + h_{\mathrm{Si}}\rho_{\mathrm{Si}})$, where ρ_{AlN} and ρ_{Si} are the AlN and silicon mass densities, respectively. Similarly, $M_1 = WL_M(h_{\mathrm{AlN}}\rho_{\mathrm{AlN}} + (h_{\mathrm{Si}} + h_M)\rho_{\mathrm{Si}})$. The longitudinal deflection of the beam is described by w as a function of $x \leq L$. Accordingly, w_c is defined as the deflection considering the longitudinal position of the center of mass, i.e. at l.

As for the case where the proof mass is composed also of iron foil on both sides, Figure 2.2, all longitudinal parameters remain the same respect to the previous case. The iron foil thickness is defined as h_M and extends on both sides of the beam and the total proof mass' mass is defined as M_2. As expected, the center of mass is vertically shifted upwards respect to Figure 2.1, into the silicon cantilever area. However, it is important to note that longitudinal-wise the position of the center of mass does not change, i.e. it is located at $l = L_M/2$.

2.2.1 Stress and displacement field

Besides the symmetry relations used in section 2.1, further assumptions are implemented in order to simplify the analytic model. As will be described in Chapter 6, the length of the beam is an order of magnitude larger than the thickness of it, therefore it is oftentimes assumed that all other stresses than T_1 are zero. However, the width of the beam is comparable to its length, therefore T_2 becomes non-zero and, since the edges are not free to move, $S_2 = 0$. This leads to the stress being expressed as $\mathbf{T} = (T_1, T_2, 0, 0, 0, 0)$. Furthermore, shear stresses are small and therefore neglected in the electric field contribution. Also due to the much

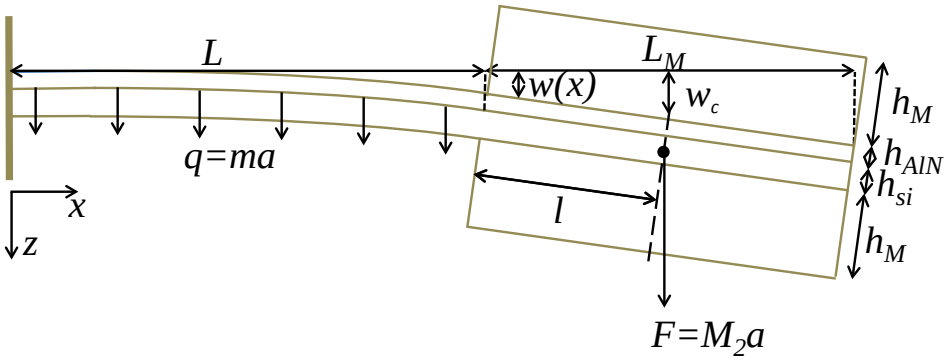

Figure 2.2: *Sketch of the second VEH described in the analysis. It consists of a silicon beam anchored in one end. The proof mass is composed of two ferromagnetic foils placed on either side of the beam.*

smaller thickness than length and width, the electric field is at all times considered in the z component, i.e. $\mathbf{E} = (0, 0, E_3)$. As a result of these assumptions, equations 2.1 and 2.2 are simplified to

$$S_1 = s_{11}^E(1-\nu^2)T_1 + d_{31}(1+\nu)E_3 \tag{2.6}$$

and

$$D_3 = d_{31}\,(1+\nu)\,T_1 + \left(\epsilon_{33}^T - \frac{{d_{31}}^2}{s_{11}^E}\right) E_3\ , \tag{2.7}$$

where $\nu = s_{12}^E/s_{11}^E$ is the Poisson's ratio. These equations can more simply be expressed as

$$S_1 = s^E T_1 + dE_3 \tag{2.8}$$

and

$$D_3 = \epsilon^T E_3 + dT_1\ , \tag{2.9}$$

where the new constants are defined as

$$s^E = s_{11}^E(1-\nu^2) \quad , \quad d = d_{31}(1+\nu) \quad , \quad \epsilon^T = \epsilon_{33} - \frac{{d_{31}}^2}{s_{11}^E}\ . \tag{2.10}$$

As will be more evident later, equations 2.8 and 2.9 can very conveniently be expressed as

$$T_1 = \frac{1}{s^E}S_1 - \frac{d}{s^E}E_3\ , \tag{2.11}$$

$$D_3 = \epsilon^T E_3 + d\left(\frac{1}{s^E}S_1 - \frac{d}{s^E}E_3\right) = \frac{d}{s^E}S_1 + \epsilon^T(1-{k_{\text{eff}}}^2)E_3\ , \tag{2.12}$$

where $k_{\text{eff}} = \sqrt{d^2/\epsilon^T s^E}$ is the effective piezoelectric coupling coefficient. Furthermore, the strain term S_1 presents two contributions: one from bending and another one from the stretching, as shown in the following equation

$$S_1 = u'(x) - zw''(x)\ , \tag{2.13}$$

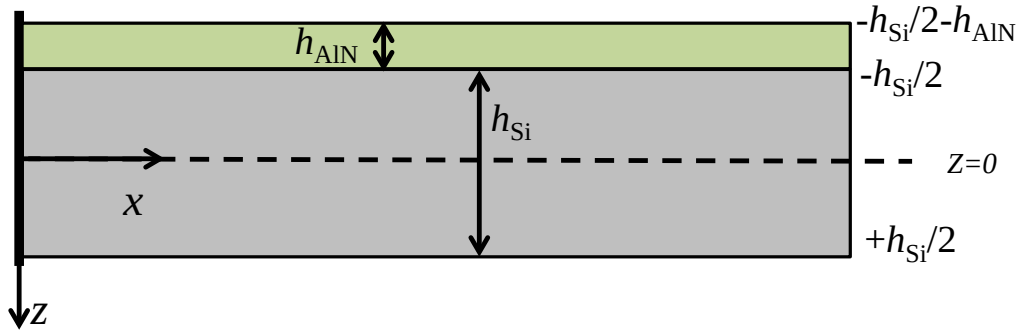

Figure 2.3: *Sideview of the vibrational system with a NS magnetic configuration. The silicon cantilever has integrated iron foils.*

where $u'(x)$ and $w''(x)$ represent, respectively, the change of length and the change of slope of the beam in the x-direction. Nevertheless, the strain due to bending scales as $4L/h$ times the bending due to stretching, where h is defined as the thickness of the beam and L its length. For the devices fabricated in this project, where $L = 3.5\,\text{mm}$ and $h \simeq 40\,\mu\text{m}$, this gives a strain due to bending that is 350 times larger than the one due to stretching. Therefore, equation 2.13 becomes

$$S_1 = -zw''(x)\ . \tag{2.14}$$

and equations 2.11 and 2.12 can be simplified to

$$T_1 = \begin{cases} -\frac{zw''(x)}{s^E_{AlN}} - \frac{d_{AlN}}{s^E_{AlN}} E_3 & \text{for } z < -h_{Si}/2 \\ -\frac{zw''(x)}{s^E_{Si}} & \text{for } z > -h_{Si}/2 \end{cases} \tag{2.15}$$

$$D_3 = \begin{cases} -\frac{d_{AlN}}{s^E_{AlN}} zw''(x) + \epsilon^T_{AlN}(1 - {k_{\text{eff}}}^2)E_3 & \text{for } z < -h_{Si}/2 \\ 0 & \text{for } z > -h_{Si}/2\ , \end{cases} \tag{2.16}$$

where the separate cases are easily understood by referring to Figure 2.3, from which it can be seen that $z < -h_{Si}/2$ and $z > -h_{Si}/2$ correspond to the silicon and AlN material parts, respectively.

2.2.2 Current and Voltage

When the beams deflect, the piezoelectric layer polarizes and a charge is induced at the electrodes. This induced charge can be found by applying Gauss' law on the AlN layer volume, this means that the displacement field in equation 2.16 is integrated over the AlN

volume and divided by its thickness

$$\begin{aligned} Q &= \oint_{\mathcal{S}} \mathbf{D}\,\mathrm{d}\mathbf{A} \\ &= W\int_0^L \frac{1}{h_{AlN}} \int_{-\frac{h_{Si}}{2}-h_{AlN}}^{-\frac{h_{Si}}{2}} D_3\,\mathrm{d}z\,\mathrm{d}x \\ &= W\int_0^L \frac{1}{h_{AlN}} \int_{-\frac{h_{Si}}{2}-h_{AlN}}^{-\frac{h_{Si}}{2}} -\frac{d_{AlN}}{s^E_{AlN}} z w''(x) + \epsilon^T_{AlN}(1-{k_{\text{eff}}}^2)E_3\,\mathrm{d}z\,\mathrm{d}x \\ &= W\int_0^L \frac{d_{AlN}}{2s^E_{AlN}}(h_{Si}+h_{AlN})w''(x) + \epsilon^T_{AlN}(1-{k_{\text{eff}}}^2)E_3\,\mathrm{d}x \\ &= \frac{d_{AlN}}{2s^E_{AlN}}(h_{Si}+h_{AlN})Ww'(L) + \frac{1}{h_{AlN}}\epsilon^T_{AlN}(1-{k_{\text{eff}}}^2)WLV \\ &= \Gamma w'(L) + CV\ , \end{aligned} \tag{2.17}$$

where C is the capacitance of the AlN layer at constant strain defined as $C = \epsilon^T_{AlN}(1-{k_{\text{eff}}}^2)WL/h_{AlN}$, V is the voltage over this capacitor defined as $V = h_{AlN}E_3$ and a coupling coefficient from cantilever end slope to charge is introduced as

$$\Gamma = \frac{d_{AlN}}{2s^E_{AlN}}(h_{Si}+h_{AlN})W \approx \frac{d_{AlN}}{2s^E_{AlN}}h_{Si}W\ . \tag{2.18}$$

In order to find the current, the time derivative of the charge is taken

$$I = \frac{\partial Q}{\partial t} = \dot{Q} = \Gamma\dot{w}'(L) + C\dot{V} \tag{2.19}$$

A back-coupling effect also takes place through the piezoelectric film, which consists on a bending produced by the charges induced in the AlN film. The internal bending moment M created in the cantilever by the field is

$$\begin{aligned} M &= \int zT_1W\,\mathrm{d}z \\ &= \int_{-\frac{h_{Si}}{2}-h_{AlN}}^{-\frac{h_{Si}}{2}} z\left(-\frac{zw''(x)}{s^E_{AlN}} - \frac{d_{AlN}}{s^E_{AlN}}E_3\right)W\,\mathrm{d}z + \int_{-\frac{h_{Si}}{2}}^{\frac{h_{Si}}{2}} z\left(-\frac{zw''(x)}{s^E_{Si}}\right)W\,\mathrm{d}z \\ &= -\frac{1}{3}W\left(\frac{{h_{Si}}^3}{4s^E_{Si}} + \frac{1}{s^E_{AlN}}\left[\left(\frac{h_{Si}}{2}+h_{AlN}\right)^3 - \frac{{h_{Si}}^3}{8}\right]\right)w''(x) \\ &\qquad + \frac{d_{AlN}}{2s^E_{AlN}}(h_{Si}+h_{AlN})Wh_{AlN}E_3\ , \end{aligned} \tag{2.20}$$

where the AlN thickness compared to the silicon one can be neglected, which leads to

$$M = -\frac{1}{12s^E_{Si}}W{h_{Si}}^3w''(x) + \frac{d_{AlN}}{2s^E_{AlN}}h_{Si}WV\ . \tag{2.21}$$

Considering that Young's modulus is $Y = 1/(s^E_{Si})$, that the moment of inertia along the x-direction of the beam is given as $I_{\text{eff}} = Wh^3_{Si}/12$ and the relation given by equation 2.18, the internal bending moment is finally expressed as

$$M = -YI_{\text{eff}}w''(x) + \Gamma V\ . \tag{2.22}$$

Both equation 2.19 and 2.22 are of relevant importance for understanding the systems developed in this thesis. The two of them depend on derivatives of $w(x)$, for which an expression is found in the next section.

2.3 Deflection and deflection slope

In order to find the relation between deflection and deflection slope of the cantilever, Euler Bernoulli static beam equation is used under the assumptions of small deflections, constant stiffness and constant moment of inertia

$$YI_{\text{eff}}\frac{\mathrm{d}^4 w(x)}{\mathrm{d}x^4} = q \ , \tag{2.23}$$

where q is the force per unit length of the cantilever. The following boundary conditions are used to solve the equation:

i The beam is anchored at $x = 0$,

$$w(x=0) = 0 \ . \tag{2.24}$$

ii The beam at the anchoring point is horizontal,

$$\left.\frac{\mathrm{d}w(x)}{\mathrm{d}x}\right|_{x=0} = 0 \ . \tag{2.25}$$

iii From equation 2.22 and considering the bending moment due to the proof mass at $x = l$,

$$\left.\frac{\mathrm{d}^2 w(x)}{\mathrm{d}x^2}\right|_{x=L} = \frac{lF + \Gamma V}{YI_{\text{eff}}} \ . \tag{2.26}$$

iv The last boundary condition is found by differentiating 2.22 respect to x,

$$\left.\frac{\mathrm{d}^3 w(x)}{\mathrm{d}x^3}\right|_{x=L} = -\frac{F}{YI_{\text{eff}}} \ . \tag{2.27}$$

The solution to the differential equation 2.23 becomes

$$w(x) = \frac{\Gamma V}{2YI_{\text{eff}}}x^2 + \frac{4F(3l+3L-x) + q(6L^2 - 4Lx + x^2)}{24YI_{\text{eff}}}x^2 \ , \tag{2.28}$$

from which the deflection slope is found to be

$$w'(x) = \frac{\Gamma V}{YI_{\text{eff}}}x + \frac{3F(2l+2L-x) + q(3L^2 - 3Lx + x^2)}{6YI_{\text{eff}}}x \ . \tag{2.29}$$

In the case of no external vibration force acting on the beam and a voltage applied to the piezoelectric material, equations 2.28 and 2.29 are written instead as, respectively,

$$w(x) = \frac{\Gamma V}{2YI_{\text{eff}}}x^2 \tag{2.30}$$

and

$$w'(x) = \frac{\Gamma V}{Y I_{\text{eff}}} x \ . \tag{2.31}$$

In order to find the deflection of the proof mass, the assumption of no bending of the proof mass and therefore a tangent line deflection assumption at the end of the beam length, i.e. $x = L$, is applied. By defining the deflection at the $x = L + l$ as w_c the following relation is found

$$w_c = w(L) + l w'(L) \equiv \Lambda w'(L) \ , \tag{2.32}$$

where Λ is defined as a geometric length factor between the deflection slope at L and at the proof mass. This factor is analyzed in short-circuit conditions where $V = 0$ and, therefore, the beam behaviour is purely mechanical. Using both $F = M_{1,2}a$ (where the subscript 1,2 refers to the two types of beams described in Section 2.2) and $q = ma$ in equations 2.28 and 2.29 the following expression is obtained

$$\Lambda = \left. \frac{w(L) + l w'(L)}{w'(L)} \right|_{V=0} = \frac{L^2(4l + 3L)m + 8(3l^2 + 3lL + L^2)M_{1,2}}{4(L^2 m + 6l M_{1,2} + 3L M_{1,2})} \ , \tag{2.33}$$

where it is important to note that Λ is independent on acceleration. Furthermore, by using equation 2.28 and considering an external force $F_{ext} = a(M_{1,2} + mL)$ the spring constant evaluated at $x = L + l$ is therefore

$$k_c = \frac{a(M_{1,2} + Lm)}{w_c} = \frac{a(M_{1,2} + mL)}{w(L) + l w'(L)} = \frac{24(M_{1,2} + mL) Y I_{\text{eff}}}{L^3(4l + 3L)m + 8L(3l^2 + 3lL + L^2)M_{1,2}} \ , \tag{2.34}$$

from which it can be observed that the spring constant is independent on acceleration as well. From this expression, the effective mass associated to the system can be easily found by applying

$$m_{\text{eff}} = \frac{k_c}{w_0^2} \ , \tag{2.35}$$

where an expression for the first mode resonant frequency w_0 is needed. This expression is found in the following section.

2.4 Mechanical resonant frequency

The highest possible power output happens when the beams deflect the most, which leads to the largest possible stresses. This happens when the beams vibrate at their resonant frequencies. Among the different modal resonant frequencies, the fundamental one is the most important in this project. This is due to the fact that, as described in Chapter 1, most ambient frequencies extend over a very low frequency range, which are the frequencies that the EH's must match in order to harvest the highest possible power. As it is well known, the fundamental mode presents the lowest possible resonant frequency. Therefore, in this work only the fundamental frequency is of interest and an expression for this important value must be found. To this end, the Rayleigh-Ritz method of maximum energy can be used. For small

deflections, the cantilever can be considered as a spring and can thus be described as a second order linear system [55]. For such a system, the maximum kinetic energy and the maximum potential energy equate when operating at resonance. In order to find both potential and kinetic energies an expression for the deflection of the beams as a function of time must be used. In the Rayleigh-Ritz method, it is assumed that under sinusoidal excitation, the system motion is equal to a quasi-static spatially dependent trial function multiplied by a time dependent sinusoidal function

$$\xi(x,t) = w(x)\cos(\omega t)\ , \tag{2.36}$$

where $w(x)$ is the spatial function from equation 2.28, t is the time variable and ω is the angular frequency of motion. The maximum potential energy of a deformed body as a deflected cantilever can be found by calculating the total strain energy, which is given by

$$E_{\text{pot}} = \frac{1}{2}\int_V \mathbf{TS}\,\mathrm{d}V = \frac{1}{2}\int_V T_1S_1 + T_2S_2 + T_3S_3 + T_4S_4 + T_5S_5 + T_6S_6\,\mathrm{d}V\ , \tag{2.37}$$

where the integral is taken over the entire volume of the elastic body. It must be noted that the system reaches its maximum potential energy when the deflection $\xi(x,t)$ is maximum, which happens when $|\cos(\omega t)| = 1$. By using equations 2.13 and 2.15 together with $S_2 = S_4 = S_5 = S_6 = T_3 = 0$ and $E_3 = 0$, i.e. the mechanical resonant frequency corresponds to the beam in short circuit, the maximum potential energy is found as

$$\begin{aligned}
E_{\text{pot}} &= \frac{1}{2}\int_0^L\int_0^W\int_{-\frac{h_{Si}}{2}-h_{AlN}}^{\frac{h_{Si}}{2}} T_1S_1\,\mathrm{d}z\,\mathrm{d}y\,\mathrm{d}x \\
&= \frac{W}{2}\int_0^L\left[\int_{-\frac{h_{Si}}{2}-h_{AlN}}^{\frac{-h_{Si}}{2}}\left(-\frac{zw''(x)}{s^E_{AlN}}\right)(-zw''(x))\ \mathrm{d}z\right. \\
&\qquad\left. + \int_{-\frac{h_{Si}}{2}}^{\frac{h_{Si}}{2}}\left(-\frac{zw''(x)}{s^E_{Si}}\right)(-zw''(x))\ \mathrm{d}z\right]\mathrm{d}x \\
&= \frac{W}{2}\int_0^L w''(x)\left[\frac{1}{s^E_{AlN}}\left(\frac{1}{3}\left(\frac{h_{Si}}{2}-h_{AlN}\right)^3 - \frac{{h_{Si}}^3}{24}\right) + \frac{{h_{Si}}^3}{12s^E_{Si}}\right]\mathrm{d}x \\
&\approx \frac{W}{2}\int_0^L w''(x)\frac{{h_{Si}}^3}{12s^E_{Si}}\,\mathrm{d}x = \frac{YI_{\text{eff}}}{2}\int_0^L w''(x)\,\mathrm{d}x\ ,
\end{aligned} \tag{2.38}$$

where the strain in the proof mass is neglected due to its must larger thickness and the AlN layer thickness is as well neglected due to $h_{AlN} \ll h_{Si}$. Regarding the kinetic energy, it reaches its maximum value when the associated velocity is at maximum. To find the expression for the velocity, equation 2.36 can be differentiated respect to time

$$\frac{\mathrm{d}\xi(x,t)}{\mathrm{d}t} = \frac{\mathrm{d}}{\mathrm{d}t}\left\{w(x)\cos(\omega t)\right\} = -\omega w(x)\sin(\omega t)\ , \tag{2.39}$$

from this expression it can be easily seen that maximum velocity happens when $|\sin(\omega t)| = 1$. Therefore, the kinetic energy can be found from

$$\begin{aligned} E_{\text{kin}} &= \int_0^L \frac{1}{2} m(\omega w(x))^2 \,\mathrm{d}x + \int_L^{L+L_M} \frac{1}{2} \frac{M_{1,2}}{L_M} (\omega \rho(x))^2 \,\mathrm{d}x \\ &= \omega^2 \left(\frac{m}{2} \int_0^L w(x)^2 \,\mathrm{d}x + \frac{M_{1,2}}{2L_M} \int_L^{L+L_M} \rho(x)^2 \,\mathrm{d}x \right) , \end{aligned} \tag{2.40}$$

where $\rho(x)$ is the linear displacement of the proof mass defined as

$$\rho(x) = (x - L)w'(L) + w(L) \, . \tag{2.41}$$

Finally, by setting $E_{pot} = E_{kin}$, the fundamental resonant frequency of the beam operated at short-circuit conditions is found to be

$$\omega_0 = \sqrt{\frac{Y I_{\text{eff}} \int_0^L w''(x)^2 \,\mathrm{d}x}{m \int_0^L w(x)^2 \,\mathrm{d}x + \frac{M}{L_M} \int_L^{L+L_M} \rho(x)^2 \,\mathrm{d}x}} \, , \tag{2.42}$$

which more simply can be expressed as

$$\omega_0 = 6\sqrt{7} \cdot \sqrt{\frac{h_{\text{Si}}^3 (5F^2(4L^2 + 6LL_M + 3L_M^2) + 5FL^2(3L + 2L_M)q + 3L^4q^2)WY}{\xi}} \, , \tag{2.43}$$

where ξ is used for simplifying the expression and it reads as

$$\begin{aligned} \xi = 36F^2L(L^3(132L^2 + 182LL_M + 63L_M^2)m + 35(16L^4 + 48L^3L_M + 63L^2L_M^2 + 42LL_M^3 + \\ + 12L_M^4)M) + 9FL^3(L^3(413L + 284L_M)m + 140(12L^3 + 26L^2L_M + 23LL_M^2 + \\ + 8L_M^3)M)q + 7L^5(104L^3m + 15(27L^2 + 36LL_M + 16L_M^2)M)q^2 \, . \end{aligned} \tag{2.44}$$

2.5 Equivalent circuit model

The EH's can be entirely modelled in electrical terms. The electrical domain of the beam is straightforwardly implemented, where the voltage between the electrodes is represented as V and the capacitance associated as a capacitor with impedance Z_C, as shown in Figure 2.4. The mechanical domain of the cantilever is modelled by translating the spring-mass-damper system associated to a beam into electrical terms [56, 57]. This means that the mass is represented by an inductance, the spring as a capacitor and the damping as a resistor, the associated impedances are, respectively, represented by Z_m, Z_s and Z_d, defined as

$$Z_m = jwm_{\text{eff}} \quad , \quad Z_s = \frac{k_c}{jw} \quad and \quad Z_d = b \, , \tag{2.45}$$

where j is the imaginary factor, m_{eff} the effective mass defined in equation 2.35, k_c the associated spring constant and b the mechanical damping. Therefore, the total mechanical impedance can be expressed as

$$Z_{\text{mec}} = \frac{1}{2\pi f C_{\text{s}} j} + 2\pi f L_{\text{m}} j + R_{\text{d}} \ . \tag{2.46}$$

In order to couple both the electrical and mechanical domains the coupling coefficients from equations 2.18 and 2.33 are used, which are referred to as transformers in the electrical equivalent circuit, as shown in Figure 2.4. To the end of fully implementing the EH's system, some other representations must be included. In the electrical domain a resistor R_l represents the load resistance connected to the harvester through which the generated power is extracted. The electrical impedance Z_{el} is therefore

$$Z_{\text{el}} = \frac{R_l}{1 + jwCR_l} \ , \tag{2.47}$$

where C represents the piezoelectric associated capacitor. By combining equations 2.46 and 2.47 one finally obtains the total impedance, which reads as

$$Z_{\text{total}} = \frac{1}{2\pi f C_{\text{el}} j + \left((2\pi f C_{\text{s}} j)^{-1} + 2\pi f L_{\text{m}} j + R_{\text{d}}\right)^{-1}} \ . \tag{2.48}$$

Both the piezoelectric force F_{piezo} and the external force F_{ext} are incorporated in the mechanical domain, where the expression for the piezoelectric back-coupled force term can be found by coupling the electrical voltage V to the mechanical domain. From equation 2.22 and considering only the electrical part, one gets $M = \Gamma V$, by implementing $w_L = \Lambda w'_x(L)$ one finally gets

$$F_{\text{piezo}} = \frac{\Gamma}{\Lambda} V \ . \tag{2.49}$$

As can be seen from Figure 2.4, not only voltage drops must be coupled, but also electrical currents. In the following part of this section, Laplace transform relations are used in order to work in the frequency domain since this makes the analysis simpler than working in the time domain, as has been done in the previous part. By Laplace transforming equation 2.19 and using the geometric transforming factor Λ, one gets

$$\mathcal{L}(I) = \frac{\Gamma}{\Lambda} sW(s) + sCV(s) \ , \tag{2.50}$$

where the L function denotes the Laplace transform and the capitalized letters refer to the frequency domain respective function, which has been also indicated by representing the functions respect to $s = jw$. From the mechanical part of the circuit represented in Figure 2.4

$$F_{\text{piezo}} + F_{\text{ext}} = m_{\text{eff}} \ddot{w}_c + b\dot{w}_c + k_c w_c \ , \tag{2.51}$$

where by applying Laplace transformation relations the following equation is obtained

$$\mathcal{L}(F_{\text{ext}}) + \frac{\Gamma}{\Lambda} V(s) = (ms^2 + bs + k) W(s) \ . \tag{2.52}$$

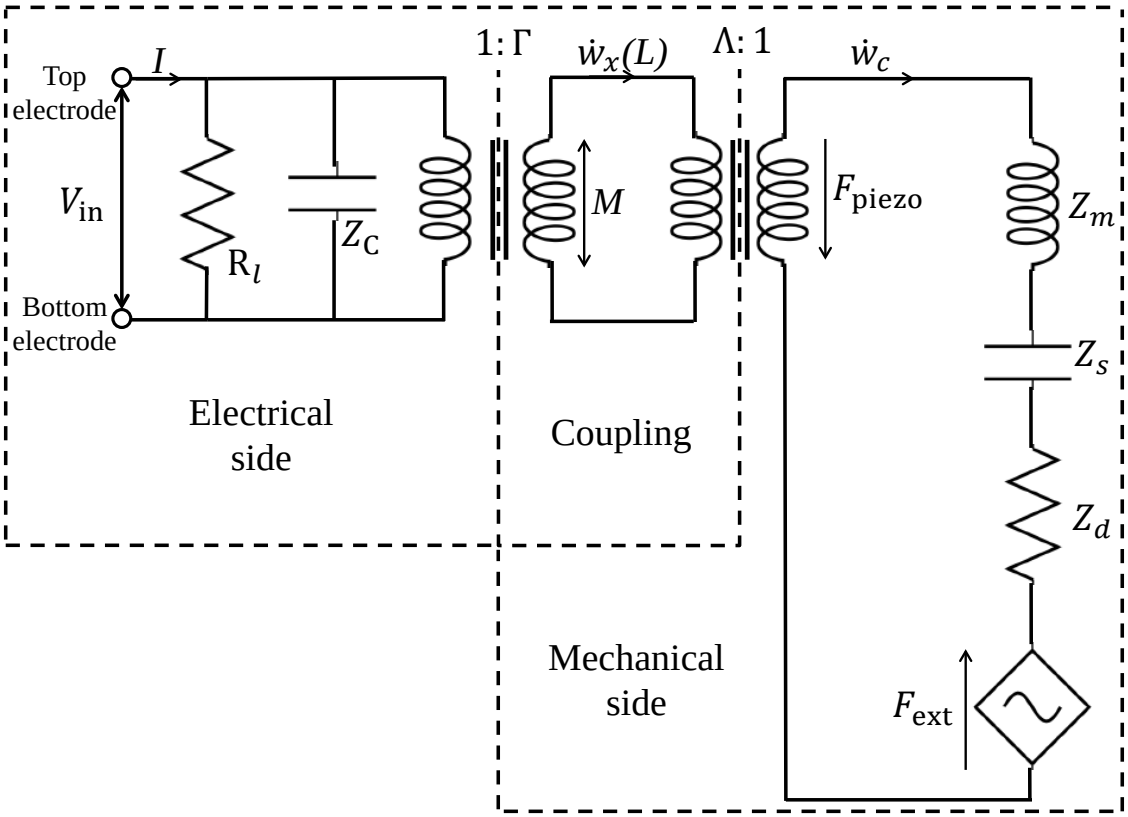

Figure 2.4: *Full equivalent circuit describing both mechanical and electrical side of the system, coupled by the transforming factors.*

It is of our interest to express equations 2.50 and 2.52 in terms of $\dot{W}(s)$ instead of in terms of $W(s)$, to this end it is used that $\dot{W}(s) = sW(s) \Rightarrow W(s) = 1/s\dot{W}(s)$, therefore both equations take the form of, respectively,

$$\mathcal{L}(I) = \frac{\Gamma}{\Lambda}\dot{W}(s) + sCV(s) \tag{2.53}$$

and

$$\mathcal{L}(F_{\text{ext}}) + \frac{\Gamma}{\Lambda}V(s) = \left(m_{\text{eff}}s + b + \frac{k_c}{s}\right)\dot{W}(s) \ . \tag{2.54}$$

By using basic electrical relations $I = \frac{-V}{R_l}$ and its Laplace transformed equation is $\mathcal{L}(I) = -\frac{1}{R_l}V(s)$, by equating this expression with equation 2.53 an expression for $\dot{W}(s)$ is obtained

$$\dot{W}(s) = \frac{\Lambda}{\Gamma}\left(-\frac{1}{R} + sC\right)V(s) \ . \tag{2.55}$$

By substituting equation 2.55 in equation 2.54 the following expression is obtained

$$\mathcal{L}(F_{\text{ext}}) + \frac{\Gamma}{\Lambda}V(s) = Z_{\text{mec}}\frac{1}{\Gamma}\left(-\frac{1}{R} + sC\right)V(s) \ , \tag{2.56}$$

where $Z_{\text{mec}} = m_{\text{eff}}s + b + k_c/s$. From equation 2.56 it is directly found that

$$V(s) = -\mathcal{L}(F_{\text{ext}})\frac{\Gamma/\Lambda}{(\Gamma/\Lambda)^2 + Z_{\text{mec}}/Z_{\text{el}}} \ , \tag{2.57}$$

which in the time domain is expressed as

$$V = -F_{\text{ext}}\frac{\Gamma/\Lambda}{(\Gamma/\Lambda)^2 + Z_{\text{mec}}/Z_{\text{el}}} \ , \tag{2.58}$$

from which finally an expression for the power extracted through R_l is obtained

$$P = \frac{|V|^2}{R_l} = \left|-F_{\text{ext}}\frac{\Gamma/\Lambda}{(\Gamma/\Lambda)^2 + Z_{\text{mec}}/Z_{\text{el}}}\right|^2\frac{1}{R_l} = \frac{|F_{\text{ext}}|^2}{R_l}\frac{(\Gamma/\Lambda)^2}{|(\Gamma/\Lambda)^2 + Z_{\text{mec}}/Z_{\text{el}}|^2} \ . \tag{2.59}$$

As can be seen from equation 2.59, the extracted power scales with F_{ext}, which is proportional to a_{in}, thus P is proportional to the square of the input acceleration (a_{in}^2).

2.5.1 Voltage versus deflection

From equation 2.50 and by using $I = -V_{\text{in}}/R_l$ one gets in the frequency domain (note that, for simplicity, the Laplace notation is not used in this subsection for the sake of simplicity, however, it will be specified when either time or frequency domain is used),

$$\begin{aligned} |V_{\text{in}}| &= \left|\frac{\Gamma}{\Lambda}\right|\left|\frac{s}{sC + 1/R_l}\right||w_c| \\ &= \left|\frac{\Gamma}{\Lambda}\right|\left|\frac{sR_l}{sCR_l + 1}\right||w_c| \ , \end{aligned} \tag{2.60}$$

which in the time domain and redefining $|V_{\text{in}}|$ as $|V|$ now reads as

$$\begin{aligned} |V| &= \left|\frac{\Gamma}{\Lambda}\right| \sqrt{\frac{w^2 R_l^2}{w^2 R_l^2 C^2 + 1}}\, |w_c| \\ &= \left|\frac{\Gamma}{\Lambda}\right| \sqrt{\frac{1}{C^2 + 1/(w^2 R_l^2)}}\, |w_c| \\ &= \left|\frac{\Gamma}{\Lambda C}\right| \sqrt{\frac{1}{1 + 1/(w^2 R_l^2 C^2)}}\, |w_c| \\ &= \left|\frac{\Gamma}{\Lambda C}\right| \sqrt{\frac{w^2 R_l^2 C^2}{1 + w^2 R_l^2 C^2}}\, |w_c| \ , \end{aligned} \tag{2.61}$$

therefore, the following equation is obtained

$$\left|\frac{V}{w_c}\right| = \left|\frac{\Gamma}{\Lambda}\right| \frac{w}{\sqrt{\frac{1}{R_l^2} + w^2 C^2}} \ , \tag{2.62}$$

which for open circuit conditions translates to

$$\left|\frac{V_{\text{OC}}}{w_c}\right| = \left|\frac{\Gamma}{\Lambda}\right| \frac{1}{C} \ . \tag{2.63}$$

For small values of the resistance in equation 2.62, it is found that $\left|\frac{V}{w_c}\right|$ is proportional to the load resistance, which is expressed as follows:

$$\left|\frac{V}{w_c}\right| = \left|\frac{\Gamma}{\Lambda}\right| w R_l \ . \tag{2.64}$$

Finally, from equation 2.62, if one now defines $\alpha = \left|\frac{V}{w_c}\right|$ and takes the inverse of its squared value, one obtains

$$\frac{1}{\alpha^2} = \left|\frac{\Gamma}{\Lambda}\right|^2 \frac{1}{R_l^2 w^2} + \left|\frac{\Gamma}{\Lambda}\right|^2 C^2 \ , \tag{2.65}$$

which will be usefull in Chapter 7 for finding the capacitande of the piezoelectric layer.

2.6 Optimal load and peak power

In order to harvest the maximal amount of power the optimal load conditions must be found. The ideal approach to finding this value is to differentiate expression 2.59 respect to both R_l and w simultaneously, which requires a highly complex treatment [58]. Instead of focusing on the power expression, a new method consisting in focusing on the piezoelectric device impedance was developed [59], which is briefly described in this section. By the Thevenin-Northon theorem, the piezoelectric device impedance can be found if both V_{OC} and I_{SC},

which are respectively the open circuit voltage and the short-circuit current, are known. Both expressions can be found from equation 2.58

$$\begin{aligned} V_{\mathrm{OC}} &= \lim_{R_l \to \infty} -F_{\mathrm{ext}} \frac{\Gamma/\Lambda}{(\Gamma/\Lambda)^2 + Z_{\mathrm{mec}} \frac{1+j\omega C R_l}{R_l}} = -F_{\mathrm{ext}} \frac{\Gamma/\Lambda}{(\Gamma/\Lambda)^2 + j\omega C Z_{\mathrm{mec}}} \\ I_{\mathrm{SC}} &= \lim_{R_l \to 0} -\frac{F_{\mathrm{ext}}}{R_l} \frac{\Gamma/\Lambda}{(\Gamma/\Lambda)^2 + Z_{\mathrm{mec}} \frac{1+j\omega C R_l}{R_l}} = -F_{\mathrm{ext}} \frac{\Gamma/\Lambda}{Z_{\mathrm{mec}}} \,, \end{aligned} \tag{2.66}$$

and from this the device impedance (Z) is expressed as

$$Z = \frac{V_{\mathrm{OC}}}{I_{\mathrm{SC}}} = \frac{Z_{\mathrm{mec}}}{(\Gamma/\Lambda)^2 + j\omega C Z_{\mathrm{mec}}} \,. \tag{2.67}$$

It is well known that maximum power is transferred when the impedance of the connected load Z_l matches the complex conjugate of the device impedance, i.e. $Z_l = Z^*$. The connected load is a resistance and, therefore, impedance matching can only happen when the phase angle of the device impedance is zero. The impedance expression can be expressed solely in terms of the system coupling coefficient K_{sys}, the mechanical quality factor Q_{mec}, the resonant frequency w_0, the electrical capacitance C and the external vibration frequency w by applying in equation 2.67 the following set of equations

$$Q_{\mathrm{mec}} = \frac{k_c}{b w_0} = \frac{m_{\mathrm{eff}} w_0}{b} = \frac{\sqrt{m_{\mathrm{eff}} k_c}}{b} \,, \tag{2.68}$$

$$K_{\mathrm{sys}}^2 = \frac{\Gamma/\Lambda^2}{k_c C} \,, \tag{2.69}$$

and equation 2.35. One finally gets

$$Z = -\frac{j}{w_0 C} \frac{j\frac{w}{w_0} + Q_{\mathrm{mec}} \left(1 - \frac{w^2}{w_0^2}\right)}{\frac{w}{w_0}\left[j\frac{w}{w_0} + Q_{\mathrm{mec}} \left(1 - \frac{w^2}{w_0^2}\right) + Q_{\mathrm{mec}} K_{\mathrm{sys}}\right]} \,, \tag{2.70}$$

which will become purely real if the angular frequency w_{real}^2 satisfies

$$\frac{w_{\mathrm{real}}^2}{w_0^2} = \frac{1}{2}\left(2 + K_{\mathrm{sys}}^2 \frac{1}{Q_{\mathrm{mec}}^2} \pm \sqrt{\left(K_{\mathrm{sys}}^2 - \frac{1}{Q_{\mathrm{mec}}^2}\right)^2 - \frac{4}{Q_{\mathrm{mec}}^2}}\right) \,, \tag{2.71}$$

which will become purely real if

$$K_{\mathrm{sys}}^2 Q_{\mathrm{mec}} - \frac{1}{Q_{\mathrm{mec}}} \geq 2 \,, \tag{2.72}$$

where the $K_{\mathrm{sys}}^2 Q_{\mathrm{mec}}$ is widely known as a coupling figure of merit (FOM) [59]. Three different cases are observed depending on the value of the coupling FOM, these cases are summarized now.

2.6.1 Branching point case

The branching point case is characterized by $K_{\text{sys}}^2 Q_{\text{mec}} = 2 + \frac{1}{Q_{\text{mec}}}$, where impedance matching is achieved at a single angular frequency w_{bp} given by

$$\frac{w_{\text{real}}^2}{w_0^2} = \frac{1}{2}\left(2 + K_{\text{sys}}^2 \frac{1}{Q_{\text{mec}}^2}\right) = \left(1 + \frac{1}{Q_{\text{mec}}}\right) , \tag{2.73}$$

at which the associated device impedance is given by

$$Z = R_{l\text{bp}} = \frac{1}{w_0 C} \frac{1}{1 + 1/Q_{\text{mec}}} \simeq \frac{1}{w_0 C} , \tag{2.74}$$

where the approximation is done for high enough Q_{mec}. In this case, the peak harvested power equals the available power P_{av} [59]

$$P_{\text{av}} = \frac{|F_{\text{ext,RMS}}|^2}{4b} = \frac{|F_{\text{ext,RMS}}|^2}{4 w_0 m_{\text{eff}}} Q_{\text{mec}} . \tag{2.75}$$

2.6.2 High-coupled case

The high-coupled case is characterized by $K_{\text{sys}}^2 Q_{\text{mec}} > 2$, and impedance matching is achieved at the two operating frequencies where the phase is zero degrees. These two optimal frequencies are directly obtained from equation 2.71 by either taking the positive or negative sign, from which a frequency close to the anti-resonant f_{pa} or resonant f_{pr} frequencies will be obtained, respectively. At these frequencies the associated impedance is found by taking either the negative or positive sign in equation 2.70

$$Z = R_{l\text{opt}} = \frac{1}{w_0 C} \frac{2}{K_{\text{sys}}^2 Q_{\text{mec}} + \frac{1}{Q_{\text{mec}}} \pm \sqrt{\left(K_{\text{sys}}^2 Q_{\text{mec}} - \frac{1}{Q_{\text{mec}}}\right)^2 - 4}} , \tag{2.76}$$

where the positive sign leads to the impedance associated to f_{pr} and the negative sign to the impedance associated to f_{pa}. At these two frequencies, since impedance matching is possible, the harvested power equals the available power defined in equation 2.75.

2.6.3 Low-coupled case

In the low-coupled case load matching is not possible and maximum harvested power is found at a frequency w_{pp} where the impedance phase is maximized

$$\frac{w_{\text{pp}}^2}{w_0} = \frac{1}{6}\left(2 + K_{\text{sys}}^2 - \frac{1}{Q_{\text{mec}}^2} + \sqrt{12\left(K_{\text{sys}}^2 + 1\right) + \left(2 + K_{\text{sys}}^2 - \frac{1}{Q_{\text{mec}}^2}\right)^2}\right) \simeq 1 + \frac{1}{2} K_{\text{sys}}^2 , \tag{2.77}$$

where the approximation is done at assumed sufficiently high mechanical quality factor (Q_{mec}) and small enough coupling coefficient (K_{sys}<0.4). The approximation in equation 2.77 can

Table 2.1: *Parameters and dimensions used in this section.*

Device parameter	symbol	Value
Cantilever width	W	6 mm
Cantilever length	L	3.25 mm
Proof-mass length	L_{M}	3.25 mm
Position center of mass	l	3.25/2 mm
Cantilever thickness	h_{Si}	40 μm
Fe foil thickness	h_{M}	150 μm
Proof mass thickness	$h_{\mathrm{M}} + h_{\mathrm{Si}}$	190 μm
AlN thickness	h_{AlN}	400 nm
Cantilever mass per length	m	$5.67 \cdot 10^{-4}$ Kg/m
Proof-mass mass	M_2	$4.78 \cdot 10^{-5}$ Kg
Quality factor (measured)	Q_{mec}	457
Silicon material constants		
Density	ρ_{Si}	2329 Kg/m^3
Compliance	S_{Si}	$6.66 \cdot 10^{-12}$ Pa^{-1}
Piossson's ratio	ν_{Si}	0.0606
AlN material constants		
Density	ρ_{AlN}	3225 Kg/m^3
Compliance	S_{11}	$2.889 \cdot 10^{-12}$ Pa^{-1}
Piossson's ratio	ν_{AlN}	0.3228
Permittivity	$\epsilon_{33}^{\mathrm{T}}$	$7.97 \cdot 10^{-11}$ F/m
Piezoelectric coefficient	d_{31}	$2.7 \cdot 10^{-12}$ C/N

be compared to the relation $f_{\mathrm{a}} = f_{\mathrm{r}}\sqrt{1+K_{\mathrm{sys}}^2}$, from which it can be inferred that $f_{\mathrm{pp}} = 2\pi w_{\mathrm{pp}}$ is approximately halfway between f_{a} and f_{r}. The associated optimal load resistance is approximately the same as in the branching point case, i.e. $R_{l\mathrm{pp}} \simeq 1/(w_0 C)$ and the harvested power can be inferred by inserting these conditions in equation 2.59

$$P_{\mathrm{p}} = P_{\mathrm{av}} \frac{8K_{\mathrm{sys}}^2 Q_{\mathrm{mec}}}{4 + K_{\mathrm{sys}}^4 Q_{\mathrm{mec}}^2 + 4K_{\mathrm{sys}}^2 Q_{\mathrm{mec}}} \equiv P_{\mathrm{av}}\Phi \ , \tag{2.78}$$

where Φ is introduced as a multiplication factor valid for this low-coupled regime.

2.7 Parameters and theoretical calculations

In this section, the theoretical values expected to be obtained are calculated following the equations presented throughout this chapter. Table 2.1 shows a list of the different parameters and dimensions used for the calculations, and Table 2.2 shows the results, which will serve later for discussion in Chapter 7. When necessary, the input acceleration considered is 0.8 g and the mechanical quality factor used is Q=457 (measured).

Table 2.2: *Theoretical results obtained by using the equations presented in this chapter and using the parameters listed in Table 2.1.*

Parameter	symbol	Value
Proof mass weight	M	$4.78 \cdot 10^{-5}$ Kg
Capacitance	C_{AlN}	3.74 nF
Coupling coefficient (slope to charge)	Γ	$1.13 \cdot 10^{-7}$ C
Geometric factor	Λ	0.0035 m
Transforming ratio	Γ/Λ	$3.24 \cdot 10^{-5}$ C/m
Spring constant	k_c	143.3 N/m
Resonant frequency	f_r	252.4 Hz
Effective mass	m_{eff}	$5.7 \cdot 10^{-5}$ Kg
Available power	P_{av}	178 μW
Harvester efficiency	Φ	0.85
Generalized electromechanical coupling coefficient	K_{sys}	0.044
Electromechanical FOM	$K_{\text{sys}}^2 Q$	0.9
Optimal load	R_{lbp}	169 KΩ
Power harvested	P_{p}	152 μW

2.8 Summary

The constitutive equations for piezoelectric materials were presented, where simplifications due to AlN properties were applied. Strain and displacement field expressions were also introduced, where it was used that the main contribution to strain is due to bending and the stretching factor can be neglected. The mechanical domain of the VEH's behaviour was linked to its electrical domain by a transforming factor that relates the charge created at the electrodes to the cantilever deflection slope. A geometric length factor was also used, which relates the deflection slope the end of the beam end (where the proof mass starts), and the deflection slope at the proof mass center of mass. The equivalent circuit model was also introduced, where not only the electrical part of the devices was analyzed, but also the mechanical one. The mechanical domain was transformed to the electrical domain by using the previously mentioned transforming and geometrical factors. Furthermore, the theoretical power harvested by the devices depending on their Q and K_{sys} associated was presented and calculated for the system under study.

Chapter 3

Broadband energy harvesting

In the previous chapter the fundamentals of vibration energy harvesting via cantilever-based devices was discussed. As it is easily seen, the main challenge in such a system is that the maximum system performance, i.e. maximum harvested power, is achieved when the VEH resonant frequency matches the external vibration source. However, most ambient vibrations present a frequency shift over time [24]. For that reason, continuously tuning the resonant frequency and widening the frequency bandwidth of the VEHs have become of utmost importance. As was introduced in Chapter 1, different methods have been investigated in order to extend the harvesting frequency range over which maximum harvested power can be obtained. Among the different methods available, the focus of this thesis is on exploiting non-linearities, as described also in Chapter 1.

The non-linear method can be classified into three types, hardening effect, softening effect and bistable behavior, where the hardening and softening effect have both been shown to increase the bandwidth of the VEH's in different frequency ranges each, as will be discussed in this chapter. In the bistable case, the cantilever's tip can present two different types of oscillations, intrawell and interwell. In the intrawell type, the tip oscillates around one of the stable positions, i.e. around either of the magnets, leading to small amplitude deflections, which translates to a low output power. In the interwell oscillations the tip swaps from one magnet to the other, which leads to larger deflections and consequently to larger output power. Nonetheless, maintaining high-energy interwell orbits in broadband energy harvesters has been recognized to present many difficulties due to the energy barrier that must be overcome to hop from one well to the other back and forth [25].

In this chapter the theoretical background needed to describe a broadband VEH is introduced. The system consists of a beam where ferromagnetic foil is incorporated on either side of it and a pair of externally located magnets interacting with the beam by magnetic forces, as depicted in Figure 3.1. The theoretical background consists on introducing the concepts in magnetism necessary to understand the magnetic interaction that takes place between the magnets and the beam, which includes FEM simulation results. The potential energy landscapes of the beam for different dimensional configurations of a and b (where a is the distance between the

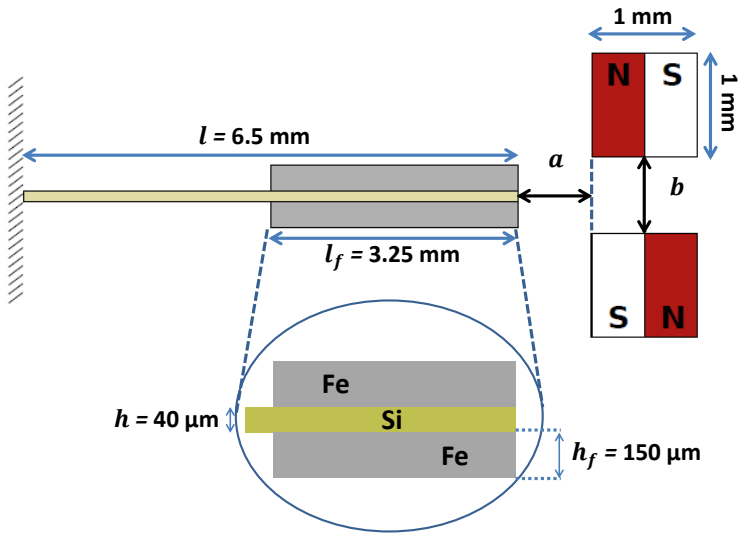

Figure 3.1: *Sideview of the vibrational system with a NS magnetic configuration. The silicon cantilever has integrated iron foils.*

magnets and the beam and b is the distance between the meagnets themselves), see Figure 3.1, are presented. Together with the potential landscapes, relevant parameters like the effective spring constant results are also shown two different magnets configurations and for a sweep over both a and b values. Furthermore Duffing equation is used to describe the motion of the beam's tip.

3.1 Forced Duffing oscillator

The Duffing equation is a non-linear second-order differential equation, it is extensively used to describe certain forced oscillator systems under damping conditions [18,41,60], as the system studied in this work. Erturk *et. al* [41] studied a ferromagnetic-based beam interacting with a pair of magnets. In their case, the device does not consist of a miniaturized VEH, instead, it is a 14.5 cm long beam made of ferromagnetic material. Furthermore, the beam is positioned vertically and the oscillations happen horizontally. Similar studies were performed by Cottone *et al.* [60] and Tam *et al.* [18]. For a piezoelectric generator, the Duffing equation reads as [60]

$$\ddot{x} m_{\text{eff}} = -\frac{dU}{dx}(x) - \gamma \dot{x} + F_{\text{in}}(t) \, , \tag{3.1}$$

where the one and two over-dots represent, respectively, first time and second time derivatives, x is the beam displacement, m_{eff} the effective mass, γ the damping coefficient, $F_{\text{in}}(t)$ the input or external force and $U(x)$ is the potential energy function defined as [49]

$$U(x) = \frac{(k-\alpha)}{2} x^2 + \frac{\beta}{4} x^4 \, , \tag{3.2}$$

where k is the linear spring constant associated to the system without magnetic forces acting on it, and α and β are two constants associated to the magnetic force $F_{\text{mag}} = \alpha x - \beta x^3$. By inserting equation 3.2 into equation 3.1, one finally gets

$$\ddot{x} m_{\text{eff}} = (k - \alpha)x + \beta x^3 - \gamma \dot{x} + F_{\text{in}}(t) \; . \tag{3.3}$$

The potential function defined in equation 3.2 is shown in Figure 3.2 for different α and β values. For all the curves, a linear spring constant of $k = 93.7$ N/m is taken. For the linear case, α and β are set to zero, this corresponds to the black curve in Figure 3.2. Associated to this curve one can find only one stable position at around $x = 0$, which corresponds to a mono-stable landscape, this holds the same for the other two cases where $\alpha - k < 0$ and $b > 0$ (red curves in Figure 3.2). In all these cases the movement of the beam is confined to the well centered at $x = 0$. On the other hand, for $\alpha - k > 0$ and $b > 0$ (blue curves in Figure 3.2) a bi-stable landscape is obtained, where two stable positions at $x = \pm\sqrt{\frac{\alpha-\kappa}{\beta}}$ are found. Besides to these stable solutions, an unstable solution at $x = 0$ can be observed. Here two types of dynamics can be observed. One corresponds to the beam oscillating between the two stable positions at $x = \pm\sqrt{\frac{\alpha-\kappa}{\beta}}$, in this case large amplitude oscillations are obtained. However, in order for these oscillations to take place, a potential barrier defined as Δ in Figure 3.2 needs to be overcome. In order to calculate this potentail barrier $\Delta = U(x = 0) - U(x = \sqrt{\frac{\alpha-\kappa}{\beta}})$ is used, by using equation 3.2 one gets $\Delta = (\frac{(\alpha-\kappa)^2}{4\beta})$. This potential barrier increases for increasing $\alpha - k$ values, which will eventually lead to the beam being confined to move around one of the stable solutions, which translates to small amplitude oscillations. From these different energy landscapes, it can be inferred that the optimal energy function is the one that presents as broad as possible a distance between stable positions and at the same time a small as possible potential barrier Δ.

By solving equation 3.3 numerically and plotting velocity respect to position a better insight is obtained regarding the different types of motion that can be observed. Figure 3.3a shows the motion associated to the mono-stable case, where the beam oscillates around its zero deflection point, which translates to small amplitude oscillations. Figure 3.3b corresponds to the bi-stable case, where the beam oscillates around one stable position. This is because the potential barrier Δ (see Figure 3.2) is large enough for the beam to overcome it, and therefore its movement is restricted to be around one of the magnets. If the acceleration (or input force) is large enough then the beam can hop the potential barrier and oscillate from one stable position to the other, however, the beam eventually collapses to the surroundings of one magnet due to damping, as seen in Figure 3.3c. Ideally, the potential barrier is as low as possible, i.e. the potential function is as flat as possible on the surroundings between the magnets. If this barrier is low enough, then the beam displacement is not restricted to one magnet and oscillates as shown in Figure 3.3d, which is the ideal type of oscillation due to its large amplitude.

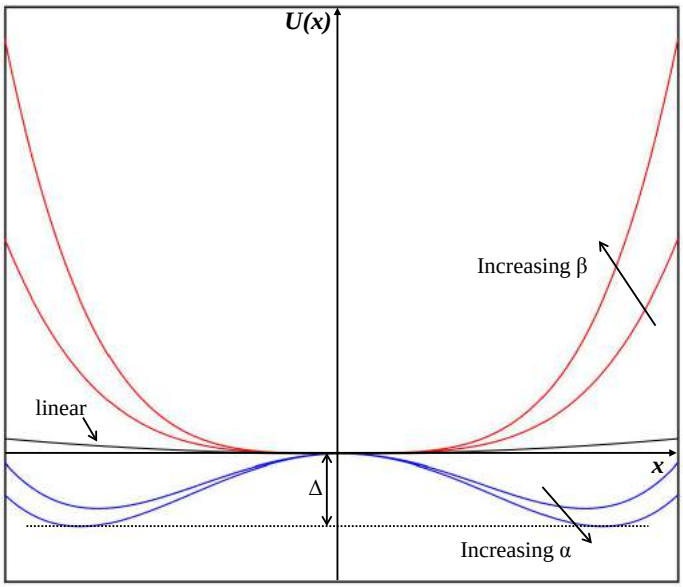

Figure 3.2: *Potential energy function for different α and β values. For the linear case $\alpha = 0$ and $b = 0$. For the bi-stable cases (blue lines), $\alpha - k > 0$. For the mono-stable cases $\alpha - k < 0$. For all the cases $k = 93.7$ N/m was used.*

3.2 Magnetic interaction

In the previous section the dynamics of the beam were explained. However, it was assumed that the value of the magnetic force was known. In this section, a brief description of the interaction between the ferromagnetic foils and magnets is presented, which constitute the basics of any electromagnetism book, for example [61].

3.2.1 Magnetic field and magnetization of materials

A magnetic material creates a magnetic field $\mathbf{H}$, by which it affects the surrounding space. Not all materials react to this field, therefore in order for the silicon beams to interact with the magnetic field ferromagnetic foil is incorporated on both sides of the beams. This ferromagnetic material will get magnetized, property represented by $\mathbf{M}$ and which is given by

$$\mathbf{M} = \chi \mathbf{H} \,, \tag{3.4}$$

where χ is the magnetic susceptibility, related to the relative permeability by $\mu_r = \chi + 1$. However, the magnetic field $\mathbf{H}$ is composed of two terms $\mathbf{H} = \mathbf{H}_0 + \mathbf{H}_d(\mathbf{M})$, where $\mathbf{H}_d$ is the demagnetized field produced by the ferromagnetic foil. Substituting this last expression,

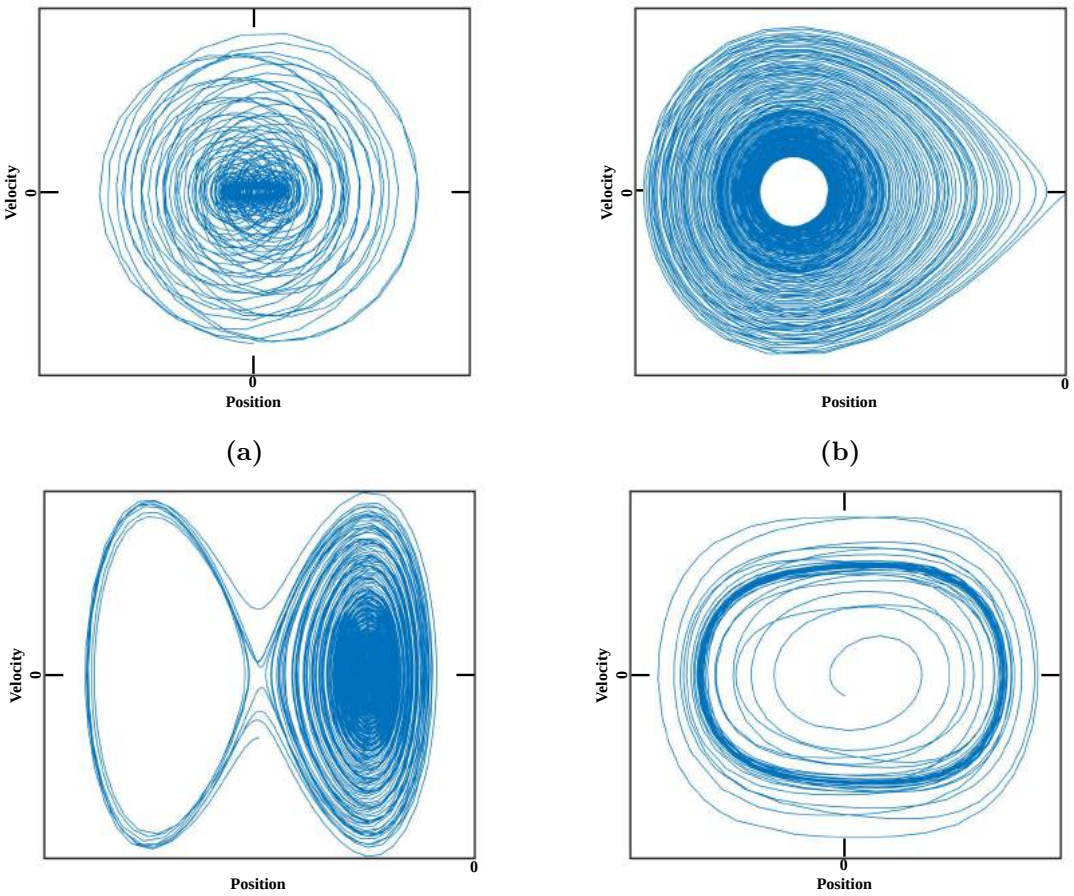

Figure 3.3: *Different position-velocity phases that correspond to four different dynamics. a) Mono-stable, the beam oscillates around zero tip deflection with small amplitude oscillations. b) Bi-stable with small amplitude oscillations around one of the stable positions, i.e. around one of the magnets. c) Bi-stable with large amplitude oscillations in the beginning whereas in the end the beams is confined to one well. d) Flat potential landscape, the beam performs large amplitude oscillations.*

equation 3.4 is more precisely expressed as

$$\mathbf{M} = \chi \left[\mathbf{H}_0 + \mathbf{H}_d(\mathbf{M})\right] \ , \tag{3.5}$$

where it can be easily seen that the problem is recursive: in order to find the magnetization the demagnetization field due to the magnetization itself must be known. For very simple geometries like ellipsoids or spheres, the demagnetization factor is easily calculated. However, for structures like the rectangular foils used in this project this is not possible.

A magnetic force is associated to this interaction, this force is given by

$$\mathbf{F} = \int\int\int_V \mathbf{M} \cdot \nabla \mathbf{B}^0 \ , \tag{3.6}$$

where $\mathbf{B}^0 = \mu_0 \mathbf{H}_0$ and ∇ is the divergence symbol.

3.2.2 Analytical model

Tam *et al.* [18] derived an analytical model based on the dynamic beam equation. Their experimental set-up consisted of a steel beam vertically located between two cylindrical magnets, as it was depicted in Figure 1.12a, Chapter 1. The beam presented dimensions of $11x1\,\text{cm}$ with a thickness of $250\,\mu\text{m}$. This set-up can be compared to the one studied in this project and three main differences stand out: the beam dimensions, the magnets shape and the magnets-beam interaction, i.e. in their case no ferromagnetic foil was necessary to be attached. In a bachelor project that was carried out in our group [62], an analytical model inspired in [18] was developed. In that model the piezoelectric effect is ignored and only the mechanical domain is analyzed, this means that the piezoelectric layer is neglected. The analytical model developed is not accurate enough mainly due to the assumptions used for the magnetization field, where it was assumed that no demagnetizing field was present, i.e. $\mathbf{H}_d = 0$ and that the resulting magnetization was linear in H. Furthermore, the magnetic field expression was evaluated assuming cylindrical magnets instead of rectangular ones.

3.3 Finite Element Method (FEM) studies

In order to have a more accurate description of the system presented in this work, FEM studies are performed using COMSOL Multiphysics 5.2 software [63]. The model used was initially developed by Anders Lei, PhD. It performs the calculation under static conditions and not in dynamic mode for the sake of diminishing an already long computational time. However, once the relevant values are obtained from these simulations, the Duffing model described in section 3.1 can be used if a dynamic description is needed, which is done at the end of this section. A schematic of the system under consideration is shown in Figure 3.1, where a North-South (NS) configuration for the magnets is used. Each capitalized letter refers to the pole of the magnet closest to the beam. Due to symmetry, out of the possible four configurations, only NS and NN configurations are analyzed in this study.

Table 3.1: *Dimensional and material parameters used for the simulations.*

Device parameters	Values
Beam length l	6.5 mm
Beam thickness h	40 μm
Foil length l_f	3.25 mm
Foil thickness h_f	150 μm
Magnet length	1 mm
Magnet thickness	1 mm
Magnetization M_{mag}	750 kA/m
Si Young modulus	150 GPa
Foil relative permeability	$\mu_r = 4000$

3.3.1 Components and materials

The system under study is composed of a silicon beam, two pairs of iron foil modeled as soft magnetic material with $\mu_r = 4000$ and two rectangular magnets. These magnets are made of NdFeB with an associated constant magnetization that changes sign depending on the magnets orientation, i.e. $M = \pm M_{\text{mag}}$. It is important to note that the iron foils are assumed to present no hysteresis and the magnetization is assumed to be linear in H. Relevant values together with the dimensions used are the ones shown in Table 3.1 and Figure 3.1.

3.3.2 Simulation procedure

The simulation combines two COMSOL modules: Solid Mechanics and Magnetic Fields and consists of three main steps. Firstly, a uniformly distributed input force (F_{in} in equation 3.3) is applied on the whole cantilever structure. Due to this input force the cantilever deflects and its new position is found in the second step. It is important to note that the exact location of the point on the beam's tip followed is the center of mass, this applies to all the parts of the analysis. Since the magnetic forces are neglected until now, this means that

$$F_k = ky(F_{\text{in}}) = -F_{\text{in}} \Rightarrow k = -\frac{\partial F_{\text{in}}}{\partial y} \, , \tag{3.7}$$

where y is the deflection of the beam in the vertical direction. Therefore, the associated linear spring constant can easily be calculated by using equation 3.7. The third step consists on the calculation of the magnetic force associated to that tip deflection. The magnetic force found from the simulation is given as a distributed force, i.e. with no specification of where on the beam the force is acting, and it is given in both dimensional components $F_{\text{mag,x}}$ and $F_{\text{mag,y}}$. As the tip deflection mainly depends on $F_{\text{mag,y}}$, only this component is considered in the analysis. From this, the equation of motion reads as

$$m_{\text{eff}}\ddot{y} = -ky + F_{\text{mag,y}}(y) = F_{\text{tot}}(y) \, . \tag{3.8}$$

It is well known that in order to find the potential energy associated to a force one must apply

$$U = -\int F dy \ , \tag{3.9}$$

where U is the potential energy and F represents either the magnetic, the spring or the total force associated to the beam in the y direction. Therefore, in order to find the potential energy from the simulation's output a mathematical tool can be used to perform a numerical integration of the resulting forces with respect to the tip displacement. Similarly to equation 3.7, the associated *non-linear* effective spring constant k_{eff} can be calculated by applying

$$k_{\text{eff}} = -\frac{\partial F_{\text{tot}}}{\partial y} \ , \tag{3.10}$$

which, compared to the linear spring constant k, is *not* a constant value through the different tip deflections generally speaking.

The aim when performing these simulations is both to find the potential landscapes of the tip displacement and the effective spring constant contour plot at around zero tip deflection. From this, the ideal dimensional values a and b for the two different magnets configurations will be estimated. As for the case of the potential landscapes, a set of input forces in the range $[-0.075, +0.075]$ N are applied to the system at specific values of a and b. These simulations were run for both NN and NS configurations.

Figure 3.4a shows the total potential energy landscape associated to the case of NS configuration for the three possible landscapes: bistable, flat potential and monostable cases. They correspond to $a = 200, 564$ and $1000\,\mu m$, respectively, all of which correspond to $b = 500\,\mu m$. Together with those cases, the linear case of no magnetic forces incorporated is also considered. Similarly, Figure 3.5a shows the total potential energy landscapes for the NN configuration case, where the different a values taken in this case are $a = 200, 385.5$ and $1000\,\mu$m, which correspond respectively to the bistable, flat potential and monostable cases. In all these cases $b = 500\,\mu m$ as well.

For the linear case, i.e. no magnets considered, a linear spring constant of $120.8\,\text{N/m}$ is found. Regarding the associated effective spring constants to all the different cases, Table 3.2 shows them, where for the bistable cases two different spring constants are shown for each NN and NS configurations. The reason is that the spring constants were calculated regarding each of the wells associated to the bistable landscape, the first values on the first row correspond to the ones associated to the possitive branch, whereas the ones on the second row correspond to the negative branch. As for the flat potential case, the spring constant taken was the one associated to zero deflection.

For the sake of completeness, Figures 3.4b and 3.5b show the total force associated to the three landscapes found in Figures 3.4a and 3.5a (only with magnets incorporated). As described above and indicated by equation 3.10, the effective spring constant can be found by calculating the slope around zero tip deflection. The blue curves in both Figures 3.4b and 3.5b corresponds to the monostable case, here the slopes are negative, however$-\partial F_{\text{tot}}/\partial y$ gives positive slope

Table 3.2: *Effective spring constants associated to the different cases considered. For the bistable cases, two spring constants are given for each magnets configuration, they correspond to the potential wells.*

Linear	Monostable		Bistable		Flat	
	NS	NN	NS	NN	NS	NN
120.8 N/m	90.66 N/m	136.5 N/m	428.3 N/m	283.9 N/m	0.9 N/m	1.7 N/m
			428.4 N/m	283.9 N/m		

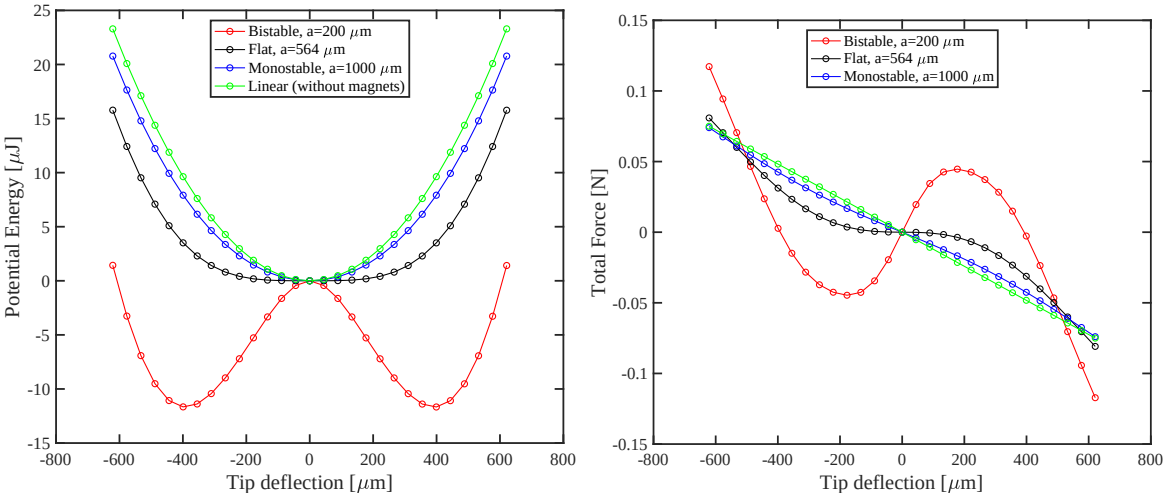

(a) **(b)**

Figure 3.4: *a) Total potential energy for a system without magnets and for* $b = 500\,\mu$m *with three different values for the distance between the cantilever tip and magnets:* $a = 200\,\mu$m, $564\,\mu$m *and* $1000\,\mu$m. *b) Total force respect to tip deflection for all the cases just presented. NS magnets configuration was used.*

sign. The black curves are flat around zero tip deflection, and therefore the associated slopes are about zero. Finally, the red curves correspond to the bistable case, around zero tip deflection the slopes are positive, which after the change of sign gives a negative slope sign.

It is of interest to find the values of a and b that lead to a flat potential landscape. The importance of the slope at zero tip deflection in order to find the effective spring constant has been explained. This means that, if the aim is to obtain a set of dimensional parameters that lead to the different landscapes, in order to reduce computational time it is *not* necessary to perform the simulations at all the input forces described above. Therefore, in this part of the study a slightly different approach is taken. Only three input forces are considered, centered at zero tip deflection, i.e. $F_{\text{in}} = 0$, and the a and b values are finely meshed from 0 to $2000\,\mu$m. The results for both NN and NS configurations are shown in Figures 3.6a and 3.6b, respectively. The line depicted as showing a zero spring constant determines the contour between the monostable and bistable cases, which at zero tip deflection present positive and negative spring constants, respectively. It can be seen that the NN configuration presents a

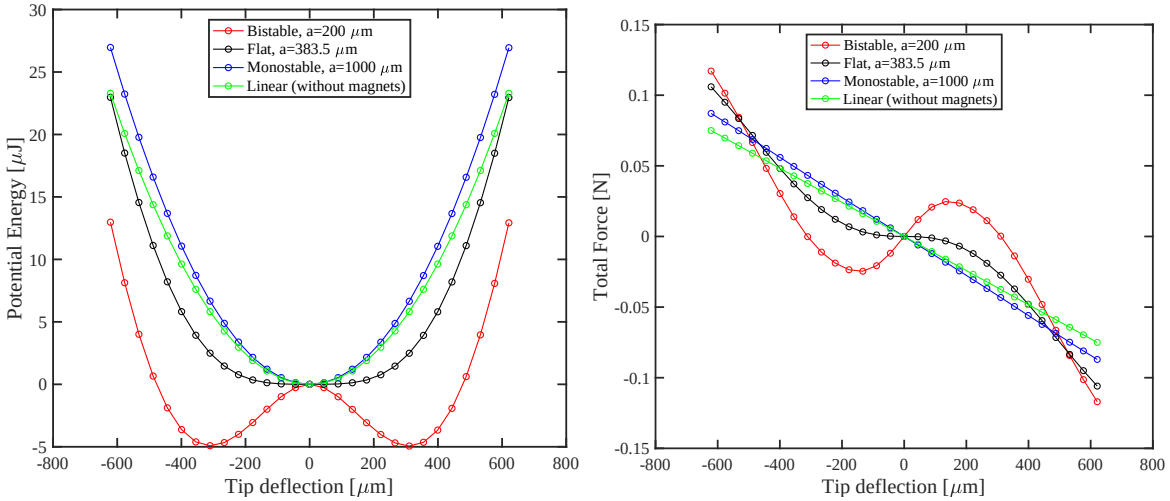

(a) **(b)**

Figure 3.5: *a) Total potential energy for a system without magnets and for* $b = 500\,\mu$m *with three different values for the distance between the cantilever tip and magnets:* $a = 200\,\mu$m, $385.5\,\mu$m *and* $1000\,\mu$m. *b) Total force respect to tip deflection for all the cases just presented. NN magnets configuration was used.*

set of dimensional values lower than $200\,\mu$m that allow for softening effect, while in the NS case a hardening effect occurs. However, at this order of magnitude, miniaturization is already guaranteed and increasing dimensional distances from $200\,\mu$m to about $400\,\mu$m does not imply not fulfilling the miniaturization requirement. With this is mind and from a practical point of view, the NS configuration has the advantage of presenting larger tolerances over the possible b values that the system can present in order to obtain a flat potential. Regardless of whether the NN or NS configuration is finally chosen for application, these results show that miniaturizated magnetoelastic broadband energy harvesting is possible and the reader is referred to Appendix D.

3.3.3 Dynamic study

As described previously in Section 3.1, a dynamic study of the center of mass on the beam's tip can be performed by using equation 3.3. The magnetic force and spring force values are directly obtained from the COMSOL simulations performed above. Regarding the external force F_{ext}, it is given as a sinusoidal function with amplitude $|F_{\text{ext}}|$. The damping coefficient γ is given by $\gamma = \frac{\sqrt{m_{\text{eff}} k_{\text{eff}}}}{Q}$, where Q is the mechanical quality factor and the effective mass is calculated by using $m_{\text{eff}} = k/(w_r) = 4.84 \cdot 10^{-5}\,\text{Kg}$, where k corresponds to the linear spring constant and w_r to the linear resonant frequency, both values found from the COMSOL simulations presented in the previous section. The value used for Q was set to 100, which falls within the low Q factors found in literature, which are normally within a range of $10 - 500$ [29]. The main reason for choosing this valie is that in this section deflection vs time studies are performed for large number of frequencies, for each of them it is of interest

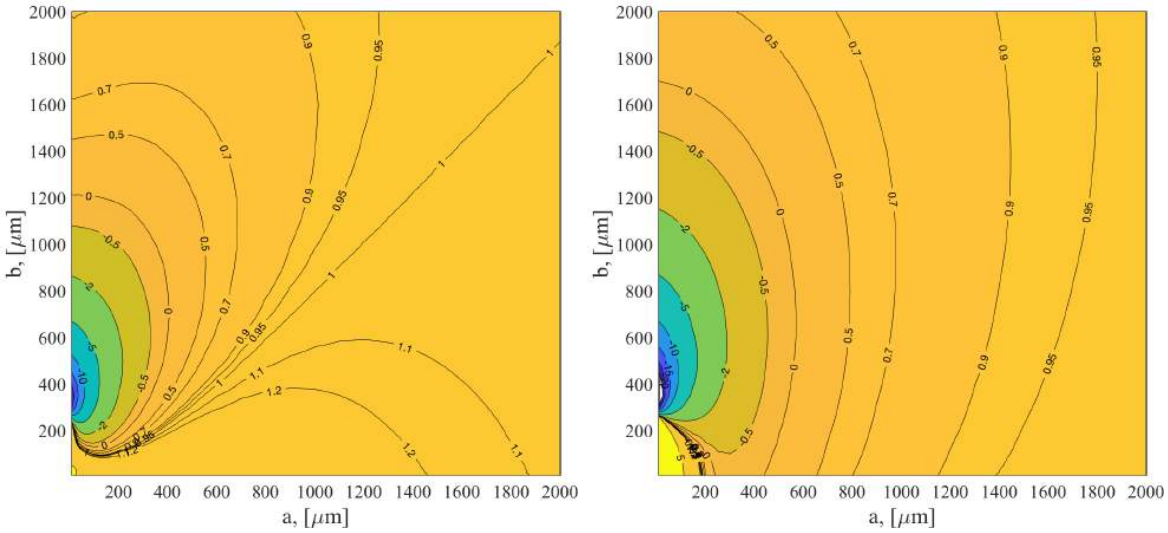

Figure 3.6: *a) Contour lines that show the different spring constant values that can be found depending on the dimensional parameters a and b for both a) the NN configuration and b) the NS configuration.*

to study the stabilized signal, i.e. without considering the transient part of it. It is well known that for higher Q larger time is required for the transient to disappear. Therefore, by choosing a low enough but still realistic Q factor, computational time is saved without loss of generality. The Duffing equation is solved using Matlab R2017b [64], where the initial conditions set are $x(t=0)=0$ and $v(t=0)=0$. It is important to note that out of the two different magnets configurations, i.e. NN and NS, only the NS case is studied. This is due to the magnet configuration used for characterizing our devices: NS. The input acceleration is, by default, 0.1 g unless another value is clearly stated.

First, the linear case corresponding to the green line in Figure 3.4a (no magnetic forces) is analyzed. Two kinds of studies are performed. First, a sweep over a range of frequencies between 10 Hz and 300 Hz with a step of 1 Hz is performed under the conditions stated in the previous paragraph. From this study, the RMS deflection is plotted with respect to frequency and Figure 3.7 is obtained. A very steep curve is observed associated to its natural resonant frequency. For the second study, instead of performing a sweep, the driven frequency is only the resonant frequency associated to its linear spring constant of 120.8 N/m: $f_r = 251.4$ Hz. Figure 3.8a shows the position displacement respect to time, it can be observed that a transient occurs between the initial time at which the force is applied and until the movement stabilizes. For this reason, in all the analysis left to be presented in this section (and in the previous Figure 3.7), the last third (red curve in Figure 3.8a) of the time-slot analyzed is red-marked and used for the RMS analysis and phase plots. The corresponding phase plot of velocity respect to position is shown in Figure 3.8b, where it can be observed that the movement starts, as the initial conditions were set, at zero deflection and zero velocity. The beam gains momentum until its oscillation amplitude stabilizes (red curve on the contour). The contour

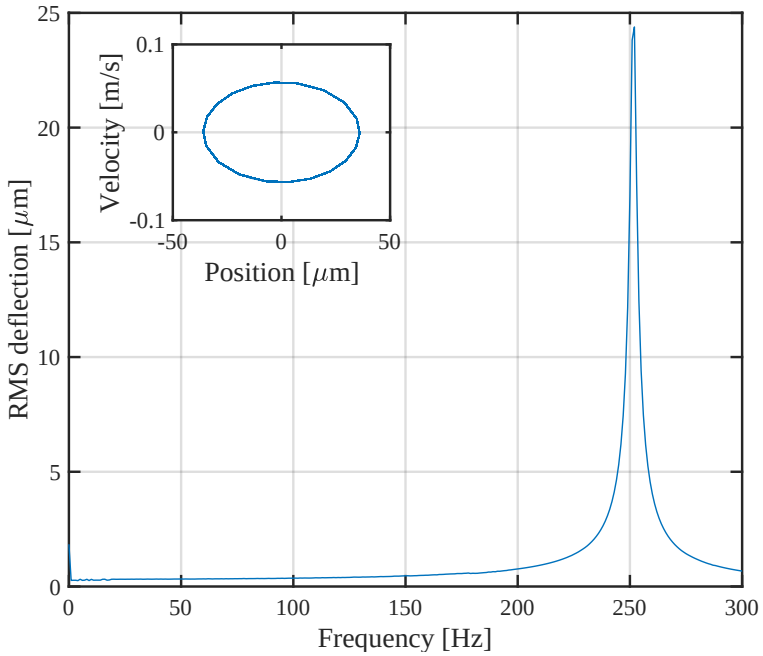

Figure 3.7: *RMS deflection values for the linear case for a sweep of frequencies between* 0 Hz *and* 300 Hz *in steps of* 1 Hz*. The inset shows the velocity versus position phase for the last third of the data set at resonant frequency.*

associated to the last third of the data is shown also as an inset in Figure 3.7, where only the last third is represented. From now on, only the last third of the data will be shown in the phase analysis, which will be included as an inset in each case.

Now the magnets are set into the set-up in a NS configuration. First, the mono-stable case is considered, this corresponds to the blue curve in Figure 3.4a. The results after performing a sweep over frequencies with the same characteristics as in the previous case, are shown in Figure 3.9a.

The peak, as expected from the effective spring constant, is located at 218 Hz, and it flats out rapidly once away from that frequency. Figure 3.9b shows the position of the tip respect to time at its resonant frequency, as in the previous case, a transient is observed. Its corresponding phase plot is shown in Figure 3.9a as an inset.

As for the bi-stable case, the red curve in Figure 3.4a, two frequencies are of interest. They correspond to the two potential wells associated to this case observed in Figure 3.4a. The two effective spring constants were previously shown in Table 3.2 and the frequency associated to both positive and negative branch is: 473.5 Hz. Figure 3.10a shows the RMS deflection values for a frequency range sweep between 0 Hz and 550 Hz in steps of 1 Hz. It is important to note here that the initial conditions here were changed respect to all the other cases studied. The position at $t = 0$ is the potential well on the positive side of its associated potential landscape in Figure 3.4a. In addition, the time analysis instead of being 2 seconds as in all the other cases, this time it is 3 seconds. The reason for this is that it takes longer time for

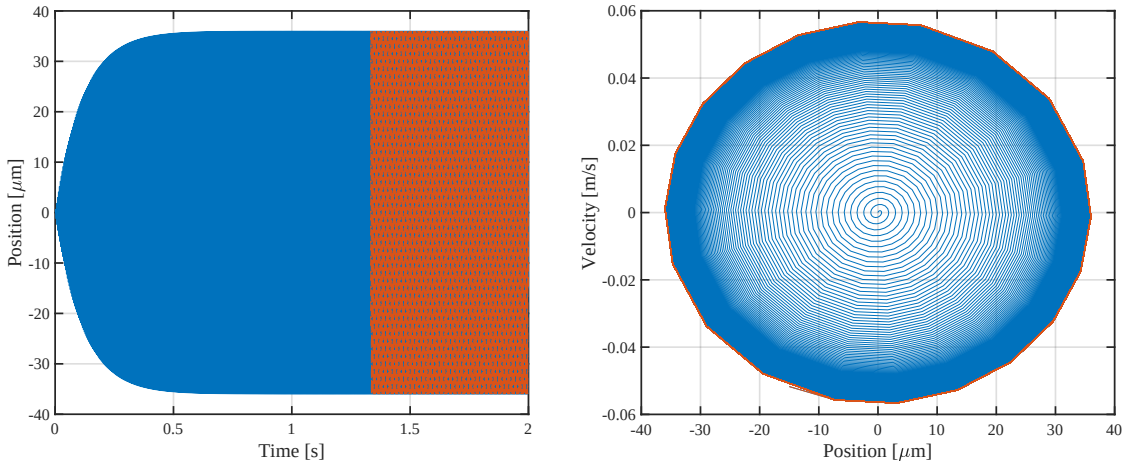

(a) **(b)**

Figure 3.8: *Analysis of the beam motion for the linear case, i.e. no magnets incorporated. a) Position versus time when the beam is excited at its natural frequency, where the red curve corresponds to the last third part of the data set. b) phase plot of the velocity versus position when excited at its natural frequency as well.*

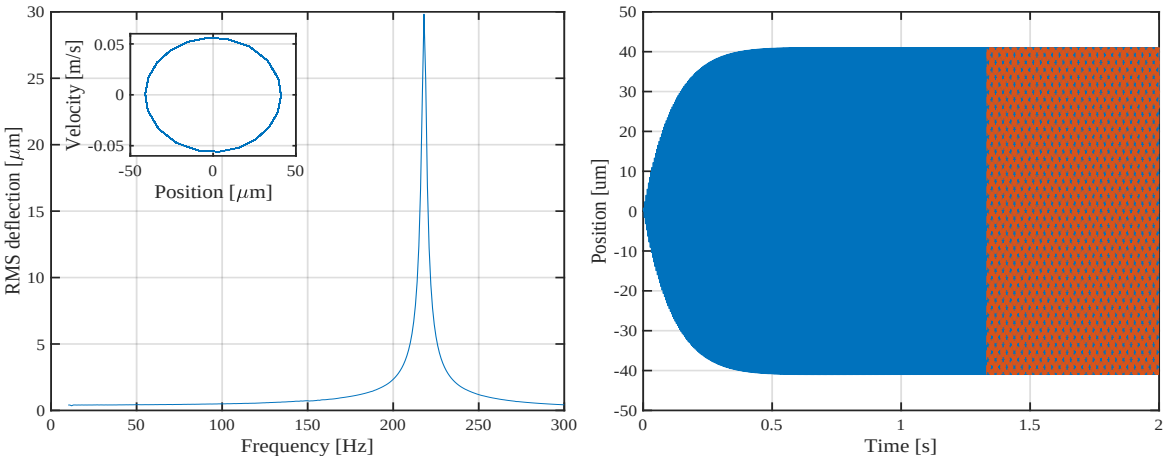

(a) **(b)**

Figure 3.9: *Analysis of the motion of the monostable case for the NS configuration. a) RMS deflection versus frequency with an inset of velocity versus position for resonant frequency. b) Position versus time at resonant frequency, where the red curve corresponds to the last third part of the data set.*

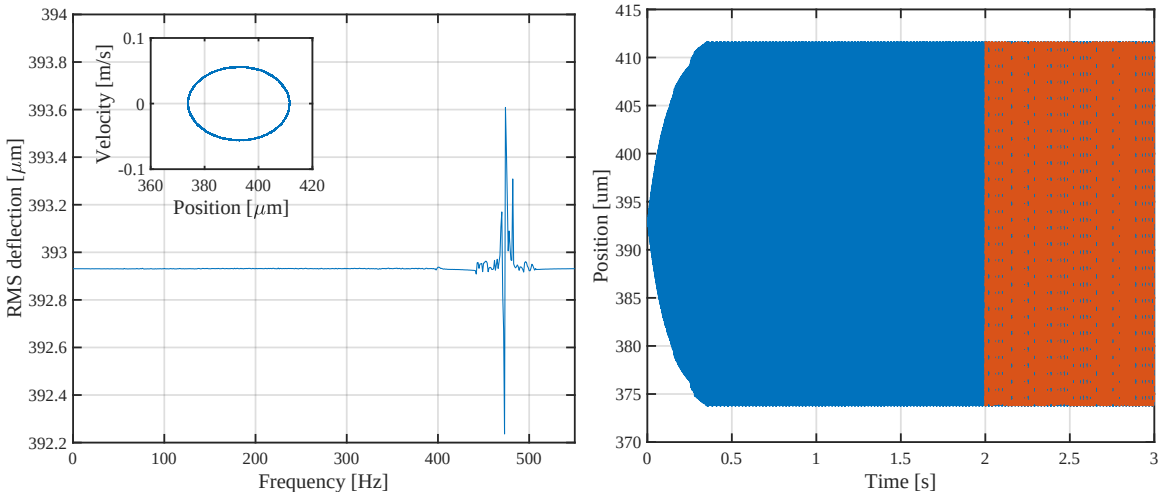

Figure 3.10: *Analysis of the motion of the beam's tip under a bistable case for the NS configuration. a) RMS deflection versus frequency with an inset of velocity versus position at 473.5 Hz. b) Position versus time at 473.5 Hz, where the red curve corresponds to the last third part of the data set.*

the signal to stabilize. The inset in Figure 3.10a shows the velocity versus position phase when the beam is excited at the resonant frequency associated to the well, that is 473.5 Hz, which as seen in Figure 3.10a leads to the largest deflection, as expected. Figure 3.10b shows the associated position versus time plot at the same frequency. It can be argued that the reason why the beam does not hop over the potential barrier is that the base acceleration is very low. Therefore, a trial with a higher acceleration was performed, this is shown in Figure 3.11a, where an input acceleration of 2 g is applied. It can be observed that even as such a high acceleration level (in terms of realistic ambient vibrations) the beam is still trapped within one of the potential wells. The corresponding position versus time plot at the same frequency (473.5 Hz) is shown in Figure 3.11b. The energy barrier required to be overcome can be directly taken from Figure 3.4a by using $\Delta = U(x=0) - U(x = \pm\sqrt{\frac{\alpha-\kappa}{\beta}}) = 12\,\mu$J. When the beam position is at $x = \pm\sqrt{\frac{\alpha-\kappa}{\beta}}$, i.e. at the center of any of the two potential wells, its associated potential energy is at a minimum, which corresponds to maximum kinetic energy, which reads as $E_\mathrm{k} = \frac{1}{2}m_\mathrm{eff}v^2$, where v is the velocity of the beam, and m_eff is already known. Therefore, the velocity required to hop over the potential barrier is found to be 0.7 m/s, which is an order of magnitud larger than the velocities associated to Figure 3.10a, which shows how unrealistic interwell oscillations are for this energy landscape.

Finally, the dynamics associated to the flat potential landscape represented as a black curve in Figure 3.4a are studied. Figure 3.12a shows the RMS deflection versus frequency, which can be compared to all the other cases presented above and a clear improvement in the bandwidth at which large deflections occur is observed. In addition, the RMS deflection that the beam experiences increases respect to its linear counterpart. Furthermore, the frequencies are

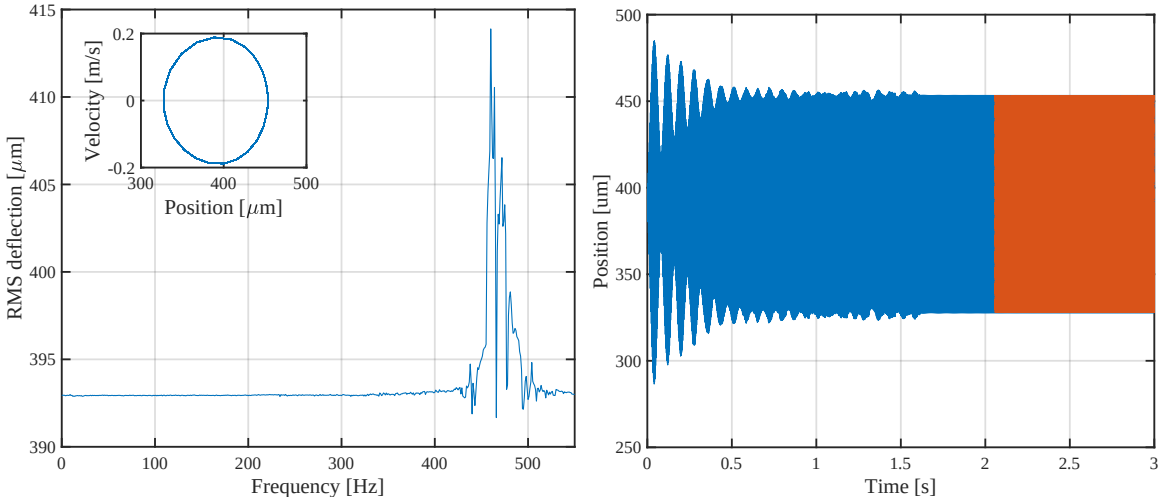

Figure 3.11: *Analysis of the motion of the beam's tip under a bistable case for the NS configuration at* 2 g. *a) RMS deflection versus frequency with an inset of velocity versus position at 473.5 Hz. b) Position versus time at 473.5 Hz, where the red curve corresponds to the last third part of the data set.*

lowered, which is more convenient for harvesting ambient vibrations, as explained in Chapter 1. Figure 3.12b shows the position versus time of the tip when excited at the frequency that leads to the largest deflection found through the sweep in Figure 3.12a: 43 Hz, and its corresponding phase is shown as an inset in Figure 3.12a. From these studies, the benefits of obtaining a potential energy landscape that is as flat as possible are totally apparent, at least in the realm of harvesting energy from ambient vibrations.

3.4 Summary

In this chapter the fundamentals for understanding broadband energy harvesting from vibrations were introduced. The forced Duffing oscillator was presented for different non-linear conditions and their corresponding phase diagrams were showed generally. COMSOL Multiphysics was used as a tool for simulating our set-up under static conditions. From these simulations the optimal dimensional parameters a and b were obtained from two different magnetic configurations: NS and NN. These dimensional parameters showed that miniaturized broadband energy harvesting is possible. From these simulations the potential energy of the beam at its center of mass was obtained for different dimensional parameters. To the end of continuing the study in dynamic mode, the Duffing equation was used and the results for the three distinct cases were showed, i.e. the monostable, bistable and flat potential cases. The flat potential landscape proved to be the best alternative for harvesting energy from ambient vibrations.

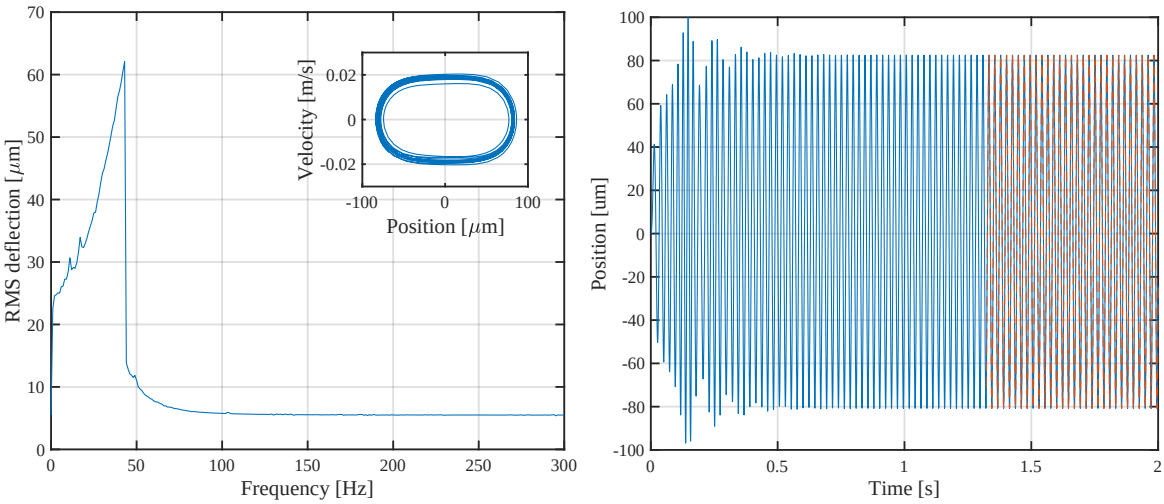

(a) **(b)**

Figure 3.12: *Analysis of the motion of the beam's tip under a flat potential landscape case for the NS configuration. a) RMS deflection versus frequency with an inset of velocity versus position at 43 Hz. b) Position versus time at 43 Hz, where the red curve corresponds to the last third part of the data set.*

Chapter 4

Deposition of AlN with piezoelectric properties

Until now, the focus has been put on studying the harvesters in electromechanical terms. In this chapter, the focus is shifted to how a good quality piezoelectric material can be achieved. This material is key in the development of the VEHs since it transforms energy from the ambient vibrations to energy in the electrical domain. In this work the material chosen is AlN.

The interest in using AlN as piezoelectric material in microelectromechanical systems (MEMS) is mainly due to the process compatibility with silicon technology and the availability of low temperature methods for its deposition. Furthermore, in the field of vibrational energy harvers AlN layers with good piezoelectric properties have been achieved [29].

AlN has been reported to be deposited by a range of different methods like sputtering [29], chemical vapor deposition [65], laser hemical vapor deosition [66] and molecular beam epitaxy [67]. However, most of these cases require a high temperature (>500°C) during deposition, which leads to substrate degradation or degradation of the AlN film itself. The use of reactive sputtering methods for depositing high quality piezoelectric AlN layers is very extensive, and allows for deposition at room temperature. For these reasons, it was decided to deposit AlN via sputtering methods.

In order to achieve good quality layers different parameters during the deposition process must be controlled. However, another factor before the AlN deposition that affects the piezoelectric quality of the layers: the substrate onto which this material is deposited. This chapter deals with different parameters that play an influence in the acquisition of good AlN films, it starts with a description of the properties that the AlN layer must show, then the influence of oxygen content and the substrate used is presented. Furthermore, a description of the methods used for its deposition with focus on the reactive sputtering method is given. It is important to note that the influence of oxygen content was not included in the reactive sputtering section but explained separately, since a low oxygen level (<5%) is assumed during deposition. Finally,

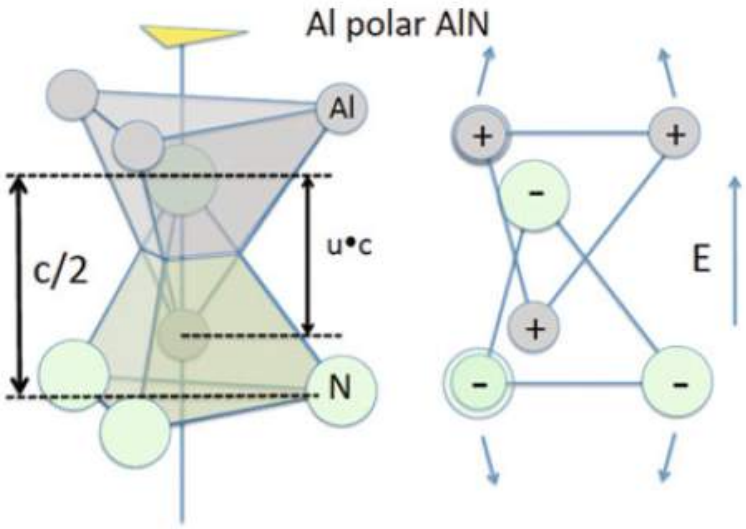

Figure 4.1: *AlN structure as combination of Al and N ions coordinated in tetrahedrons. Also, a cross section view is included, spanned by the height of the tetrahedron and the base of the lowest triangle which shows the ion displacement upon application of an electric field. Image taken from [68].*

as a way of properly defining a useful piezoelectric material, the concept of frequency corner is introduced.

4.1 Properties of AlN as piezoelectric material

AlN grows in the wurtzite structure, which is characterized by presenting a hexagonal crystal arrangement with typical lattice constants of about $a = 3.11$ Å and $c = 4.98$ Å [68]. Figure 4.1 shows the AlN structure as combination of its two compound atoms Al and N. Each type of atom is pictured at the corner points of a tetrahedron pointing against each other where the distance between equivalent ions along the c-axis (seen as an axis alongside the structure) is given by $c/2$. Furthermore, the distance between different next-neighbor ions along the c-axis is given bu $u \cdot c$. An AlN wurtzite structure typically links these parameters as $c/a = 1.60$ and $u = 0.375$. An important property of this structure is that it lacks a mirror plane or a twofold axis [68], i.e. an axis around which a 180° rotation would turn the direction of a vector along the c-axis and provide the same geometry. This polar characteristic of AlN allows for piezoelectricity. Two types of polarization can be found in AlN: Al polarity or N polarity, asigned as whether the type of atoms located at the top side closest to the surface (applicable to 001 oriented films) are Al atoms or N ones, respectively.

The two main properties that will guarantee a good piezoelectric layer are the crystallographic orientation and the piezoelectric coefficient, both of wich are inter-linked. The optimal crystallographic orientation that should be aimed at is c-axis orientation, other crystal orienta-

Table 4.1: *Properties of AlN film obtained by Jackson et al. [70] for two different wafers.*

Device	FWHM (002)	Oxygen	Non-(002) peaks	Dielectric constant	d_{31} (pm/V)	Power (μW)
1	8.5	No	No	8.90	2.04	0.67
2	9	No	Yes	8.83	0.84	0.24

tions like (102) and (103) will be detrimental to the performance of the piezoelectric quality. The crystallographic orientation directly influences the piezoelectric constant, which must be around $10\epsilon_0$ [29].

4.1.1 Crystal orientation and piezoelectric constant

AlN layers, in order to present a good piezoelectric behaviour, must have a perfect (002) texture. Traditionally, in order to asses the quality of the AlN piezoelectric film, x-ray diffraction (XRD) techniques are used and the full width at half maximum (FWHM) of this preferable peak, i.e. (002), is measured. The smaller the FWHM, the better the quality of the piezoelectric material is. However, it was found that a small FWHM value can be associated to a worse quality AlN film if non-c-axis orientation traces are found compared to a larger FWHM where only the preferable orientation is found [69]. This is shown in Figure 4.2, where a FWHM of 7.7°, Figure 4.2a, presents a better piezoelectric coefficient (2.13 pm/V) than Figure 4.2b, where a FWHM of 2.6° is observed and a lower piezoelectric coefficient is achieved (0.91 pm/V). Therefore, when assessing the quality of the piezoelectric layer, the presence of other crystal orientations plays a more important role than the FWHM of the c-axis peak. Similarly, Jackson *et al.* [70] studied the effect of different orientation peaks in terms of power harvested by implementing AlN layers in a cantilever-based silicon structure. Table 4.1 shows the different AlN properties obtained for two different devices: number one and number two, and Figure 4.3a and 4.3b show their respective scanning electron microscope (SEM) images. Device number two harvested around half the amount of power that device number one harvested, which is attributed to the presence of non-(002) peaks. However, note that device one not only did not present non-(002) peaks, but presented also a smaller FWHM. From the SEM images it can be seen that device number two, Figure 4.3b, presents tilted AlN orientations, which by XRD measurements were found out to be (102) and (103) peaks. On the other hand device number one, Figure 4.2a, does not show tilted structures and circular grains on the top figure are observed. This can be compared to the elongated islands that device number two show in its corresponding top figure. As a conclusion, it is clearly observed the importance that both the presence of non-(002) peaks and the FWHM of the (002) peak play in obtaining a good quality piezoelectric layer, Section 4.3 will deal with further this in terms of substrate influence.

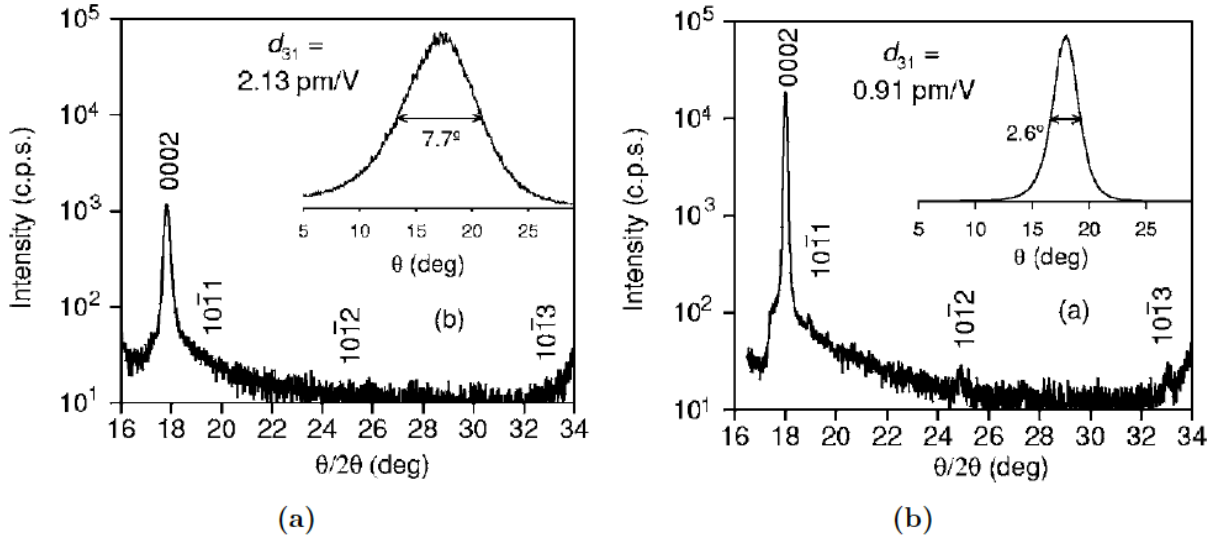

Figure 4.2: *XRD results [69] where a) shows only (002) orientation while b) presents traces of (102) and (103) orientations.*

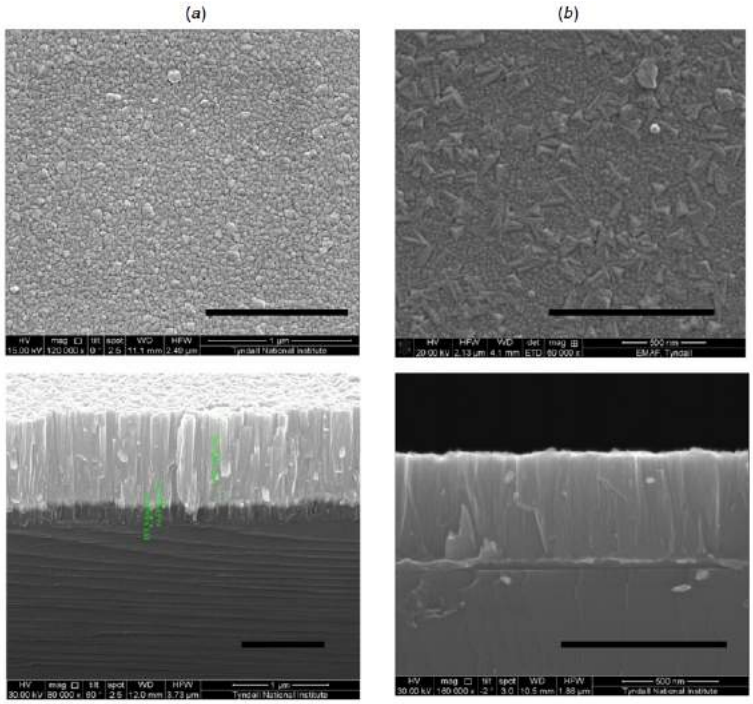

Figure 4.3: *SEM images taken from [70] where a) corresponds to device number one, and b) corresponds to device number two.*

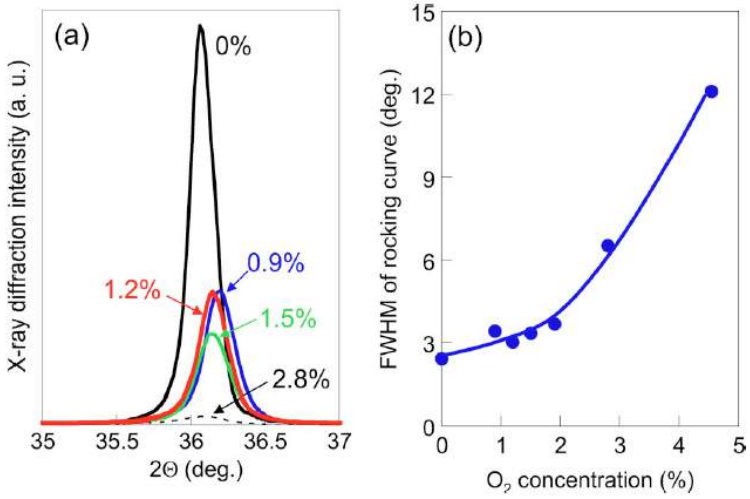

Figure 4.4: *a)X-ray diffraction peaks found for different oxygen concentrations, where a lower peak value is obtained for larger O_2 concentrations. b) FWHM of the rocking curves respect to O_2 concentration. Both images are taken from [71].*

4.2 Influence of oxygen level

The oxygen level during deposition has been observed to hinder the FWHM of the (002) peak [71]. Akiyama *et al.* [71] studied the influence of the sputtering gas oxygen concentration on piezoelectric response of aluminium nitride thin films. They deposited 400 nm of AlN on (100) silicon wafers by a RF magnetron reactive sputtering technique, varied the O% during the deposition from 0.0% to 6.3% and investigated the influence on the crystal structures of the AlN films. Figure 4.4a shows the XRD peaks found for a scan from 10° to 80°, however, since only the peaks associated to the silicon substrate and the c-axis oriented film were found, Figure 4.4a only shows the results from 35° to 37°. It can be seen how the peak value of the (002) orientation diminishes for increasing O_2 concentrations. In Figure 4.4b the FWHM of the rocking courves increases for increasing O_2 concentrations. It can be therefore inferred that larger O_2 concentrations hinder the piezoelectric quality of the AlN layer. Akiyama *et al.* [71] also detected a change of sign of the piezoelectric coefficient once a certain O_2 threshold is overpassed. However, they did not arrive at a conclusion about the change of polarization mechanism related to the oxygen content in the samples. Furthermore, Vergara *et al.* [72] studied the influence of oxygen content in grain size, which is related to the crystal quality of the AlN layer in the sense that larger grain seizes lead to better AlN quality. In their experiments it was found that O_2 content affects it negatively.

4.3 Influence of substrate material

As has been presented above, in order to achieve AlN with high piezoelectric quality it has to show a (002) preferred orientation. In this section the influence of different metals used as

bottom electrodes prior to the AlN deposition is presented.

A number of comparative studies have been performed in order to understand the influence of the substrate material in the piezoelectric behaviour of (002)-oriented AlN films [72–75]. Hervas *et al.* [76] studied the quality of AlN layers deposited on $Al_{0.9}Si_{0.1}$, Cromium (Cr), molybdenum (Mo) and titanium (Ti) electrodes, which at the same time were deposited on (100)-oriented silicon substrates. The AlN thickness for all cases was of 900 nm, which was deposited by RF sputtering of an Al target under a high purity N_2 and Ar gas mixture and at a temperature of 300°C. The substrate bias voltage (V_s) was varied for the sake of further understanding of the optimal deposition conditions. Among the metals aforementioned, only Al presents the same symmetry as AlN (hexgonal symmetry), however, it was the Mo metal the one that provided with higher grain size, followed closely by Al. A similar study [74] was performed with Al, copper (Cu), Ti and Mo as bottom electrodes. Figure 4.5 shows the XRD results of AlN deposited on the different metals, from where Mo showed a good (002)-orientation and also the lowest non c-axis orientation peak, which was previously demonstrated to affect the piezoelectric quality in comparable terms as the FWHM of the (002) orientation peak, which was introduced in Section 4.1.1. They also studied the texture coefficient (TC) and RMS roughness of the AlN film on the bottom metals, which showed that Mo presented the highest TC and the lowest RMS roughness. In terms of these two parameters, Mo was followed by Ti, Cu and Al. Furthermore, the surface morphology of the AlN deposited on Mo presented larger and more uniform grains compared with the AlN deposited on the other metal substrates. The better performance of Mo over the other metals might be related to the lattice mismatch between the AlN and Mo layer, which was found to be the smallest one among the other metals, about 0.87% [74]. Furthermore, they also pointed out that the thermal expansion coefficient of Mo ($4.8{\cdot}10^{-1}$ 1/K) is very close to the AlN one ($4.2{\cdot}10^{-1}$ 1/K). Besides Mo, another metal widely used as substrate for (002)-oriented AlN growth is platinum (Pt) in (111) orientation [29, 75, 77]. Compared to Mo, this metal presents an hexagonal structure, which matches very well with the AlN structure. However, the thermal expansion coefficient of Pt is about 8.210^{-1} 1/K [78]. This value is not close to the one obtained for AlN, as was the case of Mo. However, the lattice mismatch in the Pt(111)/AlN(002) case is of about 2.9% [77].

To conclude this section, two metals stand above the other considered materials. Mo and Pt seem both to present good qualities that favor the c-axis orientation of piezoelectric AlN films.

4.4 Reactive sputtering conditions

Once the appropriate substrate is chosen, a number of different deposition parameters like nitrogen concentration, power, sputtering pressure and substrate temperature affect the AlN quality. This section explains how these parameters influence the piezoelectric quality of AlN and how it can be improved.

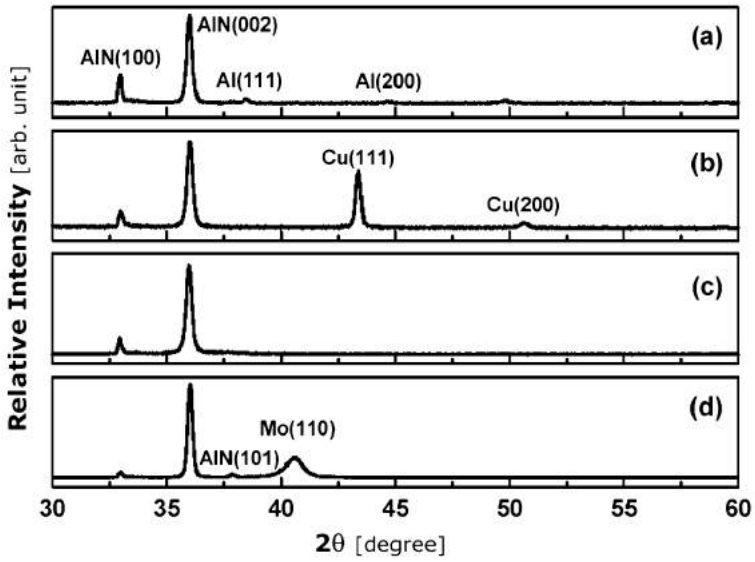

Figure 4.5: *XRD patterns [74] for AlN films deposited on a) Al/Si, b) Cu/Si, c) Ti/Si and d) Mo/Si.*

4.4.1 Nitrogen level, power, sputtering pressure and substrate temperature

Ohuchi *et al.* [79] studied the XRD peak diffraction dependence on the nitrogen level content, RF power and sputtering gas. Figure 4.6 shows the XRD patterns for different nitrogen concentrations, where the deposition rate is also indicated. It can be seen that for larger nitrogen concentrations the deposition rate diminishes, and at the same time the crystal structure changes. For 20% N_2 concentration ony the (101) peak is observed, as the concentration increases until 35%, this peak vanishes and the (102) peak appears. However, as this concentration increases even further, both (101) and (102) peaks are detected and the (002) peak appears. Finally, for a concentration >75%, only the (002) peak is detected. They also studied the diffraction peaks in terms of different sputtering gases with N_2 maintained constant at 12%. These results are showed in Figure 4.7, which show the same trend as those shown in Figure 4.6. For low deposition rates (equivalent to using a low atomic mass gas) the crystal orientation detected is only the (002) peak, this is equivalent to Figure 4.6 for 100-75% N_2 in terms of deposition rate. For larger atomic mass, the N_2 + Ar mixture is reproducibly observed. When using a N_2 + Kr mixture the growth is observed in multiple directions and, finally, for Xe as reactive gas, an amorphous structure is observed. Ohuchi *et al.* also studied the crystallographic orientation in terms of the RF power used. The deposition rate was found to increase linearly with power in a range from 200 W to 800 W. At 500 W, the (101) peak was obtained and for decreasing RF power this peaks drops and the (002) peak appears, which is in good agreement with the figures just presented. The explanation that Ohuchi *et al.* provided was that close-packed structures like (002) present a low-energy configuration, this means that when the adatoms arrive at the surface they need time to recombine to lower

state configurations before new atoms arrive. This time is guaranteed by low deposition rates, which in terms of the cases studied translates to high nitrogen concentrations, low RF power and low atomic mass sputtering gas. As the deposition rate increases high-energy configurations such as (101) orientation, which do not demand adatoms rearrangement, appear. It is important to note that, besides achieving a low enough deposition rate by lowering the RF power or increasing the nitrogen content, and therefore lowering the kinetic energy of the arriving particles at the substrate, this kinetic energy must be high enough to allow for good mobility on the substrate so that the atoms can rearrange [80].

Similar experiments [81] were performed, where AlN was deposited at different nitrogen concentrations. These results are shown in Figure 4.8, they show the same trend as those shown in Figure 4.6. For 25% N_2 a (100) preferred orientation is detected, as the concentration of the gas increases both (100) and (101) appear, for up to 75% of nitrogen (002) orientation peak appears, however both (100) and (101) stay. Finally, for a pure nitrogen sputtering, a (002) preferred orientation is observed, with a very small contribution of a (100) peak.

Another parameter that needs to be controlled during the deposition is the sputtering pressure. This parameter was studied at two different nitrogen concentrations by Ababneh *et al.* [80]. Figure 4.9a shows the XRD results at 300 W, 100% nitrogen content, i.e. no argon present, at three different sputtering pressures: 0.006 mbar, 0.004 mbar and 0.002 mbar, where the FWHM is showed to be 0.36°, 0.32° and 0.28°, respectively. As it was shown in Section 4.1.1, a lower FWHM of the preferred (002)-orientation peak is normally associated to better piezoelectric quality layers. Therefore it can be inferred that the lowest pressure value is preferred. It was also seen in Section 4.1.1 that the orientation peaks present in the XRD scans play a more important role than the FWHM does. Figure 4.9a shows a larger intensity (002) preferred orientation peak for lower sputtering pressures, this can be understood in terms of kinetic energy, i.e. for lower pressures the mean free paths of the atoms is larger, this means that the number of colisions is smaller and therefore the atoms arrive at the substrate with higher kinetic energies, which increases the mobility of the adatoms so that a (002) preferred orientation is obtained [80]. Figure 4.9b shows the XRD peaks obtained at the same sputtering conditions as Figure4.9a but at 75% nitrogen concentration instead, where the other 25% is argon gas. This time the intensities of the (002) peaks are reduced considerably. Furthermore, (101) orientation is dominant at 0.006 mbar, at 0.004 mbar the (002) orientation overtakes the (101), which is still clearly present, and finally at 0.002 mbar only (002) orientation is detected. In order to understand the (101) orientation detected it must be beared in mind that in this case argon gas is present, which increases the deposition rate. As described in this previously in this section, a higher deposition rate does not provide enough time for the adatoms to rearrange into a low-energy configuration like (002) orientation and a hihg-energy configuration as (101) is detected instead [80]. Another way for increasing the adatoms mobility is by increasing the substrate temprature, which for AlN is typically in the range 200-500°C [68, 71, 82].

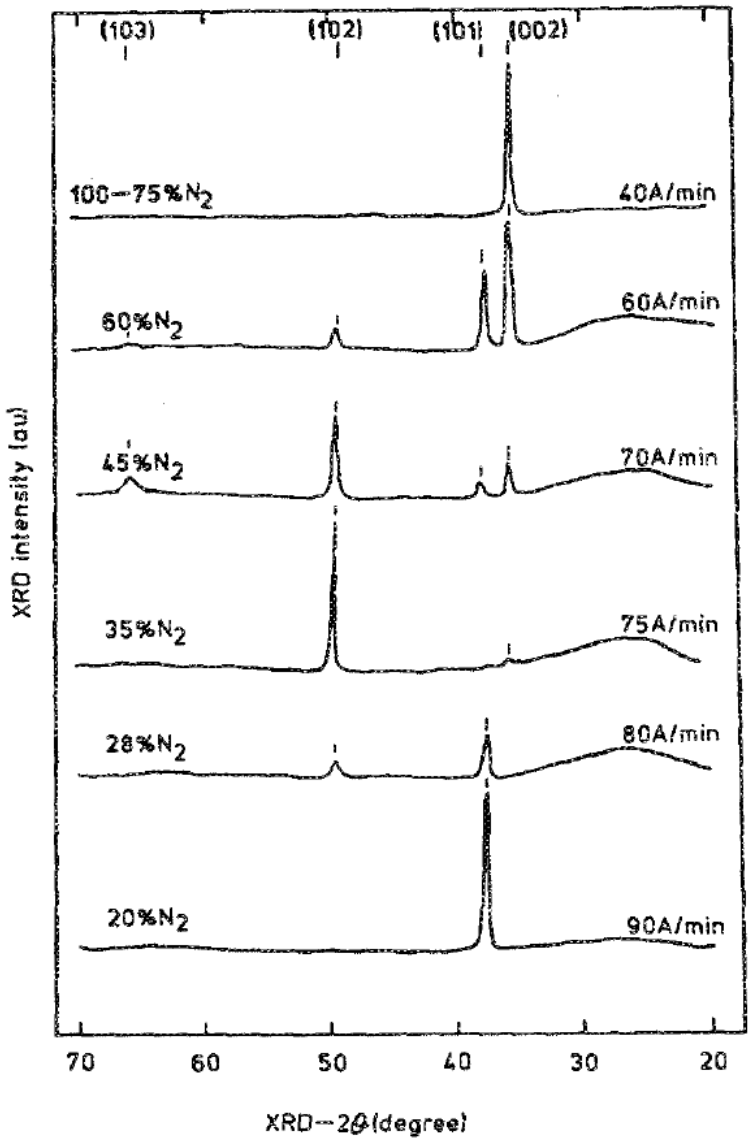

Figure 4.6: *XRD patterns [79] for AlN films deposited at different nitrogen concentrations. For each nitrogen concentration the deposition rate measured is also indicated.*

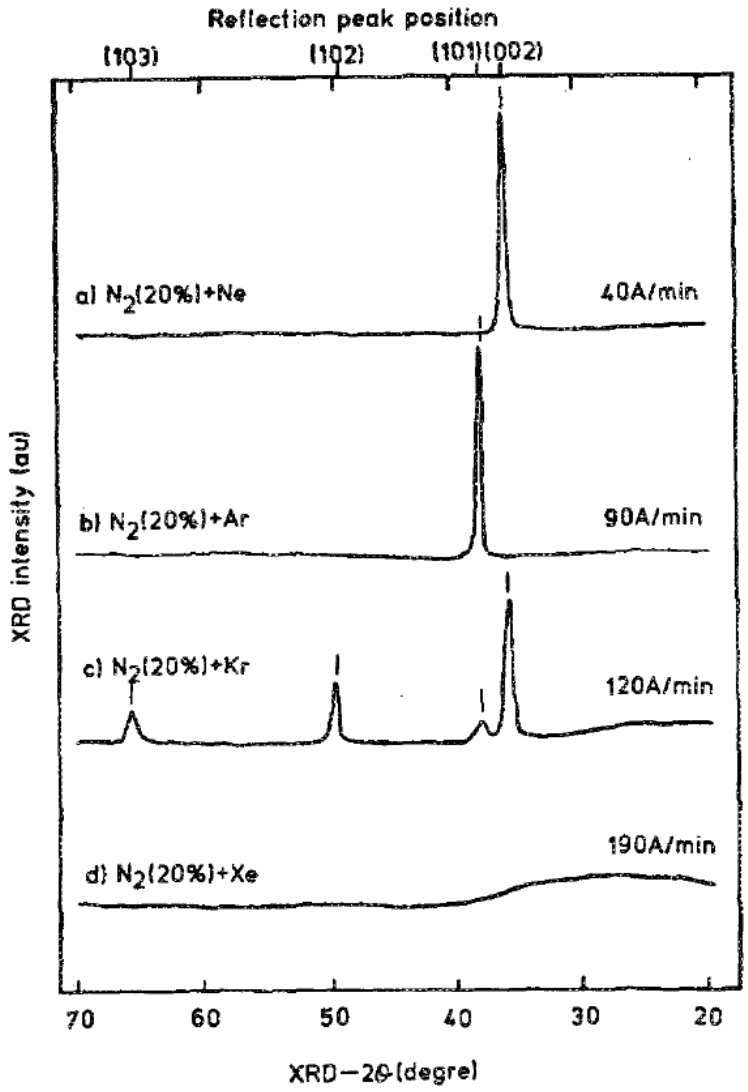

Figure 4.7: *XRD patterns [79] for AlN films deposited using different sputtering gases with N_2. For each sputtering gas the deposition rate measured is also indicated.*

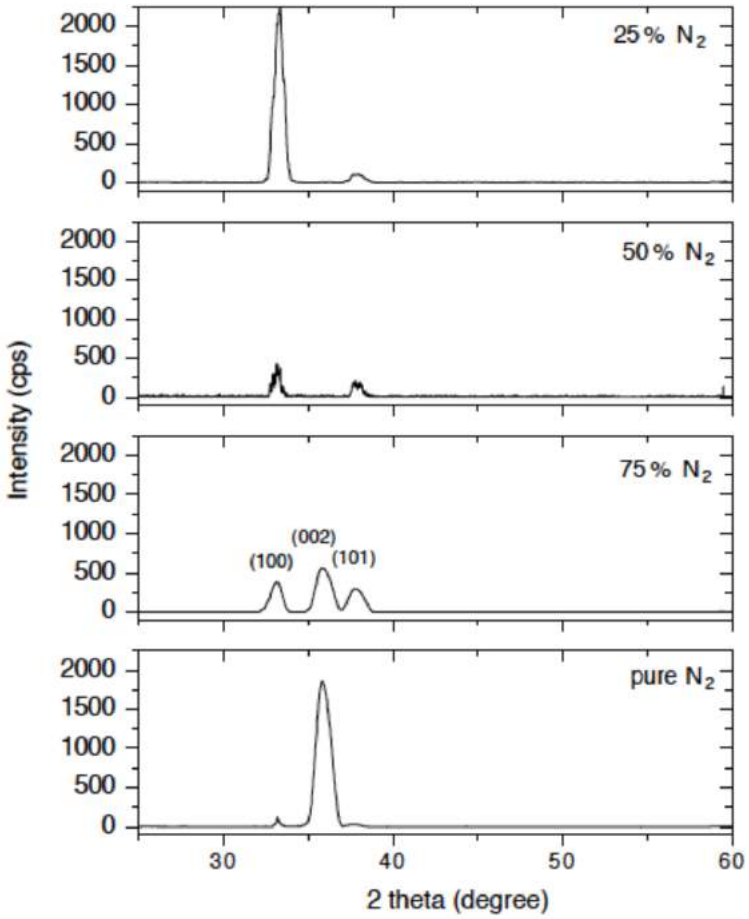

Figure 4.8: *XRD patterns [81] for AlN films deposited using different N_2 concentrations.*

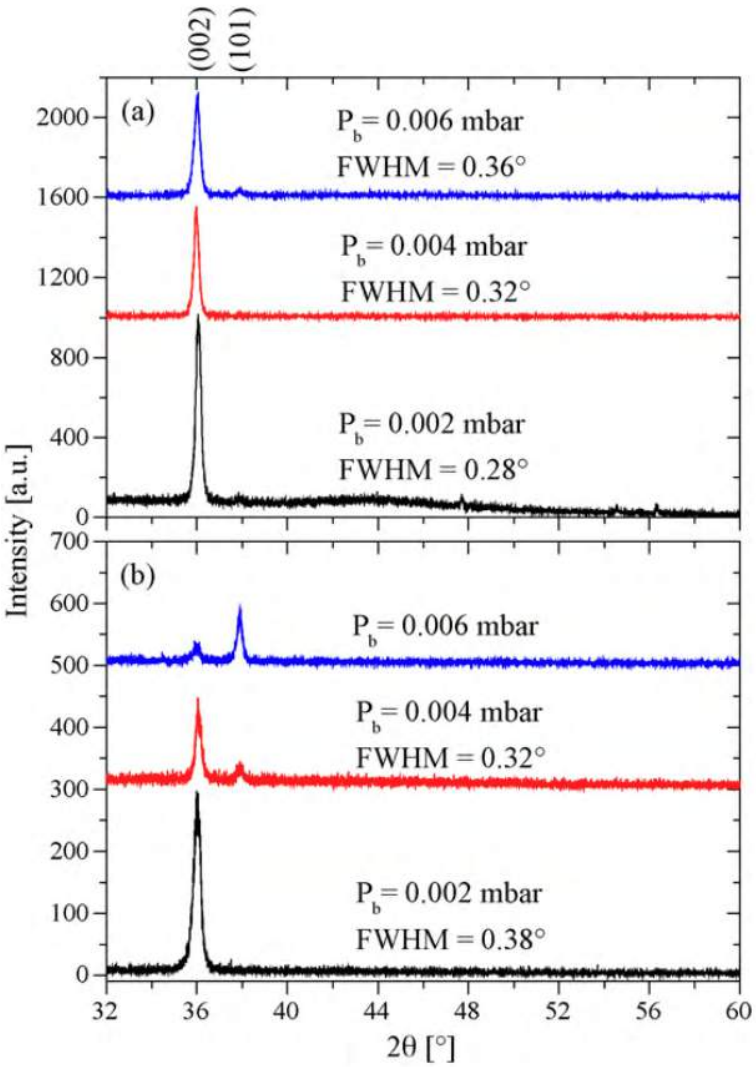

Figure 4.9: *XRD patterns [80] for AlN films deposited using 300 W as RF power at different sputtering pressures at two different N_2 concentrations: a) 100% and b) 75%.*

4.5 Corner frequency

Corner frequency or cut-off frequency refers to a frequency that marks a limit in the device response. In our case, where the piezoelectric material can be ideally modelled as a capacitor, in reality it must be accounted as a capacitor C and a resistor R in parallel. The associated impedance to the capacitor and resistor are respectively $\frac{1}{2\pi fC}$ and R, where j stands for the imaginary component and f is the frequency at which the device is operated. For frequencies lower than a certain threshold, which can be called corner frequency f_c, the impedance associated to the capacitor is high and, therefore, the current goes through the resistor. This means that for frequencies lower than f_c the piezoelectric-based device is not properly operated, i.e. one cannot take advantage of the piezoelectric effect. However, for frequencies higher than f_c, the impedance associated to the capacitor is low enough so that the current goes through the capacitor instead of through the resistance, and therefore the piezoelectric-effect can be exploited. To the end of finding the corner frequency, where both impedances are equated, one obtains

$$R = \frac{1}{2\pi f_c C} \Rightarrow f_c = \frac{1}{2\pi C} \, , \tag{4.1}$$

where the capacitance is expressed as

$$C = \frac{\epsilon_r \epsilon_0 A}{h} \, , \tag{4.2}$$

where A and h are respectively the area and the thickness of the piezoelectric material, and ϵ_0 and ϵ_r are the vacuum and relative permittivities, correspondingly. Similarly, the resistance can be expressed as

$$R = \frac{\rho h}{A} \, , \tag{4.3}$$

where ρ is the material resistivity. Therefore, using these two last equations and substituting them in equation 4.1 one finally gets

$$f_c = \frac{1}{2\pi \epsilon_r \epsilon_0 \rho} \, . \tag{4.4}$$

In order for the material implemented in our devices to be useful, this corner frequency should be lower than the resonant frequency. In other words, the resistivity must be large enough, for example for $\epsilon_r = 9$ and aiming at a resonant frequency of $f = 200\,\mathrm{Hz}$, then equation 4.4 gives a resistivity that must me larger than $10^9\,\Omega\mathrm{cm}$.

4.6 Summary

Basic crystal properties of AlN were presented, based on the fact that the optimal crystal orientation for cantilever-based energy harvesting is (002), different substrates were considered for finding which one would serve the best to our purpose. Among the different metals considered, Mo and Pt were found to be the most adequate. Sputtering technique was the

technique chosen to deposit AlN on our devices due to its extensive use and compatibility with micro- and nano-electronic processing, necessary for the development of our devices. Different parameters that play an important role during the deposition were analysed. These parameters include the nitrogen concentration level, which is optimal in a 75%-100% range, associated to a low deposition range. Similarly, a low RF power is recommended to be used, which is also linked to a lower deposition rate. Regarding pressure, low deposition pressures were found to be recommended. Furthermore, substrate heating improves adatoms mobility, which improves the (002) preferred orientation of the films. Finally, an important property to be considered when implementing the piezoelectric material, frequency corner, is addressed.

Chapter 5

Process development

This chapter describes the steps followed in order to overcome different challenges encountered during the fabrication of our devices. It comprises four parts, as can be seen in Figure 5.1. The first part consists in removing the pinholes that were being obtained when performing a potassium hydroxide (KOH) wet etching. The second part consists in obtaining a good quality AlN layer that presents piezoelectric properties. The third part deals with the strengthening of the structures, which consists in rounding the anchoring point of the beams. Finally, the fourth part is about etching through the metals and piezoelectric layers, which proved to be more cumbersome than expected.

5.1 Avoiding pinholes

The first main problem encountered was related to pinholes appearing after the KOH etch of our structures. Three different stacks of layers acting as masking materials for defining the beams were tried. The first trial consisted of oxide/nitride/oxide layers, the second one of polysilicon/nitride/oxide and the last one solely of a 2.7 μm thick oxide layer. All these three trials are shown in Figure 5.2 and the thicknesses are shown in Table 5.1.

Table 5.1: *Layer thickness for different trials.*

First trial		Second trial		third trial	
Layer	Thickness [nm]	Layer	Thickness [nm]	Layer	Thickness [nm]
Oxide	1100	Oxide	1100	Oxide	2700
Nitride	180	Nitride	180	None	-
Oxide	380	Polysilicon	100 and 430	None	-

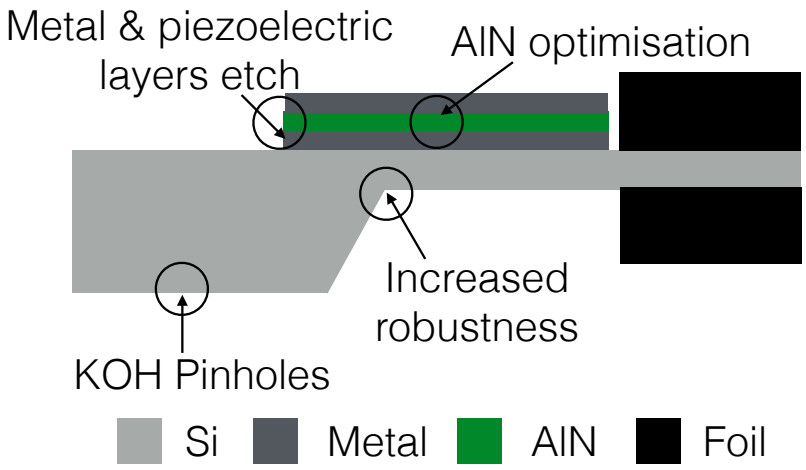

Figure 5.1: *Sketch of the developed beams that summarizes the focus of the development process with its four main parts: AlN optimization, getting rid of pinholes on the wafer surface, increasing the robustness of the beams and etching through the metals and piezoelectric layers.*

First trial	Second trial	Third trial
oxide	polysilicon	none
nitride	nitride	none
oxide	oxide	oxide
silicon substrate		
oxide	oxide	oxide
nitride	nitride	none
oxide	polysilicon	none

Figure 5.2: *Schematic of the different trial layers used for the definition of the beams with KOH etching techniques.*

5.1.1 First trial

In the first trial a stack consisting of oxide/nitride/oxide is used previous to the KOH etch, with the thicknesses indicated in Table 5.1. The first oxide layer is grown by wet oxidation, the nitride layer is deposited using low pressure chemical vapor deposition (LPCVD) and the third layer is deposited using an LPCVD tetraethylorthosilicate (TEOS) deposition furnace. The TEOS-deposited oxide layer is defined in a buffered hydrofluoric (BHF) bath after a lithography process is applied. Afterwards, the resist is stripped and the nitride layer is defined by dipping the wafer in a phosphoric acid bath at 160°C. Once this is done the TEOS-deposited oxide layer is removed and the beam is defined in a KOH bath. Once this is done, both the nitride and oxide layers are stripped in a phosphoric acid and a BHF baths, respectively. Figure 5.3 shows the resulting pinholes on the wafer.

In an aim to avoid the pinholes and at the same time maintain the same layer structure, it was decided to perform the KOH etch without removing the TEOS-deposited oxide layer. This showed to improve the resulting wafer, however, pinholes are still easily spotted on the wafer, as shown in Figure 5.4. The picture was taken after the metal layers were deposited, however, it serves for the purpose.

5.1.2 Second trial

Due to some contamination observed after the oxide deposition (particles spotted under the microscope), in a second trial a polysilicon layer replaces the TEOS-deposited oxide layer, as

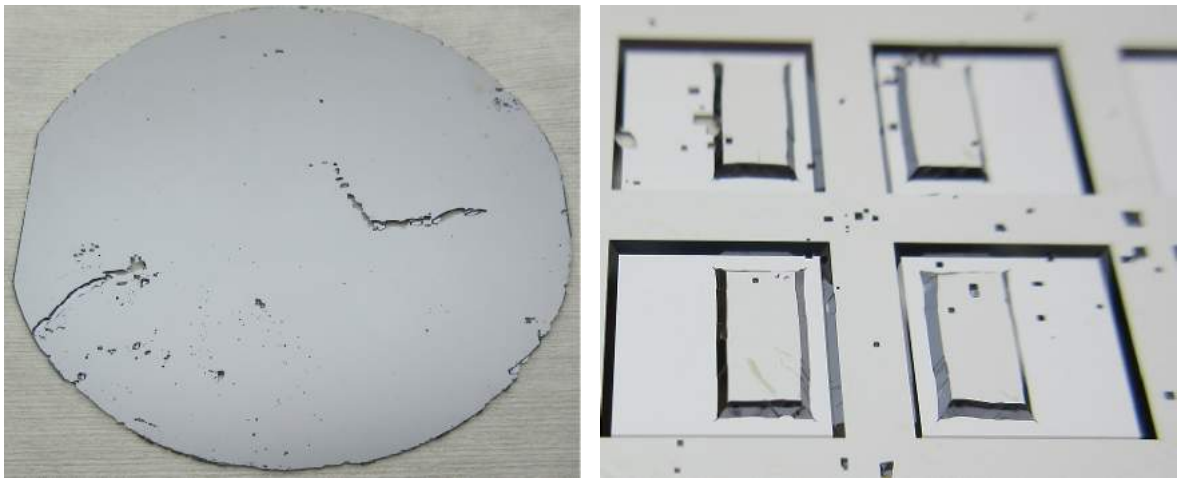

(a) **(b)**

Figure 5.3: *Pinholes that appear after the KOH etch both on the front-side a) and on the backside b) of the wafer.*

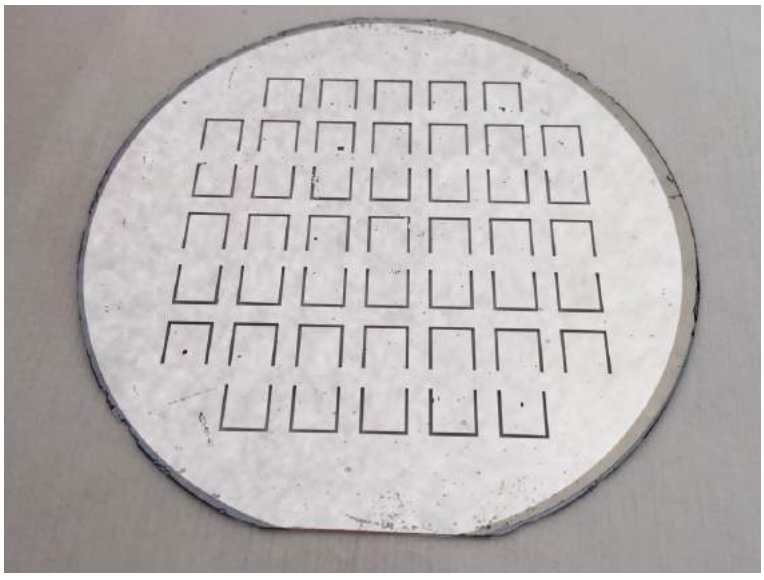

Figure 5.4: *Resulting wafer when performing the KOH etch without removing the TEOS-deposited oxide layer. A metal layer is included.*

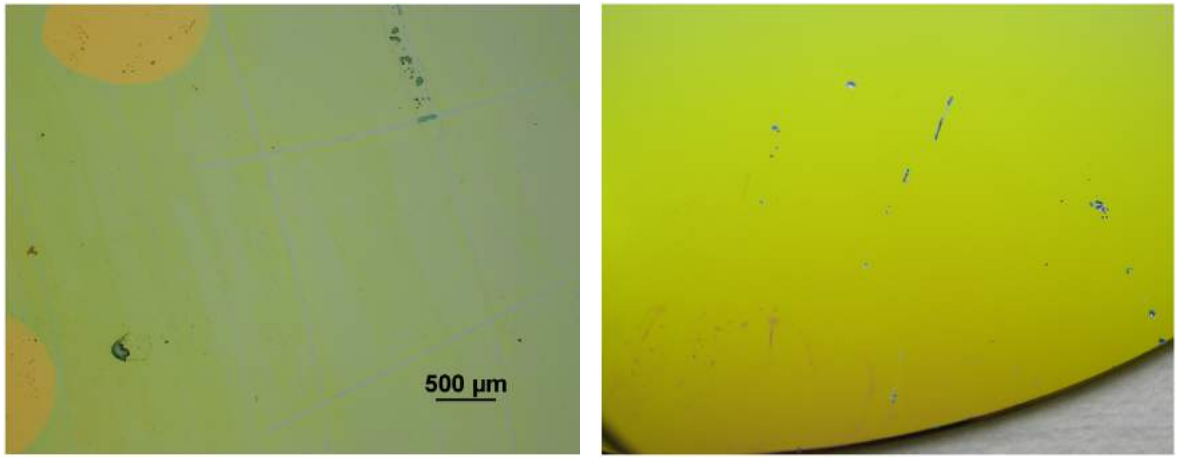

(a) **(b)**

Figure 5.5: *a) Marks on the wafer rigth after dipping it in phosphoric acid. b) Pinholes appearing after a 3 hours KOH etch.*

specified in Figure 5.2 and with the thickness indicated in Table 5.1: 100 nm. The SiO_2 and nitride layers are respectively grown and deposited as described in the previous section. The polysilicon layer is deposited in a LPCVD furnace and the wafer is brought to a phosphoric acid bath at 160°C. Figure 5.5a shows the wafer rigth after a phosphoric acid etch, where already some marks can be distinguished. If the polysilicon layer has been protective enough through the etch in the phosphoric acid bath, when performing a KOH etch, no wholes should be spotted. Figure 5.5b shows the same wafer after about 3 hours of KOH etch, about half the time required in our fabrication process. One can argue that the polysilicon layer was not thick enough, to that end a new test was performed. This time the polysilicon layer had a thickness of 430 nm while the nitride layer was kept the same and the lithography process described in the previous section was carried out. A portion of the resulting wafer is shown in Figure 5.6, where some pinholes are spotted again even though the polysilicon thickness was 4.3 times larger than in the previous case. In order to discard the option that the nitride layer was the one causing the pinholes, a wafer with only this layer was dipped into a KOH bath, the result was that no pinholes appeared, which indicated that the problem was introduced by the polysilicon. The two materials that could be used for masking the nitride layer etching have given problems, therefore, it was decided to look for a replacement of the nitride layer.

5.1.3 Third trial

A third trial was made by using only oxide as masking material for the whole process. The selectivity between silicon and oxide is not as large as between nitride and silicon. However, with a thick enough oxide layer the KOH etch process should present no problem. The used thickness of the oxide layer was 2700 nm. In order to etch through this layer a BHF bath was used, which presents an etching rate of $75 - 80$ nm/min, this means that for a thickness of 2700 nm the resist used (AZ5214E, with a thickness of 1.5 μm) as masking material must

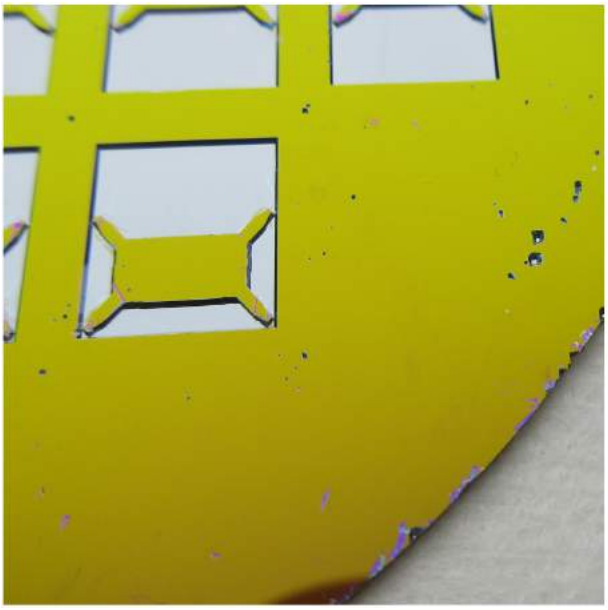

Figure 5.6: *Wafer after a KOH etch where a* 430 nm *thick polysilicon layer was used as masking material during the previous phosphoric acid etch.*

withstand at least 36 min of etching. When performing the etch the resist withstood only 15 min. This is due to the kind of post-baking that the resist underwent: 1 min at 90°C. The largest amount of time the resist could withstand is half an hour, this can be achieved by a hard bake at 120°C. However, since the time needed in our case is about this limit, it was decided to shift to a dry etching method. The wafer where the BHF was already started (wafer 1) was finished by using an advanced oxide etcher (AOE). Another wafer (wafer 2) was brought solely to the AOE. Figure 5.7a and Figure 5.7b show respectively wafer 1 and wafer 2 after the KOH etch has been performed, which clearly shows that a dry etching of a thick oxide layer is the optimal option. It can be argued that the pinholes in the first trial arose due to the same reason, i.e. due to the BHF bath. However, in that case no delamination of the resist was observed since the oxide thickness was much thinner. Nevertheless, it is not totally discarded as a cause of pinholes. No more investigation was conducted in this regard since the use of only one layer of oxide instead of three different layers is more appealing due to the reduction in furnace usage and ease of fabrication. Therefore, for the last set of devices this one-thick-oxide layer approach is taken.

5.2 AlN and metal layers deposition

The deposition of the AlN layer and its corresponding bottom and top electrodes was performed using Cryofox explorer 700 from Politeknik, which was available at Danchip cleanroom facilities. This machine had been used previously by another group that was trying to deposit AlN, but the crystal quality was not very good and some work was done by us trying to opti-

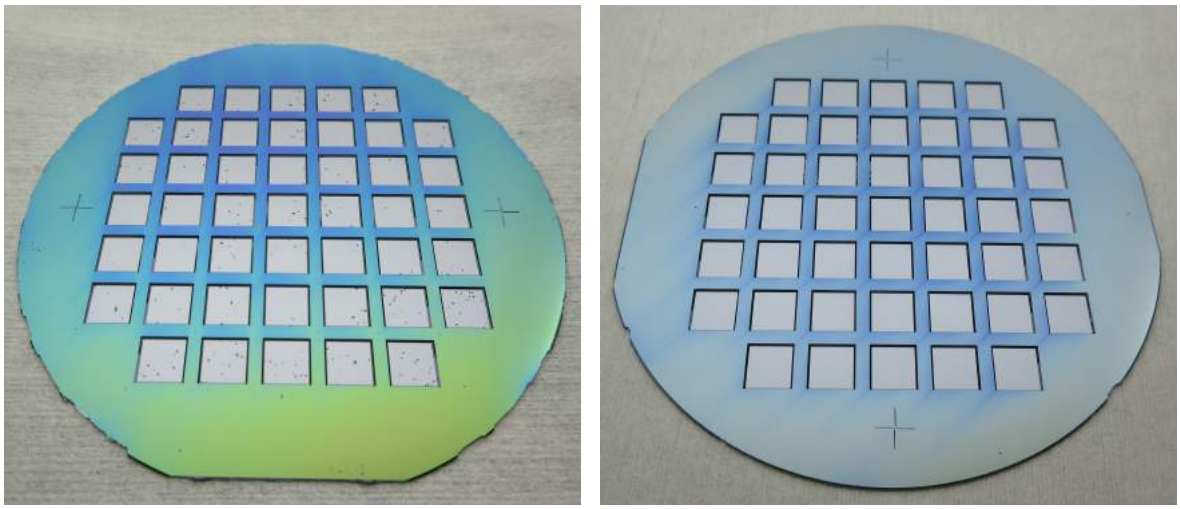

(a) **(b)**

Figure 5.7: *a) Wafer 1 after the KOH etch with pinholes developed on the structures. b) Wafer 2 after the KOH etch, the surface is free of any pinhole.*

mize the process, the result was a decent quality AlN layer. However, this machine presented many problems both when starting a process and during processing, and not only for our specific deposition purpose. For this reason, Danchip decided to decommission the machine and it was no longer possible to deposit AlN using this machine. Another sputtering machine was tried, where a leakage of oxygen while using the nitrogen gas line was detected. For the second set of wafers and due to the lack of time left it was decided to send them to PIEMACS Sarl S.A., where the AlN layer and its corresponding metal electrodes were deposited. This section describes the optimization of AlN at Cryofox together with some problems encountered. It also introduces the leakage problem encountered at the second machine that was tried and, finally, provides with the set of parameters used by PIEMACS Sarl S.A. to deposit the AlN layer.

5.2.1 Deposition with Cryofox explorer 700

Cryofox explorer 700 is a machine that allows for DC and RF sputtering together with e-beam evaporation. In our project, the e-beam mode was used for metal deposition while the RF sputtering mode for the AlN deposition. It is important to note that when running a stack process, all the layers must be set in the recipe unless venting is not a problem. As it was described in Chapter 4, a high oxygen level is detrimental to the AlN quality, therefore venting must be at al costs avoided. Furthermore, if any problem during the deposition of the layers or in between arises, most of the time the machine needs to be vented due to the in-built mechanism of it, which does not allow for a simple restarting process. As will be seen throughout this section, this simple characteristic ruined many of our samples when different problems were encountered during the depositions.

The most important part of this stack deposition is doubtlessly the RF sputtering one, during which AlN is deposited. The set of parameters that can be changed are: nitrogen gas percentage (where the remaining percentage corresponds to the sputtering gas, which is argon), oxygen gas percentage, RF power, base pressure, plasma ignition pressure, sputtering pressure and deposition time. Besides these parameters, other settings allow to change the cryovalve opening percentage (i.e. how open the valve through which the gases diffuse to the chamber is) and the substrate temperature (i.e. heat on or heat off of the wafer holder). It must be beared in mind that turning the heat on for the AlN deposition requires between an hour or two afterwards in order to get to less than 60°C, which is a requirement for the e-beam process to start. This means that if one aims at depositing AlN at high temperatures, this extra time should be counted on before the deposition of the last metal electrode starts. Regarding the e-beam deposition, the parameters that can be adjusted are the thickness of the layer, the deposition rate, the base pressure and the voltage. Another problem that arises when using this deposition method is that if the crystal cannot monitor the deposition rate the process automatically stops, which leads to the machine having to be vented.

Previous to our project, a bachelor project [83] was carried out by another group, where they tried to deposit AlN with the Cryofox. The result was a not very good quality layer, which did not even had the right stoichiometry. Table 5.2 shows the set of parameters that they tried, where it can be seen that three main parameters were changed: sputtering pressure, substrate temperature and the bottom substrate onto which AlN is deposited (i.e. silicum or a metal layer). It must be noted that when stating room temperature it means that the substrate heat mode was off, and the default temperature is room temperature. However, due to the plasma created during processing, the substrates experience a self-heating process. In order to characterize the samples, they underwent x-ray photoelectron spectroscopy (XPS) and x-ray difraction (XRD) performed by the bachelor students. The results showed a very poor quality piezoelectric layer, where not only different AlN orientation peaks were present (which proved to be detrimental to the AlN piezoelectric quality, as seen in Chapter 4), but also the (002) peak intensity was most of the time not the highest among all of them. Only one sample, wafer number 10, showed a (002) preferred orientation peak with no other crystal orientations present, as shown in Figure 5.8b.

Regarding the XPS results (which were not only analyzed on the surface but also throughout the sample thickness by argon etching method), the Al:N ratio was considerably off from being 1:1. Except for wafer 1, which showed worse off results, the Al and N percentages were about 60% and 40%, which leads to a Al:N ratio of 1.5. Even though for wafers 5 and 6 the gas ratio was changed, as shown in Table 5.2, it did not seem to affect that much the Al:N ratio compared to the other gas compositions. However, their report does not state the fitting procedure of the XPS analysis in order to find those ratios, therefore the uncertainty of their results is unknown.

In order to optimize the AlN quality, it was decided that the inmediate parameter to be changed was the gas ratio, i.e. argon and nitrogen percentages. The reason for this is that, as described in Chapter 4, a large nitrogen percentage is necessary for obtaining (002)-orientation

Table 5.2: *Parameters used in previous bachelor project [83] for AlN deposition*

Wafer number	Sputter pressure [mbar]	Ar:N_2 ratio	Power [W]	Temp [°C]	Deposition time [min]	Cryovalve %	Substrate material
1	$5.3 \cdot 10^{-3}$	9:1	800	room	120	7	Si
2	$4.0 \cdot 10^{-3}$	3:1	1000	room	120	7	Mo
3	$4.0 \cdot 10^{-3}$	3:1	1000	200	360	10	Si
4	$4.0 \cdot 10^{-3}$	3:1	1000	200	210	10	Si
5	$4.0 \cdot 10^{-3}$	1:1	1000	200	210	10	Si
6	$4.0 \cdot 10^{-3}$	1:1	1000	room	120	10	Si
7	$6.7 \cdot 10^{-3}$	3:1	1000	room	120	10	Si
8	$6.7 \cdot 10^{-3}$	3:1	1000	200	210	10	Si
9	$6.7 \cdot 10^{-3}$	3:1	1000	room	120	10	AlN/Mo
10	$6.7 \cdot 10^{-3}$	3:1	1000	room	120	10	Al

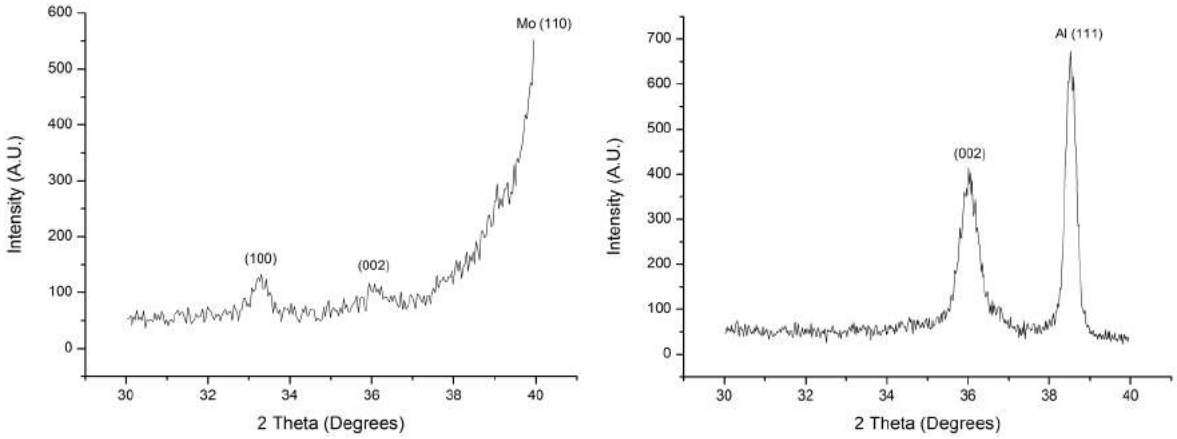

(a) **(b)**

Figure 5.8: *XRD results for a grazing incidence approach, scans were perfromed from 30° to 40°, both figures taken from [83] a) wafer 9. b) wafer 10.*

direction in the AlN film, and this is a requirement not fulfilled in the bachelor project.

A more detailed describtion about the Cryofox is given now, before the deposition parameters are set. At this point it is important to note that, even though the AlN layer was always deposited using the Cryofox, one of the two metals discussed in Chapter 4 that provide the best AlN quality (platinum) was not available as target at the Cryofox. Therefore, in order to test the use of this metal as bottom layer for AlN, the Wordentec QCL 800 was used instead. For the other metal, molybdenum, Cryofox is utilized.

As stated before, the Cryofox machine allows for both e-beam and sputtering deposition. However, each method requires a different mask whose purpose is to improve the homogeneity of the layer, as shown in Figure 5.9. These masks are located beneath the wafers, as shown in Figure 5.10 and will rotate around the center through the quadrant of the circle where the wafers are specified to be. It is important to note at this point that the AlN deposition and metal deposition takes place under the wafer position and not above it. Only one mask per run can be used, which means that in order to change the masks from e-beam to sputtering technique and the other way around, the machine must be vented. As described above, the idea is to deposit AlN in sputtering mode, however, the availability of the metal that serves as bottom electrode/seed layer (molybdenum) was in the e-beam mode. Since, as stated in this section, venting the chamber is avoided at all costs due to oxygen contamination, a compromise in film homegeneity had to be found, i.e. either the AlN or the molybdenum film would have a lower homogeneity. As the critical deposition is the AlN one, one would choose to sacrifice the homogeneity of the metal layer. However, from the shape of the masks shown in Figure 5.9, it can be easily seen that the e-beam mask will lead to a higher deposition rate than the sputtering one. The results obtained showed that even by using the e-beam mask for a sputering deposition the AlN deposition rate was 56 nm/min, which for a deposition of the aimed thickness: 400 nm, would require 12 hours. Here it is important to note that one of the requirements when using this machine was that the user must check the machine during the process since it has been experienced that the plasma suddenly stops working, which leads to a system failure and which at the same time represents a problem to Danchip facilities. Furthermore, the molybdenum targets available were very small in diameter (one inch). This meant that not many depositions could be run before finishing the target in the middle of a deposition, which led to failure errors and therefore venting the machine during tests (as an estimate, one can say that no more than 200 nm can be deposited before changing the target and using the e-beam mask). Therefore lowering the deposition rate of this material was not convenient. Due to these two reasons, the e-beam mask was decided to be used throughout the deposition process. Furthermore, in order to lower the chances of finishing the target material, the initial considered thickness of the molybdenum seed electrode was lowered from 100 nm to 50 nm. The reason for choosing in the beginning twice as much was based on the thicknesses found in literature. Likewise, the AlN thickness was aimed at 400 nm for the same reason [29]. Aiming at this AlN thickness with a deposition rate of 56 nm/min meant that the deposition had to be performed in two steps since the maximum deposition time per layer allowed by the machine was of 500 min. Therefore, the deposition was split into two identical

(a) **(b)**

Figure 5.9: *Default masks that are recommended to be used during sputtering and e-beam deposition in order to achieve a as high as possible uniformity. a) Sputtering process mask. b) E-beam process mask.*

ones (in terms of sputtering conditions): one that lasted 500 min and another one that lasted 220 min. This led to more problems since many times the main problem encountered was that plasma did not ignite, therefore if the first layer is deposited smoothly but this problem arises while trying to deposit the second layer, then the machine must be vented an the sample must be discarded.

With all these details set, the machine was ready to try the parameters set by us. As stated before, our first aim was to increase the relative nitrogen gas flow respect to argon while maintaining the other parameters constant and measure both the Al:N ratio and the crystal structure. The results obtained showed what was expected, an increase in nitrogen flow leads to a decrease in Al:N ratio. For a 70% of nitrogen gas flow the ratio achieved was of 1.18. When analyzing the spectra it is important the prior knowledge that the user has on the nature of the sample. In our case, the elements expected to be found are straight forward: aluminum, molybdenum, nitrogen and oxygen. Argon could also be expected to be found due to the fact that this material is used as sputtering ion both during the AlN deposition and during the XPS analysis, as stated above throughout this section. However, the percentage is expected to be very low, and traces below 0.5% are not detected by the system. Once selecting the elements, a spin-orbit state must be assigned for each of them. Once selecting the state, a fitting curve is added to each element and the accuracy of the fitting can be judged for each of the layers analysed. When different spin-orbit states are available for a single element, the procedure followed is to compare their accuracy and select the one that seems better off. The XPS technique is a science in itself, and no further analysis optimization was performed.

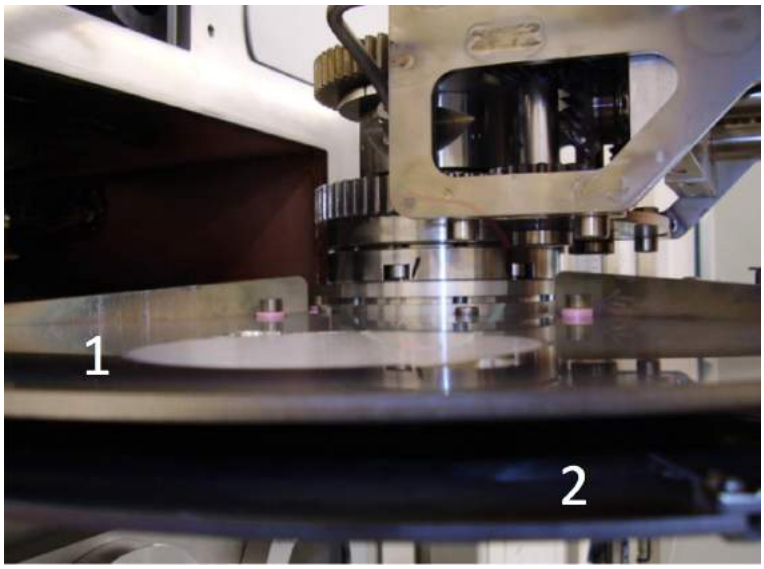

Figure 5.10: *Cryofox's load-lock. The wafers are loaded in the upper part marked with number 1 and the corresponding mask is loaded at position 2.*

Table 5.3: *Parameters used for the sputtering deposition of AlN with Cryofox explorer 70.*

Sputtering		E-beam	
N_2 gas flow	60, 70 and 80%	Voltage	10 kV
Ar gas flow	40, 30 and 20% of total gas flow	Mo dep. rate	0.3 Å/pers
Power	1 kW	Ti dep. rate	0.08 nm/pers
Pressure	4×10^{-3} m bar	Pressure	2×10^{-6} m bar

Different nitrogen percentages were tried: 60%, 70% and 80%. The sputtering conditions for all the samples were the same except for the gas flow percentage, as shown in Table 5.3. The layer structure was the following. On top of the silicon wafer 50 nm of molybdenum were deposited, then a variable thickness of AlN and finally 50 nm of molybdenum to seal it. Figure 5.11a and Figure 5.11b show the XPS analysis of the first two cases, i.e. 60% and 70% of nitrogen gas, respectively. The Al/N ratios obtained were respectively 1.26 and 1.18. Regarding the 80% nitrogen gas flow case, the ratio obtained was 0.5. This means that for increasing nitrogen concentrations the Al/N ratio diminished, as expected. Among these test samples, it is straight forward to select the one where AlN was deposited under 70% nitrogen flow, perform XRD measurements and check whether the quality is good enough.

Regarding the XRD analysis, the experiments were performed using a copper radiation instrument. The type of measurements were the so called Bragg-Bentano or lock-coupled in the θ:2θ mode. This means that the x-ray tube is fixed and the sample rotates at θ°/min, while the detector does the same at $2\theta^\circ$/min. This type of measurement can be compared to the one the bachelor students did: grazing incidence. Compared to the lock-coupled measurements,

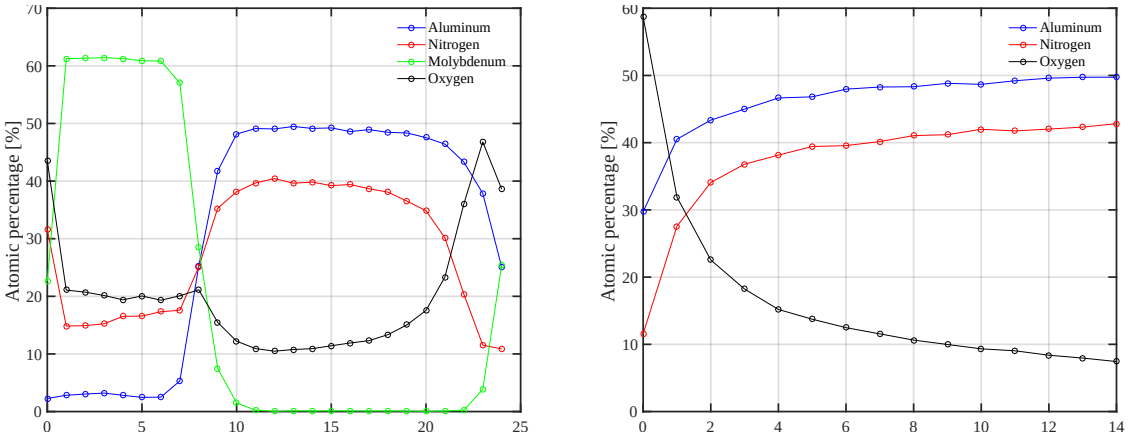

Figure 5.11: *XPS analysis of a pair of samples deposited under the same sputtering conditions except for the nitrogen flow percentage using Cryofox explorer 700. The plots represent the atomic percentage of the different material components versus the etching step at which each elemt scan is performed. Two different nitrogen percentages are analyzed a) 60% N_2 b) 70% N_2.*

the grazing incidence method maintains the sample (and equivalently the x-ray tube) fixed while scanning, only the detector moves. Furthermore, the incidence angle is not larger than 5° (in their specific project it was only 0.5°). This means that the penetration depth of the x-rays is much lower and, therefore, the scan is limited to the surface of the sample. However, the samples that they were analysing had thicknesses that were less than 100 nm, this can be compared to ours, which were about four times as thick, i.e. 400 nm of AlN. In our case, a lock-coupled approach was taken. Not only the sample so far described was analyzed, but as stated earlier in this section, another sample where Ti/Pt were used as bottom layers was analyzed. The thicknesses were 10 nm for titanium and 100 nm for platinum, both deposited using the Wordentec QCL 800 in e-beam mode.

Sweeps from 30° to 40°, with an step size of 0.03° and a measuring time of 3 seconds for both samples were performed. This is shown in Figure 5.12. It can be seen that for the molybdenum case only the (002) oriented peak for AlN is observed. On the other hand, for the platinum case, both (002) and (101) orientation peaks are observed together with the underlying platinum layer. From that figure, it is apparent that molybdenum used as bottom layer provides us with a better quality AlN layer. Therefore, the deposition process parameters used to fabricate the first set of VEH's in our project are finally the ones stated in Table 5.3 with 70% of nitrogen content and the devices fabricated showed piezoelectri response.

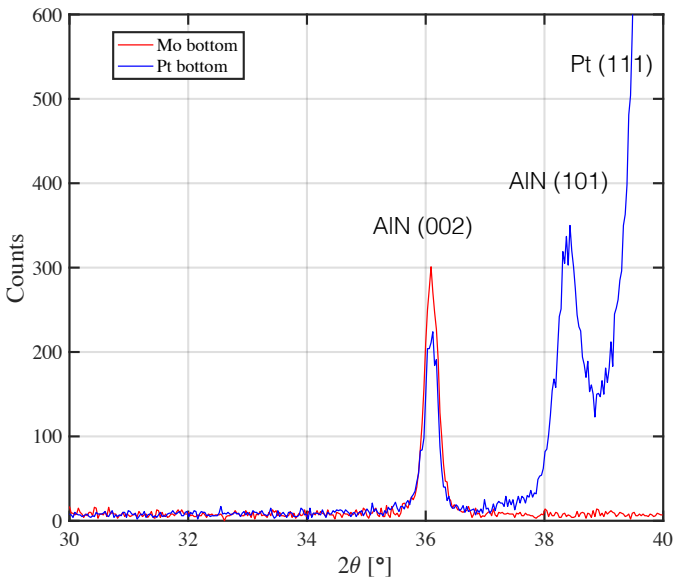

Figure 5.12: *Characterization of two samples, one with molybdenum as bottom layer (*50 nm*) with the deposition conditions as shown in Table 5.3. The other sample has a layer structure of Ti/Pt with thicknesses of 10 nm and 100 nm, respectively, beneath the AlN. For both cases the AlN presents a thickness of about* 400 nm.

5.2.2 Desposition with Lesker CMS 18

As described in the previous section, the Cryofox was decommissioned due to, among others, some of the reasons explained in the previous section. Therefore, the sputter-system Lesker CMS 18 was also tried. This machine does not allow for e-beam deposition, but both DC and RF sputtering are possible. The machine is divided into three parts: the load-lock, the process chamber and the controller section, where the computer is located. The gases that can be used during sputtering are argon, nitrogen and oxygen. Both the nitrogen and oxygen lines join into a single common line, which is directly connected to the process chamber. Before the joint point, each line has its own valve and before using nitrogen gas, the closure of the oxygen valve is always checked. However, a high oxygen level has consistently been experienced during depositions using nitrogen as a reactive gas. It is important to note that when depositing the metal electrodes, the oxygen percentage fell down to normal levels. As an example Figure 5.13 shows the XPS results that correspond to the 50% flow of nitrogen with the deposition parameters of 150 W as RF power, 5 mTorr as sputtering pressure and with substrate heating mode off. It can be observed how the oxygen level rises up when going from the top molybdenum layer to the AlN layer, which is clearly connected to the fact that the leakage occurs through the line used for pumping in the nitrogen. Similar results were obtained for other nitrogen percentage flows, which adds no further understanding of the process. Due to this leakage problem that was not solved by the Danchip staff responibles, this machine was discarded for out purpose.

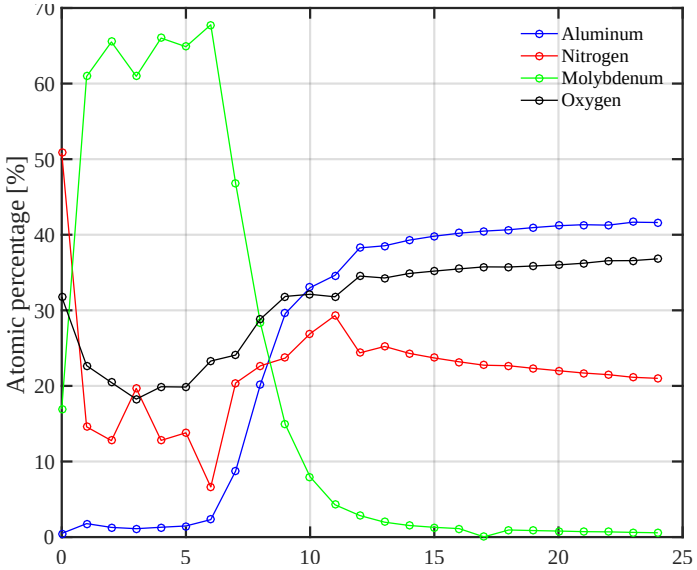

Figure 5.13: *Results from the XPS analysis of a sample with Mo/AlN/Mo layers deposited using Lesker CMS 18. The plot represents the percentage of each material versus the etching step at which the scans are run for analyzing the composition.*

Table 5.4: *Parameters used by PIEMACS Sarl S.A. for reactive sputtering deposition of AlN*

Nitrogen content	80%
Argon content	20%
Sputtering pressure	5.23 mTorr
RF Power	6 W
Substrate temperature	300°

5.2.3 Deposition by PIEMACS Sarl S.A.

Due to the unsuccessful trials and the shortage of time it was decided to send processed wafers (i.e. wafers with the beams already defined) to the Swiss company PIEMACS Sarl S.A. where the AlN deposition of the second set of the devices that were fabricated took place. The technique used was again RF reactive sputtering and the parameters they used are shown in Table 5.4, where it can be seen that a large nitrogen percentage is used, as expected. Furthermore, heating mode is used and the substrate is kept at 300°. The general layer structure is Pt/AlN/Pt/Ti/Si, this is shown in Figure 5.14, where the top platinum layer was not included in order to perform XRD measurements on the same wafer. Furthermore, XRD measurements were performed by them, this is shown in Figure 5.15, where both (002) and (004) orientation peaks for the AlN are observed, this means that the layer shows a c-axis orientation, which is in agreement with high quality AlN-based piezoelectric layers.

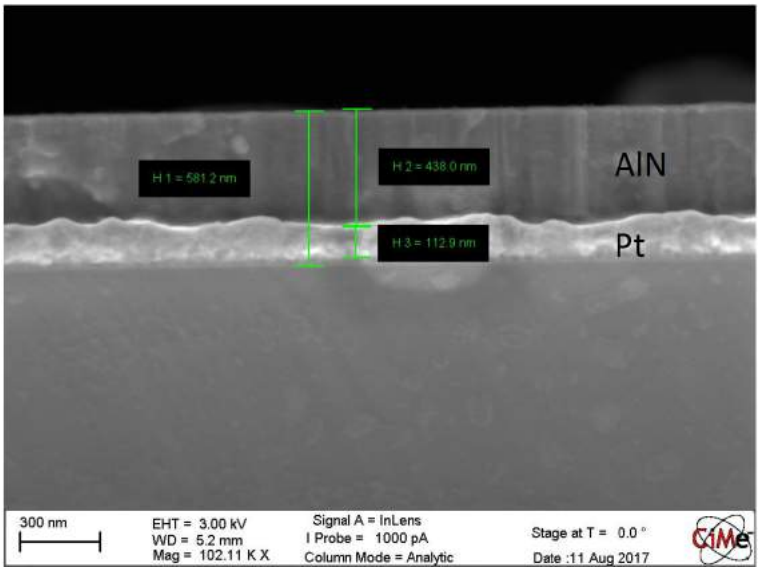

Figure 5.14: *SEM image of a wafer where the AlN/Pt/Ti/Si layer structure was deposited by PIEMACS Sarl S.A. under the processing conditions shown in Figure 5.4.*

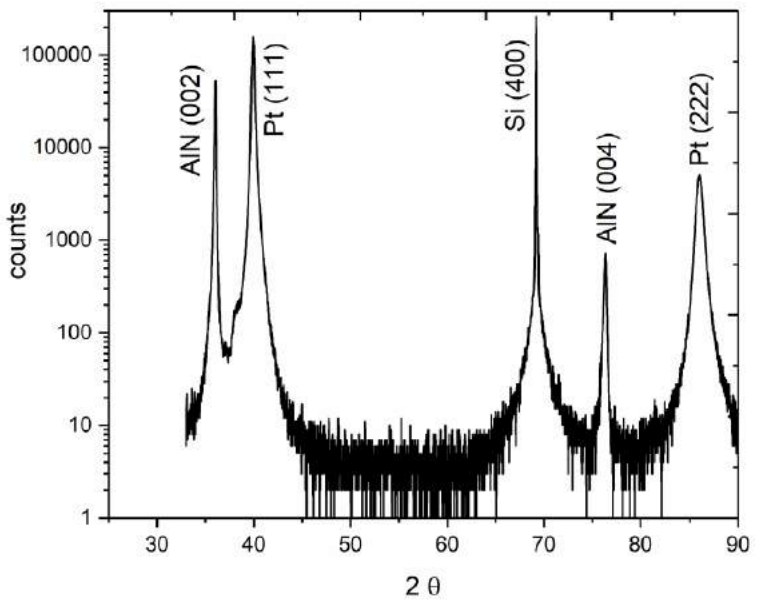

Figure 5.15: *XRD analysis of a wafer where the AlN/Pt/Ti/Si layer structure was deposited by PIEMACS Sarl S.A. under the processing conditions shown in Figure 5.4.*

5.3 Corner rounding

Typical VEHs use silicon as substrate due to the well established Si micro- and nano-fabrication techniques, however, some research groups [84, 85] have studied using metal substrates instead. This is due to their higher plastic deformation which, compared to the highly brittle material that silicon is, clearly displays an advantage in the relative displacement that the beams can undergo. These larger deflections translate to larger strains on the piezoelectric material and, therefore, higher output power. Furthermore, using a metal structure presents the advantage of lowering the natural resonant frequency even without a seismic mass [84], which is important when aiming at harvesting energy from ambient vibrations, as explained in Chapter 1. Nevertheless, an important drawback of using metal substrates is the restriction in micro- and nano processing techniques that these metals can undergo. Here a silicon-based two-step and lithography-free fabrication process that increases the beam's robustness without compromising its dimensions is presented. The process consists in growing an oxide layer after the cantilever has been defined by KOH wet etching. This etching results in two different silicon directions present on the surface, (111) and (100). The oxide growth on these two different directions present the highest difference among the other possible Si faces, which leads to a consumption of the Si that results in a rounded corner of the anchoring point and therefore the robustness is increased. This corner rounding method has been used previously in other fields by other research groups [86]. Simulations were carried out using Silvaco Athena software [87]. The simulation takes into account the different oxide growth rates on the (111) and (100) silicon surfaces due to the dependence of the linear rate constant on the surface atom density which is higher for the (111) silicon surface compared to the (100) surface. In addition, the software takes into consideration the highly doped surface of our wafers. Figure 5.16 shows the results from the simulation. Figure 5.16a shows the corner of the beam after the KOH etch which is implemented as a geometrical etch in the simulation code. Figure 5.16b shows the beam after 40 minutes of oxidation at 1100 °C, which corresponds to an oxide thickness of 619 nm and 764 nm on the (100) and (111) surfaces, respectively. Figure 5.16c shows the corner structure after 80 minutes of oxidation and the oxide thicknesses are 876 nm and 1079 nm on the corresponding (100) and (111) surfaces. The total oxidation time is 126 minutes and the final oxide thicknesses on the (100) and (111) surfaces respectively, are 1100 nm and 1352 nm. Finally, Figure 5.16d shows the corner structure after the oxide layer has been removed.

SEM images were taken just after the KOH etch was performed, Figure 5.17a, and after the corner rounding treatment was applied, Figure 5.17b. It is clearly seen that a rounding effect is achieved and a curvature radio of 1.8 μm is measured. In Figure 5.17b the simulation result from Figure 5.16d is included on top of the SEM image to the end of comparing the experimental and simulated results. It is clearly seen the accuracy of the simulation tool. The performance of the cantilevers with and without this corner rounding will be further investigated in Chapter 7.

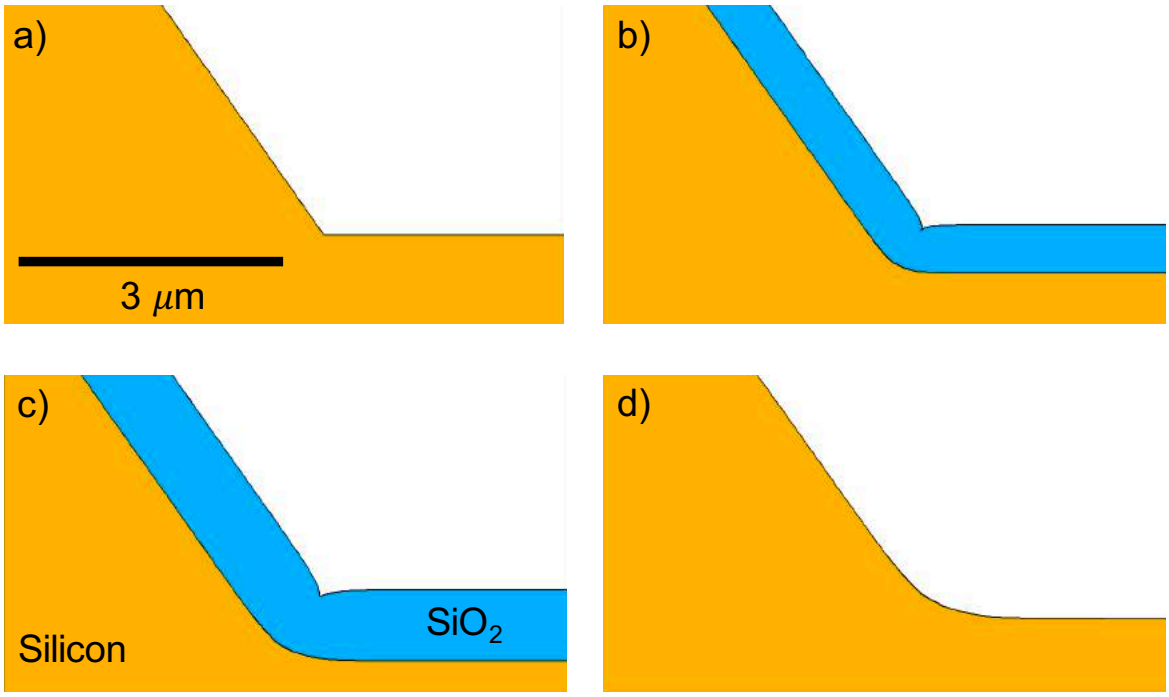

Figure 5.16: *Results from the corner rounding process simulation. a) As etched, b) After 40 minutes of oxidation, c) After 80 minutes of oxidation, d) After 126 min of oxidation and removal of the oxide.*

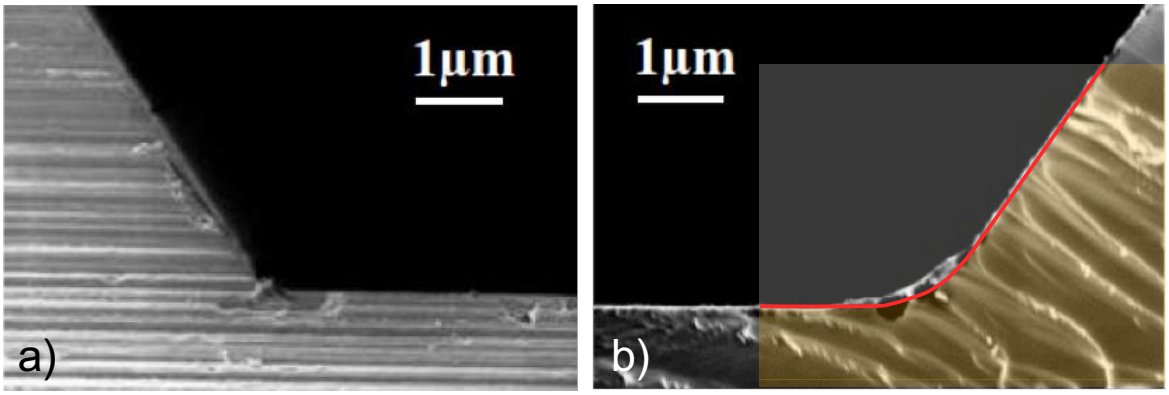

Figure 5.17: *SEM images of the corner structure of the beam a) before and b) after the oxide growth. The simulation result, Fig. 5.16d, is shown as the transparent structure overlaid on the SEM image. The solid red line shows the location of the surface of the simulation structure.*

5.4 Platinum and AlN etching

In order to etch through the AlN layer different methods can be followed. For an anisotropic etching either dry etching or ion beam etching techniques can be used. For the dry etching case it has been reported that a fluoride based etching can lead to a high etching rate of up to 140 nm/min [88]. However, this is not a batch process and is more expensive than its wet etching counterparts. To wet etch AlN tetramethylammonium hydroxide (TMAH) has been reported to etch with a rate of 22 nm/min with a lateral etching under 2 nm/min at room temperature and with a 25 wt.% [89]. This chemical solution etches through Si as well, nevertheless, the etching rate in Si is only 0.27 μm/min at 70 °C for a (100) oriented silicon wafer [90]. For an AlN thickness of only 400 nm the etching time is about 18 min at room temperature. This duration translates into a silicon etch of about 5.5 μm on the backside of the wafer if the etching was performed at 70°C. However, due to safety restrictions, in our cleanroom facilities the use of TMAH was limited to a 2% concentration, which would lead to a very slow etching rate. Acqua Regia has also been reported as an etchant of AlN and Pt as well. The initial idea was to use two different masks for the process of etching through the metals and piezoelectric material: one for the top electrode and another one for the AlN and bottom electrode, this would prevent any short-circuit derived from undercutting the AlN layer. However, the result was a poor adhesion of 10 µm AZ 4562 resist to the AlN layer while performing the Aqua Regia etch, which led to the resist detaching from the AlN surface after a few minutes of etching with Aqua Regia at 80°C. For this reason, only one mask was used to etch through the three-stack layer and no short-circuit was observed during the tests.

Due to the high temperature of the etching the resist cannot withstand more than ca. 10 min of etch, otherwise, cracks start developing on the resist, as seen in Figure 5.4. The solution was to re-do the lithography process three times, with the same parameters for each of them, in order to etch through the three layers. It is important to note at this point that the titanium adhesion layer is also etched through in this process. In addition, the etching rate of the AR solution decreases thourgh time within already the 10 min that it is used. For this reason, the wafers were dumped into a new chemical bath right after the chemicals were mixed for each of the three etching process. In order to detect whether all the layers have been etched away, Energy Dispersive X-Ray analysis technique (EDX) is used. Figure 5.19a and 5.19b, respectively, show the wafer after etching the top electrode and after performing the final etch.

5.5 Summary

In this section the main challenges encountered through the fabrication process were described. Pinholes appearing on the surface of the wafers were avoided by changing the mask materials used for the KOH etch. Fine quality AlN layer was deposited on the first type of beams developed in this project. However, due to many issues encountered by the user of the machine, it was decommissioned and AlN was no longer deposited by us. In addition, The

Table 5.5: *Aqua Regia composition and approximate etch rates.*

Parameter	Value
H_2O	400 ml
HCl	350 ml
HNO_3	50 ml
Etch rate in Pt	$\approx$ 10 nm/min
Etch rate in AlN	$\approx$ 26 nm/min

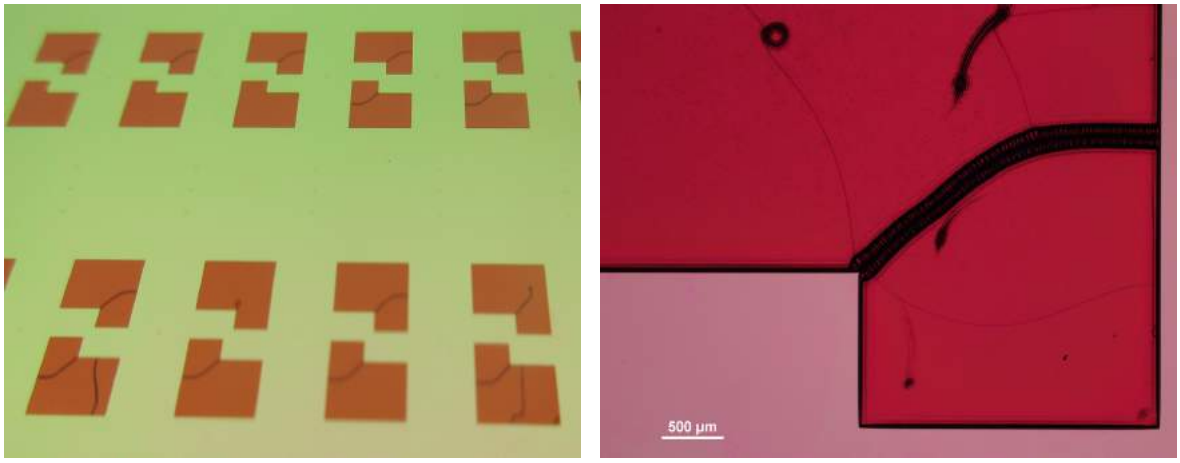

(a) **(b)**

Figure 5.18: *Wafer with cracks developed on the resist after* $\approx$ 10 min *of etching in AR under the conditions described in Table 5.5. a) Regular picture b) Microscope picture.*

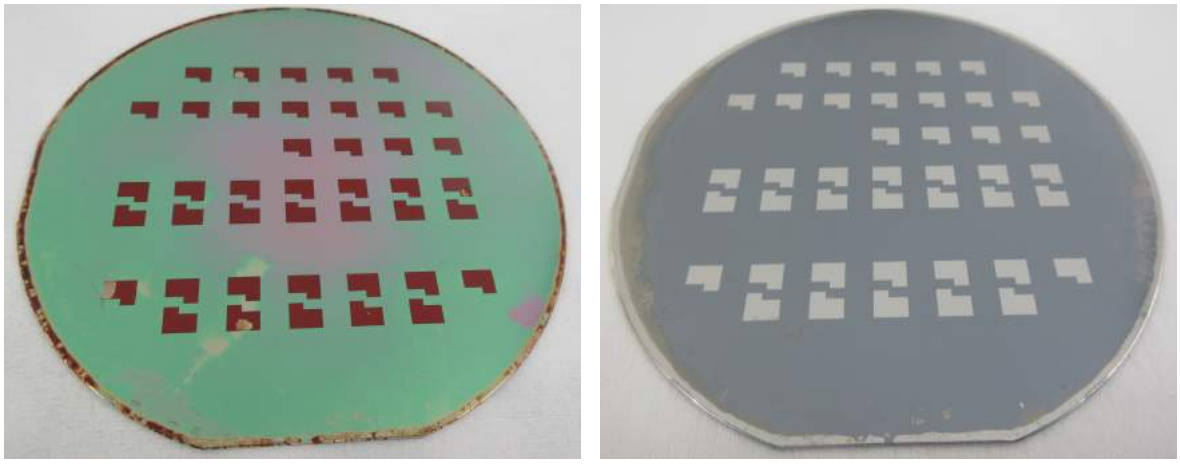

(a) **(b)**

Figure 5.19: *Three-stack etching in AR solution. a) After etching top electrode, with AlN left on the wafer. b) After etching through the three layers and stripping resist.*

anchoring point of the beams was enhanced in terms of robustness by performing a rounding of the corner using thermal techniques. Finally, in order to etch through the AlN layer and metal layers a solution of Aqua Regia was finally used at 80°C. This etch demanded performing a lithography process an extra time with the same mask design due to the chemical attack that the resist experienced.

Chapter 6

Design and Fabrication

In this chapter two different fabrication processes together with their corresponding mask designs are described. In the first section the mask designs are presented while in the second section the fabrication process is introduced. In each section, two subsections are considered.

The first subsections consider the first set of cantilevers fabricated during this project. They consist of a beam with a silicon built-in mass where AlN was used as piezoelectric material and molybdenum was used both as bottom electrode and to seal the AlN layer, in this case Al was used as top electrode and as contact electrode on the backside. It is important to note that the deposition of the metals and the piezoelectric material was performed after the beams were released.

The second subsections correspond to the fabrication of the final devices, where no built-in mass is included, just the beam. The piezoelectric material used is also AlN, however, the bottom and top elctrodes are platinum layers. Besides these differences, the deposition of the metal/piezoelectric/metal stack was performed this time before the beams were released. In addition, a strengthening of the beams was also included in this process. Finally, a ferromagnetic proof mass is incorporated.

The fabrication process description includes the development both inside and outside the cleanroom facilities for the two cases aforementioned. Furthermore, it is important to note that in both cases (100)-oriented silicon wafers are used.

6.1 Mask designs

6.1.1 Mask design for the first set of beams

The mask designs used for the first set of beams was exactly the same one used by A. Lei in his PhD thesis [53]. Only three masks were needed for our fabrication process, the set of masks is shown in Figure 6.1. The relevant dimensions are included in Section 6.1.2, this is

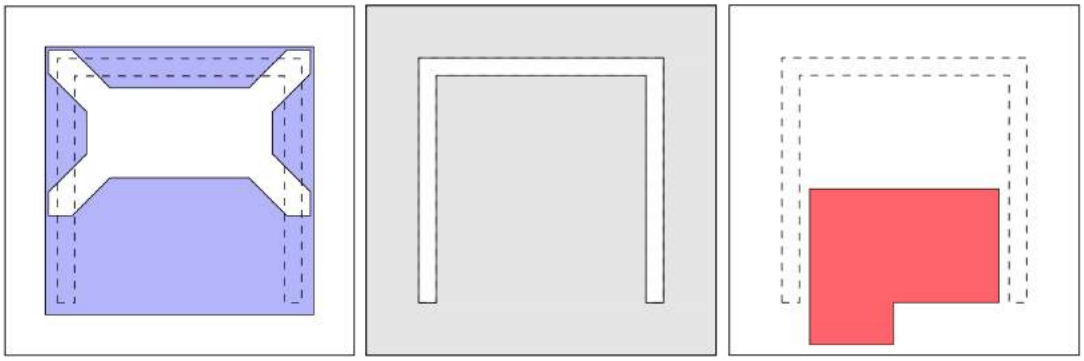

(a) (b) (c)

Figure 6.1: *Mask set used for the fabrication of the second set of devices. a) For the KOH etch. b) For the trench etch (or beam release). c) For structuring the top electrode. The figure is taken from [53].*

so because the values used are the same as for the second set of beams. The first mask to be considered is shown in Figure 6.1a. Due to the fabrication process including a built-in silicon proof mass (which is defined by KOH wet etching) the anisotropic nature of the KOH etch, i.e. the etch rates on the different silicon plane orientations, needs to be taken into account in the mask design. To create this design, first of all the mask designed for the trench etching shown in Figure 6.1b must be considered: this mask has an opening of 500 μm, which is defined in Figure 6.2 as W_T. The opening in the mask for the KOH etch must be this width plus twice W_b, where W_b is defined as $W_b = H/\sqrt{2}$ and where H is the desired depth to be etched thorugh the wafer, as shown in Figure 6.2. For the first set of beams discussed in this subsection the wafer thickness is 500 μm, which results in a W_b value of about 350 μm. If twice the W_b value was not considered, then the mask design would lead to the etch finishing before reaching the required depth, just as shown by the V-shaped etching in Figure 6.2. Besides this, the convex corners of the proof mass must also be considered. Here a corner compensation structure is included. The idea is to introduce pointed blocks at each of the convex corners in the proof mass, this is shown in Figure 6.3. The pointed block structures of length L prevent the etch of the otherwise convex corners. The width of the pointed blocks (W) must be twice the desired depth H. The last mask considered is shown in Figure 6.1, which is used for the definition of the top electrode, where the dark area represents where the metal electrode will stay.

6.1.2 Mask design for the second set of beams

The final set of masks used for the fabrication of the second set of beams is presented in Figure 6.4, where all the images present the silicon area where each device is fabricated represented in light grey. The first mask to be used, shown in 6.4a, defines where the silicon etch should take place, therefore, the blue area represents the opening of the mask, which by using positive resists translates to the resist opening. It is important to note that in this set

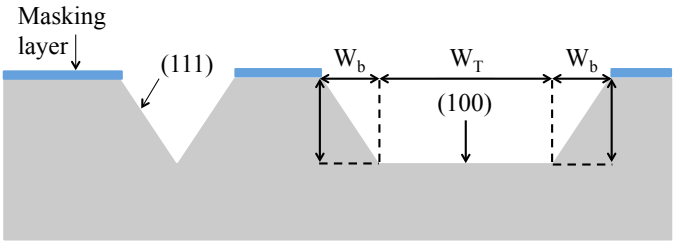

Figure 6.2: *A sketch of the KOH etch on silicon where, on a (100) oriented wafer, both the (100) and (111) planes are observed.*

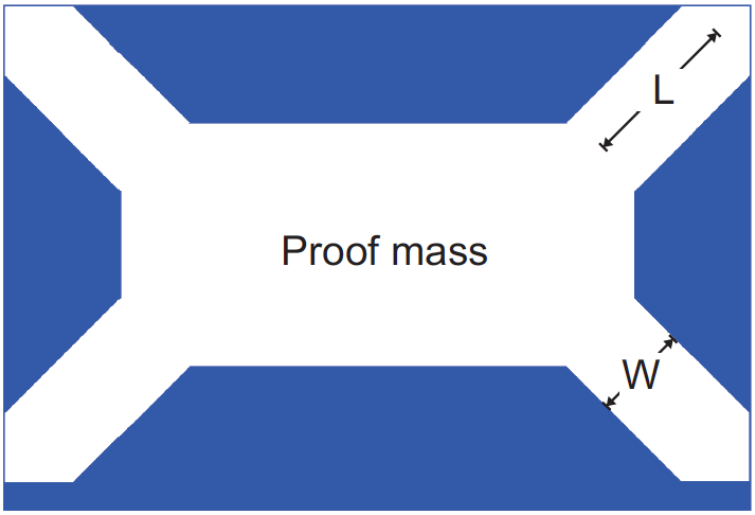

Figure 6.3: *Corner compensation structure designed for obtaining the convex corners of the built-in silicon proof mass. Image taken form [54].*

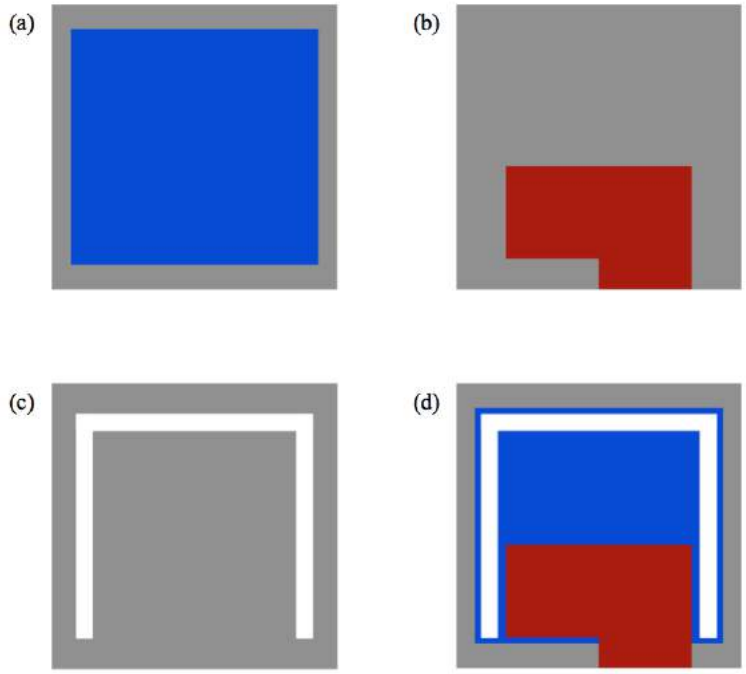

Figure 6.4: *Mask set used for the fabrication of the second set of devices. The silicon device area is included in all the designs by a grey area. a) KOH mask. b) Top electrode definition. c) Trench etch (or release of beams) mask. d) All masks included.*

the thickness of the wafer is changed to 380 μm. This means that now $W_b = 240\,\mu$m. Since no built-in silicon proof mass is developed during the fabrication, the corner compensation structures are not included in the design. Figure 6.4b shows the mask used that will define the top electrode, this means that the read area is the section where the top electrode is not etched away. The same mask is used for etching away the piezoelectric material and bottom electrode underneath. The next and last mask to be used is shown in Figure 6.4c, where the white parts represent the openings where the remaining silicon is etched away in order to free the cantilever. Lastly, in Figure 6.4d, the three masks used are combined together. The dimensions used in the designs are clearly shown in Figure 6.5.

6.2 Fabrication process of the first set of beams

The first set of AlN-based unimorph VEH's are fabricated using n-type 100 oriented silicon wafers with a thickness of 500 µm. These cantilevers have a built-in mass defined with a KOH etching, this means that the mass material is also silicon. With this first set of masks no magnetic forces are tested, therefore no ferromagnetic foil is included.

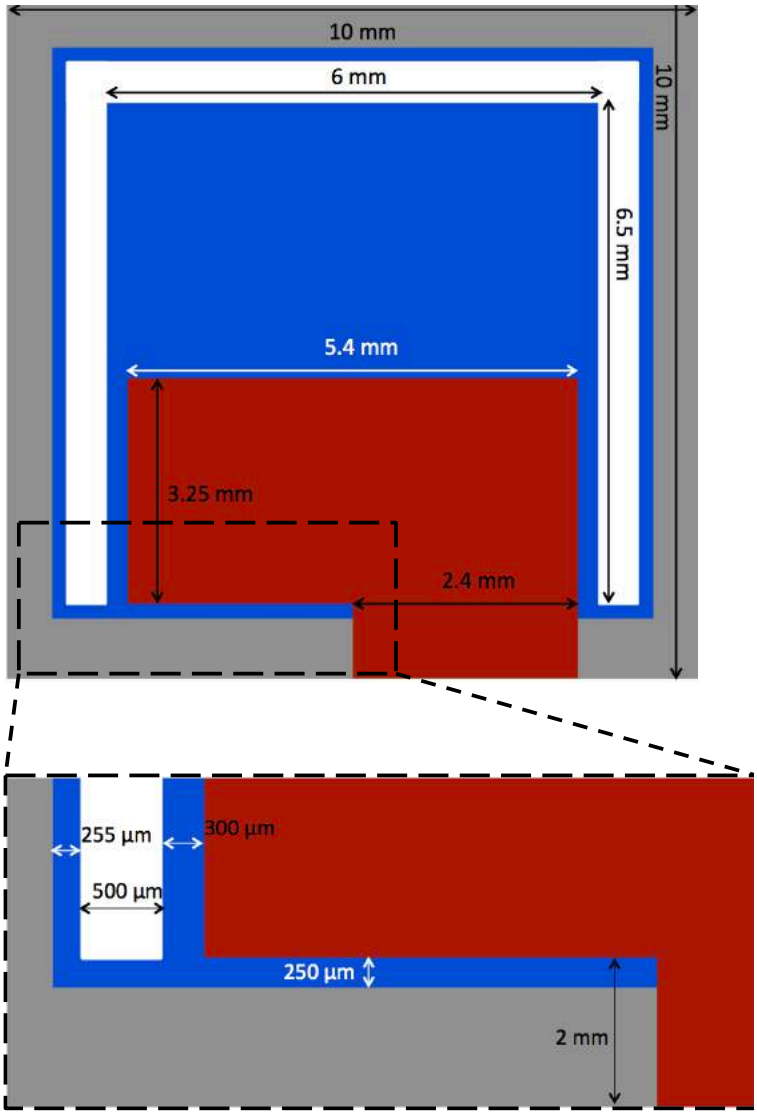

Figure 6.5: *Relevant dimensions of the different masks with a zoom in for the smallest dimensions.*

6.2.1 Overview of the VEH development

A cross-sectional view of the process flow is shown in Figure 6.6. The process starts with a phosphorous doping of the wafers, which is followed by the deposition of a three-stack layer that consists of oxide/nitride/oxide layers, as shown in Figure 6.6a. Each layer is etched, Figure 6.6b-c in order to finally perform a KOH etch, Figure 6.6d. Once this is done a lithography process is performed to the end of releasing the beams by a dry etching method, Figure 6.6e. After this, the bottom electrode, piezoelectric material and top electrode are deposited, Figure 6.6f. Finally, the top electrode definition and backside electrode deposition still need to be performed, which is shown in Figure 6.6g-i.

6.2.2 Detailed description of the fabrication process

6.2.2.1 Masking and KOH etching

In this step the beam is defined by KOH wet etching, where a nitride layer is used as masking material. In order to reduce the stress caused by the nitride layer an oxide layer is grown before the nitride layer deposition. The nitride layer is deposited using low pressure chemical vapor deposition (LPCVD) technique. To pattern the nitride layer an oxide layer must be deposited on top of it. This three-stack layer is shown in Figure 6.6a. The 380 nm SiO_2 layer was deposited using tetraethylorthosilicate (TEOS) as a source. The oxide layer is defined by a BHF etch and the nitride is etched by using a phosphoric acid bath, Figure 6.6b. The SiO_2 layer is etched also with a BHF solution, where resist is used as masking material, Figure 6.6c. The KOH etch is performed at 80°C with an etching rate of about 1.3 μ/min, this is shown in Figure 6.6d.

6.2.3 Release etch

In this step the beams are released from the rest of the silicon wafer. The remaining part that needs to be etched corresponds to less than 40 µm since the KOH already etched away part of it, as seen in Figure 6.6d. At this point of the fabrication process the wafer is very fragile and the spinning of resist is done at manual spinners, where the vacuum is more gentle compared to automatic resist spinning machines.

The etching process is performed by using an advanced silicon etching (ASE) machine, this step is shown in Figure 6.6e. There are some requirements to take into consideration. First of all, the machine applies vacuum to the wafer in order for it to be clamped. Since the wafer at this point of the fabrication is so fragile and the intention of this process is to etch all the way through the wafer, it becomes compulsory to bond it to a carrier wafer in order for it not to break into pieces. This means that the cooling system of the machine does not work as it would with just a simple wafer. Consequently, the resist risks getting easily burnt. For this reason, a 5 µm thick resist is used as mask. The material used for bonding the wafer

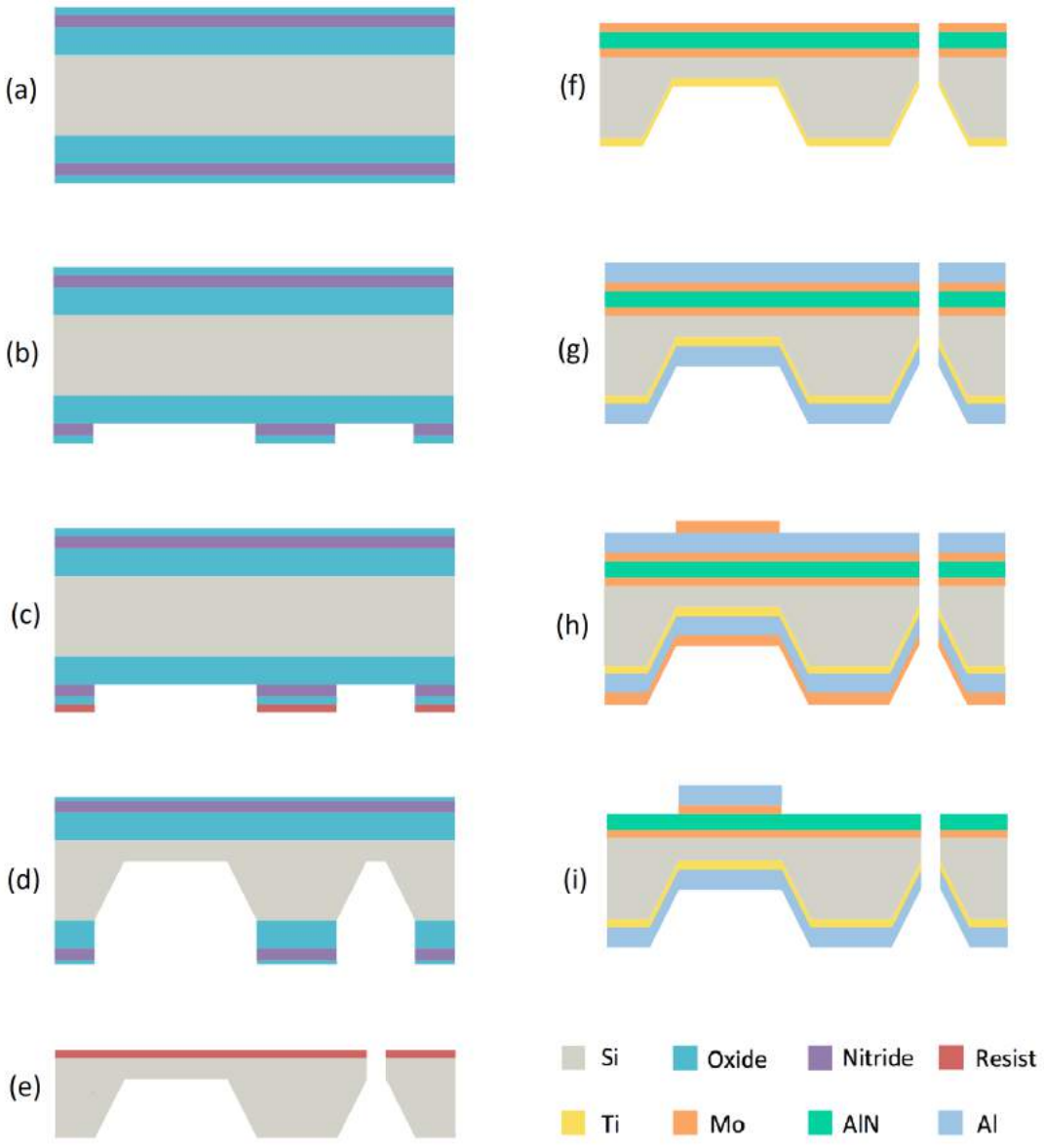

Figure 6.6: *Process flow that shows the most important fabrication steps.*

Table 6.1: *Parameters used during the etching of the silicon trenches.*

Common parameters		Multiplexed parameters		
Parameter	Setting	Parameter	Etch	Passivation
Temperature	10°C	SF_6 Flow	260 sccm	0 sccm
No. of cycles	5.50 ± 0.34	O_2 Flow	26 sccm	0 sccm
Process time	10 min	C_4F_8 Flow	0 sccm	120 sccm

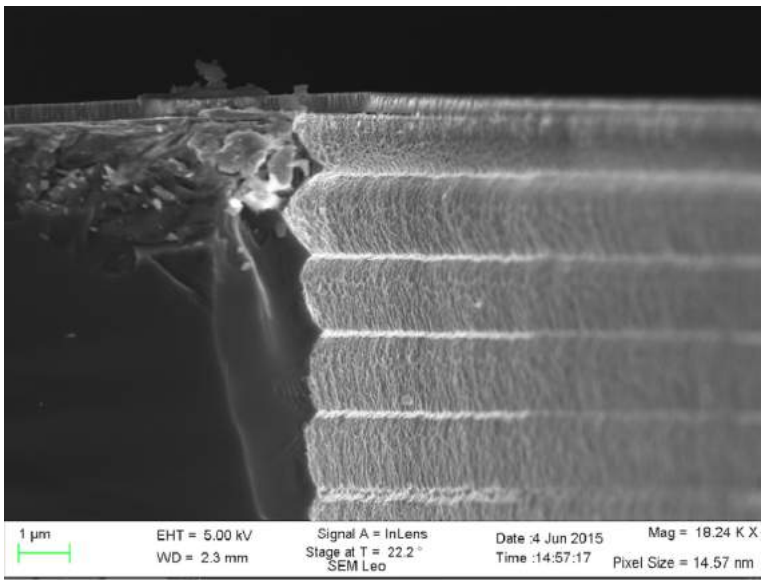

Figure 6.7: *Side walls formed due to switching between passivation and etching mode.*

is crystal bond, which melts at 90°C. Hence, both to bond the wafer and unbond the wafer from the carrier wafer, it is required to heat the substrate up to that temperature and slide one wafer over the other. In the ASE machine, in order to have a better control of the angle of the side walls and make them as vertical as possible, a passivation part is included. It consists on dividing each etching cycle into two parts. One part consists on the etching itself, where SF_6 and O_2 are used as chemical reactants. After this the plasma is switched off and an inert layer is deposited on the entire substrate, this protects the substrate from further etching (passivation mode). When the plasma is turned on again the directional ions collide with the passivation layer at the bottom of the trench and sputter it off, leaving that part ready for reacting with the chemical etchants. This cycle is repeated until the whole structure is released and the parameters used are shown in Table 6.1. The side walls therefore formed are shown in Figure 6.7. The parameters used for the silicon etch are shown in Table 6.1. Once the deep etching has taken place, the wafers are unbonded at 90°C and rinsed in water very carefully.

The reason why the beams are released before the metals and piezoelectric material were deposited is that it would save us the steps of etching through the piezoelectric material and the bottom electrode, with their corresponding lithographic steps.

6.2.4 Bottom electrode/AlN/top electrode stack deposition

In this step the piezoelectric layer is deposited together with the bottom and top electrodes. The method selected for the AlN deposition was reactive RF sputtering technique using the Cryofox explorer 700. For details, see Section 5.2.1.

6.2.5 Top and backside electrode definition

Aluminium will serve as contact electrode both on the front and back side of the wafer. On the top side of the wafer, an Al layer of 400 nm is deposited all over the wafer, this can be seen in Figure 6.6g. In order to define this top electrode, an Al wet etching bath is used. Mo can be used as masking material for this purpose, therefore a Mo layer with the desired electrode shape is deposited using a shadow mask on that side of the wafer, the thickness of that layer is of 50 nm, Figure 6.6h. The same process is performed on the backside of the wafer, however, Mo is deposited all over the wafer without any shadow mask, as seen in Figure 6.6h. After the immersion of the wafer on the Al wet etching solution the definition of the Al layer is done. Now this pattern must be transferred to the Mo layer underneath. This can be done with the inductive coupled plasma (ICP) dry etching machine, where a recipe for Mo etching has already been developed. Since the Mo layers both beneath and on top of the Al layer have the same thickness, they will be removed after the same amount of time. This etching of the Mo layer proved to be a key step in not short-circuiting our devices, this is so because even though the Mo layer was deposited in e-beam mode, which is a directional technique, it was not directional enough to avoid short-circuiting the beams by themselves. To remove the Mo on top of the Al layer on the backside of the wafer the same procedure is followed. Both front side and backside of the wafer at the end of this step are shown in Figure 6.9 and schematically in Figure 6.6i. The black/grey spots in Figure 6.9 on the backside are thought to be created while etching the trenches to release the beams, where some gas diffuses towards the backside of the wafer.

6.2.6 Dicing

The final step: dicing the devices, i.e. the procedure to single the chips out, is performed with a DISCO DAD 321 Automatic Dicing Saw. The normal process followed to dice them out is to use an electro-statically adhering tape that holds the wafer still on the dicer's chuck, where vacuum is applied. Once the wafer is in place, a diamond blade with a thickness of about 50 µm cuts the wafer at a certain hight so as to leave some silicon underneath (100 µm). The normal procedure followed afterwards is to peel off the tape manually. However, in a previous project [53] it was shown that it leads to breaking the very fragile devices. Instead, the diced wafer is taken to an acetone bath where the tape will peel off itself partially. In order for it to be fully removed a pair of tweezers are used very gently.

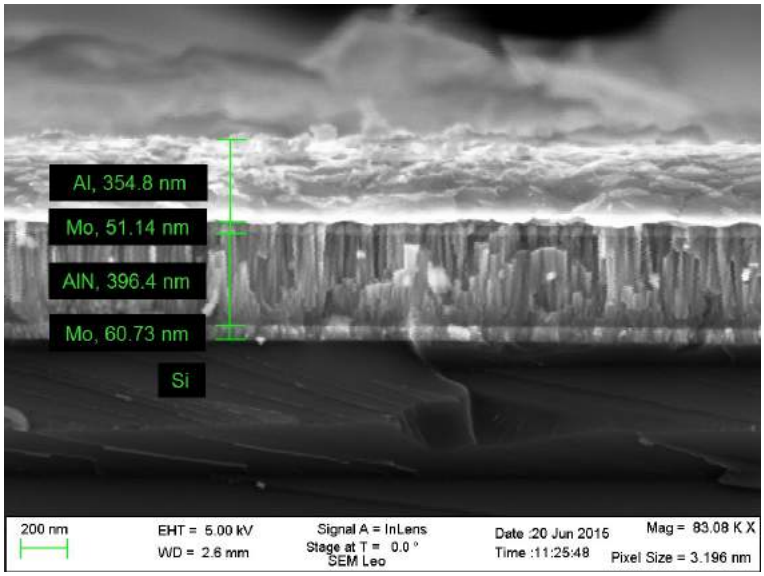

Figure 6.8: *SEM image of the Al/Mo/AlN/Mo stack.*

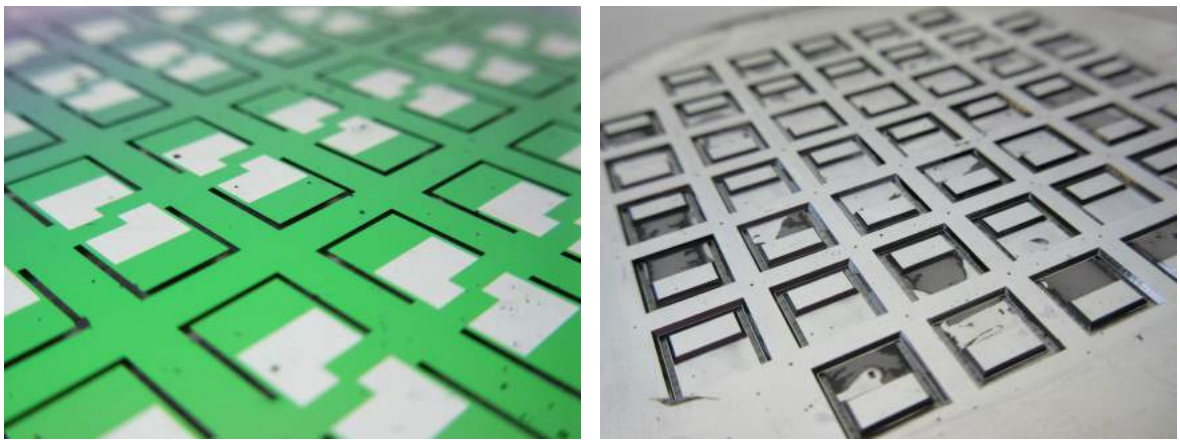

(a) **(b)**

Figure 6.9: *Final devices before being diced out. (a) Front side view. (b) Backside view.*

6.3 Fabrication process of the second set of beams

The second set of AlN-based unimorph VEH's were fabricated using n-type (100) oriented silicon wafers with a thickness of 380 µm and a resistivity of <0.0015 Ωcm. To complete the fabrication process, the ferromagnetic material was prepared and incorporated into the beam outside the cleanroom facilities. This section encloses first an overview of the whole process followed by a detailed description of the main steps.

6.3.1 Overview of the VEH development

A cross-sectional view of the process flow is shown in Figure 6.10, which corresponds to the second set of masks presented in section 6.1. The starting point is the growth of about 3 µm thick oxide layer that will serve as a mask layer for the KOH etch of the wafer backside, as shown in Figure 6.10b, and the KOH etch is shown in Figure 6.10c. Once the beam is defined, a corner rounding takes place by growing an oxide layer, Figure 6.10e. This is followed by a stack deposition of bottom electrode, piezoelectric material and top electrode, Figure 6.10g. After this, 10 µm AZ4562 resist is spun on the wafer, followed by a UV light exposure and a TMAH-based development. The top electrode is then defined by Acqua Regia etching, leaving only the top electrode areas with 50 nm of platinum as contact electrode. After this, other two lithography processes are performed with the same resist and mask in order to finish the etching through the AlN and bottom electrode, Figure 6.10i. Then, a lithography process is performed and a dry etching of silicon releases the beams, Figure 6.10k. Now the wafers are ready to be diced out, after which the magnetic foil is glued to both sides of the beams, as shown in Figure 6.10l.

6.3.2 Detailed description of the fabrication process

6.3.2.1 Masking and KOH etching

This part consists on generally the same steps as in Section 6.2.2.1. However, this time only a thick oxide layer is used as masking material for the KOH etching. As described in Section 5.1.3, Chapter 5, this time the oxide layer is etched witht a dry etching method. As in Section 6.2.2.1, KOH is used as etchant. The aimed thickness for our beams is 40 µm. This means that the amount of silicon needed to be etched away this time is $380 - 40 = 340\,\mu$m (the wafers are thinner compared to the first set of devices). The chemical used to etch through the silicon substrate is KOH. The etching rate for silicon is about 180 times larger than for the masking material, therefore, with a thick enough oxide layer it will work fine as a mask. The minimum thickness needed is found by the following procedure.

The KOH etching rates on silicon and SiO_2 are 1.4 µm/ min and 7.7 nm/ min, respectively. Since 340 µm must be etched through, this demands an etching time that lasts about 243 min. After this period of time, the thickness of an oxide layer that would be etched away is 1870 nm,

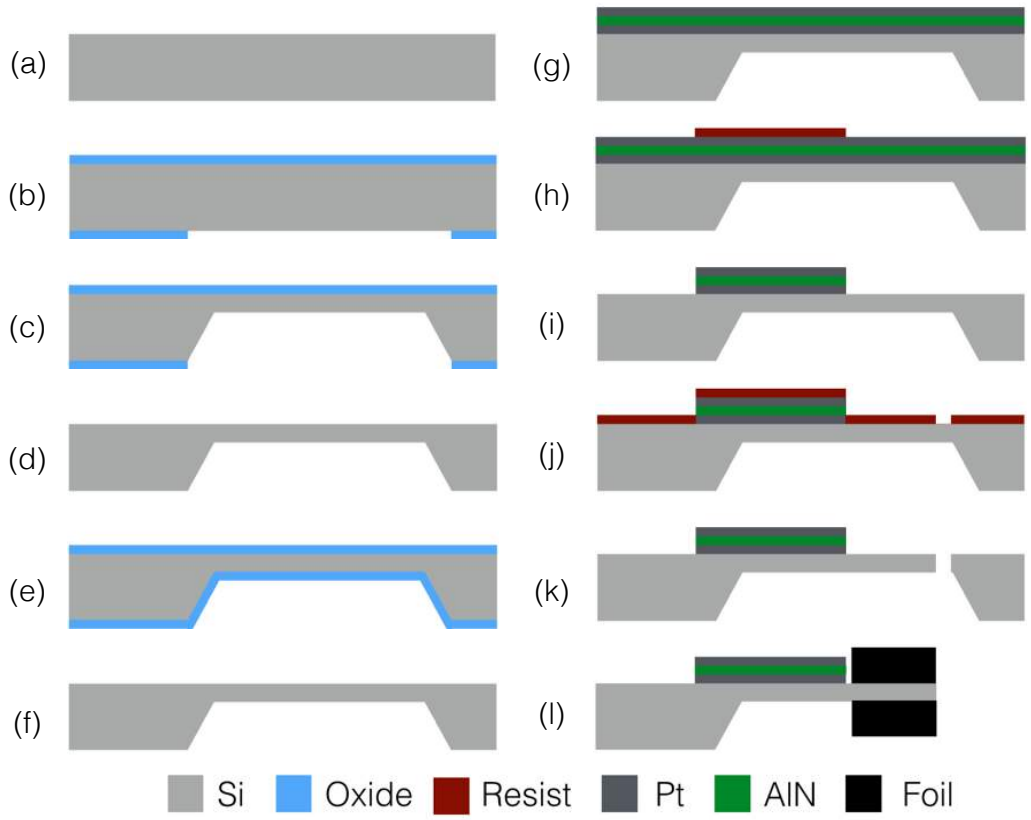

Figure 6.10: *Process flow that shows the most important fabrication steps for the fabrication of the second set of devices.*

which is the minimum thickness that should be aimed at for using this oxide layer as masking material. In order to be sure that the oxide withstands the whole process and does not lead to pinholes, a layer of around 3000 nm was finally grown on both sides of our wafers by wet thermal oxidation.

6.3.2.2 Oxide growth for increasing the robustness

A 1100 µm thick oxide is grown at 1100°C after the beams have been defined. The sole purpose of this layer is to round the corner of the anchoring point, as described in Section 5.3. Therefore, after the layer has been grown, it is removed right afterwards.

6.3.2.3 Bottom electrode/AlN/top electrode stack deposition

The whole stack composed of the bottom electrode, piezoelectric material and top electrode was decided to be deposited using the same machine in the same run for the reasons explained in Chapter 4. This deposition is performed by PIEMCS Sarl S.A., wich consits of a stack structure Ti/Pt/AlN/Pt with thickness of 10 nm/100 nm/400 nm/50 nm. For more details the reader is referred to Section 5.3.

6.3.2.4 Bottom electrode/AlN/top electrode stack etching

The etching of the three-stack layer is performed by wet etching. Aqua Regia is the solution chosen for this purpose, which is a mixture of nitric acid and hydrochloric acid. The exact composition used is HCl:HNO_3:H_2O with a 7:1:8 ratio at 80 °C. The masking material is AZ 4562 10 µm thick resist. In order to etch through the three layers, a total amount of time of about half an hour is needed. This means that a one-time-deposited resist will not withstand the etching process at such high temperatures, as described in Chapter 5. Therefore, the lithography step is re-done three times in total (10 min each) using the same resist parameters and mask.

6.3.2.5 Release etch

This step is performed exactly as described previously in Section 6.2.3 for the first set of beams.

6.3.3 Dicing

In this step, the procedure followed is exactly the same as the one described in Section 6.2.6. Figures 6.11a and 6.11b show the step followed to detach the beams from the electrostatic tape used for holding still the wafer while dicing it: the wafer was dipped in an acetone bath.

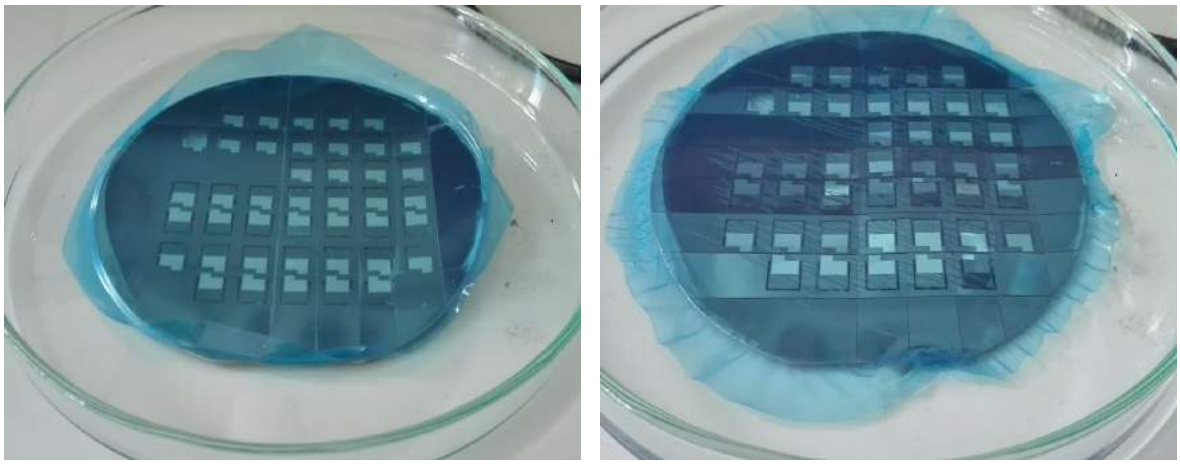

(a) **(b)**

Figure 6.11: *Procedure followed to detach the beams from the electrostatic tape. a) The wafer is dipped in a petridish filled with acetone. b) After a minute inside the petridish the tape starts to detach and some curls are formed.*

6.3.3.1 Ferromagnetic foil implementation

The ferromagnetic foil is bought in 50 mm by 50 mm pieces, the material chosen was iron, from the company Goodfellow. The thicknesses tried was of 150 μm. For this thickness, it is not difficult to cut the foil into pieces that fit our cantilever's tip, the use of a pair of scissors would do the job. Nonetheless, this would leave very deflected corners, which does not lead to planar foils that can afterwards adjust to the beam surface. For this reason, it was decided to follow a milling procedure, where the iron pieces were milled into rectangles with a width of 5.5 mm and a length of 3.25 mm. A supporting structure must be used for milling, which is made out of PMMA. The surfaces are pollished so that the structure milled follows the designed dimensions. In order for the foil to stick to the surface a double side polished tape and blue tape is used. The blue tape is generally not necessary for milling, however, a strong adhesion to the double side tape was experienced, without being able to take off the foil. For this reason the blue tape serves as an intermediate layer, see Figure 6.12, from which the milled foil can be easily peeled off by submerging the stack in an acetone bath, similarly to how it is described in Section 6.3.3. The resulting small ferromagnetic pieces are implemented into the beams by a hand-picking process and gluing them to the silicon surfaces, the process presents a couple of pitfalls. Firstly, it is *not* a batch process, which slows down industrial production and increases the price. Secondly, it was experienced that functional harvesters became useless after gluing the foils on either side. Sometimes the reason was that the foil stepped over the top electrode and therefore the devices were short-circuited. Other times, even though much care was put on not surpassing the limit between top electrode and silicon beam, a bit more glue than the required one would also ruin the harvesters. For these reasons, the hand-picking process followed is far from being the ideal one. However, some functional devices were obtained and measurements were performed on them.

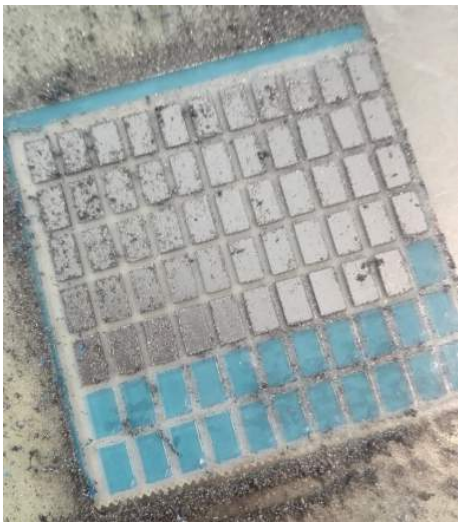

Figure 6.12: *Ferromagnetic foil after being milled. The blue spots correspond to the blue tape that serves as interface between the PMMA (white) surface and the foil. Some foil pieces have fallen off from the blue tape while milling. The other pieces are easily peeled away by dipping them in an acetone bath.*

6.4 Summary

The mask designs for the two types of devices developed in this project were presented. They were substantially similar and the main difference was the non-inclusion of the proof mass in the second case. Furthermore, the fabrication process of both beams was presented. For the first type of beams a set of oxide and nitride layers served as masking material for the KOH etch. After this, the beams were released and the piezoelectric material and metal contacts were deposited without venting the deposition chamber. Finally, the metal layers were defined without having to etch through the AlN layer. For the second type of devices, only an oxide layer was used as masking material for the KOH etch. However, another thermal step was added so as to round the anchoring point of the beams. Once the beams were defined and without releasing them (as opposed to the first set of beams), the stack deposition of metals and AlN layers was performed, this time at PIEMACS Sarl S.A., in Switzerland. This was followed by the metal and piezoelectric etch, which was perfromed by using an Aqua Regia solution at 80°. Afterwards, the beams were released and diced. Finally, ferromagnetic foil was hand-picked placed on both sides of the beams.

Chapter 7

Characterization of VEHs

Two main characterization methods are used. The first method consists in measuring the impedance of the device under static conditions using an impedance analyzer, from this characterization basic properties as capacitance, phase, dielectric constant, permittivity, resonant frequency and impedance itself are either measured or calculated. In addition, a magnetic setup is included in the set-up for characterizing the second types of beams. By doing this, non-linear effects due to magnetic forces are studied, where the effects of critical dimensional parameters like distance between magnets and distance between magnets and the beam are analysed.

The second method used consists in exciting the beam employing a shaker, which vibrates at a specified acceleration and over a target frequency range, and by connecting the VEHs to a load resistance this characterization method allows to find the power dissipated through the load resistance, or in other words, the harvested power, among others.

The devices characterized correspond to the second type described in Chapter 6, where the proof mass consists of ferromagnetic foil. Three beams of that type are analyzed: beam 09, 12 and 18.

7.1 Set-ups description

7.1.1 Impedance measurements set-up

The impedance characterization is performed with two different machines. The reason is just the replacement of the old one with a new one. The machines are Agilent 4294A Precision Impedance Analyzer and Agilent E4990A Impedance Analyzer. Nevertheless, the measuring method holds the same for both machines and the properties are measured identically. Both of the impedance analyzers are connected to an Agilent 4294A impedance probe, which is at the same time connected to a holder that serves as intermediate between it and the devices. The top electrode of the beam is in contact with a pogo-pin from the holder and a set of other

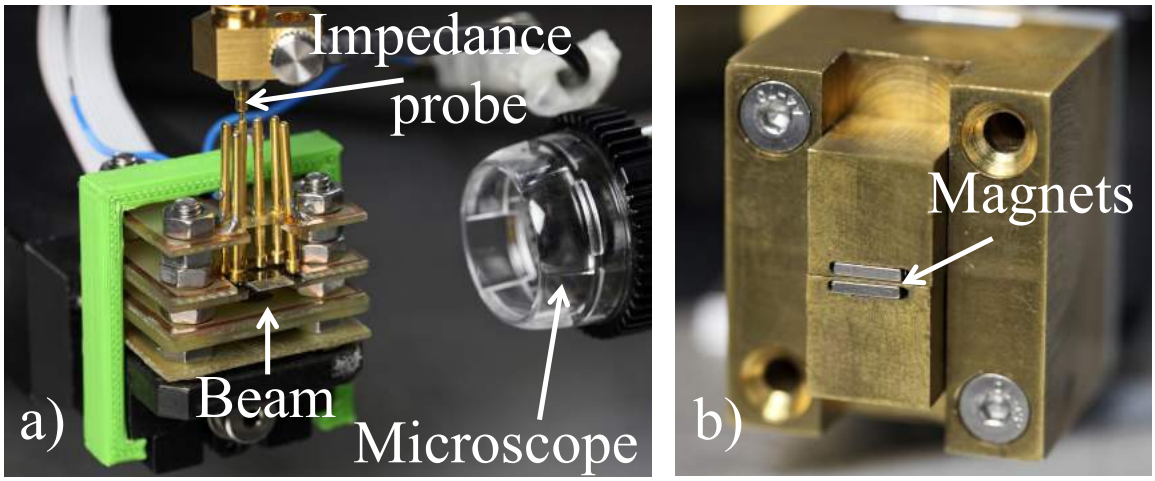

Figure 7.1: *Parts of the set-up used for the electrical characterization. a) Beam holder with the pogo-pins holding the beam still and one of them connected to the impedance set-up. Also, the microscope used for measuring distances. b) Holder for the magnets with the rectangular magnets located at the center.*

pogo-pins secure it by pressing on the edge structure, as depicted in Figure 7.1a. Part of the backside frame structure of the device lies on a metal structure which is also connected to the impedance probe. Frequency sweep analysis are performed on the devices, where a varying sine voltage source with an amplitude of 50 mV is always used. This type of measurement provides both the impedance and phase values, from which properties like the resonance frequency, anti-resonant frequency, or capacitance, among others, can be found.

To analyze the non-linear response of the devices, a pair of NdFeB magnets are included into the system. Figure 7.1b shows the pair of magnets and Figure 7.2 shows the schematic of the whole set-up. In order to have a precise control over the positioning of the magnets in the three spatial dimensions, a XYZ 300 TR stage model from Quater Research and Development is used, Figure 7.3. The beam holder is also positioned on a structure that allows for movement in the three spatial coordinates. In order to measure both the distance between magnets b and magnets and beam a, a Dino-Lite edge digital microscope model AZ7915MZTL together with DinoCapture 2.0 software [91] are used, as seen in Figure 7.1. Due to the magnetic attraction between the magnets themselves, maintaining a specific distance between them proves to be cumbersome. For that reason, a set of spacers with defined thickness are inserted in between.

7.2 Shaker measurements set-up

In this section the set-up used for measuring the deflection of the beam under base excitation is presented. Two slightly different set-ups were used, where the electronic equipment was kept the same but the self-supporting structures were improved. First, an overall description of the set-up is given, without specific structural components. After that, a comparison of

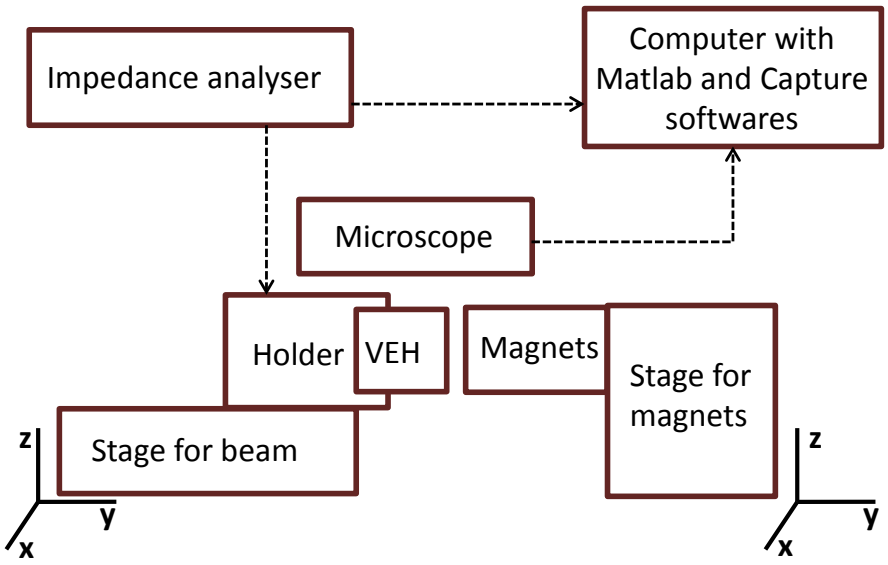

Figure 7.2: *Schematic figure that shows the impedance measurement set-up used for characterizing both linear and non-linear response of the devices. The system incorporates therefore the magnetic system used for characterizing the latter one.*

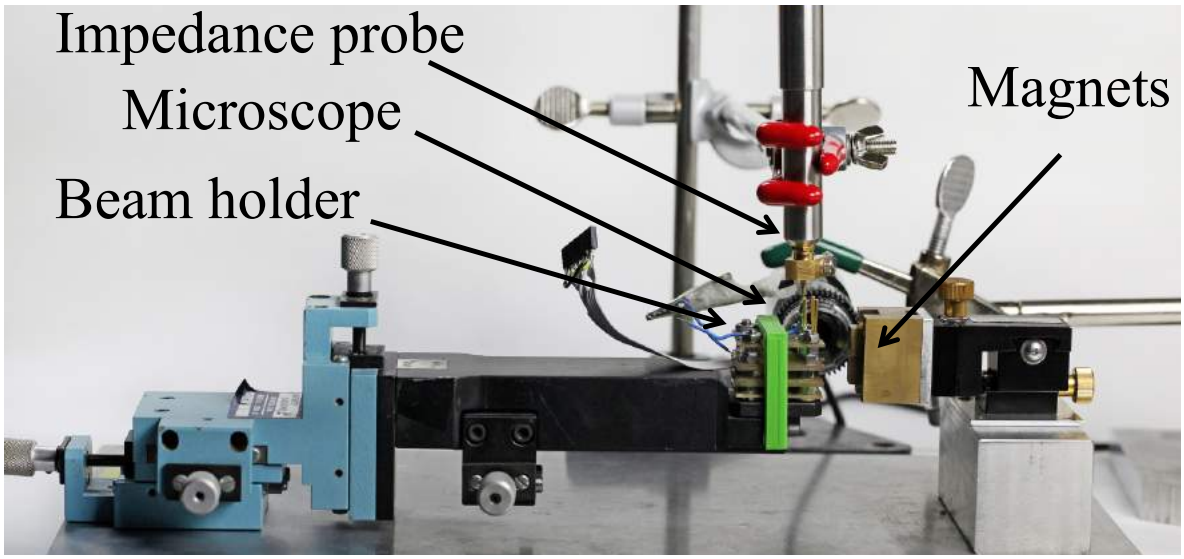

Figure 7.3: *Whole set-up used for the impedance characterization.*

the two set-ups used is given and finally, the method used for measuring/calculating the base acceleration is presented.

7.2.1 Different set-ups used

All the components used in the shaker measurement setup are schematically shown in Figure 7.4. The shaker acquired is a Brüel and Kjær type 4810 mini-shaker, which serves for the purpose of simulating the ambient vibrations. In order for it to vibrate at the required frequencies and with the appropriate waveform, the Agilent 33220A Arbitrary Function Generator is used, which at the same time is connected to the computer through a USB cable. The signal generated by the function generator is amplified by the Pioneer VSX-405RDS Mk II audio amplifier, see Figure 7.4. The energy harvester is connected in parallel to a resistance box, where different load resistances can be selected. The voltage drop is measured in the data acquisition (DAQ) box, which is at the same time connected to the computer, where a Labview software program [92] is implemented. The beam displacement can be tracked by using a Micro-Epsilon opto NCDT 2300-10 laser sensor, which presents a resolution of $0.15\,\mu$m (see Appendix B.4 for further information). Unless otherwise stated, the spot of the laser beam hits the cantilever at approximately the center of mass longitudinally. To measure the acceleration, a Brüel and Kjær accelerometer type 4507 B 004, which is powered by a Brüel and Kjær Constant Current Line Drive (CCLD) signal conditioner type 1704-A-001. Note that the accelerometer was acquired at the end of the project, and therefore was not used during most of the measurements, for more information the reader is referred to Section 7.2.2. Nevertheless, when using the accelerometer it will be clearly stated throughout the characterization part. Regarding the input values that are normally changed during these measurements, these are: frequency range, measurement time (how long a measurement at each frequency takes), frequency step size, amplitude of the voltage input (the peak to peak voltage V_{pp}) and the value of the load resistance connected to the harvester. This means that an important parameter as input acceleration (a_{in}) is cannot be set directly. In order to have control over it a relation between V_{pp} and a_{in} needs to be found. It is important to note that what is defined as input acceleration is the actual acceleration of the holder where the beams are mounted, which is not necessarily the acceleration of the shaker. The following subsection describes the two different methods used both to measure a_{in} and find the relation between a_{in} and V_{pp}.

As mentioned in the beginning, two supporting structures for measuring the displacement were used. The first one was based on using a rod-based support to hold the laser sensor and under the shaker a metal structure on top of a wide sponge, which would limit to some extent the noise due to base vibrations, this is shown in Figure 7.5 left. However, this proved to be not enough to cancel existing noise vibrations and an improvement was done in this regard. Figure 7.5 right shows the new measuring set-up, where three main improvements are observed. First, the laser sensor is securely attached to a bridge-like structure which is screwed to a ThorLabs Nexus base. Second, the base structure for the shaker is now a three

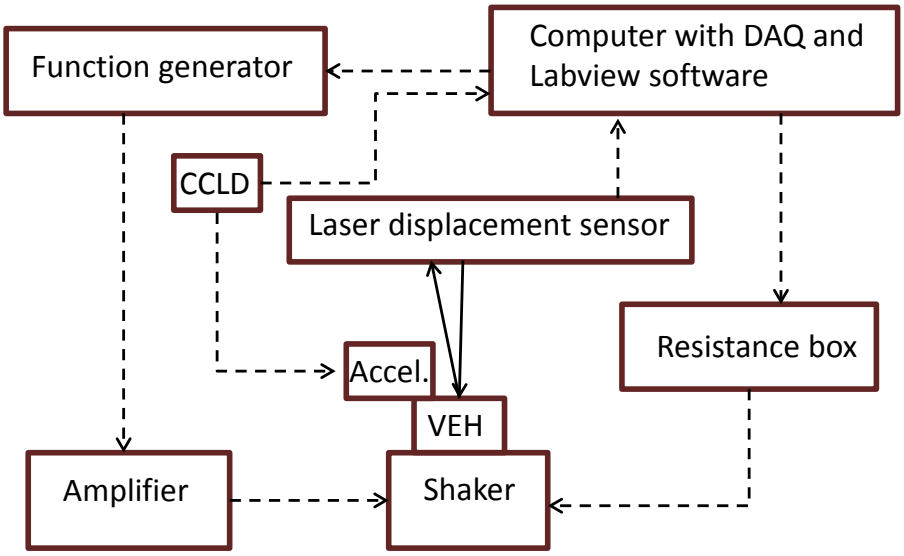

Figure 7.4: *Schematic figure that shows the shaker measurement set-up used for characterizing the devices.*

free-degree of movement stage, which allows to position the beam at the laser spot without having to move around the laser itself. This also means that positioning the laser beam at the optimal mid-range focus point becomes much less cumbersome than before. Lastly, the shaker is screw to the stage, which helps in limiting the sometimes observed shifting of the shaker positioning when measuring at high accelerations. A picture of the whole new set-up is shown in Figure 7.6 with specifications of the compounds.

7.2.1.1 Typical deflection measurements using the first set-up

In this section, as a way of showing the pitfalls of the measuring method and how to proceed to analyze the data, measurements performed on one of the beams developed are shown. Figure 7.7 shows the deflection versus time measurement at a driving frequency of 350 Hz for a device whose resonant frequency is 390.9 Hz. Note that the deflection is manually centered to zero deflection. It is apparent that the deflection does not follow a single frequency excitation but presents a combination of input signals. Figure 7.8 shows the Fast Fourier Transform (FFT) of the deflection versus time data. Three important things are observed. Firstly, contributions from frequencies < 100 Hz are easily pinpointed. Secondly, the driving frequency, as expected, presents the largest contribution to the spectra. Lastly, the resonant frequency of the beam at 390.9 Hz also contributes to the mixed-box of frequencies observed. It is well known from the theory of driven damped harmonic oscillator that in the beginning of the signal there will be an exponential decay and the information it contains is both about the driving frequency and the resonant frequency of the beam. After some time that is related to the quality factor

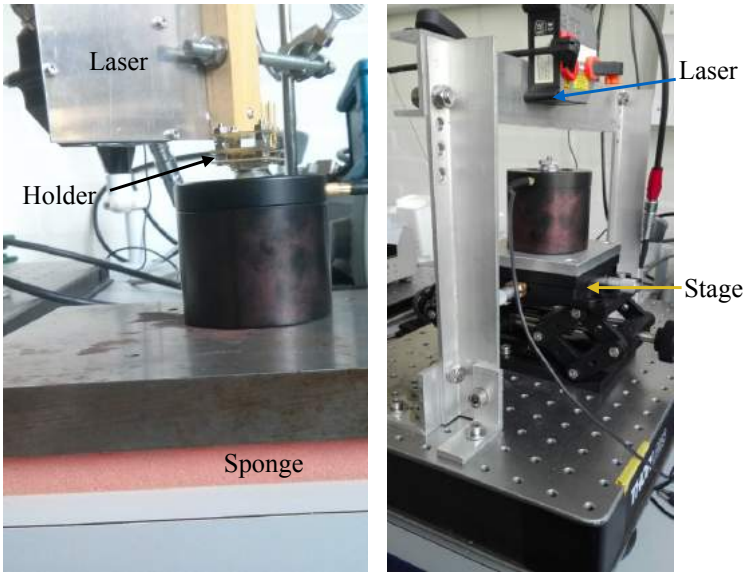

Figure 7.5: *Old versus new set-ups used for characterizing the devices in terms of deflection, output voltage, power, etc.*

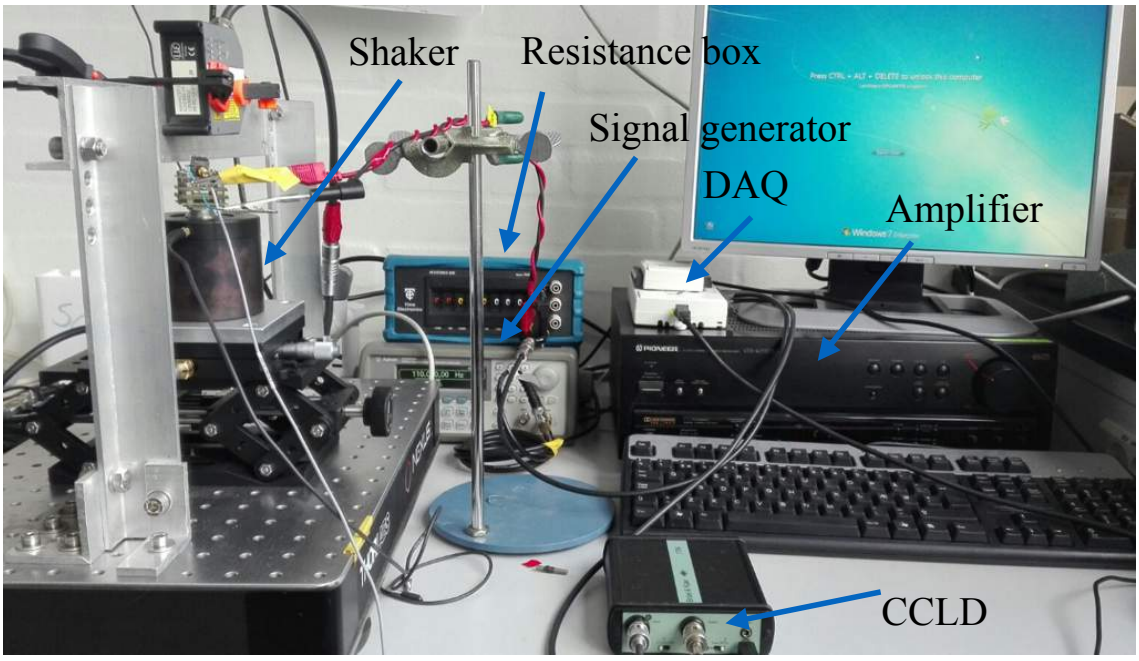

Figure 7.6: *Whole set-up used for the shaker-based measurements.*

(Q) of the beam, the signal will be stabilized and show the harmonic movement due to the driving source. This is shown in Figure 7.9, which represents the FFT of the deflection but only of the second half of the data set, i.e. once the oscillation has been stabilized. It is observed in Figure 7.9 that the peak from the resonant frequency is gone, as expected. Now that the presence of frequency contributions is known, it is necessary to implement a filter. Figure 7.10 shows the deflection versus time data of the raw data, the data filtered with a Butterworth filter of order 2 and lastly the signal filtered with the same type of filter but of order 3 instead. The frequency around which the signal is filtered is the driving frequency (350 Hz) and the bandwidth of the filter is 40 Hz. Since the resonant frequency is outside the bandwidth range, the contribution from it to the signal is not observed. In order to see the difference between applying an order 2 or 3 filter, it must be noted that the RMS deflection obtained after applying them are 1.3184 μm and 1.3183 μm, respectively. This means that the difference in deflection is under the resolution of the laser. Therefore, applying a filter of second order works perfectly fine for this study. The same type of filter, this time around the resonant frequency, is again implemented with the same bandwidth and Figure 7.11 is obtained. Now the decay due to the resonant frequency is observed and one way of finding the associated Q factor is by analyzing this decay. Figure 7.12 shows the natural logarithm of deflection taking the values of the absolute peaks shown in Figure 7.11, from where if the first second of the data is taken, a linear fit can be performed in order to obtain the envelope of the curve by bearing in mind that

$$x = x_0 e^{-\zeta w_r t} \Rightarrow \log x = \log x_0 - \zeta w_r t \ , \tag{7.1}$$

where x is the displacement, x_0 the displacement at $t = 0$, ζ the damping ratio and w_r the resonant frequency. Therefore, from the linear fit the factor ζ is obtained and, since it is related to Q by

$$Q = \frac{1}{2\zeta} \ , \tag{7.2}$$

then the mechanical quality factor is known. Figure 7.13 shows the absolute peaks within the first second of Figure 7.12 and the linear fit, which gives $\zeta = 1.612/w_r = 6.56 \cdot 10^{-4}$. From this value, by using equation 7.2 one finally gets $Q = 762$. It is important to note that the beam presented in this section does not correspond to the other ones presented in this chapter. Following the same method presented in this section, a mechanical quality factor of 457 is found for beam 09, on which harvested power is measured later on.

7.2.2 Acceleration measurement method

Two different methods for knowing the base acceleration of the harvesters are used. Before the acquisition of an accelerometer, the acceleration is not measured but calculated, this is described in detail in the rest of this section.

The first method used consists in measuring the displacement of the holder under a certain input V_{pp}. The displacement of the holder under a sinusoidal signal is given by equation

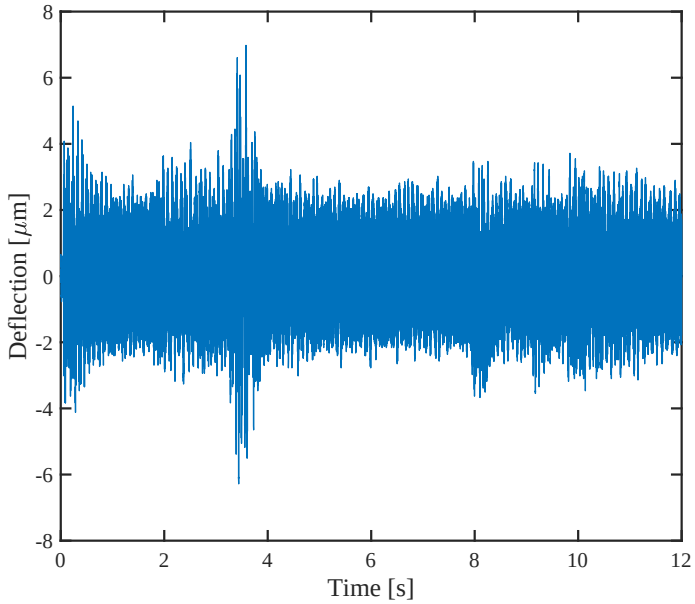

Figure 7.7: *Plot of the beam's deflection versus time at a driving frequency of* 350 Hz *for a device whose resonant frequency is* 390.9 Hz. *A combination of different signals is observed.*

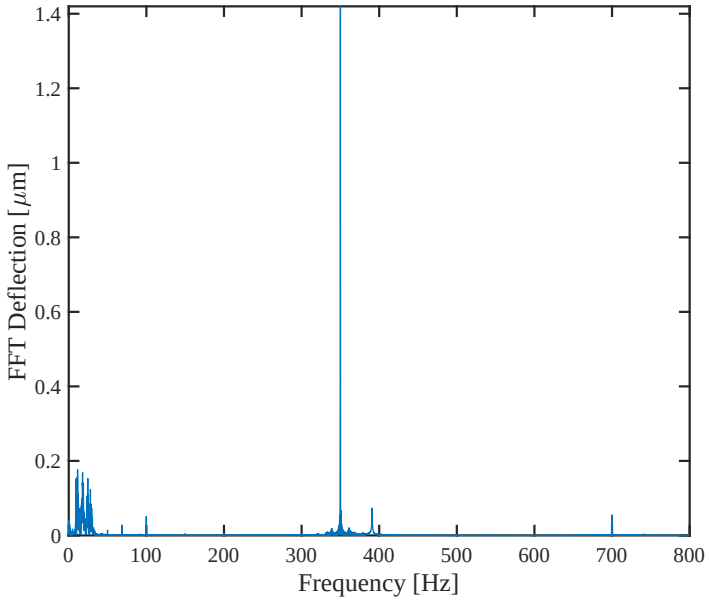

Figure 7.8: *FFT of the deflection data shown in Figure 7.7.*

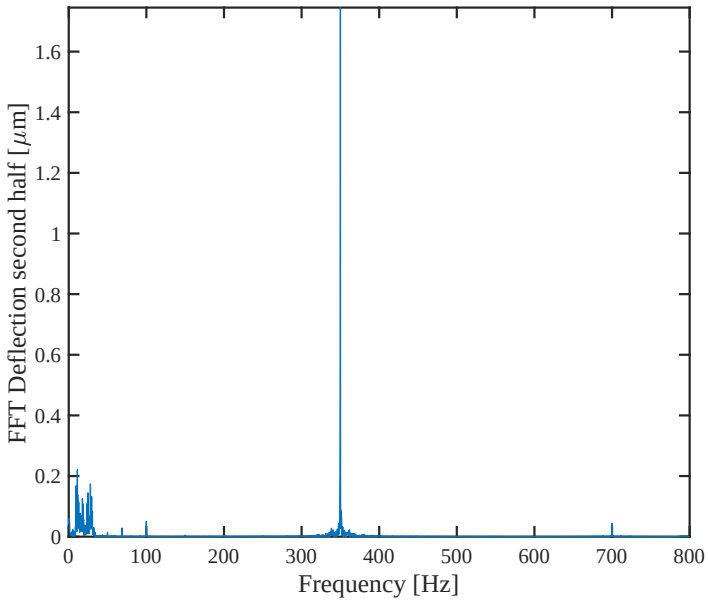

Figure 7.9: *FFT of the second half of the deflection data shown in Figure 7.7.*

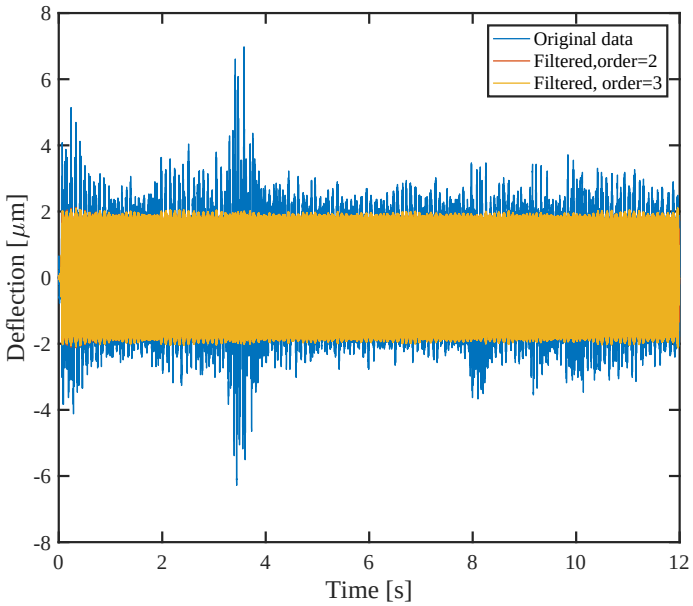

Figure 7.10: *Raw and filtered data of the deflection data shown in Figure 7.7. A Butterworth filter was applied at 350 Hz with a bandwidth of 40 Hz and two different orders of the filter were applied: order 2 and 3.*

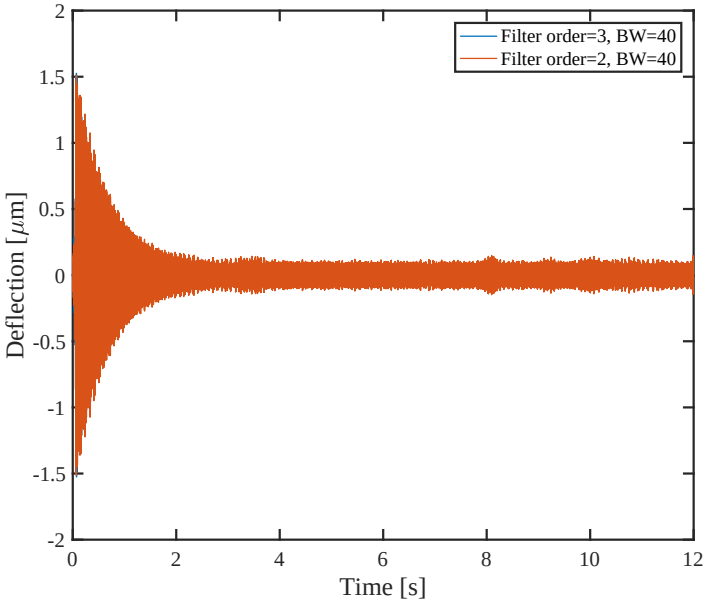

Figure 7.11: *Raw and filtered data of the deflection data shown in Figure 7.7. A Butterworth filter was applied at 390 Hz with a bandwidth of 40 Hz and two different orders of the filter were applied: order 2 and 3.*

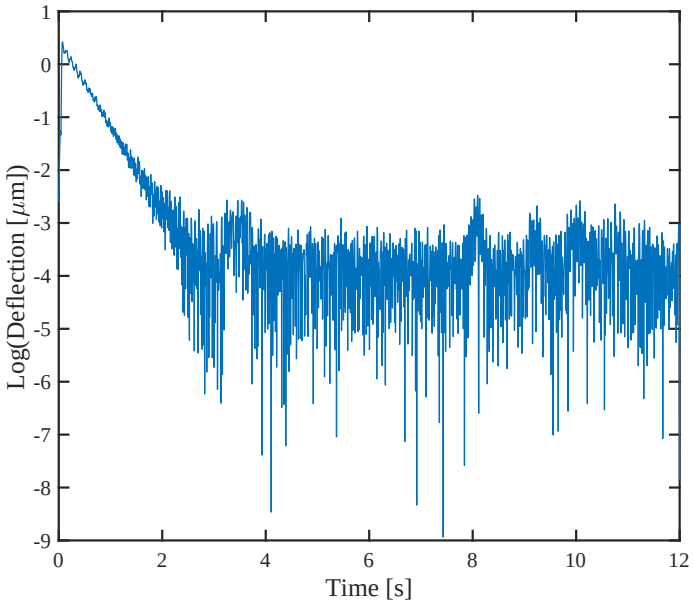

Figure 7.12: *Logarithm of the deflection data shown in Figure 7.11.*

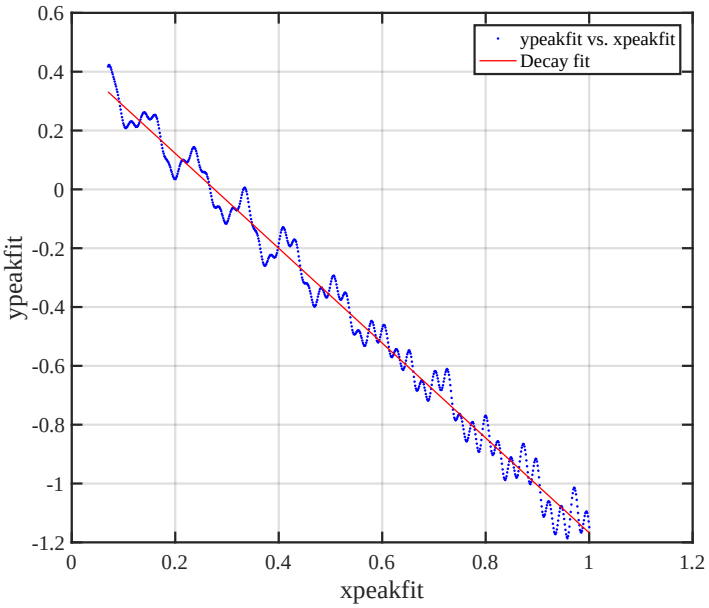

Figure 7.13: *Plot of the the peaks found within the first second in Figure 7.12 and linear fit to the data.*

7.3, where $y(t)$ is the displacement of the holder in the vertical direction, w is the signal's frequency, A_0 the displacement amplitude and t is the time variable.

$$y(t) = A_0 \cos(wt) \tag{7.3}$$

From this, the maximum acceleration at which the holder is excited can be calculated, this leads to the following equation:

$$a_{\max} = |\ddot{y}_{\max}|^2 = w^2 |y_{\max}| \tag{7.4}$$

the upper dots represent the derivative of the variable respect to time. In order to perform the calibration and find out the relation between V_{pp} and the acceleration of the holder, a sweep over frequencies for a range of V_{pp} values is done and the displacement of the holder is measured. Since the V_{pp} is an input value and the maximum displacement of the holder for each V_{pp} can be measured, the acceleration that corresponds to each V_{pp} can be easily found by plotting $\ddot{y}_{\max}$ for each V_{pp}.

The second method used consists in implementing the piezoelectric-based Brüel and Kjær accelerometer type 4507 B 004, which is powered by a Brüel and Kjær Constant Current Line

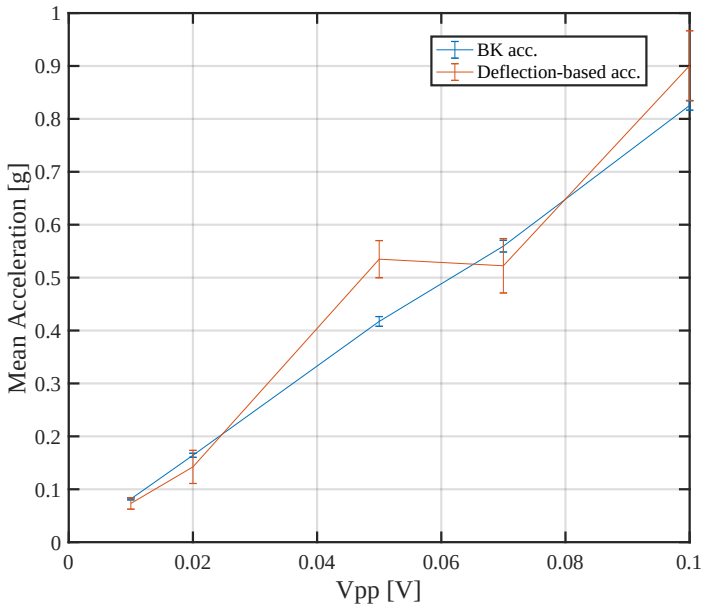

Figure 7.14: *Base acceleration of the beam's holder versus V_{pp} using the two methods described in this section.*

Drive (CCLD) signal conditioner type 1704-A-001. For more details about the accelerometer Appendices B.2 and B.3 can be checked.

To test the accuracy of each method, the holder of the beams was subjected to different V_{pp} and both methods to find the acceleration were used at the same time. This is shown in Figure 7.14, where it is obvious that the second method outperforms the first one. However, the accuracy of the deflection-based method is, in the worst case scenario, off only for about 0.1 g. Furthermore, from Figure 7.14 a linear relation between V_{pp} and base acceleration can be found by fitting the blue curve. By doing so a slope of 8.2 g/V is found.

7.3 Characterization of the beams

Within this section different characterization methods take place. It is important to note that the robustness characterization part does *not* include the piezoelectric material and only the beam's structural silicon robustness was tested. Once the robustness tests have been performed the piezoelectric material is implemented into the fabrication process and the final characterization in electro-mechanical terms is performed.

Table 7.1: *Dimensional and material parameters for the energy harvesting system.*

Device parameter	Value
Beam length (l)	6.5 mm
Beam thickness (h)	40 μm
Foil length	3.25 mm
Foil thickness	100 μm
Magnet length	1 mm
Magnet thickness	1 mm
Magnet width	5.5 mm
Magnetization	750 A/m
Si Young modulus	150 GPa

7.3.1 Robustness characterization

As described previously in Chapter 5, the robustness of the beams at the anchoring point was enhanced throughout the development of the devices. In order to asses the increased robustness of the beams, the enhanced beams are characterized together with the regular ones, i.e. beams where no enhancement of the robustness at the anchoring point was performed are also characterized. The characterization method that is performed corresponds to the one described in Section 7.2, where the resistance box is not implemented due to the lack of piezoelectric material incorporated in the devices. In all the measurements, the beams are excited at their specific resonance frequency. However, a frequency sweep is performed with a step size of 0.1 Hz in order to avoid shock effects that would arise if the beams were suddenly excited at their resonant frequency. The base acceleration is increased until each of the beams break and this breakage acceleration is written down. Table 7.1 shows the beams dimensions and Table 7.2 shows the resonant frequency and the base acceleration at which both types of beams broke. It is important to note that in all cases the beams broke at the anchoring point, as expected.

The cumulative failure distributions for the regular and enhanced devices, based on the data in Table 7.2, are shown on Figure 7.15 together with the fitted Weibull cumulative distribution functions. The characteristics of the fitted Weibull functions are listed in Table 7.3. For the regular devices the shape parameter, also known as Weibull modulus, is $k_r = 6.73$ and the scale parameter is $\lambda_r = 3.26$, while for the enhanced devices the corresponding values are $k_e = 3.49$ and $\lambda_e = 6.29$, respectively. The mean value of the failure acceleration is 3.0 g and 5.7 g for the regular and enhanced devices, respectively. This demonstrates the effect of the corner rounding process that increases the robustness of the energy harvesters.

Table 7.2: *Breaking accelerations for both the regular and the enhanced devices.*

Enhanced		Regular	
f_r [Hz]	acc. [g]	f_r [Hz]	acc. [g]
269.6	3.3	302.4	2.4
283.0	2.4	284.5	3.5
291.9	5.1	302.6	2.0
276.7	7.4	306.2	3.1
264.4	6.1	299.4	3.1
268.6	7.0	296.9	3.8
285.8	5.5	310.9	3.5
281.3	8.3	335.5	2.9
277.7 ± 9.5		304.8 ± 14.6	

Table 7.3: *Parameters for the fitted Weibull distribution functions to the failure accelerations of for the regular and enhanced devices.*

Parameter	Regular	Enhanced
Shape parameter	6.73	3.49
Scale parameter	3.26	6.29
Mean value [g]	3.0	5.7
Standard deviation [g]	0.5	1.8

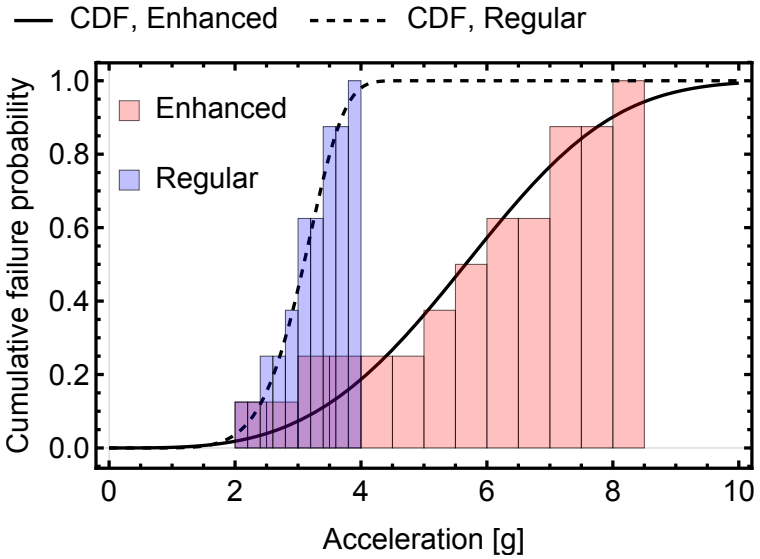

Figure 7.15: *Cumulative failure distribution for the regular and enhanced devices. The solid and dashed lines represents the fitted Weibull cumulative distribution functions (CDF) for the enhanced and regular devices respectively.*

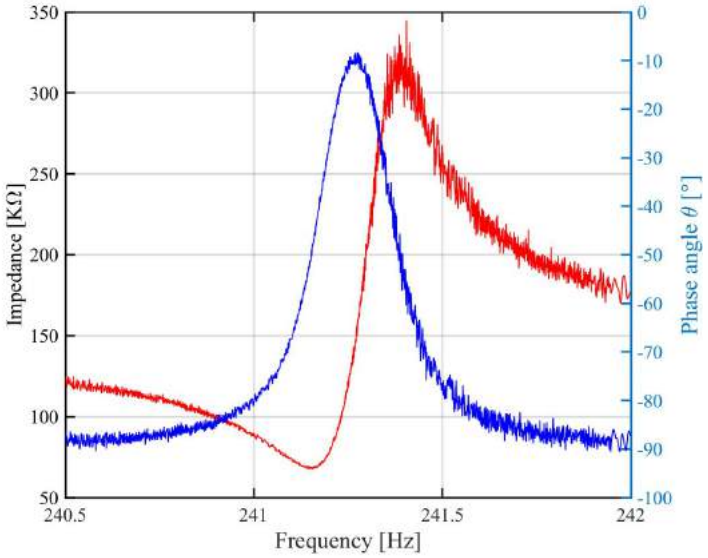

Figure 7.16: *Impedance measurement performed on beam 09.*

7.3.2 Impedance characterization

In this part of the characterization the impedance measurements of the different beams that are used later on for deflection, voltage and power characterization are presented here. The numbering system agrees with the numbers that were associated while measuring on them: beam 09 and 12. The section is devided into two subsections, one for impedance measurements without any external set-up introduced, and another where the magnetic set-up is used as well.

7.3.2.1 Impedance measurements

Figure 7.16 shows the impedance magnitude and phase of beam 09 around its resonant frequency. The resonant frequency is found to be 241.1 Hz, which corresponds to an impedance magnitude of 67.5 kΩ. The anti-resonant frequency corresponds to about 241.4 Hz, which corresponds to an impedance magnitude of 330.4 kΩ. The maximum phase angle is about -8°, which corresponds to an impedance magnitude of about 160 kΩ.

Figure 7.17 shows the impedance magnitude and phase of beam 12 around its resonant frequency, which is about 240.6 Hz. The maximum phase is not as high as for the previous case with beam 09 shown in Figure 7.16, in this case the phase rises up until about -67°, which corresponds to an impedance magnitude of 181 kΩ. The low value of the maximum phase compared to the one for beam 09 might be associated to a lower coupling efficiency figure of merit, described in Section 2.6.

Regarding the capacitance,C, it was measured on six devices and the mean value was found

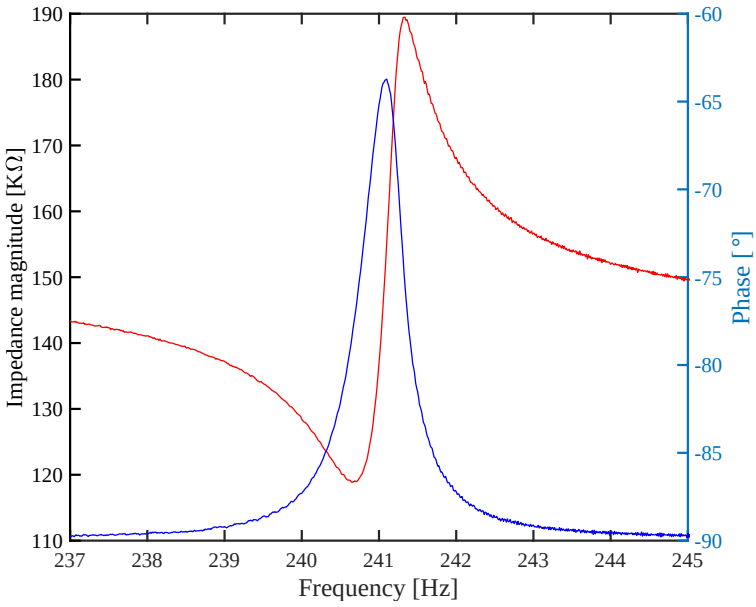

Figure 7.17: *Impedance measurement performed on beam 12.*

to be 4.532 nF with a standard deviation of 0.007 nF. Therefore, its associated relative permittivity is easily found by using

$$C = \frac{\epsilon_r \epsilon_0 A}{h_{\text{AlN}}}\,, \tag{7.5}$$

where A is the electrode area, h_{AlN} the piezoelectric material thickness, ϵ_0 the vacuum permittivity and ϵ_r the relative permittivity of the piezoelectric material. Therefore, by following equation 7.5 it is found that $\epsilon_r = 9.16$, which is about the expected value found in literature [93].

7.3.2.2 Impedance measurements with magnetic set-up implemented

For this part of the characterization of the beams, where the piezoelectric layer together with the metal electrodes are also included, the procedure described in Section 7.1.1 is followed. The aim of these measurements is to study the effect of the magnetic forces at different distances both between magnets and between magnets and beam. In other words, according to the set-up shown in Figure 3.1, the effect of the magnetic field for different a and b values is studied. It is important to note that all the dimensions of the energy harvesters are the same as the ones shown in Table 7.1 except for the foil thickness, which is in this case set to 150 μm.

One now is referred to the impedance measurement performed on beam 12, shown in Figure 7.17, where a resonant frequency of about 240.6 Hz was found. The associated spring constant can be found by using $k_{\text{eff}} = m_{\text{eff}}(2\pi f_r)^2$, where m_{eff} is found by using $m_{\text{eff}} = \frac{33}{140}mL + M_t$ [50], which at the same time was found by using Rayleigh's method. Therefore, the associated spring constant is $k_{\text{eff}} = 99\,\text{N/m}$.

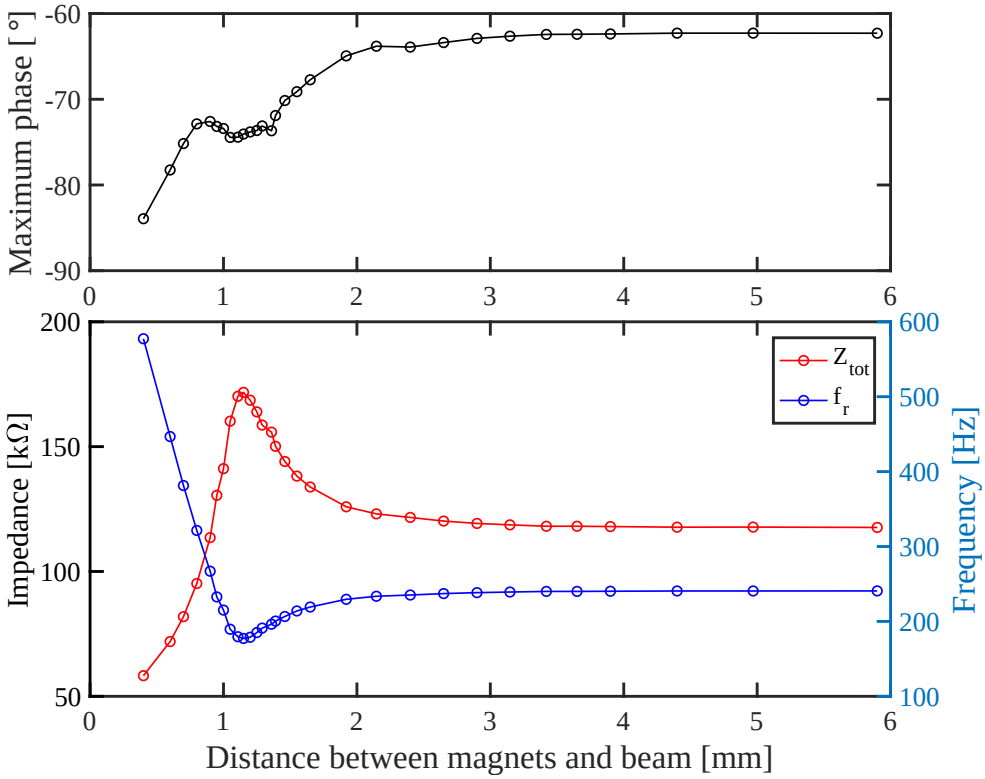

Figure 7.18: *Phase, impedance magnitude and resonant frequency for different distances between magnets and beam, i.e. for different values of a and $b = 0.52\,\text{mm}$.*

Once the magnetic set-up is implemented, non-linear effects are studied. First, a b value is selected and the effect of decreasing a values is analyzed. For $b = 0.520\,\text{mm}$, Figure 7.18 shows the resonant frequency, its associated impedance magnitude and the maximum phase for different a values. For values of $a > 3\,\text{mm}$ no significant change in the variables respect to the linear ones is observed. In the range $a = 3\,\text{mm} - 1.1\,\text{mm}$ the resonant frequency decreases, which means that a softening effect takes place. For distances lower than 1.1 mm the resonant frequency increases due to hardening effect.

In order to understand the behaviour of the impedance magnitude one is referred to equation 2.48. A softening effect clearly relates to a decrease in the impedance associated to the spring constant $Z_s = \frac{k_{\text{eff}}}{jw}$. However, the electrical term in equation 2.48 means that at lower frequencies the impedance contribution from that term tends to increase the total impedance, whereas for higher frequencies the contribution is to decrease the total impedance. This is better pictured in Figure 7.19, where the impedance magnitude versus frequency is plotted for all the different cases considered previously in Figure 7.18, i.e. different a values. From Figure 7.19 the capacitor-like tendency of the impedance is easily observed. Furthermore, since the change in spring constant is associated to a change in effective mass, these two factors also affect the impedance values, this is observed in Figure 7.19. Figure 7.22 shows the relative spring constant values for a range of dimensions that are $a = [400 - 2500]\,\mu\text{m}$ and

$b = [320 - 3140]\,\mu$m. To calculate the relative spring constant values $\frac{f_{\text{eff}}}{f_0} = \frac{k_{\text{eff}}}{k_0}$ is used. This means that by taking each resonant frequency associated to each pair of a and b values and dividing it by the resonant frequency for the linear case the relative spring constant is found. Figure 7.22 clearly shows the two distinct zones that Figure 3.6b in Chapter 3 predicted, i.e. softening and hardening regimes. However, an important thing must be noted. When performing these measurements, if the magnets are close enough the beam will start bending towards either of the magnets. This means that once softening effect is no longer obtained, the results should not be directly compared to the simulation results, where a zero tip deflection was always considered.

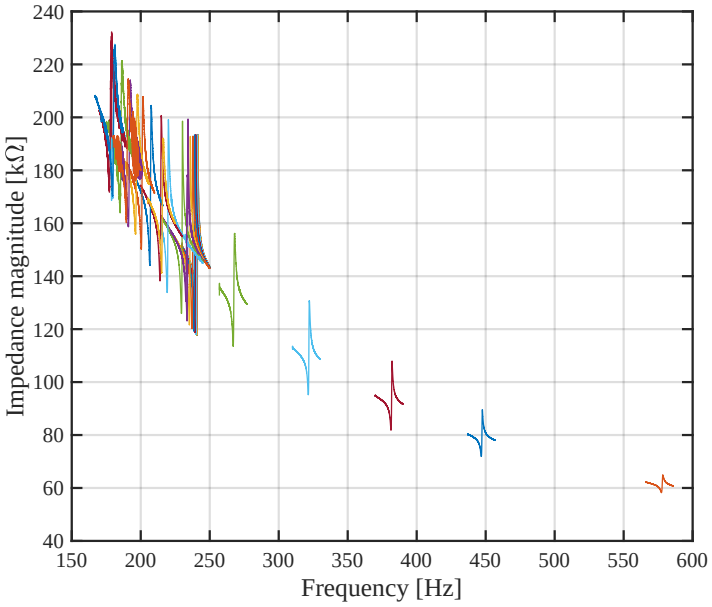

Figure 7.19: *Impedance magnitude versus resonant frequency for all the different points represented in Figure 7.18, where* $b = 0.52\,\text{mm}$.

7.3.3 Piezoelectric coefficient

The piezoelectric coefficient d_{31} is also found by using the Micro-Epsilon opto NCDT 2300-10 laser sensor and the Hewlett Packard E3611A DC power supply. The method consists in applying different DC voltages on the beam's electrodes and measuring its deflection with the laser. For each input voltage the position is measured for eight seconds and the mean value is taken. This mean deflection value versus the different voltages can be fitted to a straight line, from which d_{AlN} can be found by using both equation 2.18 and equation 2.30. Doing

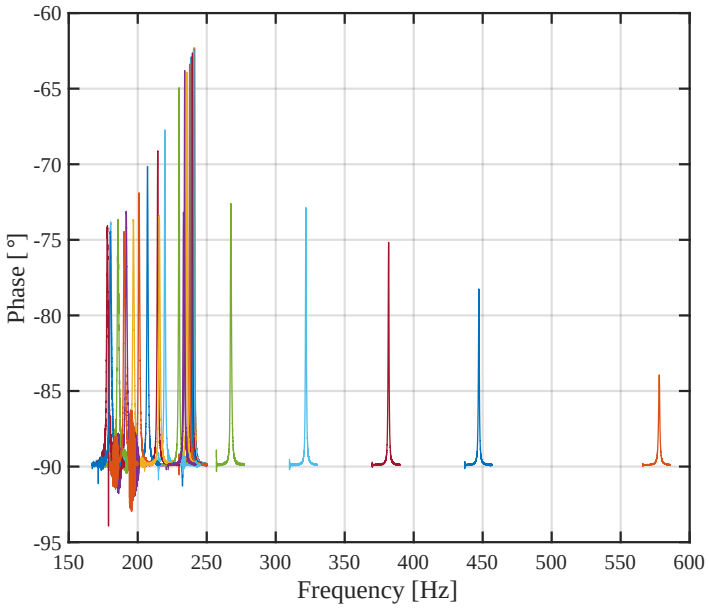

Figure 7.20: *Impedance phase versus resonant frequency for all the different points represented in Figure 7.18, where* $b = 0.52\,\text{mm}$.

this, the slope of the fitted straight line reads as follows

$$d_{\text{AlN}} = \text{slope}\frac{4s_{\text{AlN}}YI_{\text{eff}}}{h_{\text{si}}Wx^2}\ , \tag{7.6}$$

where the values used except for the slope are the ones shown in Table 2.1. Figure 7.23 shows the experimental results obtained for beam 18. A linear fit gives a slope of $4.57 \cdot 10^{-7}\,\text{m/V}$, which introduced into equation 7.6 results in $d_{\text{AlN}} = 3.94 \cdot 10^{-12}\,\text{C/N}$. By using $d_{\text{AlN}} = (1-\nu^2)d_{31}$, one finds the piezoelectric coefficient, which is $d_{31} = 3.53 \cdot 10^{-12}\,\text{C/N}$. This value is in relatively good agreement with [94], where the piezoelectric coefficient presents a value of $d_{31} = 2 - 2.7 \cdot 10^{-12}\,\text{C/N}$. It is important to note that the mean value displacement shown is obtained by subtracting the offset that the laser beam always inserts by default. The beam used to measure displacements is in focus within a 10 mm range, where the designation of what for example 1 mm is starts from the spatial location when the beam starts to be on focus. When measuring it is always tried to place the beam in the middle of this range. Therefore, what in Figure 7.23 is shown as displacement is the subtraction of the mean position at 0 V to all the measurements at different voltages.

Note that this piezoelectric constant is found before any ferromagnetic foil is implemented.

Now, once the associated piezoelectric constants have been found, equation 2.18 can be used to find the Γ factor. By using the just found $d_{\text{AlN}} = 3.94 \cdot 10^{-12}\,\text{C/N}$ constant and other values shown in Table 2.1, $\Gamma = 1.84 \cdot 10^{-7}\,\text{C}$, which is in good agreement with the theoretical

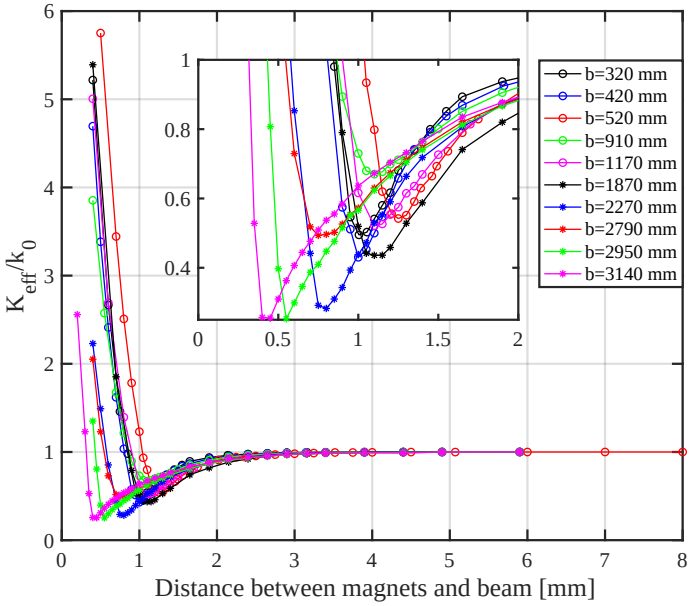

Figure 7.21: *Relative spring constant for different b (distance between magnets) by sweeping over a (distance between magnets and beam's tip).*

result obtained in Table 2.2. Using the experimental result, the expected displacement of the center of mass of the beam for a sweep over the voltage can be calculated by using equation 2.30, which as a reminder reads as

$$w(x) = \frac{\Gamma V}{2Y I_{\text{eff}}} x^2 \,, \tag{7.7}$$

where $w(x)$ is the beam displacement and x in this case the center of mass of the beam. The results are shown in Table 7.4, where the theoretical values are compared to the experimental ones. What was explained in this section about the laser positioning of the beam and the offset that was implemented when analyzing the data must be beared in mind: the offset was changed to zero for the positioning at 0 V. From Figure 7.23 it is clearly observed that the experimental results obtained for high voltages follow very well the linear fitting. Nevertheless, the experimental displacement values obtained for low voltages are considerably off the trend.

Now that Γ is obtained, one can calculate the turns ratio Γ/Λ by using the Λ factor obtained in Chapter 2, Table 2.2. The turns ratio obtained is $\Gamma/\Lambda = 6.22 \cdot 10^{-5}$ C/m.

7.3.4 Harvesting characterization

In this section the beams with active piezoelectric material are characterized in terms of power, voltage and others. The devices are actuated by the shaker, just as described in Section 7.2,

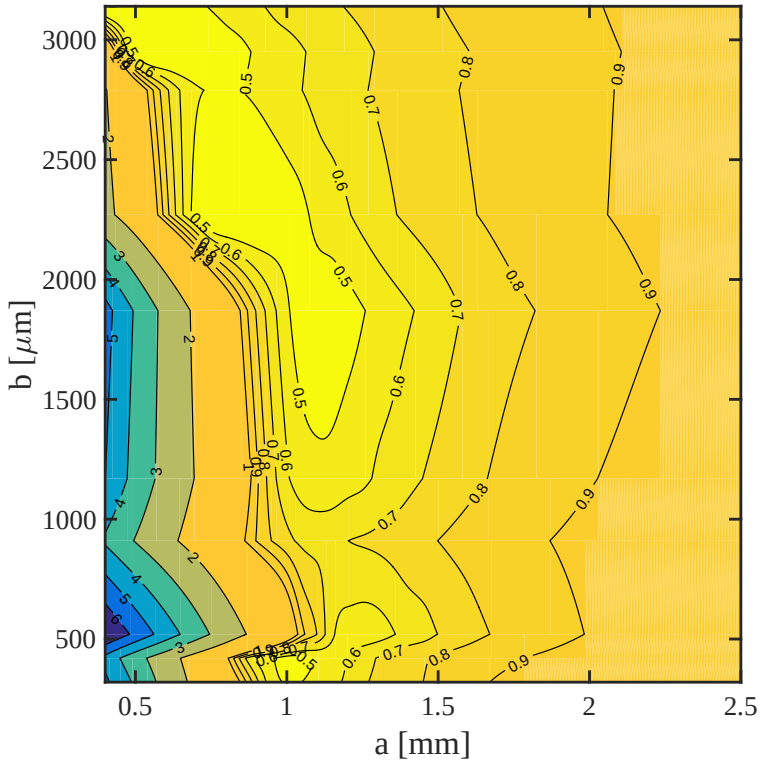

Figure 7.22: *Contour plot of the relative spring constant respec to to both a and b. The data corresponds to the one also represented in Figure 7.21.*

and a base acceleration of 0.8 g is used, which is measured by the holder deflection method. The first part of the section will deal with the description of how each data point is obtained and processed, which is based on Section 7.2. After clarifying this, a proper characterization takes place.

7.3.4.1 Deflection and Voltage

Deflection and voltage are the beam-related parameters that are directly measured with our set-up. Other parameters like power are derived values. As described in Section 7.2, the beams are actuated by a shaker at defined frequencies and the beams deflection and output voltage are measured at all times. Typical displacement and voltage measurements are depicted in Figures 7.24 and 7.26. As it can be observed, the raw data that is obtained (red curves) consists in deflection or voltage signals as function of time for the time slot that each measurement took place. The measuring time used during characterization always consists of eight seconds, however, for the sake of clearness only 0.5 seconds of the time slots are shown. Two excitation frequencies were chosen, one that is about the resonant frequency of the beam: 240.3 Hz, and another one further away from it: 238 Hz. At all times, a load resistance of 150 kΩ is used. Figures 7.24a and 7.24b show the deflection of the beam at both selected frequencies. A Fast Fourier Transform (FFT) is applied to each signal and the results are

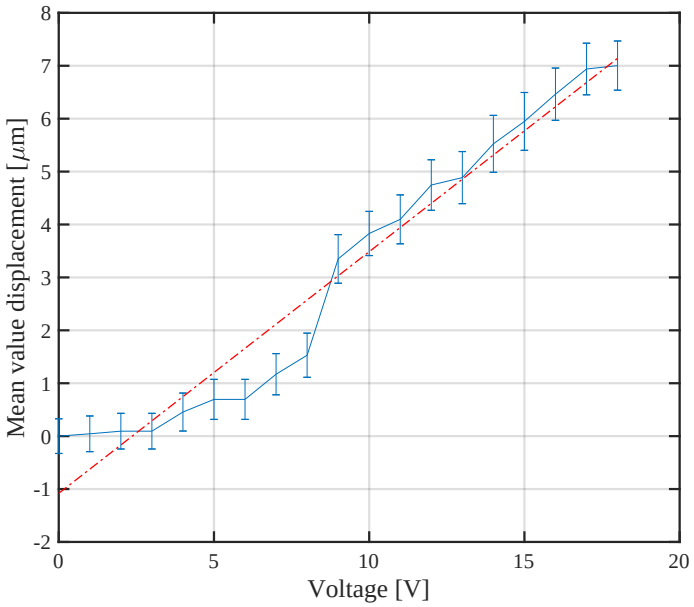

Figure 7.23: *Mean deflection versus applied voltage.*

Table 7.4: *Deflection values theoretically obtained and experimentally obtained.*

Voltage $[V]$	$w(x)$ from theory $[\mu m]$	$w(x)$ from experiments $[\mu m]$
1	0.36	0.04
3	1.09	0.09
5	1.83	0.7
10	3.66	3.8
14	5.13	5.5
18	6.60	7

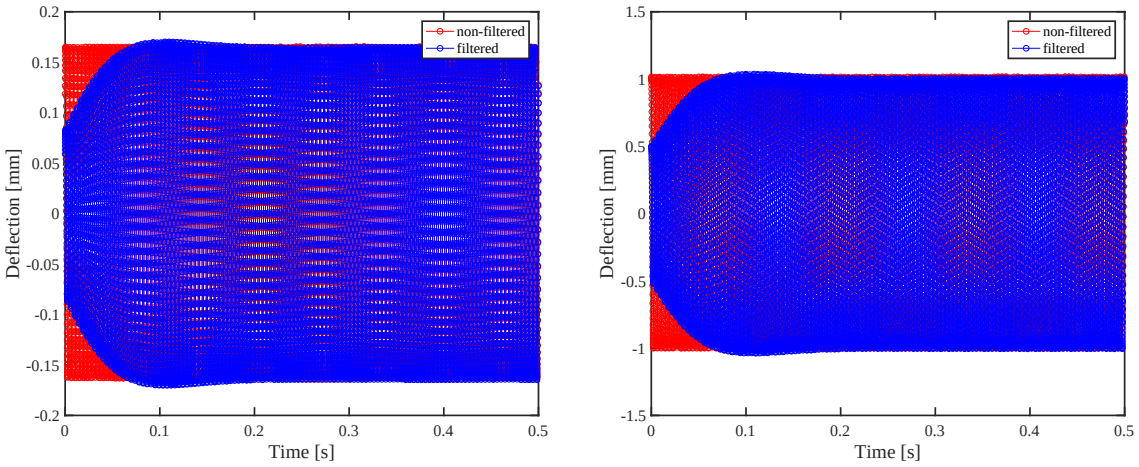

Figure 7.24: *Deflection versus time plots for a frequency excitation at a) 238Hz and b) 240.3 Hz.*

shown in Figure 7.25. It can be observed that the only peak observed in Figure 7.25a corresponds to the excitation frequency. In Figure 7.25b the only peak observed also corresponds to the excitation frequency, however, since this frequency corresponds to the resonant one, the magnitude of the peak increases an order of magnitude respect to the one in Figure 7.25a.

It is important to note that in order to perform the data analysis a Butterworth filter of order 2 was used. Figure 7.26a shows a voltage measurement versus time at an excitation frequency that is *not* the resonant frequency: 238 Hz. The red curve corresponds to the voltage without any filter applied. It can be observed that the signal is a composition of sine signals at different frequencies. The same occurs when at about the resonant frequency. Figure 7.26b shows the same kind of plot but at 240.3 Hz instead. The red curve, as in the previous case, is a composition of different excitation frequencies. In order to find those contributing frequencies, a FFT is applied to both signals, i.e. at both applied frequencies. Figure 7.27a shows the FFT of voltage at an excitation frequency of 238 Hz. The red peaks correspond to the unfiltered signal, where it can be observed that the largest peak corresponds to 50 Hz, this is noise due to the many electronic components used during the measurements, furthermore, its corresponding harmonics are also observed at $n \cdot 50Hz$, where n corresponds to any integer number. Besides these peaks, a peak at 238 Hz is also observed, which doubtlessly corresponds to the excitation frequency. In contrast, by applying a Butterworth filter of order two with a bandwidth of 10 Hz, the blue peak is obtained, which is the only dominant peak of the filtered signal. The same analysis was performed at an excitation frequency of 240.3 Hz, which is about the resonant frequency. The FFT of the voltage signal is observed in Figure 7.27b, if one looks at the unfiltered signal (red peaks), a similar behaviour is observed regarding the previous case: the largest contribution corresponds to noise at 50 Hz and its corresponding harmonics. However, two differences are spotted. One is that the contribution from the resonant frequency or similarly, the excitation frequency is quite apparent in the resonant

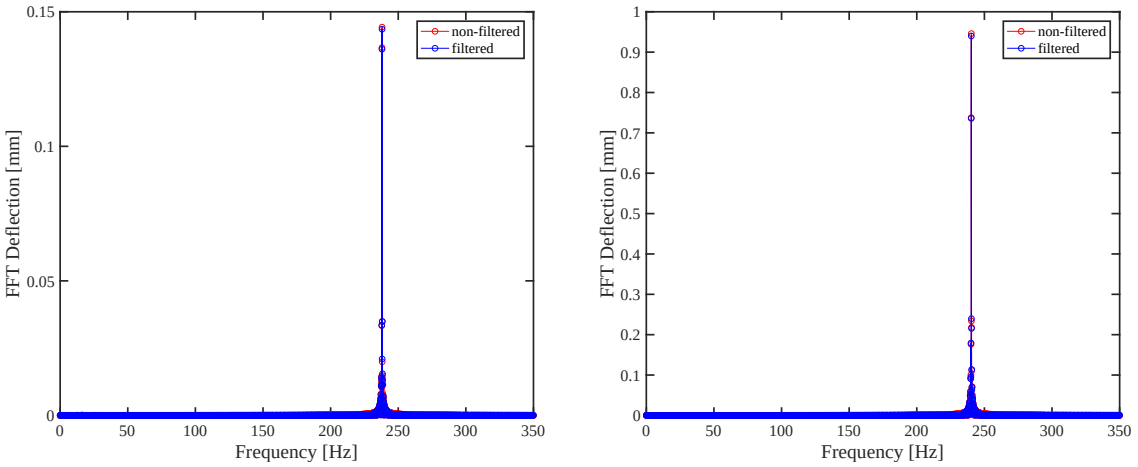

Figure 7.25: *FFT of the deflection for a frequency excitation at a) 238Hz and b) 240.3 Hz.*

case. This contribution reaches a maximum voltage of about 0.3 V, in contrast to Figure 7.27a, where the contribution from the excitation frequency was only of 0.05 V. The other difference is that small peaks close to the noise peaks are also observed, which might be related to the resonant frequency harmonics and some other electrical noise. After applying the filter with the same parameters as in the previous case, the largest contribution is again obtained for the excitation frequency. The effectiveness of the filter can be observed by looking back at Figures 7.26a and 7.26b for the voltage, where the blue line corresponds to the filtered signal. The filter used in all cases is a Butterworth filter of order 2 with a 10 Hz bandwidth for the reason explained in Section 7.2.1.1. Even though in the deflection signals no other apparent peaks than the excitation frequency were observed, the filter was anyways applied since the ambient vibration noise experienced in the lab varied from day to day due to the location of the lab.

Figure 7.28 shows the deflection of the beam for a sweep over frequencies at different load resistance values together with the maximum deflection at open circuit condition (black line). Each point in the plot is a result of calculating the RMS value for each set of filtered data as the one plotted in Figure 7.24. One can observe in Figure 7.28 that the maximum RMS deflection happens at the resonant frequency for all load resistances. In Figure 7.28 the load quality factor Q is also included, this was calculated differently from Section 7.2.1.1, instead it was calculated as

$$Q = \frac{fr}{FWHM}\,, \tag{7.8}$$

where FWHM stands for the full width at half maximum of each of the curves and f_r is the resonant frequency.

If each of the maximum deflection points for each of the resistances is taken and the RMS deflection is plotted versus resistance, then Figure 7.29 is obtained, where it can be observed

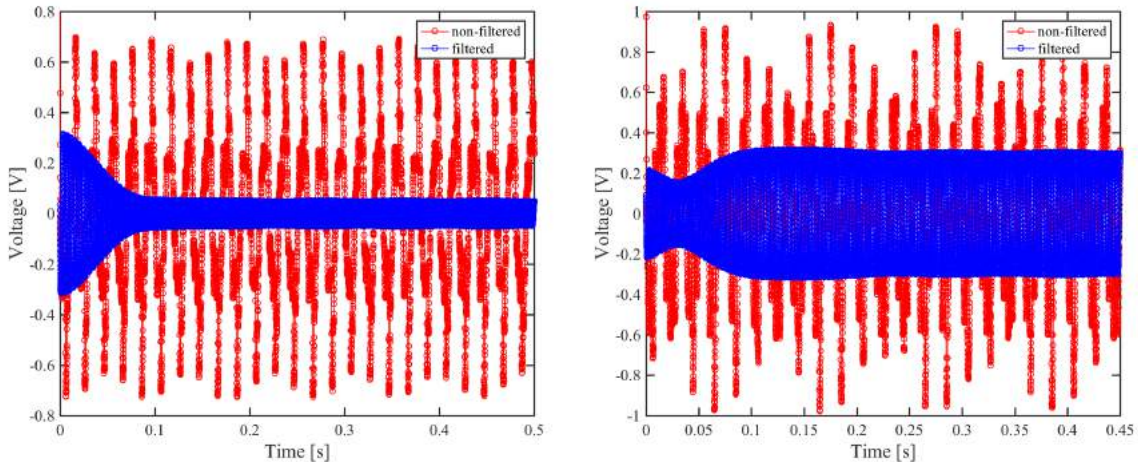

(a) **(b)**

Figure 7.26: *Voltage versus time plots for a frequency excitation at a) 238Hz and b) 240.3 Hz.*

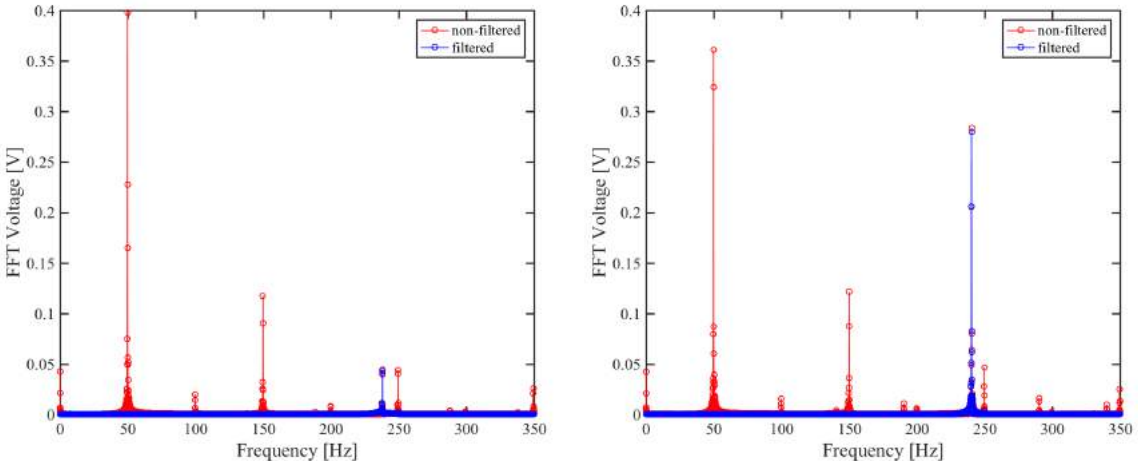

(a) **(b)**

Figure 7.27: *FFT of the voltage for a frequency excitation at a) 238Hz and b) 240.3 Hz.*

that a minimum RMS value is obtained for a load resistance of about 150 kΩ, which is in reasonable agreement with the optimal resistance found from the impedance measurements shown in Figure 7.16, where an optimal load resistance of about 160 kΩ was obtained. Since optimal power transfer is obtained at about that load, the deflection of the beam reaches a minimum.

In terms of voltage, Figure 7.30 shows the RMS voltage versus frequency for different resistance values and Figure 7.31 shows the maximum RMS voltage versus load resistances. The procedure followed to obtain each data point in Figure 7.30 was the same as the one used for the deflection analysis, that is, the RMS value of the filtered voltage versus time for each excitation frequency applied. This figure can be compared to Figure 7.28, where a maximum RMS deflection is obtained at about 240.3 Hz. Together with this, Figure 7.30 also shows the maximum value V_{OC}, i.e. open circuit voltage obtained, as a black straight line. Similar to Figure 7.28, Figure 7.31 shows the maximum RMS voltage for different load resistances, where the horizontal line again represents the maximum open circuit voltage.

Figure 7.32 shows the RMS voltage obtained for each deflection point of the beam, it confirms what is expected form Section 2.5.1, that voltage is linear with deflection. It can be observed in Figure 7.32 that different slopes are obtained for different load resistance values, where the steepest line corresponds to the open circuit condition and the blue horizontal line corresponds to the maximum open circuit voltage. By taking each slope in this figure and plotting them versus load resistance Figure 7.33 is obtained, where it is easily observed that for small resistance values the slope is proportional to the load resistance, as predicted in Section 2.5.1. In that Section it was also presented that if one defines $\alpha = \left|\frac{V}{w_c}\right|$ and takes the squared inverse of it, then the following relation holds

$$\frac{1}{\alpha^2} = \left|\frac{\Gamma}{\Lambda}\right|^2 \frac{1}{R_l^2 w^2} + \left|\frac{\Gamma}{\Lambda}\right|^2 C^2 \,, \tag{7.9}$$

this is represented in Figure 7.34, where the points are fitted to a line and the associated equation is also shown. From the slope of the linear regression and using equation 7.9, one obtains

$$113571 = \left|\frac{\Gamma}{\Lambda}\right|^2 \frac{1}{2\pi f} \,, \tag{7.10}$$

where the frequency can be represented by the resonant frequency since all measurements are performed at around that value. Therefore, $\left|\frac{\Lambda}{\Gamma}\right|$ is found to be $5.08 \cdot 10^5$ m/C. By taking the inverse of it one finds what is defined as the turns ratio

$$\left|\frac{\Gamma}{\Lambda}\right| = 1.97 \cdot 10^{-6} \mathrm{C/m} \,. \tag{7.11}$$

This turns ratio can be compared to the one found in Section 7.3.3, which is an order of magnitude higher than the found this time. The discrepancy is not clear yet, however, the discussion will continue later.

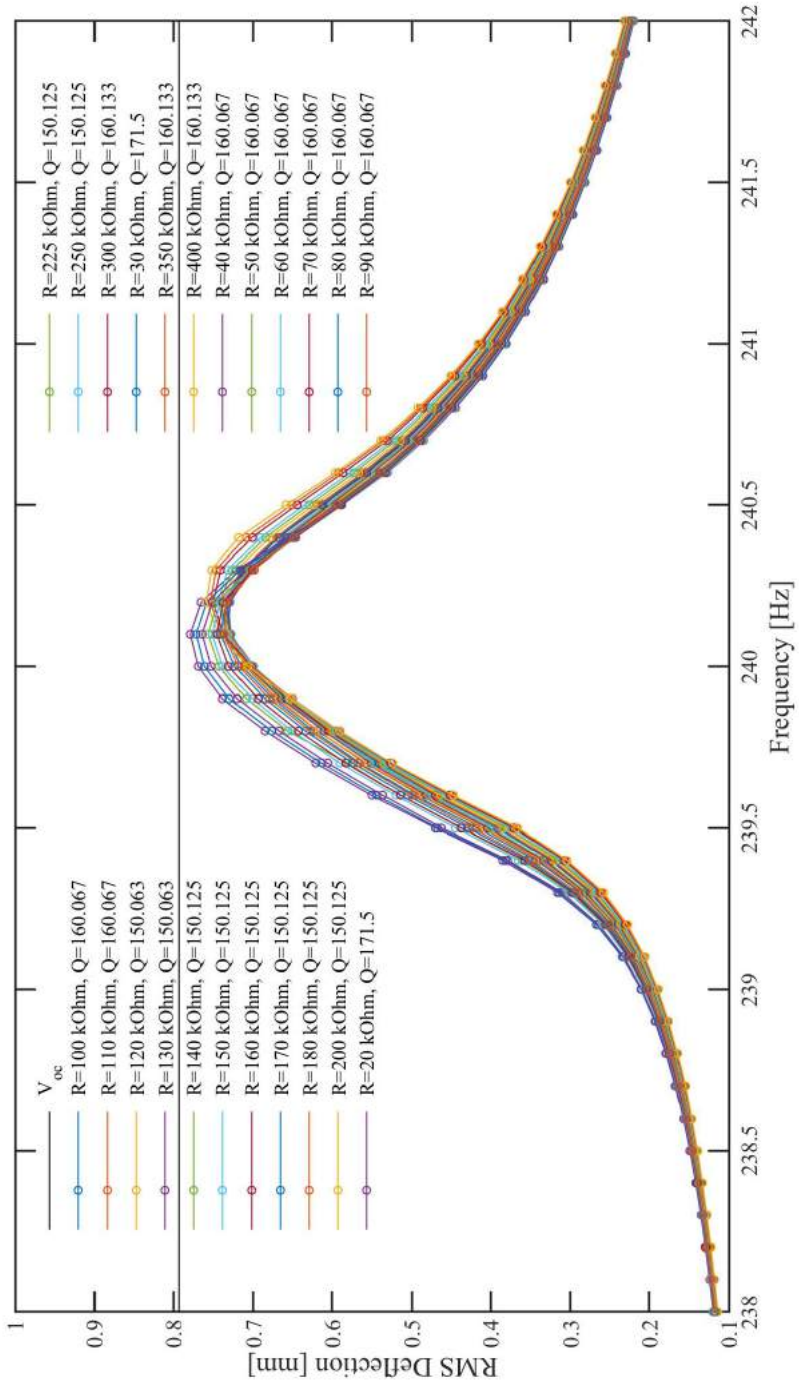

Figure 7.28: *RMS deflection versus frequency at different resistance values obtained for beam 09.*

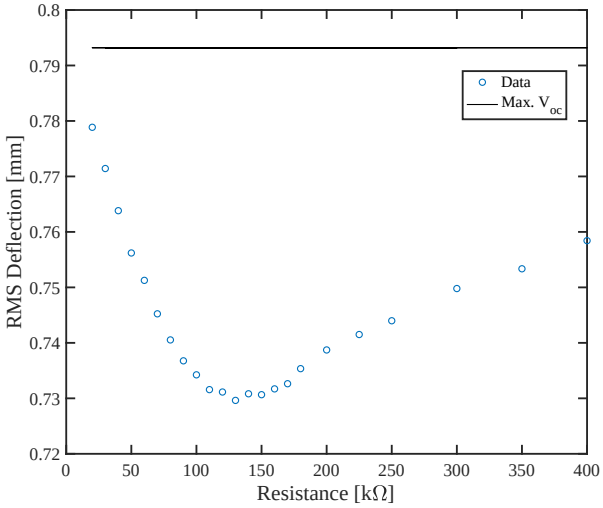

Figure 7.29: *Maximum RMS deflection versus excitation frequency for beam 09.*

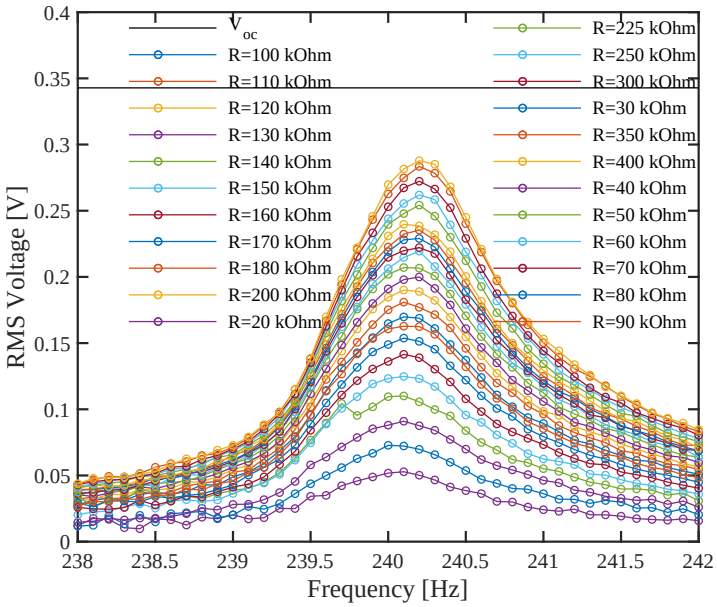

Figure 7.30: *RMS voltage versus frequency for beam 09. The black line corresponds to mavimum voltage at open circuit condition.*

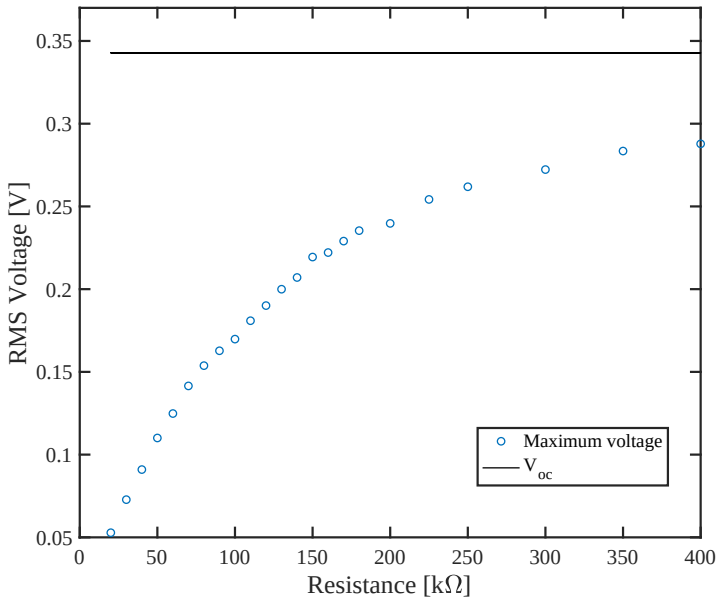

Figure 7.31: *Maximum voltage versus resistance values. The black line corresponds to mavimum voltage at open circuit condition.*

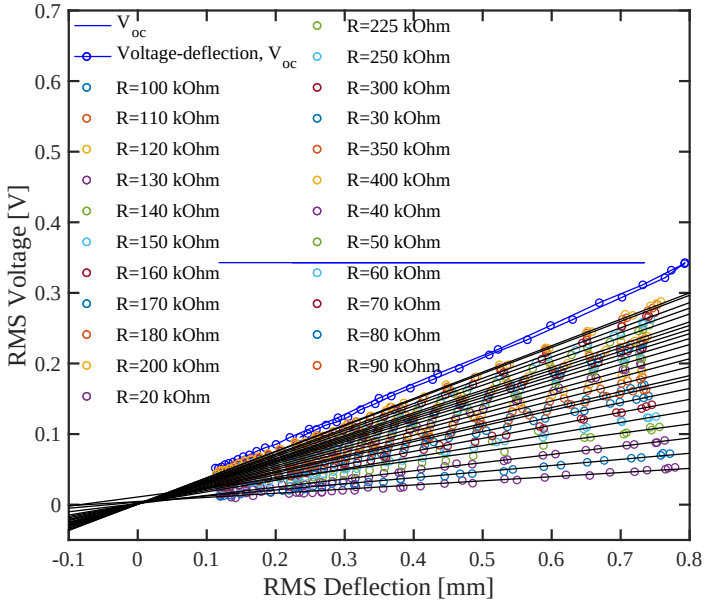

Figure 7.32: *RMS voltage versus deflection for different load resistances, where a linear relation between both of them is observed.*

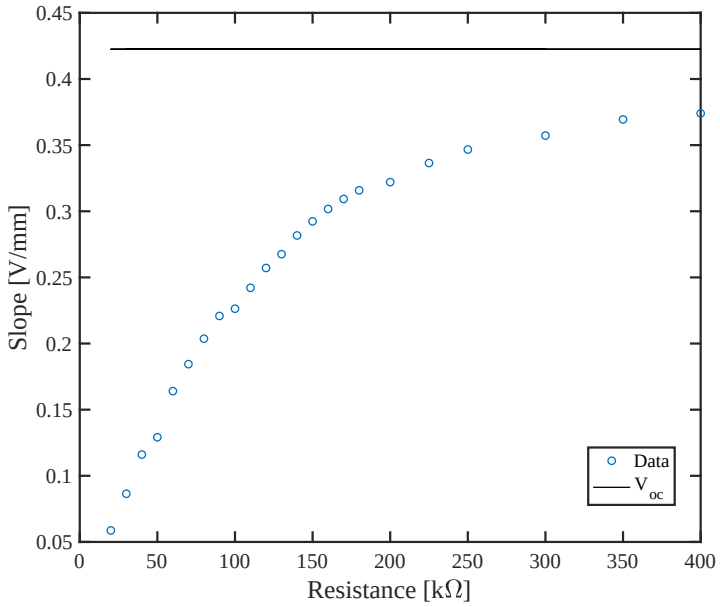

Figure 7.33: *The slope of every line in the previous figure is taken an each of them represents a point in this plot. The horizontal black line represents the open circuit voltage slope.*

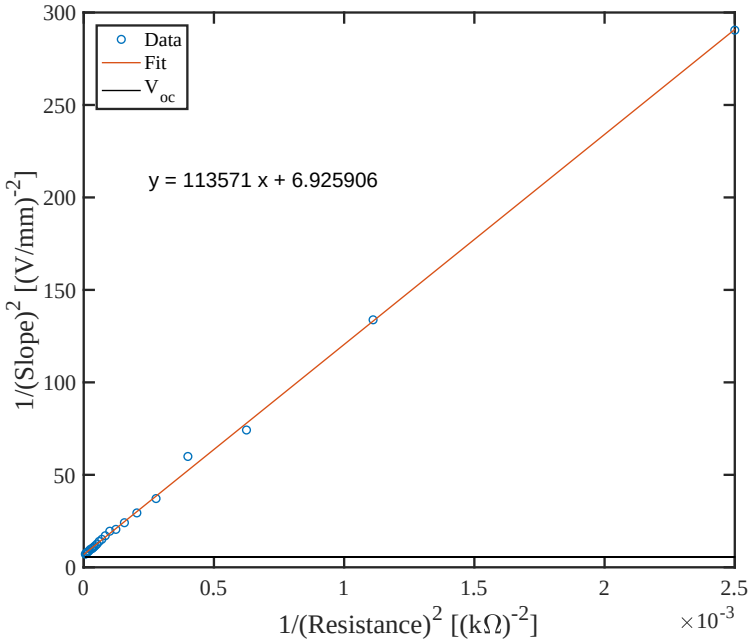

Figure 7.34: *Inverse of the squared slopes found in Figure 7.33 represented versus the inverse of each of its corresponding load resistances.*

From the linear regression one finds that the offset value is $6.93\,\mathrm{mm}^2/\mathrm{V}^2$, by using again equation 7.9 the capacitance associated to the piezoelectric material can also be found

$$C = \sqrt{\frac{6.93 \cdot 10^{-6}}{\left|\frac{\Lambda}{\Gamma}\right|^2}} = 5 \cdot 10^{-9}\mathrm{F} = 5\,\mathrm{nF}\ , \tag{7.12}$$

which is very close to the experimental value found in Section 7.3.2: 4.5 nF. This is an indicator that the turns ratio found in this section seems more plausible than the one found in Section 7.3.3.

7.3.4.2 Output power

Figure 7.35 shows the power harvested versus different excitation frequencies for different load resistances connected to the device at a base acceleration of 0.8 g. Together with this, Figure 7.35 also shows the associated load quality factor Q, calculated as explained in Section 7.3.4.1. Maximum output power happens at the beams resonant frequency, which is observed in all the curves. Figure 7.36 takes the values of maximum RMS output power from Figure 7.35 and plots them for each load resistance, from where a maximum RMS output power of about 0.32 μW is obtained at a load resistance value of 150 kΩ, this can be compared to the associated impedance at maximum phase angle of about 160 kΩ, at which maximum power transfer is expected. However, within the range 70 kΩ-200 kΩ approximately, a considerably similar amount of power is obtained, which is 0.30 μW. Figure 7.37 shows the RMS output power versus the tip deflection for different resistance values, from which it can be observed that generally speaking larger deflections lead to higher harvested power. This power can be compared to the calculated one in Chapter 2, shown in Table 2.2, which is 475 times larger than the one obtained. This is partially due to a non-linear effect caused by large enough base accelerations, which can be understood by plotting in Figure 7.38 the maximum RMS power harvested at different accelerations (blue curve) with a connected load resistance of 150 kΩ. At a value of about 0.4 g the system already enters a non-linear regime behaviour, therefore for the acceleration used of 0.8 g the power harvested must be smaller than the one expected from Chapter 2. However, if the same calculations performed for 0.8 g are done at 0.14 g (in the linear regime), the output power calculated is of 4.6 μW, and measured is 0.0075 μW. It was also thought that maybe when implemeting the ferromagnetic foil the method used is not the optimal one in terms of affecting the performance of the devices. Therefore, it was decided to compare the impedance measured before implementing the ferromagnetic foil and after doing so, on another working beam. This is shown in Figure 7.39, where the impedances before (red curve) and after (blue curve) present the same impededance values, which indicates that the procedure followed to add the proof mass does not change electrical response of the device. Therefore, explaining why the obtained power compared to the expected one is about 4 times smaller is, at the moment of writing, not fully accomplished.

7.4 Summary

Some of the devices fabricated during this work were characterized. In terms of robustness, the enhanced devices withstood a mean acceleration of 5.7 g, which is almost twice as much as the regular devices did. The piezoelectric material showed a good piezoelectric constant, $d_{31} = 3.53 \cdot 10^{-12}\,\mathrm{C/N}$, which was obtained by applying a voltage to the electrodes and measuring the deflection of the center of mass of the beam. The turns ratio obtained by using these experimental results was $\Gamma/\Lambda = 6.22 \cdot 10^{-5}\,\mathrm{C/m}$. The devices were also characterized in terms of deflection, voltage and power for different base accelerations, where the maximum RMS power obtained was of $0.32\,\mu\mathrm{W}$ at a load resistance of $150\,\mathrm{k}\Omega$. Non-linear affects due to magnetic forces interacting with the beam were also studied with impedance-based methods, where softening and hardening effects were both observed. A range of values that allow for an almost flat potential landscape, i.e. very low spring constant values were obtained.

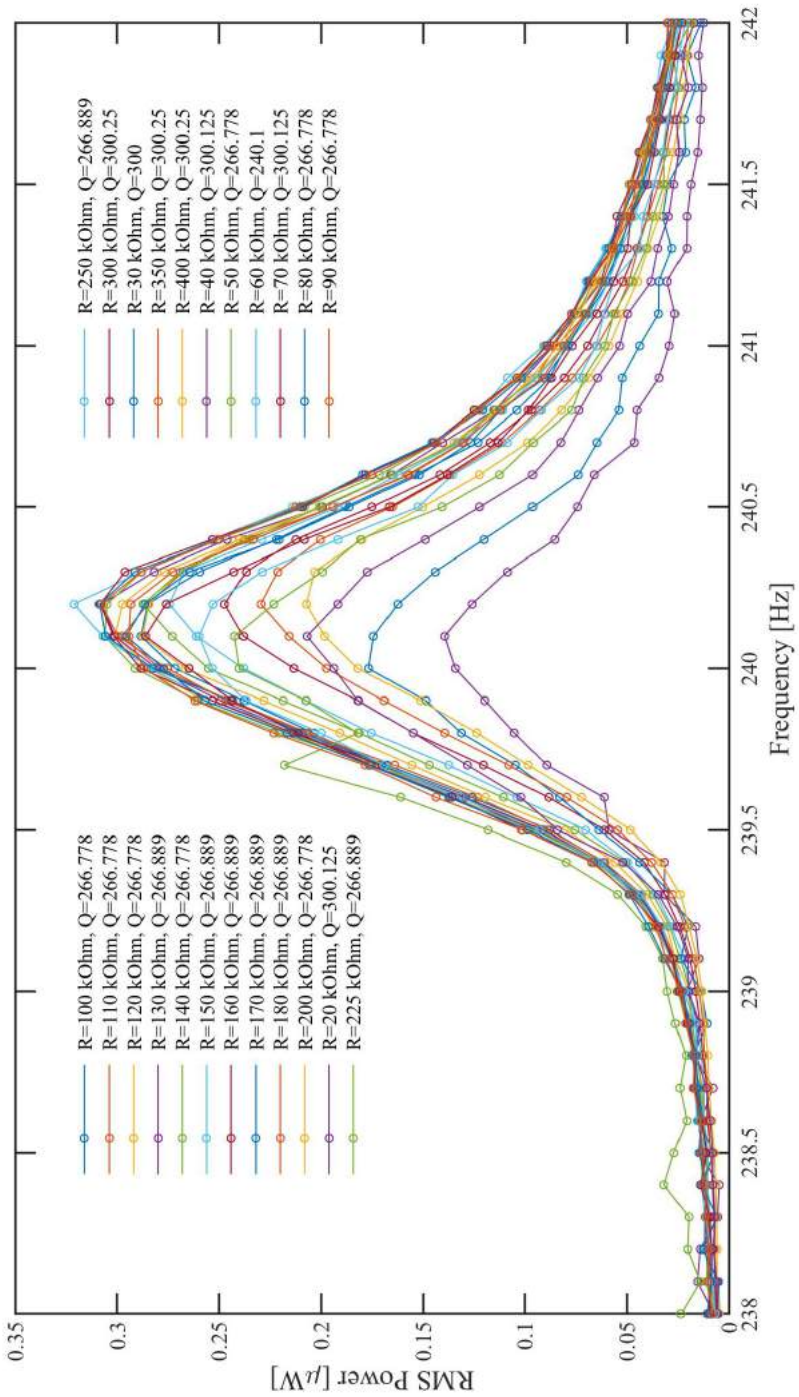

Figure 7.35: *Maximum RMS power versus excitation frequency for beam 09.*

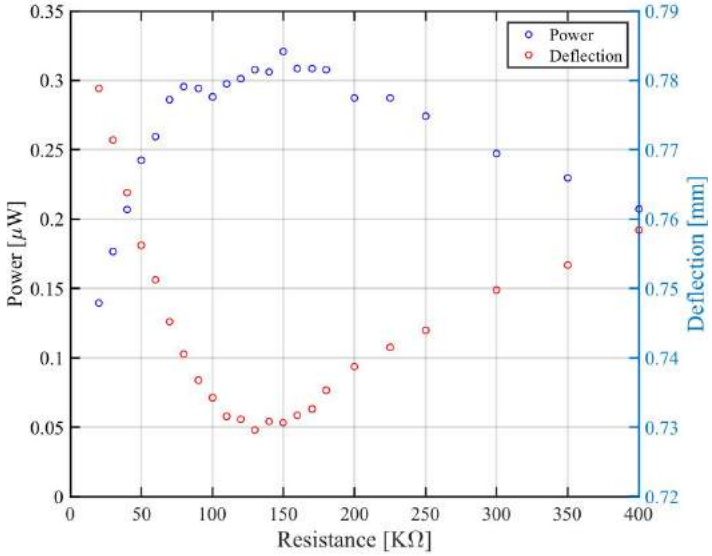

Figure 7.36: *Maximum RMS power and deflection versus load resistance for beam 09.*

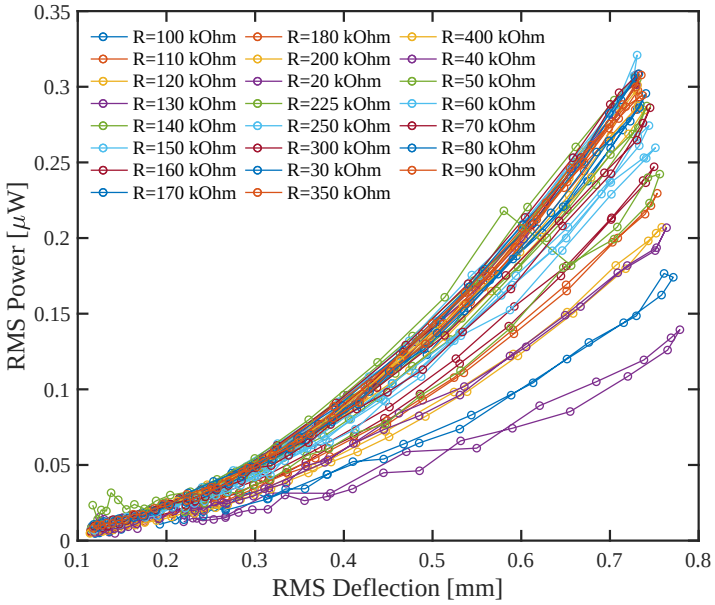

Figure 7.37: *RMS power versus RMS deflection for different load resistances. The figure correspond to beam 09.*

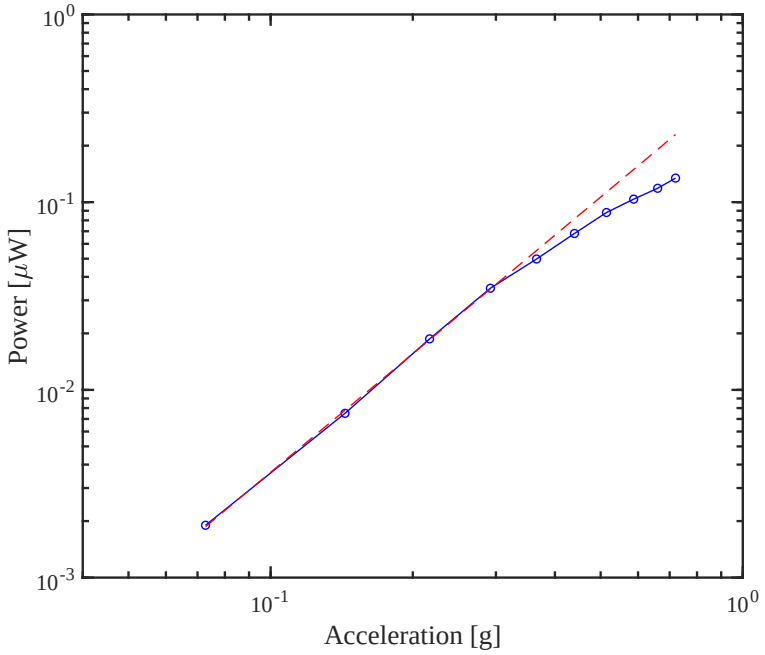

Figure 7.38: *RMS maximum power harvested for different acceleration values (blue curve). A linear fit (red line) is added so that it is easily observed that at a base acceleration of about* 0.4 g *the system already enters a non-linear regime behaviour.*

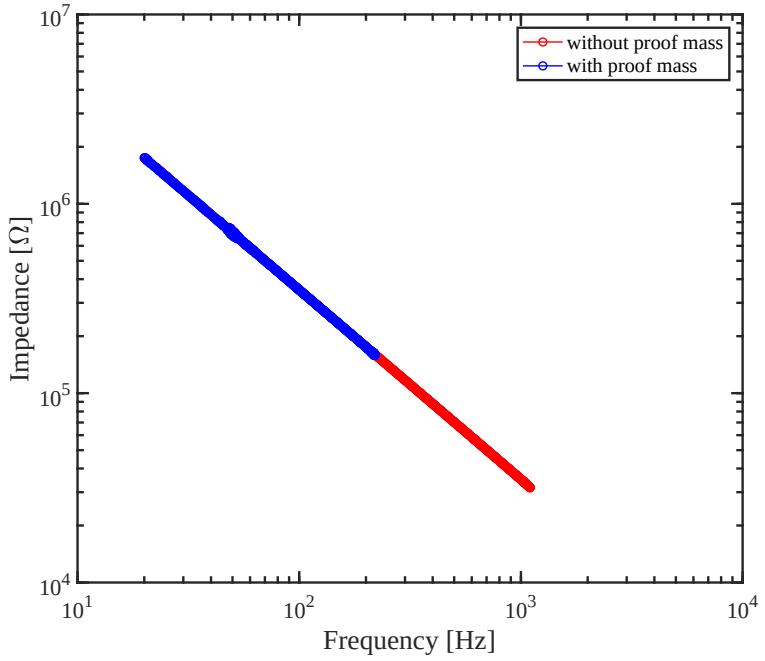

Figure 7.39: *Impedance measurements on beam 09 without (red) and with (blue) the ferromagnetic foil implemented.*

Chapter 8

Conclusion and Outlook

The main objective of this project was to develop a functionable energy harvester whose fabrication process was fully compatible with MEMS processes, that was robust enough to withstand external excitations and handling and, moreover, that was capable of harvesting energy over a wide frequency bandwidth. Throughout the fabrication process an active piezoelectric material with (002) crystallographic orientation was obtained. Besides this part of the fabrication, the process flow followed during projects previous to this work was adequately changed. The robustness of the VEHs was improved by lowering the stress at the anchoring point of the beams, which improves the harvesters lifetime at harsh environments and not appropriate handling. Magnetic forces were incorporated into the system by a pair of magnets to the end of interacting with the beam. In order to obtain such an interaction, ferromagnetic material on the beams' tip was decided to be implemented. Therefore, a set of beams without a built-in proof mass was also developed. The proof mass was afterwards incorporated as small pieces of ferromagnetic foil glued to the silicon structure. For these VEHs the piezoelectric material was deposited by a Swiss company. The reason was that the machine previously used was decommissioned due to several problems that it presented to the user. Furthermore, an attempt to deposit AlN with another machine ended up being unproductive. The fabrication process for this new set of harvesters was accordingly changed not only because of the new proof mass but also because the working electrodes that the company could provide with consisted of another material. In order to characterize the devices a new pair of set-ups were developed/improved. First, for the impedance characterization, a more robust set-up was achieved where a pair of magnets were also incorporated. Control in the three dimensional directions over both the magnets and the beam was obtained. Secondly, for the shaker-based measurements the noise obtained was lowered by setting a bridge-like structure where the laser sensor was assembled and where the shaker was screwed to a plate on top of a noise-reduction platform. Regarding the broad band characteristic of the devices, in terms of impedance-based measurements, a frequency shifting response of the harvesters due to different dimensional distances between the magnets and the beam and between the magnets themselves was observed. Both softening and hardening effects were obtained by implementing the magnetic forces. However, results in terms of power harvested for the different

magnets configurations was not tested due to lack of time.

In terms of more specific optimizations and experimental results, the following highlights are mentioned. Regarding the fabrication process, a (002) orientation AlN film with a thickness of 400 nm was obtained on the surface of molybdenum electrodes. XRD experiments showed no other orientation of the film under lock-coupled measurements, which was an improvement respec to the AlN film quality obtained by other groups using the same machine. A set of beams with enhanced robustness were fabricated and tested over increasing accelerations at thier natural resonant frequencies. It was found that regular beam withstood 3 g with a standard deviation of 0.5 g, whereas the enhanced ones withstood almost twice as much input acceleration, rising the previously obtained value up to 5.8 g with a standard deviation of 1.8 g. Furthermore, the process followed to increase the robustness was a two-step and lithography-free process wich consisted on growing a SiO_2 film after KOH etching the beams and stripping it right afterwards. Since the machine where AlN was being deposited was decommissioned, wafers with increased robustness were sent to a company that deposited the film together with its corresponding bottom and top metal layers, which were not the same as the previously used ones. Therefore, the fabrication process was accordingly changed and fully working harvesters were obtained.

Impedance measurements were done to study the interaction between beam and magnets and validate the COMSOL model used for simulating the effect different dimensional parameters on the beam's behaviour. A softening effect was clearly observed, which lowered the relative effective spring constant to 0.25, this value was obtained for a distance between between magnets and beam of about 450 μm and a distance between magnets of about 3.14 mm. This corresponds to a reduction in resonant frequency from 241 Hz to 123 Hz. Regarding the power harvested by our devices, they were only tested without any magnetic force. The results obtained were that they do not outperform harvesters of about the same size already developed by other groups since the peak power obtained was0.32 μW. This power was lower than the expected from theoretical calculations, however, non-linear effects at the input acceleration of 0.8 g were observed, which is partially a casue for this discrepancy.

8.1 Outlook

Some sugfestions for future work include the followings. The hand-picked procedure followed to implement the ferromagnetic proof mass proved to be not very convenient, as described earlier in this chapter. A solution to be investigated could involve electroplating a ferromagnetic /magnetic material.

Furthermore, the ferromagnetic proof mass must be re-sized to smaller dimensions without compromising the effectiveness of the harvester. This means basically that its longitudinal dimension must be shortened so as not to overstep into the top metal electrode, this reduction will be limited by the precision that the electroplating technique can provide and it must be bear in mind that a too shortened proof mass will eventually lead to an increase in resonant

frequency and a reduction in harvested power (assuming same thickness).

Characterizing the harvested power once magnetic forces are implemented into the system is doubtlessly included into future work. Nevertheless, this involves optimization of the measurement set-up. So far, the set-up is ready to excite only the beam, leaving the magnets at a static positioning. This is not realistic since both beam and magnets are excited in real environments. Therefore, if an accurate broadband study is to be performed, a bigger and more powerful shaker must be acquired and a new holder developed.

Further work would also include reducing the electrode area that covers the non-active piezoelectric layer, probably halving it. By doing this the impedance magnitude associated to that area would double, which leads to more output current and, therefore, more available power. Since the pogo pins that make contact to this area are not large, a reduction in area of about 50% widthwise sounds very realistic.

Appendix A

Masks layout

A.1 KOH mask for first set of beams

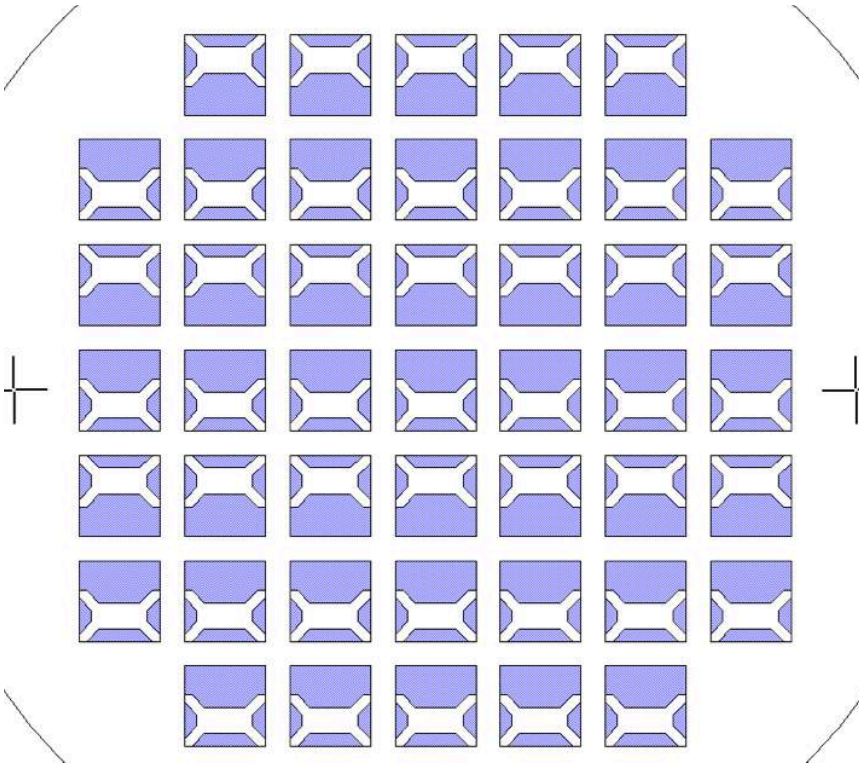

A.2 Deep etch mask for first set of beams

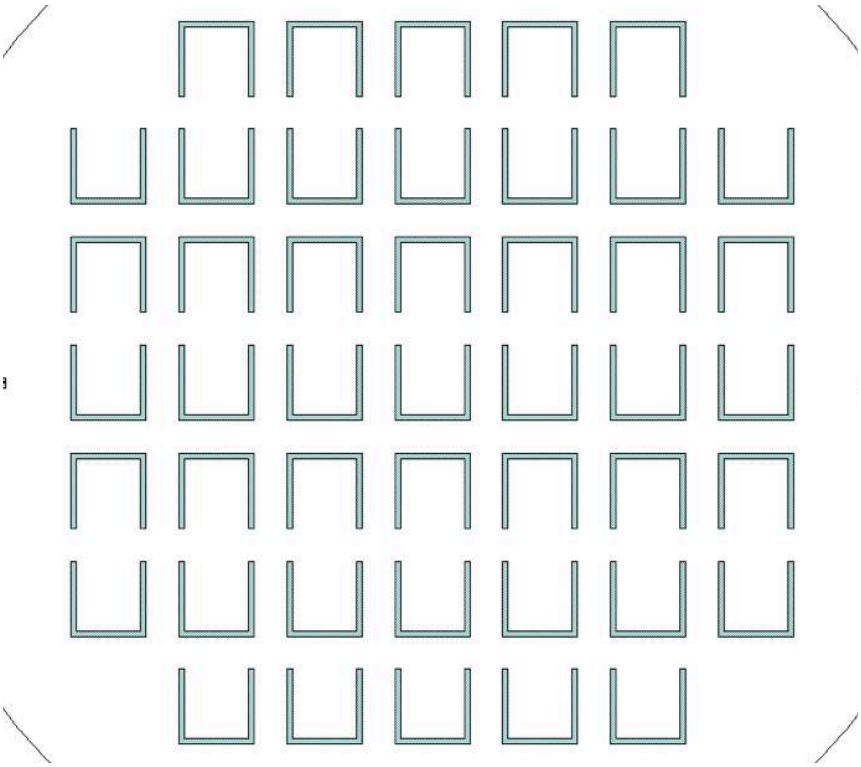

A.3 Top electrode mask for first set of beams

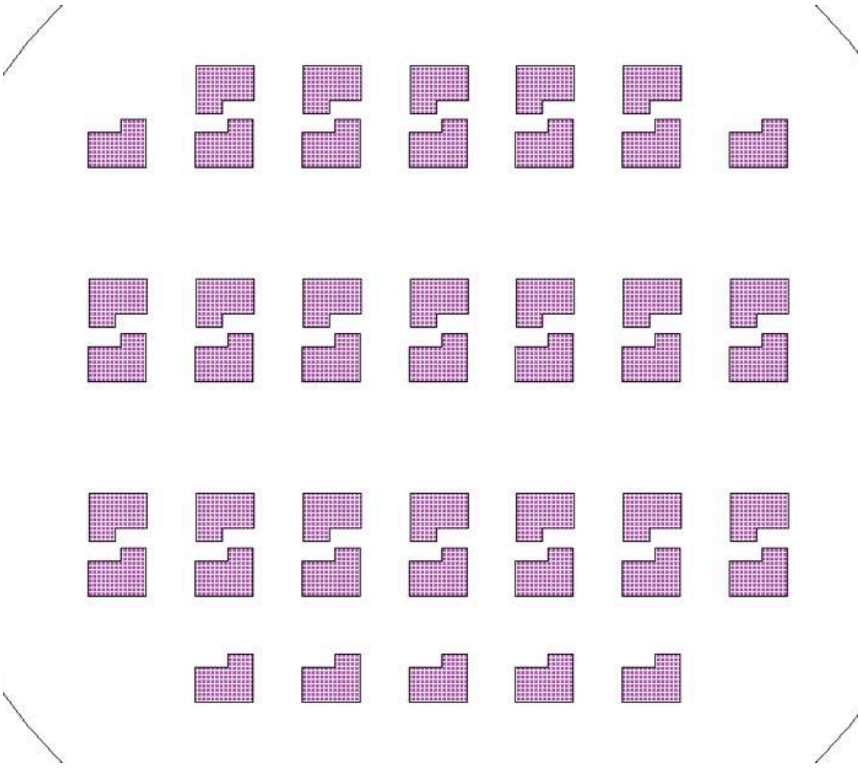

A.4 KOH mask for second set of beams

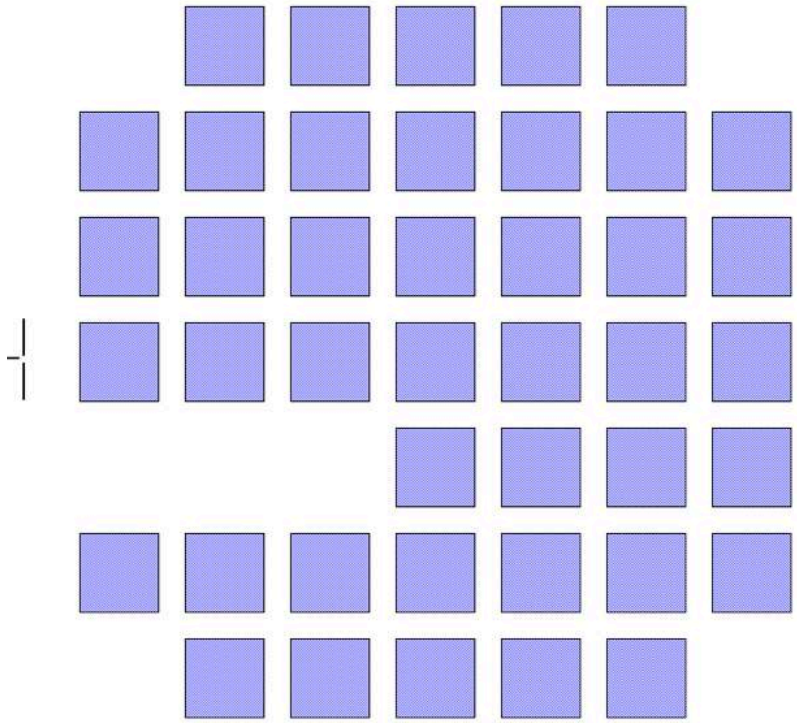

Appendix B

Data Sheets

B.1 B&K Mini-Shaker Type 4810

Mini-shaker Type 4810

Uses

- Accelerometer calibration
- Vibration testing of small objects
- Mechanical impedance and mobility measurements
- Experimental modal analysis

Features

- Force rating 10 N (2.25 lbf) sine peak
- Frequency range DC to 18 kHz
- First axial resonance above 18 kHz
- Max. displacement 4 mm (0.16 in) peak-to-peak
- Max. bare table acceleration 550 m/s^2
- Rugged construction
- Optimized performance using Power Amplifier Type 2718

Description

Mini-shaker Type 4810 is of the electrodynamic type with a permanent field magnet. It is well-suited as the force generator in general vibration tests, mechanical impedance and mobility measurements, and experimental modal analysis where only smaller force levels are required. It can also be used in the calibration of vibration transducers, both to determine their sensitivity, by comparison with a standard accelerometer, as well as their frequency response, up to 18 kHz.

The suspension system consists of radial flexure springs that restrict the moving element to almost perfectly rectilinear motion. Laminated flexure springs provide a high degree of damping to minimise distortion due to flexure resonances.

The object to be vibrated is attached to the table by means of a 10–32 UNF screw, the thread size commonly used for mounting accelerometers. Performance limits defined by the maximum displacement (4 mm), maximum force (10 N or 7 N depending on frequency), and the first axial resonance of the moving element (above 18 kHz), are shown in Fig. 1.

Fig. 1 *Sine performance curves for Type 4810*

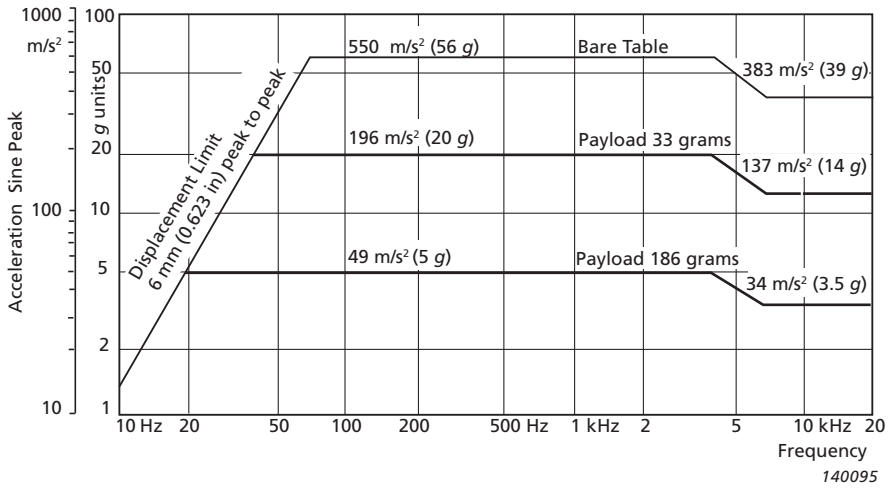

Specifications – Mini-shaker Type 4810

COMPLIANCE TO STANDARDS

The CE marking is the manufacturer's declaration that the product meets the requirements of the applicable EU directives

RCM mark indicates compliance with applicable ACMA technical standards – that is, for telecommunications, radio communications, EMC and EME

China RoHS mark indicates compliance with administrative measures on the control of pollution caused by electronic information products according to the Ministry of Information Industries of the People's Republic of China

WEEE mark indicates compliance with the EU WEEE Directive

Temperature: According to IEC 60068–2–1 & IEC 60068–2–2
Operating temperature: 5 to 40 °C (41 to 104 °F)
Storage temperature: –25 to +70 °C (–13 to +158 °F)
Humidity: According to IEC 60068–2–3
Damp Heat: 90% RH (non-condensing at 40 °C (104 °F))

SPECIFICATIONS
Force Rating (Peak):
10 N (2.25 lbf). 65 Hz to 4 kHz
7 N (1.5 lbf). 65 Hz to 18 kHz
Frequency Range: DC to 18 kHz
First Major Armature Resonance: Above 18 kHz

Max. Bare Table Acceleration (Peak):
550 m/s^2 (65 Hz to 4 kHz)
383 m/s^2 (6.5 kHz to 18 kHz)
(1 m/s^2 = 0.102 *g*)
Max. Displacement (Peak-To-Peak): 4 mm (0.16 in)
Dynamic Weight of the Moving System: 18 grams
Dynamic Flexure Stiffness: 2 N/mm (11.5 lb/in)
Magnetic Field: Permanent magnet
Max. Input Current: 1.8 A_{rms}
Coil Impedance: 3.5 Ω at 500 Hz
Connection: Microsocket 10–32 UNF
Table Diameter: 14 mm (0.55 in)
Fastening Thread: 10–32 UNF

WEIGHT AND DIMENSIONS
Weight: 1.1 kg (2.4 lb)
Diameter: 76 mm (3 in)
Height: 75 mm (2.9 in)

Ordering Information

Type 4810 Mini-shaker
includes the following accessories:
- AO-0069: Cable for connection of Type 4810 to Power Amplifier Type 2718
- YQ-2962: Threaded Steel Stud, 0.3 in 10–32 UNF

Optional Accessories

TRUNNION

WA-0429	Trunnion

POWER AMPLIFIER

Type 2718	Power Amplifier (75 VA)

STINGERS

WZ-0066	Nylon Stinger Kit

FORCE TRANSDUCERS

Type 8230	CCLD Force Transducer (+44/–44 N range)
Type 8230-001	CCLD Force Transducer (+220/–220 N range)
Type 8230-002	CCLD Force Transducer (+2200/–2200 N range)
Type 8230-003	CCLD Force Transducer (+22000/–2200 N range)
Type 8230-C-003	Charge Force Transducer (+22200/–2200 N range)
Type 8231-C	Charge Force Transducer (+110000/–2200 N range)
Type 8203	Force Transducer/Impact Hammer
Type 8001	Impedance Head

ADAPTORS AND STUDS

UA-2052	Set of 10 Stud Adaptors, 10–32 UNF to ¼–28 UNF
UA-2054	Set of 20 Bushing Adaptors, 10–32 UNF to ¼–28 UNF
UA-0125	Mounting Equipment (includes isolated studs YP-0150 and non-isolated studs YQ-2960)
JP-0150	Adaptor, 4 mm Socket Pair to BNC Plug for use with old Type 2706

BP 0232 – 15 2014-08

Brüel & Kjær Sound & Vibration Measurement A/S
DK-2850 Nærum · Denmark · Telephone: +45 77 41 20 00 · Fax: +45 45 80 14 05
www.bksv.com · info@bksv.com

Local representatives and service organisations worldwide

Brüel & Kjær

B.2 B&K Accelerometer Type 4507 B 004

PRODUCT DATA

CCLD Accelerometer Types 4507 and 4508
CCLD TEDS Accelerometer Types 4507-B and 4508-B
Charge Accelerometer Types 4507-C and 4508-C

CCLD[*] Accelerometer Types 4507 and 4508 consist of a ThetaShear® accelerometer and a CCLD preamplifier in a lightweight titanium housing with integrated 10–32 UNF connectors. TEDS[†] version is also available. Types 4507-C and 4508-C are the charge types similar to the CCLD accelerometers but come without the preamplifier.

Uses and Features

Uses
- Structural analysis measurements
- Multichannel modal analysis measurements
- General purpose

Features
- Robust titanium housing with integrated hermetic titanium connector
- Easy fit to different test objects using a selection of mounting clips
- Lower sensitivity to RF (Radio Frequency) electromagnetic fields
- Low-weight ThetaShear design gives high sensitivity-to-weight ratio and very low sensitivity to environmental factors
- Triaxial mounting facility
- Excellent low-frequency response
- Low magnetic sensitivity

CCLD Accelerometers
- Connect directly to CCLD power supply
- CCLD principle allows the use of inexpensive cables
- Output impedance allows the use of long cables
- Built-in, low-noise preamplifiers with ASICs give more than 100 dB dynamic range
- Choice of sensitivities from 10 mV/g to 1 V/g
- Hermetic connector

Charge Accelerometers (Types 4507-C and 4508-C)
- Sensitivity of 5 pC/g
- Operating temperature up to 250°C (482°F)

[*] CCLD: Constant Current Line Drive, also known as DeltaTron® (ICP® and IEPE compatible)
[†] TEDS: Transducer Electronic Data Sheet

Description

Accelerometer Types 4507 and 4508 are specifically designed to withstand rough environments. A combination of high sensitivity, low mass and small physical dimensions makes them ideal for modal measurements such as automotive body and power-train ones as well as for modal analysis on aircraft, trains and satellites. The main difference between the Types 4507 and 4508 is the position of the coaxial connector, which is on the top surface perpendicular to the main axis for Type 4508 (top-mounted connector) and on the side surface parallel to the main axis for Type 4507 (side-mounted connector).

Design

Fig. 1
Exploded view of Miniature CCLD Accelerometer Type 4508 (top mounted connector) showing the ThetaShear design and built-in CCLD preamplifier

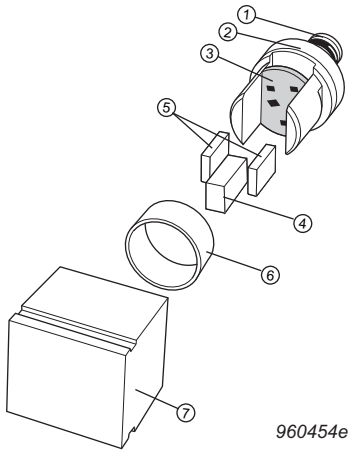

The 10–32 UNF connector (1) is an integrated part of the top piece (2), which also contains the preamplifier (3) (not Type 4507-C or 4508-C). The slotted cylindrical stanchion holds a central seismic mass (4) flanked by two piezoelectric plates (5). This assembly is clamped rigidly by a ring (6). The parts are firmly held together without the use of any bonding agent other than friction, a principle which has proved extremely reliable in Brüel & Kjær DeltaShear® accelerometers. This assembly is hermetically welded to the titanium housing (7).

Mounting

Special effort has been put into making the mounting process as flexible as possible. The accelerometer housing has slots that allow the use of mounting clips so that the accelerometers can be easily fitted to a number of different test objects, or removed, for calibration. UA-1407, UA-1475 and UA-1478 are sets which each contain 100 plastic mounting clips. UA-1564 is a set of 5 high-temperature mounting clips.

Fig. 2
High-temperature Mounting Clip UA-1564

Specifications:

Temperature range:	–55° to +175°C (–67° to +347°F)
Acceptable if discolouring:	up to +250°C (+482°F)
Weight:	5.7 grams (0.20 oz)
Maximum acceleration:	
(with 5 gram accelerometer):	50 g peak
(Perpendicular to mounting surface):	250 g peak
Material:	Base – Anodized aluminium; Spring – Stainless steel
Mounting:	10–32 UNF

Common Specifications for all Plastic Mounting Clips

Temperature range: –54°C to +50°C (–65° to +122°F)
For brief use (<1 hour): up to +80°C (up to +176°F)

Maximum acceleration: 10 g peak
Perpendicular to mounting surface: 70g peak

Material: Glass reinforced polycarbonate

Fig. 3
Mounting Clip UA-1407

120593

Fig. 4
Mounting Clip UA-1407 in use with Type 4508

990007/2

Specifications:

Weight:	0.4 gram (0.014 oz)
Upper limiting frequency, 10%:	
– Type 4507 mounted with grease:	3 kHz
– Type 4507 dry mounting:	1.5 kHz
– Type 4508 mounted with grease:	4 kHz
– Type 4508 dry mounting:	2 kHz

Fig. 5
Mounting Clip with Thick Base UA-1408

990013/2

Fig. 6
Mounting Clip with Thick Base UA-1475 can be filed down to suit the needs of your mounting surface. Here it is mounted on a tube with Type 4508

990008/2

Specifications:

Weight:	0.7 gram (0.02 oz)
Upper limiting frequency, 10%:	
– Type 4507 mounted with grease:	3 kHz
– Type 4507 dry mounting:	1.5 kHz
– Type 4508 mounted with grease:	4 kHz
– Type 4508 dry mounting:	2 kHz

Fig. 7
Swivel Base UA-1478

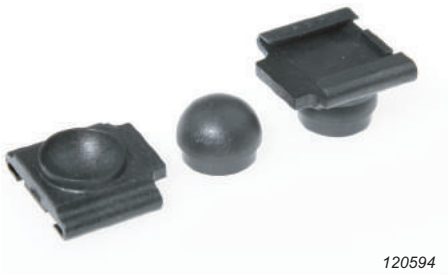

120594

Fig. 8
Swivel Base UA-1478 mounted on a sloping surface with Type 4508

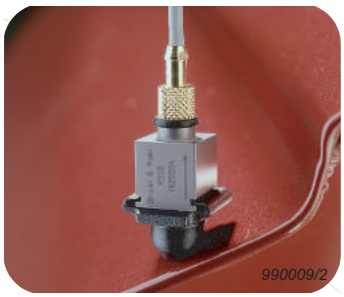

990009/2

Specifications:	Weight:	0.8 gram (0.028 oz)
	Upper limiting frequency, 10% (mounted with grease):	
	– Excited along accelerometer's axis of sensitivity and with mounting surface of hemispherical part perpendicular to excitation direction:	2.3 kHz
	– Excited along accelerometer's axis of sensitivity and with mounting surface of hemispherical part at 45° to excitation direction:	1.7 kHz

Fig. 9
Spirit Level UA-1480

990010/2

Fig. 10
Spirit Level UA-1480 in use on Swivel Base UA-1478

990011/1

Specifications:	Max. dimensions:	85 × 23 × 17 mm (3.3 × 0.9 × 0.7 in.)
	Material:	Black anodized aluminium

Environmental Sensitivity

Some of the most troublesome environmental factors encountered when using piezoelectric accelerometers are temperature transients. By careful choice of materials, mechanical design and the shear concept, however, the influence of these factors has been reduced to a minimum. Special effort has also been made to minimise interference from RF (Radio Frequency) electromagnetic fields.

High humidity is another environmental factor that can influence the accuracy of piezoelectric transducers. Careful design and manufacturing have reduced this effect to a minimum for the Type 4507 and 4508 families. Furthermore, all CCLD members of the families (see Specifications) are equipped with hermetically sealed (glass) connectors, that make them completely independent of humidity and aggressive gases.

Calibration

Fig. 11
Calibration Clip DV-0459

120709

Each accelerometer is individually calibrated and supplied with a comprehensive calibration chart. Long-term stability and reliability are ensured by artificial ageing during the production process.

Field checking and system calibration are straightforward using Brüel & Kjær's Hand-held Vibration Calibrator Type 4294.

For calibration of Types 4507/4508, Calibration Clip DV-0459 is available (Fig. 11).

Specifications

Material:	
– Base:	Stainless steel (hardened)
– Spring:	Stainless steel spring
Mounting surface diameter:	21 mm
Mounting thread:	10–32 UNF
Weight:	17 grams

CCLD Accelerometers

CCLD is a generic name identifying accelerometers and signal-conditioning products that operate on a constant-current power supply and give output signals in the form of voltage modulation on the power supply line. One of the advantages of this system is that it allows you to use inexpensive cables.

Accelerometers Types 4507 and 4508 can be used with all vibration setups with CCLD input modules.

The built-in, low-noise preamplifiers are made using thick film technology. They comprise ASICs including a special reference voltage that ensures very stable bias voltage over the entire operating temperature range.

The low-output impedance allows long cables connection of between the accelerometer and measurement equipment.

Charge Accelerometers

Accelerometer Types 4507-C and 4508-C can be used in high-temperature applications up to 250°C (482°F), and the use of an external conditioning amplifier allows variable amplification for optimum signal-to-noise ratio. Brüel & Kjær has a wide range of equipment to support piezoelectric charge accelerometers, and Types 4507 and 4508 can be connected to the following:

- LAN-XI Front Panel UA-2105-060 – usable with Type 2647
- Charge to CCLD Converter Type 2647 (with TEDS) – which enables the accelerometers to be used with CCLD power supplies
- NEXUS™ Charge Conditioning Amplifier Type 2692 – suitable for conditioning the signal
- Measuring Amplifier Type 2525 – suitable for conditioning the signal
- Charge Amplifier Type 2635 – suitable for conditioning the signal

Cables and Connectors

In order to distinguish the individual accelerometers in a multichannel measurement setup, coloured cable markers (UA-1243) are available to fit cables which are 1.6 mm and 2 mm in diameter.

Types 4507 and 4508 require cables with 10 – 32 UNF connectors. For general, non-critical use, standard cables AO-0463 and AO-0531 are recommended (not for Type 4507-C or 4508-C) since they are very flexible and economic.

For Types 4507-C and 4508-C, low-noise or super low-noise cables AO-0038, AO-0122, AO-0406 or AO-1382 are recommended (see Ordering Information for details).

Maximum Cable Length (CCLD only)

The maximum output voltage of a CCLD accelerometer when driving long cables depends on the supply current at which it is operating and on the capacitive load due to the connecting cable.

The maximum cable length in metres (for distortion ≤ 1%) is given by:

$$L = 140\,000 \times \frac{I_s - 1}{f \times V_o \times C_m}$$

where:
I_s = supply current (mA)
f = frequency (kHz)
V_o = output voltage (V_{peak})
C_m = cable capacitance (pF/m)

Characteristics

Frequency Response

The following frequency response information is included on each accelerometer's accompanying calibration chart. However, certain accelerometers have this information built in electronically (TEDS) as well.

The upper frequency limits given in the specifications are the frequencies where the deviation from the reference sensitivity is less than 10%. It is approximately 30% of the mounted resonance frequency. This makes the assumption that the accelerometer is correctly mounted on the test structure – a poor mounting can have a marked effect on the mounted resonance frequency.

The lower frequency limits and phase response are determined by the built-in preamplifiers. The lower frequency limits are given in the specifications for deviations from reference sensitivity of less than 10%.

Increased measurement accuracy can be achieved by dividing the actual measurement by the individual frequency response.

Frequency response curves generated from the individual TEDS values are given on the calibration chart for the major part of the frequency range. At low frequencies, the curves given are typical.

The calibration chart also includes the individual TEDS values that, together with a general formula, best fit the measured frequency response. The expression can be used for frequency response compensation in the specified frequency range.

The relative frequency response, including amplitude and phase, is given by:

$$S_{rel}(f,T) = (\text{Sign}) \times (1 + b(T - T_{ref})) \times \frac{j\frac{f}{f_{hp}}}{\left(1 + j\frac{f}{f_{hp}}\right)} \times \frac{1}{\left(1 + j\frac{f}{f_{lp}}\right)} \times \frac{1}{\left(1 + \left(j\frac{f}{f_{res}}\right)^2 + j\frac{f}{Qf_{res}}\right)} \times \left(j\frac{f}{f_{ref}}\right)^{\frac{a}{\ln 10}}$$

where:

Sign	= Polarity	b	= Temperature Coefficient
T	= Temperature	T_{ref}	= Reference Temperature
f	= Frequency	f_{hp}	= High-pass Cut-off Frequency
f_{lp}	= Low-pass Cut-off Frequency	f_{res}	= Resonance Frequency
f_{ref}	= Reference Frequency	Q	= Quality Factor
a	= Amplitude Slope/Decade		

Combining this equation with the amplitude sensitivity S_{ref}, f_{ref} and T_{ref} gives you:

$$S(f,T) = S_{ref} \times \frac{S_{rel}(f,T)}{|S_{rel}(f_{ref},T_{ref})|}$$

Implementation of this formula in either real-time data acquisition systems or in post-processing will support an automatic update of amplitude and/or phase.

Triaxial Measurements

Types 4507-B-004, -B-005, -B-006 and 4507-C are equipped with three sets of mounting slots. These make it possible to perform triaxial measurements by successively mounting the accelerometer in three directions perpendicular to each other. This is easily done when the accelerometer is mounted in one of the mounting clips. However, it requires that the measurements take place on a non-variant system.

Applications

The features of Types 4507 and 4508 make them ideal for modal analysis on ground vehicles, aircraft and satellites. These applications often involve large, composite structures that require multiple measurement points. Types 4507 and 4508 excel in such situations, providing ease of handling, reliability and fast calibration. With a rugged construction, Types 4507 and 4508 can also be used in a wide range of measurement environments. They also have low sensitivity to temperature transients, which is advantageous when it comes to making measurements at low frequencies.

Compliance with Standards

CE, C-Tick	CE-mark indicates compliance with: EMC Directive and Low Voltage Directive. C-Tick mark indicates compliance with the EMC requirements of Australia and New Zealand
Safety	EN 61010–1 and IEC 61010–1: Safety requirements for electrical equipment for measurement, control and laboratory use. UL 3111–1: Standard for Safety – Electrical measuring and test equipment
EMC Emission	EN/IEC 61000–6–3: Generic emission standard for residential, commercial and light industrial environments. EN/IEC 61000–6–4: Generic emission standard for industrial environments. CISPR 22: Radio disturbance characteristics of information technology equipment. Class B Limits. FCC Rules, Part 15: Complies with the limits for a Class B digital device.
EMC Immunity	EN 50082–1: Generic immunity standard. Part 1: Residential, commercial and light industry. EN 50082 – 2: Generic immunity standard. Part 2: Industrial environment. **Note 1:** The above is guaranteed using Cable AO-1382 only. **Note 2:** Sensitivity to RF (in accordance with EN 50082 – 2) 4507, 4507-B, 4507-B-003, 4507-B-004, 4508, 4508-B and 4508-B-003: <60 µV 4507-001, 4507-B-001, 4508-001 and 4508-B-001: <10 µV 4507-002, 4507-B-002, 4507-B-005, 4507-B-006, 4508-002, 4508-B-002 and 4508-B-004: <100 µV
Temperature	IEC 68 – 2 – 1 & IEC 68 – 2 – 2: Environmental Testing. Cold and Dry Heat. Operating Temperature: 4507, 4507-001, 4507-B, 4507-B-001, 4507-B-003, 4507-B-004, 4508, 4508-001, 4508-B, 4508-B-001 and 4508-B-003: –54° to +121°C (–65° to +250°F) 4507-002, 4507-B-002, 4507-B-005, 4507-B-006, 4508-002, 4508-B-002 and 4508-B-004: –54° to +100°C (–65° to +212°F) 4507-C and 4508-C: –74° to +250°C (–101° to +482°F)

Specifications – Miniature CCLD Accelerometer Type 4507

	Sensitivity	Sensitivity Tolerance	Measuring Range	Frequency Range, 10%	Phase Response, ± 5°	Built-in ID (TEDS)	Output Impedance	Bias Voltage	Start-up Time (± 10% of final bias)	Inherent Noise (broadband)/ Equivalent Vibration Level		Temperature Coefficient of Sensitivity	Sensing Element	Sealing	Humidity	Mounting Slots (pairs)
Units	mV/ms^{-2}	%	ms^{-2}	Hz	Hz		Ω	V	s	μV	μg	%/°C			%	
4507	10	±5	700	0.3 – 6 k	2 – 5k	No	<30	13 ± 1	5	<35	<350	0.09	PZ23	Hermetic	100	1
4507-001	1	±5	7000	0.1 – 6 k	0.5 – 5k	No	<30	13 ± 1	50	<8	<800	0.09	PZ23	Hermetic	100	1
4507-002	100	±10	70	0.4 – 6 k	2 – 5k	No	<30	13 ± 2	5	<150	<150	0.18	PZ27	Hermetic	100	1
4507-B	10	±5	700	0.3 – 6 k	2 – 5k	Yes	<30	13 ± 1	5	<35	<350	0.09	PZ23	Hermetic	100	1
4507-B-001	1	±5	7000	0.1 – 6 k	0.5 – 5k	Yes	<30	13 ± 1	50	<8	<800	0.09	PZ23	Hermetic	100	1
4507-B-002	100	±10	70	0.4 – 6 k	2 – 5k	Yes	<30	13 ± 2	5	<150	<150	0.18	PZ27	Hermetic	100	1
4507-B-003	10	±5	700	0.3 – 6 k	2 – 5k	Yes	<30	13 ± 1	5	<35	<350	0.09	PZ23	Hermetic	100	None
4507-B-004	10	±5	700	0.3 – 6 k	2 – 5k	Yes	<30	13 ± 1	5	<35	<350	0.09	PZ23	Hermetic	100	3
4507-B-005	100	±10	70	0.4 – 6 k	2 – 5k	Yes	<30	13 ± 2	5	<150	<150	0.18	PZ27	Hermetic	100	3
4507-B-006	50	±5	140	0.2 – 6 k	1 – 5k	Yes	<30	13 ± 2	10	<80	<160	0.18	PZ27	Hermetic	100	3

Specifications – Miniature CCLD Accelerometer Type 4508

	Sensitivity	Sensitivity Tolerance	Measuring Range	Frequency Range, ± 10%	Phase Response, ± 5°	Built-in ID (TEDS)	Output Impedance	Bias Voltage	Start-up Time (±10% of final bias)	Inherent Noise (broadband)/ Equivalent Vibration Level		Temperature Coefficient of Sensitivity	Ambient Temperature Range	Sensing Element	Sealing	Humidity	Mounting Slots (pairs)
Units	mV/ms^{-2}	%	ms^{-2}	Hz	Hz		Ω	V	s	μV	μg	%/°C	°C			%	
4508	10	±5	700	0.3 – 8 k	2 – 5 k	No	<30	13 ± 1	5	<35	<350	0.06	–54 to 121	PZ23	Hermetic	100	1
4508-001	1	±5	7000	0.1 – 8 k	0.5 – 5 k	No	<30	13 ± 1	50	<8	<800	0.06	–54 to 121	PZ23	Hermetic	100	1
4508-002	100	±10	70	0.4 – 8 k	2 – 5 k	No	<30	13 ± 2	5	<150	<150	0.12	–54 to 100	PZ27	Hermetic	100	1
4508-B	10	±5	700	0.3 – 8 k	2 – 5 k	Yes	<30	13 ± 1	5	<35	<350	0.06	–54 to 121	PZ23	Hermetic	100	1
4508-B-001	1	±5	7000	0.1 – 8 k	0.5 – 5 k	Yes	<30	13 ± 1	50	<8	<800	0.06	–54 to 121	PZ23	Hermetic	100	1
4508-B-002	100	±10	70	0.4 – 8 k	2 – 5 k	Yes	<30	13 ± 2	5	<150	<150	0.12	–54 to 100	PZ27	Hermetic	100	1
4508-B-003	10	±5	700	0.3 – 8 k	2 – 5 k	Yes	<30	13 ± 1	5	<35	<350	0.06	–54 to 121	PZ23	Hermetic	100	None
4508-B-004	50	±5	140	0.2 – 8 k	1 – 5 k	Yes	<30	13 ± 2	10	<80	<160	0.12	–54 to 100	PZ27	Hermetic	100	1

Specifications – Miniature Charge Accelerometer Types 4507 C, 4508 C

	Charge Sensitivity	Sensitivity Tolerance	Measuring Range	Frequency Range, +10%[a]	Mounted Resonance Frequency	Transverse Sensitivity	Transverse Resonance	Min. Leakage Resistance at 20°C	Capacitance	Sensing Element	Base Strain Sensitivity (In base plane at 250 με)	Temperature Transient Sensitivity (3 Hz LLF, 20dB/decade)	Magnetic Sensitivity (50 Hz – 0.03 T)	Ambient Temperature Range	Max. Operational Shock (±Peak)	Max. Operational Continuous sinusoidal acceleration (Peak)	Sealing	Humidity	Mounting Slots (pairs)	Weight
Units	pC/ms^{-2}	%		Hz	kHz	%	kHz	GΩ	pF		$ms^{-2}/με$	$ms^{-2}/°C$	ms^{-2}/T	°C	kms^{-2}	kms^{-2}		%		grams
4507-C	0.45	±15	2 mms^{-2} to 20 kms^{-2}	0.1 to 6 k	18	<5	18	20	360	PZ23	0.005	0.2	1	–74 to 250	50	20	Welded	90	3	4.5
4508-C	0.45	±15	2 mms^{-2} to 20 kms^{-2}	0.1 to 8 k	25	<5	18	20	360	PZ23	0.005	0.6	1	–74 to 250	50	20	Welded	90	1	4.5

[a] Using NEXUS Conditioning Amplifier Type 2692

Common Specifications – Types 4507 and 4508 (CCLD only)

DYNAMIC
Mounted Resonance Frequency:
4507: 18 kHz
4508: 25 kHz
Transverse Sensitivity: <5% of sensitivity

ELECTRICAL
Constant Current Supply: 2 to 20 mA
Supply Voltage (unloaded):
+24 to +30 V DC (for full specification range)
Min. +18 V DC (reduced measuring range)
Polarity: Positive (for an acceleration in the direction of the engraved arrows)

ENVIRONMENTAL
Max. Non-destructive Shock (±Peak): 50 kms^{-2}; 5000 g
Temp. Transient Sensitivity (3 Hz lower limiting frequency):
4507: 0.2 ms^{-2}/°C
4508: 0.3 ms^{-2}/°C
Base Strain Sensitivity (mounted on adhesive tape 0.09 mm thick): 0.005 ms^{-2}/με

Magnetic Sensitivity: 3 ms^{-2}/T
Temperature Range:
4507, 4507-001, 4507-B, 4507-B-001, 4507-B-003, 4507-B-004, 4508, 4508-001, 4508-B, 4508-B-001 and 4508-B-003:
–54° to +121°C (–65° to +250°F)
4507-002, 4507-B-002, 4507-B-005, 4507-B-006, 4508-002, 4508-B-002 and 4508-B-004:
–54° to +100°C (–65° to +212°F)

PHYSICAL
Case Material: Titanium
Sensing Element: Piezoelectric
Design Configuration: ThetaShear
Connector: 10 – 32 UNF coaxial
Dimensions (H×W×L): 10 × 10 × 10 mm (0.4″), excl. connector
Weight: 4.8 gram (0.17 oz.)

Note: All values are typical at 25°C (77°F), unless measurement uncertainty is specified. All uncertainty values are specified at 2σ (i.e., expanded uncertainty using a coverage factor of 2)

Ordering Information

Types 4507/4508: Miniature CCLD Accelerometers
Types 4507-B/4508-B :Miniature CCLD TEDS Accelerometers
Types 4507-C/4508-C: Miniature Charge Accelerometers
Include the following accessories:
- Carrying Box
- Individual Calibration Chart
- One Mounting Clip (not 4507-B-003 or 4508-B-003)

OPTIONAL ACCESSORIES

AO-0531	Cable AC 0208 with 10–32 UNF to BNC connectors, 5 m (16.4 ft) –5 to 70°C (23 to 158 °F)
AO-0463	Cable AC 0208 with 10–32 UNF connectors, 1.2 m (4 ft) –5 to 70°C (23 to 158°F)
AO-0038	Super low-noise Teflon cable, AC 0005 with 10–32 UNF connectors, 1.2 m (4 ft), 250°C (482°F)
AO-0122	Reinforced super low-noise cable, AC 0200 with 10–32 UNF connectors, 3 m (10 ft), 250°C (482°F)
AO-0406	Double-screened low-noise cable AC 0104 with 10–32 UNF connectors, 5 m (16 ft), 250 °C (482°F). Includes adaptor JP 0145
AO-1419	Low-noise cable AC 0066 with 10–32 UNF connectors, 1.2 m (4 ft), 250°C (482°F)
AO-1382	Low-noise, double-screened Teflon cable AC 0104 with 10–32 UNF connectors, 1.2 m (4 ft), 200°C (392°F)

Cables AO-0038, AO-0122, AO-0406 and AO-1382 are recommended for use with Miniature Charge Accelerometers Types 4507-C and 4508-C

Different lengths of the cables are available

UA-1243	3×30 pieces of 1/2/3 markers for Cable AC-0104
UA-1244	As above, for Cable AC-0005 and AC-0208
YJ-0216	Mounting Wax
QS-0007	Cyanoacrylate Adhesive
WB-1372	DeltaTron Power Supply
UA-1407	Set of 100 Mounting Clips
DV-0459	Calibration Clip
UA-1418	Set of 25 dummy accelerometers for mass loading
UA-1478	Set of 100 swivel bases
UA-1475	Set of 100 mounting clips with thick base
UA-1564	Set of 5 high-temperature mounting clips
JP-0192	Solder connector adaptor

CALIBRATION SERVICES

4507-CFF	Re-calibration (sensitivity)
4508-CFF	Re-calibration (sensitivity)

BP 1841 – 15 2012-12

HEADQUARTERS: Brüel & Kjær Sound & Vibration Measurement A/S · DK-2850 Nærum · Denmark
Telephone: +45 7741 2000 · Fax: +45 4580 1405 · www.bksv.com · info@bksv.com

Local representatives and service organisations worldwide

Brüel & Kjær

B.3 B&K CCLD Signal Conditioner Type 1704-A-001

PRODUCT DATA

Battery-powered CCLD Signal Conditioners: Type 1704-A-001, one-channel, and Type 1704-A-002, two-channel

Type 1704-A is a range of CCLD conditioner/amplifiers designed for field and lab use. It includes features like a built-in, rechargeable battery optimised for in situ measurements.

They provide signal conditioning, amplification and gain for CCLD compatible:

- *Accelerometers*
- *Charge Accelerometers (using Type 2647 Inline charge amplifier)*
- *Microphones*
- *Tacho Probes*

Uses and Features

- Provides power for microphones, accelerometers and other CCLD-compatible transducers
- Industry standard CCLD power is compatible with wide range of DeltaTron® and ICP® sensors
- Built-in Li-Ion battery and charger – ready to measure when you are
- Powered and charged from PC's USB connector (with optional cable): no need for an extra mains adaptor
- Wide range of gains (×1, ×10 and ×100) amplify signal before A/D to improve noise floor
- Selectable acoustic bandpass and A-weighting (type 0) filters remove unwanted frequencies
- Switches to quickly change settings and LEDs for fast verification of configuration
- Both 2 × BNC and 3.5 mm stereo output connectors provide options to connect to A/D converters or sound cards

Description

Fig. 1 *Connectors, switches and LEDs on Type 1704-A-002:*
1) CCLD power for accelerometers, microphones and tacho probes;
2) LED overload and CCLD cable fault detection;
3) BNC outputs for connection to instrumentation;
4) 3.5 mm stereo socket for soundcard connection;
5) CCLD On/Off – can be used without CCLD power as voltage amplifier and filter;
6) Gain and filters to improve dynamic range;
7) 13 hours of battery life;
8) USB Micro-B for powering and charging

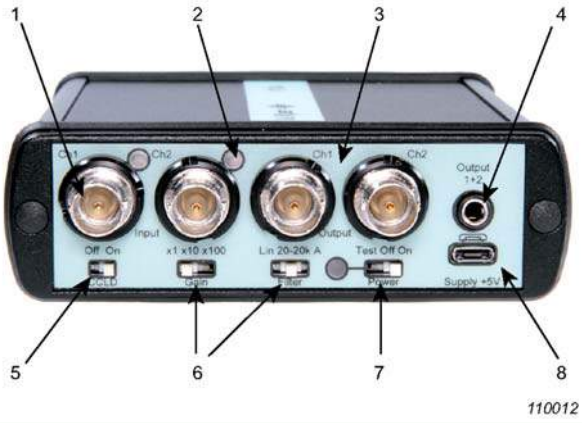

The Type 1704-A range of conditioners provides CCLD (Constant Current Line Drive) power for CCLD transducers such as microphones, accelerometers, and tachometer probes. Type 1704-A-001 is a one-channel version while Type 1702-A-002 is a two-channel version.

CCLD power is a de facto standard in the dynamic test and measurement world and has many manufacturer specific names such as DeltaTron®, ICP® (Integrated Circuit Piezoelectric), IEPE (Integrate Electronics Piezoelectric) and ISOTRON®. Type 1704 CCLD signal conditioners are compatible with transducers using any of the above trade names.

CCLD conditioning has advantages because it allows the transducer power to be delivered using the same coaxial cable that the transducer uses to return the measurement signal. This reduces cabling costs and improves noise immunity compared to multi-conductor cables.

Connectors

The Type 1704-A range of conditioners have all their connectors, switches and status LEDs located on the front of the unit (see Fig. 1).

Flexible Powering Options

Type 1704-A uses a Micro-B USB connector for power and charging the built-in rechargeable battery. Power comes from either the provided mains adaptor or from a powered USB port of a computer using the optional USB cable. A quick glance at the front of Type 1704-A confirms status and settings when making measurements in the field.

The built-in rechargeable battery is not only more convenient than replacing non-rechargeable batteries but also makes for a lower cost of ownership. The rechargeable battery has at least 500 cycles, each lasting for 15 hours (Type 1704-A-001) or 13 hours (Type 1704-A-002)

Gain and Filtering

Type 1704 includes analogue gain and filtering. Available gains settings include ×1 (0 dB), ×10 (+20 dB) and ×100 (+40 dB). Adding gain before the analogue to digital conversion can improve the system's noise floor. Likewise, the selectable acoustic band-pass filter can remove unwanted frequencies before the analogue to digital conversion. An A-weighting type 0 filter is also selectable.

Accessories

Fig. 2
Type 1704-A includes ZG-0863 for powering and charging from the mains

Fig. 3
Optional accessories include Soft Carrying Case KE-0463 and Cable AO-1494 to power and charge direct from a PC's USB connector

Brüel & Kjær's Family of CCLD DeltaTron Signal Conditioners

Type 1704-A is part of a larger family of CCLD DeltaTron signal conditioners. From small, battery- or USB-powered units to large, computer-controlled systems, Brüel & Kjær has a unit to fit your needs.

Table 1 *Features of Brüel & Kjær's Family of CCLD DeltaTron Signal Conditioners*

	1704-A	1704-C-102	WB-1453	2693 DeltaTron NEXUS	2694-A
Mains (AC) Power	✓	✓	–	✓	✓
USB Power	✓	✓	–	–	–
Battery Power	✓	–	✓	Optional	–
Number Channels per Unit	1 or 2	2	3	1 – 4	16
Manual Control	✓	✓	N/A	✓	–
Computer Control	–	–	–	✓	✓
Read Transducer's Electronic Datasheet (TEDS)	–	–	–	✓	✓
Uni (Fine) Gain Adjustment	–	–	–	✓	–
Multiplexer Output	–	–	–	–	✓
Maximum Number Channels from one PC	–	–	–	99 per COM or USB port	256 per COM or USB port
Maximum Frequency (kHz at filters –5% point)	55	55	25	100 (–10%)	50 (–10%)
Minimum Frequency (Hz at filters –5% point)	2.2	2.2	0.1	0.1 (–10%)	0.1 (–10%)
Maximum Gain	× 100 (40 dB)	× 100 (40 dB)	× 1 (0 dB)	× 10000 (80 dB)	× 100 (40 dB)
Minimum Gain	× 1 (0 dB)	× 1 (0 dB)	× 1 (0 dB)	× 0.1 (–20 dB)	× 0.316 (–10 dB)
A-weighting (type 0)	✓	–	–	✓	Optional
Single and Double Integration Filters	–	–	–	Optional	Optional
Constant Current Supply (mA)	3 – 4.1	3 – 4.1	3	4 or 10	6

Compliance with Standards

CE C-Tick	CE-mark indicates compliance with EMC Directive and Low Voltage Directive C-Tick mark indicates compliance with the EMC requirements of Australia and New Zealand
Safety	EN/IEC 61010–1 and ANSI/UL 61010–1: Safety requirements for electrical equipment for measurement, control and laboratory use
EMC Emission	EN/IEC 61000–6–3: Generic emission standard for residential, commercial, and light-industrial environments CISPR 22: Radio disturbance characteristics of information technology equipment. Class B Limits FCC Rules, Part 15: Complies with the limits for a Class B digital device
EMC Immunity	EN/IEC 61000–6–1: Generic standards – Immunity for residential, commercial and light industrial environments EN/IEC 61000–6–2: Generic standards – Immunity for industrial environments EN/IEC 61326: Electrical equipment for measurement, control and laboratory use – EMC requirements **Note:** The above is only guaranteed using accessories listed in this Product Data
Temperature	IEC 60068–2–1 & IEC 60068–2–2: Environmental Testing. Cold and Dry Heat Ambient Operating Temperature: –10 to +50°C (14 to 122°F) Storage Temperature: –25 to +70°C (–13 to +158°F)
Humidity	IEC 60068–2–78: Damp Heat: 93% RH (non-condensing at 40°C (104°F))
Mechanical	Non-operating: IEC 60068–2–6: Vibration: 0.3mm, 20ms^{-2}, 10 – 500Hz IEC 60068–2–27: Shock: 1000ms^{-2} IEC 60068–2–29: Bump: 1000 bumps at: 400ms^{-2}
Enclosure	IEC 60529: Protection provided by enclosures: IP 20
RoHS	RoHS compliant

Specifications – Type 1704-A

		Gain ×1 (0 dB)	Gain ×10 (+20 dB)	Gain ×100 (+40 dB)
Input Connector	Channel 1 and 2*	BNC		
Output Connector	Channel 1 and 2*	BNC or 3.5 mm stereo plug		
Amplifier Gain		0 dB (×1), 20 dB (×10); 40 dB (×100)		
Gain Tolerance		± 1%		
Excitation Voltage		22 V ± 2 V (typ. 21 V)		
Excitation Current		3 to 4.1 mA (nom. 3.55 mA)		
Maximum Input Voltage (peak)		± 10 V		
Input Protection		35 V_p (non-destructive)		
Maximum Output Voltage (peak)		± 10 V		
Output Impedance		50 Ω		
Cable Fault Voltage Levels		2.5 V and 18 V		
Total Harmonic Distortion		< 90 dB (0.003%) @ 1 kHz 1 V_{rms}		
DC Offset		< 5 mV		
Frequency Range (–5%)		2.2 Hz to 55 kHz	2.2 Hz to 55 kHz	2.2 Hz to 55 kHz
Frequency Range (–3 dB)		0.8 Hz to 100kHz	0.8 Hz to 100 kHz	0.8 Hz to 75 kHz
Filters		Linear (none), Acoustic Bandpass, A-weighting (type 0)		
Acoustic Bandpass Filters	60 dB/decade	22.4 Hz to 22.4 kHz (–3 dB)		
Spectral Output Noise Lin. (μV/√Hz)	(1 Hz)	< 0.2	< 1.5	< 15
	(10 Hz)	< 0.05	< 0.3	< 3
	(100 Hz)	< 0.025	< 0.15	< 0.8
	(1 kHz)	< 0.025	< 0.15	< 0.8
	(10 kHz)	< 0.025	< 0.15	< 0.8
	(100 kHz)	< 0.025	< 0.15	< 0.8
Broadband Electrical Output Noise, Lin. (μV_{rms})	(1 Hz to 10 kHz)	2	12	70
	(1 Hz to 100 kHz)	11	75	210 (50 kHz)
Broadband Output Noise (μV_{rms})	in Acoustic Bandpass (Lin.)	2.5	18	100
	with internal Acoustic Bandpass filter	13	22	100
	post-processed A-weighting	1.75	13	75
	with internal A-weighting filter	14	20	75
Crosstalk (dB)*	CCLD Powered Enabled, Linear filter	–115	–105	–91
	Direct (CCLD Off), Linear filter	–125	–105	–100
Battery Life (hours)	Type 1704-A-001 (1704-A-002)	15 (13)		
	after low battery level	1		
Number of Battery Charging Cycles		500		
Time to Charge (hours)	Mains (AC) or USB Can charge while using	6 (4 if charge only)		
Size		125 × 110 × 35 mm (4.9 × 4.3 × 1.4″)		
Weight		326 g (11.5 oz.)		
Temperature Range (operating)		–10 to +50°C (14 to 122°F)		
Temperature Range (charging)		0 to 50°C (32 to 122°F)		

* Type 1704-A-002 only

POWER SUPPLY

Internal Battery: Built-in Li-ion battery typically providing 15 hours (Type 1704-A-001) or 13 hours (Type 1704-A-002) of continuous use. Charging time is approximately 6 hours

Mains Supply: Supported by Power Supply ZG-0863 (included). 90 – 264 V AC, 40 – 65 Hz. Includes adaptors for US, UK, Europe and Australia/New Zealand

Ordering Information

Type 1704-A-001 1-channel Battery-powered CCLD Signal Conditioner and Type 1704-A-002 2-channel Battery-powered CCLD Signal Conditioner include the following accessories

- ZG-0863 Power Supply, 90 – 264 V AC, 1.5 m Cable with micro-USB-B

OPTIONAL ACCESSORIES

AO-1494 Cable, USB-A (M) to USB-B (M), 1.8 m
KE-0463 Soft Carrying Case
Type 2647-A/B/C/D Charge to CCLD Converters for measuring with charge accelerometers

TRADEMARKS

DeltaTron is a registered trademark of Brüel & Kjær Sound & Vibration Measurement A/S · ICP is a registered trademark of PCB Piezotronics Inc. · ISOTRON is a registered trademarks of ENDEVCO Corporation

BP 2387 – 12 2012-07

HEADQUARTERS: Brüel & Kjær Sound & Vibration Measurement A/S · DK-2850 Nærum · Denmark
Telephone: +45 7741 2000 · Fax: +45 4580 1405 · www.bksv.com · info@bksv.com

Local representatives and service organisations worldwide

Brüel & Kjær

B.4 LD2300-10 Laser Triangulation Sensor

MICRO-EPSILON

More Precision

optoNCDT // Laser displacement sensors (triangulation)

- Eight models with measuring ranges from 2mm to 300mm
- Adjustable measuring rate up to 49.14kHz
- INTERFACE: Ethernet / EtherCAT / RS422 Analog ouput via C-Box
- A-RTSC: Advanced Real Time Surface Compensation
- Certified: Calibration certificate included
- Measurement of diffuse and specular surfaces
- Thickness measurement of transparent materials
- Configuration via web interface

The optoNCDT 2300 is the new, high performance version of Micro-Epsilon laser triangulation sensors and offers an adjustable measuring rate of up to 49.14kHz. The entire electronics is already integrated in a compact sensor housing which is a worldwide unique feature of this sensor class. The new A-RTSC (Advanced Real Time Surface Compensation) feature is a development of the company's already proven RTSC technology and, with its improved dynamic range, enables a more precise real time surface compensation during the measurement process. The threshold value of the compensation range can be easily configured via the software.

Data output is via Ethernet, RS422 or EtherCAT. The C-Box enables analog signal output. All sensor configurations are carried out using a user-friendly web interface. The optoNCDT 2300 is particularly used for high speed applications such as the monitoring of vibrations or measurements on challenging surfaces.

optoNCDT 2300-2 ... 2300-100
Diffuse reflection

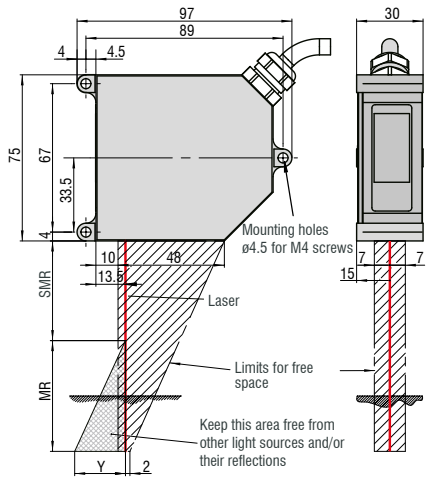

MR	SMR	Y
2	24	1.5
5	24	3.5
10	30	6.5
20	40	10.0
50	45	23.0
100	70	33.5

optoNCDT 2300-2 ... 2300-20
Direct reflection

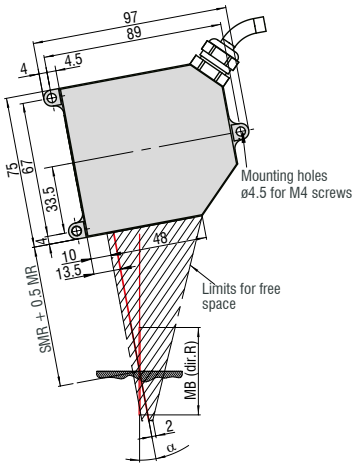

MR	SMR + 0.5 MR	α
2	25	20.5 °
5	26.5	20 °
10	35	17.5 °
20	50	13.8 °

optoNCDT 2300-200 /2300-300

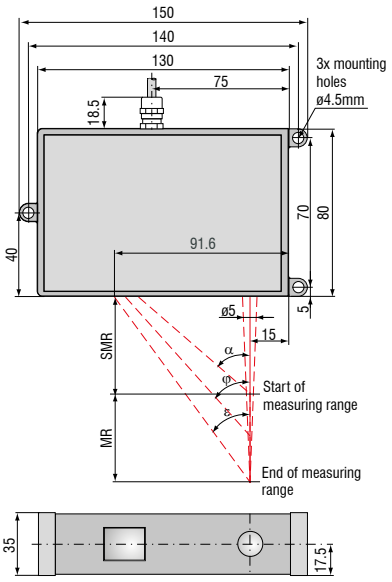

MR	α	φ	ε	A	B
200	25.1 °	16.7 °	13.1 °	91.6	76
300	18.3 °	12.2 °	9.6 °	99.4	81

Appendix C

Process flows

First set of beams developed.

Step	Process	Machine	Comments	Parameters
1.	**Cantilever and proof mass definition**			
1.1	New wafers			Double side polished 4” Thickness: 380 um±5 um
1.2	RCA cleaning	RCA (4.014)		
1.3	Phosphorus Predep.	Furnace A4 Phosphorus Predep. (5.001)		Recipe: POCL1000 Temp: 1000C Time: 30 min + 20 min anneal
1.4	Wet oxidation	Furnace A3	No RCA needed if they are directly from the A4 furnace.	Target thickness: 1100 nm ±10nm Recipe: wet1100 Temp: 1100C Time: 2h 50m
1.5	SiN deposition	Furnace E3 LPCVD Nitride 6“		Target thickness: 180 nm±10nm Recipe: 2NITDAN Time: 60 min
1.6	Oxide deposition	TEOS		Target thickness: 380±20nm Recipe: TEOSPNE Time: 30 min
1.7	HMDS	HMDS oven (1.006)		Recipe: 4
1.8	Resist spin	SSE Spinner (1.028)	Resist on both sides, but only bake it the first time.	Resist: AZ5214e Thickness: 1.5um Recipe: 1.5 4inch Temperature: 90C time: 60 sec Softbake on hotplate
1.9	UV- exposure	KS Aligner MA6		Align to flat. Contact: Hard Exposure: 5 sec Mask: Mass (dark field)
1.10	Development	Developer 1 (1.007) or Developer 2 (1.008)		Developer: AZ 351 B Time: 70 sec Rinse in DI water: 5 min
1.11	BHF etch	BHF bath (3.007)	Etching of the oxide layer. Pattern transfer to the oxide.	Time: set time according to thickness measured after TEOS (etching Rate: ~70nm/ min)

				Rinse 5 min in DI water
1.12	Acetone Resist strip	Rough strip (1.012) Fine strip (1.013)		Rough time: 2 min Fine time: 3 min Rinse in DI water: 5 min
1.13	Nitride patterning	Phosphoric Acid etch (Wet Nitride etch)	Etching of the nitride layer. Pattern transfer to the nitride. Inspection with the optical microscope.	Temperature: 180C Etching rate: about 85Å/min (check it) Time: set time according to thickness of the nitride layer deposited
1.14	HMDS	HMDS oven (1.006)		
1.15	Resist spin	SSE Spinner (1.028)	Resist on both sides, but only bake it the first time. To protect the top oxide layer in the BHF bath.	Resist: AZ5214e Thickness: 1.5um Recipe: 1.5 4inch Temperature: 90C Time: 60 sec Softbake on hotplate
1.16	UV- exposure	KS Aligner MA6		Align to flat. Contact: Hard Exposure: 5 sec Mask: Mass
1.17	Development	Developer 1 (1.007) or Developer 2 (1.008)		Developer: AZ 351 B Time: 70 sec Rinse in DI water: 5 min
1.18	BHF etch	BHF bath	Open up for silicon by etching the oxide layer. Check that the KOH openings are hydrophobic.	Time: set time according to thickness measured after wet oxidation (etching rate: ~70nm/min) Rinse 5 min in DI water
1.19	Acetone Resist strip	Rough strip (1.012) Fine strip (1.013)		Rough time: 2 min Fine time: 3 min Rinse in DI water: 5 min
1.20	KOH etch	KOH 2 or 3	Cantilever definition. Careful control of etch rate necessary to achieve desired cantilever thickness.	Temperature: 86C Time: 5-6 hours Rinse in DI water
1.21	Oxide removal	BHF bath	Removes protective oxide layer on both sides.	Time: set time according to thickness measured after wet oxidation Rinse 5 min in DI water

1.22	Oxide removal	Phosphoric Acid etch	Removes nitride on both sides	Temperature: 180C Etching rate: about 85Å/min Time: set time according to thickness measured in step 1.5
1.23	BHF etch	BHF bath	Removes the oxide layer left beneath the previous nitride layer.	Time: set time according to thickness measured in step 1.4
1.24	HMDS	HMDS oven (1.006)		
1.25	Resist spin	Manual Labspin (1.051)		Resist: AZ5214e Time: 60 sec Thickness: 5 um
1.26	UV- exposure	KS Aligner (1.003)		Align to flat. Contact: Hard Exposure: 15 sec Mask: Mass
1.27	Development	Developer 1 (1.007) or Developer 2 (1.008)		Developer: AZ351B Time: 70 sec Rinse in DI water: 3min
1.28	Deep etch	ASE (3.002)	Glue wafer to a carrier wafer with crystal bonding.	Recipe: Deepetch Time: 10 min
1.29	Unbond wafer	Hotplate	Unbond wafr from carrier	Temp: >90C
1.30	Acetone Resist strip	Rough strip (1.012) Fine strip (1.013)	NO ultrasounds	Rough time: 3 min Fine time: 2 min Rinse in DI water: 5 min

Step	Process	Machine	Comments	Parameters
2.	**Piezoelectric layer deposition:**			
2.1	BHF	BHF clean	Removes accumulated surface oxide for better contact.	Time: 30 sec Rinse in DI water: 5 min
2.2	Ti deposition.	PVD Co-sputter (2.013)	Bottom contact.	E-beam Thickness: 50 nm Rate: 0.8 Å/sec
2.3	Mo deposition	PVD Co-sputter (2.013)	Bottom electrode for piezoelectric layer.	E-beam Thickness: 50 nm Rate: 0.3 Å/sec
2.4	AlN deposition	PVD Co-sputter	Piezoelectric layer.	RF-Sputter

		(2.013)		Power: 1000 W Sputter pressure: 4E-3 N_2-gas flow: 70% Ar-gas flow: 30% Thickness: 400 nm Time: 720 min = 12 hours
2.5	Mo deposition	PVD Co-sputter (2.013)	Top electrode for piezoelectric layer.	E-beam Thickness: 50 nm Rate: 0.3 Å/sec

Step	**Process**	**Machine**	**Comments**	**Parameters**
3.	**Contacts:**			
3.1	Al deposition	Wordentec (2.013)	Front side AND back side	E-beam Thickness: 400 nm Rate: 10 Å/sec
3.2	Mo deposition	PVD co-sputter (2.013)	Front side, with shadow mask	E-beam Thickness: 50 nm Rate: 0.3 Å/sec Mask: “Middle”
3.3	Mo deposition	PVD co-sputer (2.013)	Back side, no mask	E-beam Thickness: 50 nm Rate: 0.3 Å/sec
3.4	Al-etch	Al-etch (3.013)	Mo works as mask and etch stop.	Time: 1 min Rinse 5 min in DI water
3.5	Metal etch	ICP Metal Etch (3.028)	Both sides. Removes Mo, while Al and AlN works as etch stop	Time: 1 min Recipe: Mo2

Step	**Process**	**Machine**	**Comments**	**Parameters**
4.	**Dicing**			
4.1	Dicing	Saw (Disco 321) (7.006)	100 um should be left to break by hand.	Sawing depth: 400 um

Second set of beams developed.

Step	Process	Machine	Comments	Parameters
1.	**Cantilever and proof mass definition**			
1.1	New wafers			Double side polished 4” ON415 n-type Thickness: 500 um±15 um
1.2	RCA cleaning	RCA (4.014)		
1.3	Wet oxidation	Furnace A3	No RCA needed if they are directly from the A4 furnace.	Target thickness: 3000 nm ±10nm Recipe: wet1100 Temp: 1100C
1.4	HMDS	HMDS oven (1.006)		Recipe: 4
1.5	Resist spin	SSE Spinner (1.028)	Resist on both sides, but only bake it the first time.	Resist: AZ5214e Thickness: 1.5um Recipe: 1.5 4inch Temperature: 90C time: 60 sec Softbake on hotplate
1.6	UV- exposure	KS Aligner MA6		Align to flat. Contact: Hard Exposure: 5 sec Mask: Mass (dark field)
1.7	Development	Developer 1 (1.007) or Developer 2 (1.008)		Developer: AZ 351 B Time: 70 sec Rinse in DI water: 5 min
1.8	Oxide etch	AOE	Alternate between two wafers 2-3 min	Recipe: SiO_res Time: 12-15 min
1.9	Acetone Resist strip	Rough strip (1.012) Fine strip (1.013)		Rough time: 2 min Fine time: 3 min Rinse in DI water: 5 min
1.10	KOH etch	KOH 2 or 3	Cantilever definition. Careful control of etch rate necessary to achieve desired cantilever thickness.	Temperature: 86C Time: 5-6 hours Rinse in DI water
1.11	Oxide removal	BHF bath	Removes protective oxide layer on both sides.	Time: set time according to thickness measured. (etching rate: ~70nm/min) Rinse 5 min in DI water
1.12	Oxide growth to round the corners	Furnace A3		Temp: 1100C Thickness: 1100 nm

1.13	Oxide removal	BHF bath	Removes the oxide layer.	Time: set time according to thickness measured. (etching rate: ~70nm/min) Rinse 5 min in DI water

Step	Process	Machine	Comments	Parameters
2.	**Piezoelectric and metal layers deposition**			
2.1	Wafers sent to PIEMACS Sarl, Switzerland.		Stack deposition of all the layers without venting chamber.	Thickness layers: Ti 10nm Pt 100nm AlN 400nm Pt 50nm

Step	Process	Machine	Comments	Parameters
3.	**Piezoelectric and metal layers definition**			
3.1	HMDS	HMDS oven (1.006)		
3.2	Resist spin	Labspin 02		Resist: AZ 4562 Thickness: 10 um Time: 60s Bake 3 min at 90 C
3.3	UV- exposure	Aligner MA6-2		Contact: Soft Exposure: 64 s Mask: TopElectrode_2017
3.4	Development	TMAH Manual developer		Developer: TMAH Time: 4 min (4x60)
3.5	Stack etching	Aqua Regia bath		
3.6	Resist removal	Lift off bath	NO ultrasounds	Rough time: 10 min
3.7	Repetition of steps 3.1-3.6			Repetition times: 3

Step	Process	Machine	Comments	Parameters
4.	**Beam release**			
4.1	HMDS	HMDS oven (1.006)		
4.2	Resist spin	Labspin 02		Resist: AZ 4562 Thickness: 6 um Time: 60s

Appendix D

Papers for publication

Finite Element Modelling of a Magneto Elastic Broadband Energy Harvester

Finite Element Modelling and Characterization of a Magneto Elastic Broadband Energy Harvester

L. R. Alcala-Jimenez *, A. Lei*, and E. V. Thomsen*
*Department of Micro and Nanotechnology, Technical University of Denmark, DK-2800 Kgs. Lyngby, Denmark

***Abstract*—This work presents a study on dimensional parameters that lead to efficiently harvesting energy from low frequency ambient vibrations. The system consists of a millimeter-scale beam and an external pair of magnets, which are aimed at obtaining a broadband frequency response. This study comprises static Finite Element Method (FEM) simulations for different distances between the magnets and the beam and between the magnets themselves. From the results, the tolerances of the relative positioning of the magnets and the beam are found. With the same purpose, impedance measurements are also performed for a range of distances.**

***Keywords*—** MEMS, Energy harvester, FEM, Piezelectric, Magnetoelastic, Ambient vibration.

1 Introduction

The demands on power sources limit the applicability of wireless microelectromechanical sensor systems for use in health care, wind power and automotive industries. Power source requirements for miniaturized systems are commonly long working life and physical dimensions in the millimeter-scale range. Conventional batteries imply continuous and sometimes expensive replacement cost. Furthermore, they impose a limit on system miniaturization. This means that a replacement for conventional batteries must be found. Vibration energy harvesters (VEH), which can harvest energy from ambient vibrations and convert it into electric power automatically, have become a promising alternative for a range of applications. There are three main approaches to harvest energy from vibrations, which involve the use of either electrostatic [1–3], electromagnetic [4], [5] or piezoelectric [6–10] principles. For all these cases, the main challenge is that the maximum system performance is achieved when the VEH resonant frequency matches the external vibration source. The key parameter for VEH's is the output power. This can be increased by optimizing the coupling factor, the design or the energy conversion. Most of the available published material present studies of systems under resonant excitation. However, most ambient vibrations present a frequency shift over time [11]. For that reason, either continuously tuning the resonant frequency or widening the frequency bandwidth of the VEHs has become of utmost importance before their practical implementation. Both methods can be divided into two types: active and passive.

The active mechanism consists in *continuously* having an external power supply that tunes in the harvesting frequency. Conversely, in the passive mode, power is required only *intermittently*. This frequency matching mechanism in either case can be performed both manually or in a self-tuning manner. Regardless of whether manual or self tuning takes place, or of whether a passive or active method is employed, a broad range of types of devices have been developed in order to finely tune the vibrational frequency. One possibility is changing the stiffness of the harvester by applying an axial pre-load [12], [13]. A passive method for harvesting a broad band of frequencies is by utilizing a system composed of devices where each of them harvests vibrations from different vibrational frequencies [14], and devices where non-linear effects are exploited [15–18]. Due to dimensional constraints, the latter method is more suitable for small systems. The non-linear method can be classified into three types, hardening effect, softening effect and bistable behavior, where the hardening and softening effect have both been shown to increase the bandwidth of the VEH's in different frequency ranges each. The hardening effect increases the bandwidth towards higher vibrational frequencies [19], whereas the softening effect widens the bandwidth towards lower frequencies [20], which is the region where most ambient vibrations extend over. Another advantage of the softening effect approach is that it maintains the robustness of the cantilevers, whereas the common procedure to reduce the harvested frequencies, by increasing the aspect ratio between the length and thickness of the cantilever, makes the cantilever even more fragile. This softening effect, nonetheless, is not always achieved and bistable behavior can be also observed. Bistable behavior has been reported to lead to larger outputs than their linear counterpart at sufficiently high enough vibrational accelerations, however, if the acceleration does not exceed a specific threshold, given by each particular system, the power output will be lower than in the linear case [21]. This is because under bistable behavior, the cantilever's tip can present two different types of oscillations, intrawell and interwell. In the intrawell type, the tip oscillates around one of the magnets, leading to small amplitude deflections, which translates to a low output power. In the interwell oscillations the tip swaps from one magnet to the other, which leads to larger deflections and consequently to larger output power. It has been recognized that there are many difficulties in maintaining the high-energy interwell motion state in broadband energy harvesters (BEHs) [22].

Piezoelectric-based VEHs have attracted much attention because it is feasible to produce them in millimeter-scale whilst having large power densities [23], [24]. They typically consist

of a cantilever structure with piezoelectric layers on top. For such a device, the non-linear effect can be accomplished by externally implementing a magnetic set-up and adding some ferromagnetic material to the cantilever's tip, as seen in Fig. 1. Commonly, the external magnetic set-up consists of either one or a pair of magnets. It has previously been demonstrated that the latter leads to increased generated power when compared to the former set-up [25]. For this reason, the two-magnet configuration, shown in Fig. 1, will be studied in this work. A similar system has been previously studied [26]. It consisted of a beam of about $11\,\mathrm{cm}$ large placed vertically and two cylindrical magnets, where the magnetic field was found by computing methods and was used to approximate the magnetic forces acting on the beam. However, the method presented in that study does not apply for smaller system dimensions where small square magnets are used.

A numerical study of a non-linear oscillator for broadband energy harvesting was developed [27]. Nonetheless, the study does not consider any external magnetic setup, therefore lacking any dimensional analysis. On the other hand, it has been found that for a given set-up, like the one under study in this work, the parameters that determine whether the cantilever presents a softening effect or bi-stable behavior are the distance between the magnets and the cantilever's tip, *a*, and also the distance between the magnets themselves [28], *b*, where these dimensional parameters are illustrated in Fig. 1. As a consequence, it becomes of utmost importance to study the dimensional parameters that allow for a BEH that presents a softening effect.

The aim of this work is to examine the magnet's tolerances, i.e. parameters *a* and *b*, that lead to a softening effect. These parameters are found by studying the potential energy of the system and effective spring constants for different dimensional parameters with dimensions shown in Fig. 1 and Tab. I, from which it can be seen that no piezoelectric material is included. It has been previously shown that the piezoelectric material thickness required to develop VEH's is in the range between $400-800\,\mathrm{nm}$ for commonly used materials like AlN and ZnO [9], [10] . For materials like PZT this thickness is normally not larger than about $10\,\mu\mathrm{m}$ [24]. These thickness can be compared to the dimensions presented in Tab. I, from which it can be inferred that in the mechanical-domain study presented in this work, the piezoelectric material can be neglected. In order to obtain the energy landscapes, FEM studies are performed using COMSOL multi-physics 5.2 software [29], where the studies are performed under static conditions, saving therefore computational time. In addition to these constraints, since one of the requirements for powering wireless sensor systems, as described previously, is dimensions in the millimeter-scale range, the focus of this study is on small-size cantilevers with lateral dimensions no longer than $10\,\mathrm{mm}$.

To the end of studying the system in dynamic mode, the approach taken by different research groups is to implement the force responsible for the non-linear behaviour directly into the Duffing's equations of motion [21], [30], which reads as

$$\dot{z} = v \tag{1}$$

$$\ddot{z} = -\frac{k}{m}z - \frac{b}{m}\dot{z} + \frac{F_{\mathrm{mag}}}{m} + \frac{F_{\mathrm{in}}}{m}\sin(wt) \tag{2}$$

where z is the displacement of the beam in the vertical direction, v is the velocity, m is the effective mass, k the spring constant, F_{in} the input force, ω the angular frequency of the applied force on the cantilever, b the damping coefficient offered by the mechanical domain, F_{mag} the magnetic force and dotted variables represent a time derivative. The mechanical damping is given by $b = \sqrt{mk}/Q$, where Q is the quality factor. The expression most commonly used for non-linear forces is an odd function of the displacement variable [15], given by $F_{\mathrm{mag}} = \alpha z - \beta z^3$, where both α and β are positive real numbers which depend on the dimensional parameters a and b. This expression is valid for small amplitude beam deflections and a fifth order term can be added to take into account large deflections, this term is however normally not included. This leads to an expression for the total forces given by $F_{\mathrm{tot}} = (-k+\alpha)z - \beta z^3$. In this study, the magnetic forces are directly obtained from FEM simulation results, which are inserted into Eq. 2.

The article is organized as follows: First, the simulation methods are explained, where also relevant dimensions of the system are stated. Secondly, the experimental methods used for impedance characterization are presented, together with a fabrication process description. Thirdly, the simulation results are presented, followed by the experimental ones. Finally, the article ends with conclusions.

2 Simulation Methods

The system studied in this work is depicted in Fig. 1. It is a 2-dimensional model which consists of a silicon beam with a pair of iron foils attached on either side and two external neodymium magnets. Each external magnet can present two different magnetizations, north-south or south-north. Due to symmetry, two out of four cases are studied, which are the NN and NS configurations. Each script represents the pole of each magnet closest to the cantilever and each XY pair represents the pair of magnets in the setup, as an example the NS case is depicted in Fig. 1. This means that two sets of optimal parameters will be found, one for each case.

The materials used in the simulations are silicon for the cantilever structure with a length of $6.5\,\mathrm{mm}$, see Tab. I; neodymium for the external magnets, which are modeled as squares with a constant magnetization of $M = M_{\mathrm{mag}}$; and iron for the ferromagnetic foils, which are modeled as a magnetic soft material with a magnetic relative permeability of $\mu_r = 4000$ and do not present hysteresis.

2.1 Simulation procedure

FEM studies were performed using COMSOL multiphysiscs 5.2 combining the Solid Mechanics and the Magnetic Fields modules. Each simulation can be divided into three steps. Firstly, a uniformly distributed input force is applied on the whole cantilever's structure. Secondly, the new position of

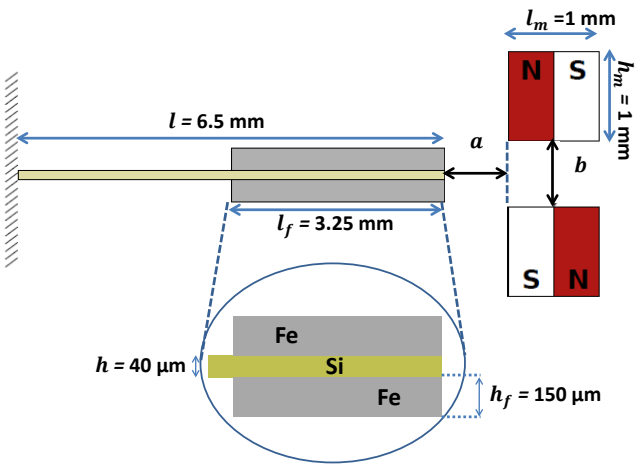

Fig. 1. Sideview of the vibrational system with a NS magnetic configuration. The silicon cantilever has integrated iron foils.

TABLE I
DIMENSIONAL AND MATERIAL PARAMETERS USED FOR THE SIMULATIONS.

Device parameters	Values
Beam length (l)	6.5 mm
Beam thickness (h)	40 μm
Beam width	6 mm
Foil length (l_f)	3.25 mm
Foil thickness (h_f)	150 μm
Foil width	6 mm
Magnet length (l_m)	1 mm
Magnet thickness (h_m)	1 mm
Magnet width	5.5 mm
Magnetization	750 kA/m
Si Young modulus	150 GPa
Foil relative permeability	$\mu_r = 4000$

the cantilever's center of mass due to this force is calculated. Thirdly, the magnetic field is introduced and its associated force on the iron foils is calculated. These steps are repeated for different input forces, from which the potential energy as a function of the beam's center of mass deflection can finally be extracted. From now on, instead of referring to the beam's center of mass deflection, since the center of mass is located at the beam's tip, only tip deflection will be used. The potential energy landscapes are obtained by performing a numerical integration of the resulting forces with respect to the tip displacement. From these steps it can be inferred that the simulations are performed only in the dimensional domain, excluding the time domain. The aim of not including the time domain is to reduce the computational time of the simulations. However, the time domain analysis is included later on in this study.

3 Experimental Methods

The energy harvesters are fabricated using standard silicon micro- and nanotechnologies on a (100) oriented Si substrate with a resistivity of 0.0015 Ωcm, which allows the silicon substrate to be used as a bottom electrode for the piezo

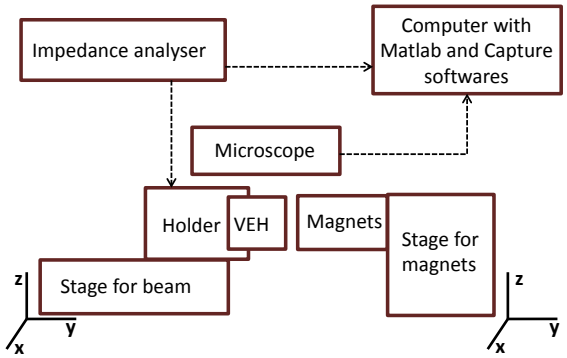

Fig. 2. Schematic of the set-up used for characterizing the electrical properties of our devices.

electric material. The process development is as follows. First, a 3000 nm thick oxide layer is grown on both sides of the wafer. Once this layer is defined by lithography and wet etching processes, the beam is made using KOH etching. After stripping the masking layer, a corner rounding of the anchoring point takes place, which consists of growing a 1000 nm wet oxide layer at 1100°C and right afterwards stripping it. After this, the piezo electric material and top and bottom electrodes are deposited by evaporation and sputtering of Pt/AlN/Pt/Ti with thicknesses of 50 nm/400 nm/120 nm /10 nm, respectively. A lithography process takes place to the end of etching through the top metal, the AlN layer and the bottom layers, which will define the electric contacts. Once this is done and the masking material is removed, another lithography process is performed to create the openings that will allow for the release of the beams. This is performed using a STS ICP Advanced Silicon Etcher system. After stripping the masking materials the energy harvesters are diced out using a Disco Automatic dicing saw, model DAD321. Finally, ferromagnetic foil is implemented on both sides of the beam by a pick-and-place operation.

Impedance measurements are performed using an Agilent E4990A Impedance Analyzer. The analyzer is connected to an Agilent 4294A impedance probe, Fig. 3, which is connected to a holder that serves as intermediate between it and the devices. The top electrode of the beam is in contact with a pogo-pin from the holder and a set of other pogo-pins secure it by pressing on the edge structure, Fig. 4a. To the end of having also contact to the bottom electrode, part of the backside frame structure of the device lies on a metal structure which is connected to the impedance probe. To analyze the non-linear response of the system, a pair of NdFeB magnets are included into the system, Fig. 4b. In order to have a precise control over the positioning of the magnets in the three spatial dimensions, a XYZ 300 TR stage model from Quater Research and Development is used, Fig. 3.

During frequency sweep analysis a varying sine voltage source with an amplitude of 50 mV is always used. The performed impedance measurements provide with both the impedance magnitude and phase values.

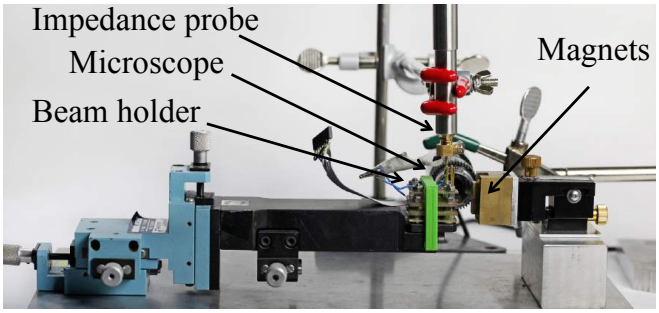

Fig. 3. Whole set-up used for the impedance measurements.

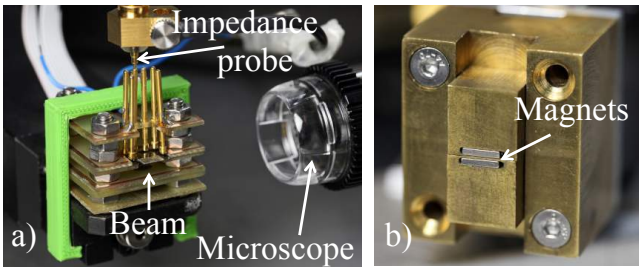

Fig. 4. Parts of the set-up used for the electrical characterization. a) Beam holder with the pogo-pins holding the beam still and one of them connected to the impedance set-up. Also, the microscope used for measuring distances. b) Holder for the magnets with the rectangular magnets located at the center.

When implementing the magnetic set-up, both the distance between magnets and beam, a, and the distance between the magnets themselves, b, are measured by using a Dino-Lite edge digital microscope model AZ7915MZTL together with DinoCapture 2.0 software [31]. Both distances a and b are changed in this study, where a is modified by using the stage of the magnets. Regarding distance b, in order to obtain specific separations between the magnets without them collapsing into each other, metal spacers of defined thickness are placed between them.

3.1 Equivalent circuit representation

To understand the electrical response of the system under study its equivalent circuit representation, shown in Fig. 5, is analyzed in this section. The piezoelectric layer is represented by a capacitor in the electrical side, whose associated impedance is referred to as Z_{el}. On the other hand, the impedances associated to the effective mass of the beam, the effective spring constant and the damping of the system are Z_{m}, Z_{s} and Z_{d}, respectively, all of these represent the mechanical domain. The mechanical, electrical and total impedance are mathematically represented by equations 3, 4 and 5, respectively

$$Z_{\mathrm{mec}} = \frac{1}{2\pi f C_{\mathrm{s}} j} + 2\pi f L_{\mathrm{m}} j + R_{\mathrm{d}} \tag{3}$$

$$Z_{\mathrm{el}} = \frac{1}{2\pi f C_{\mathrm{el}} j} \tag{4}$$

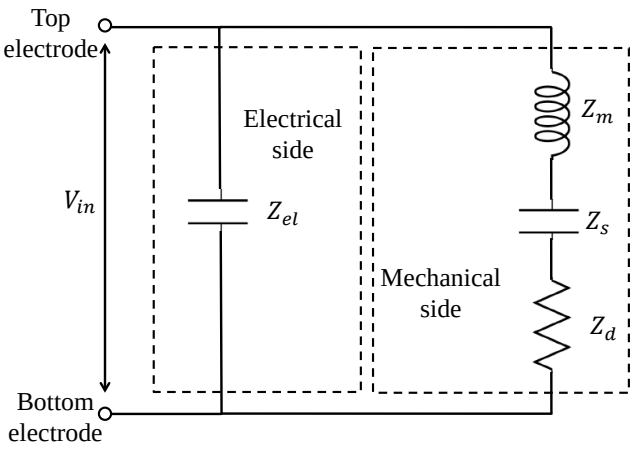

Fig. 5. Equivalent circuit representation of the system under study.

$$Z_{\mathrm{total}} = \frac{1}{2\pi f C_{\mathrm{el}} j + \left((2\pi f C_{\mathrm{s}} j)^{-1} + 2\pi f L_{\mathrm{m}} j + R_{\mathrm{d}}\right)^{-1}} \tag{5}$$

where f is the frequency, C the capacitance, L the inductance and R the resistance of the circuit elements.

The question that arises is regarding the behaviour that the total impedance presents if a hardening or softening effect takes place. By bearing in mind that the capacitance represented by C_{s} is inversely proportional to k_{eff}, its associated impedance will decrease if a softening effect takes place and increase if a hardening effect occurs. Using equation 5, the total impedance will increase under a softening effect due to the electrical contribution. Similarly, if a hardening effect occurs, the total impedance will decrease.

4 Simulation Results

Following the simulation procedure presented in Section 2.1, the total forces for a NS configuration are shown in Fig. 6. For this case, the set of input forces applied were in the range between $-0.075\,\mathrm{N}$ and $+0.075\,\mathrm{N}$. The associated magnetic forces were calculated for three different values of a: 200, 564 and $1000\,\mu\mathrm{m}$, and the total force for each case was obtained. The other dimensional parameter, b, is maintained constant at $b = 500\,\mu\mathrm{m}$. These dimensional parameters are in accordance to Fig. 1.

Fig. 7 shows the associated potential energy landscapes for the three cases just considered in Fig. 6 and the linear case, where no magnets are present. The green curve in Fig. 7 corresponds to the linear case, for which a spring constant $k_0 = 120.8\,\mathrm{N/m}$ is associated, this corresponds to a monostable behavior, i.e. only one stable solution is found. For the longest distance between magnets and cantilever tip, that is for $a = 1000\,\mu\mathrm{m}$, a monostable landscape is also found. The effective spring constant associated to this case is $k_{\mathrm{eff}} = 90.66\,\mathrm{N/m}$. This value can be compared to the case without magnets $120.8\,\mathrm{N/m}$, which means that the effect

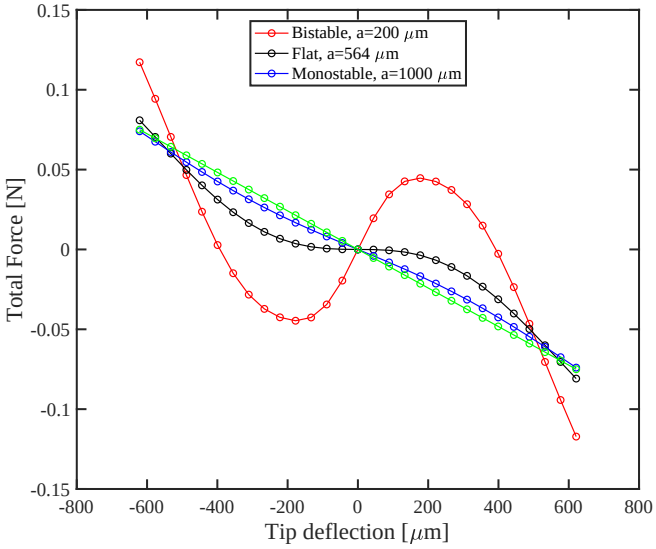

Fig. 6. Total force respect to tip deflection for monostable, bistable and flat potential cases. The NS configuration was considered and for all cases $b = 500\,\mu\text{m}$.

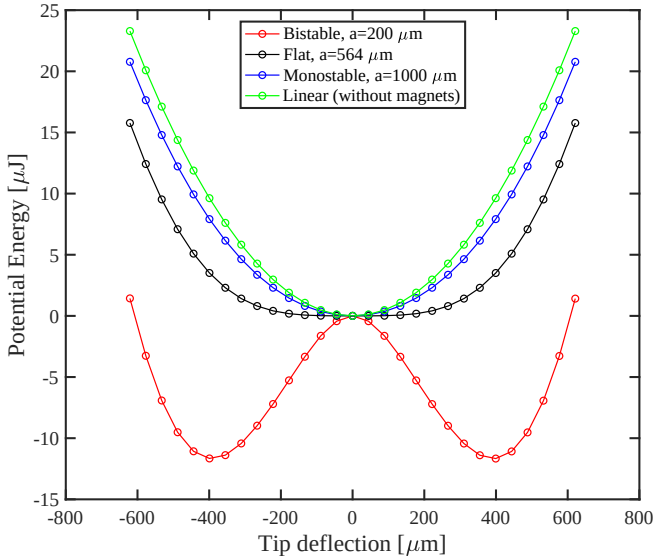

Fig. 7. Total potential energy for a system without magnets and for $b = 500\,\mu\text{m}$ with three different values for the distance between the cantilever tip and magnets: $a = 200\,\mu\text{m}$, $564\,\mu\text{m}$ and $1000\,\mu\text{m}$. The last three cases correspond to the NS configuration.

of the magnetic forces for $a = 1000\,\mu\text{m}$ leads already to a softening effect.

When the magnets are positioned at $a = 200\,\mu\text{m}$, a bistable landscape is found, i.e. two stable solutions are found, where the effective spring constants associated to the local potential energy minimums are $428.3\,\text{N/m}$ and $428.4\,\text{N/m}$ for the positive and negative branch, respectively. The spring constant associated to each tip position, together with the potential energy landscape, are shown in Fig. 8, where the black line corresponds to the linear spring constant. The procedure followed to obtain all the k_{eff} values is to find the slope of the total force around the zero tip position, that is, to find the effective spring constant which is given by $k_{\text{eff}} = \frac{dF}{dz}$, where F is the addition of magnetic and spring forces.

The black curve in Fig. 7 represents the results obtained for a distance $a = 564\,\mu\text{m}$, which leads to a flat potential landscape around zero tip deflection. The effective spring constant associated to zero tip deflection is $0.9\,\text{N/m}$. This result is compared to the linear spring constant associated to the monostable case where no magnetic set-up is included, which clearly demonstrates the spring softening effect.

In order to find a range of values that lead to a flat potential landscape a sweep over both the a and b parameters was performed, this led to the results shown in Fig. 9, which represents the different spring constant regions found for the NS configuration. It is important to note that the values shown are normalized values, i.e. k_{eff}/k_0. The line depicted as showing a zero spring constant determines the contour between the monostable and bistable cases, which at zero tip deflection present positive and negative spring constants, respectively.

The same study was performed for the NN configuration, resulting in the contour lines shown in Fig. 10. In order to compare both configurations, from Fig. 10 and Fig. 9 the a and

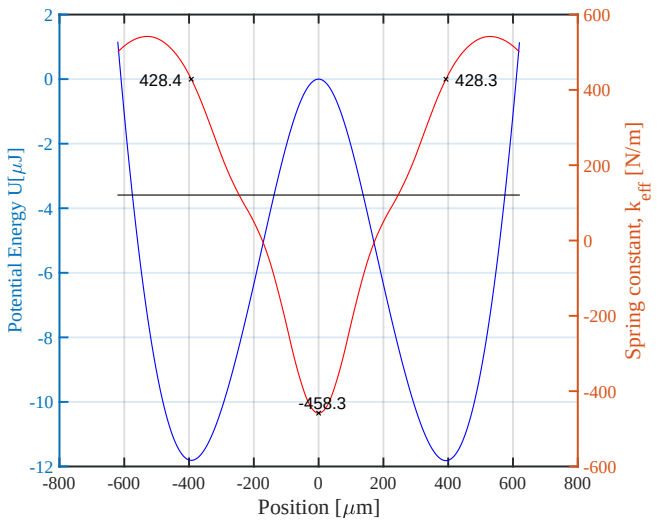

Fig. 8. k_{eff} and total potential energy associated to the bistable case ($a = 200\,\mu\text{m}$ and $b = 500\,\mu\text{m}$) for the NS configuration. The black line represents the spring constant associated to the linear case

b parameters that lead to a flat potential were merged, which are shown in Fig. 11. It can be seen that the NN configuration presents a set of dimensional values lower than $200\,\mu\text{m}$ that allow for softening effect, while in the NS case a hardening effect occurs. However, at this order of magnitude, miniaturization is already guaranteed and increasing dimensional distances from $200\,\mu\text{m}$ to about $400\,\mu\text{m}$ does not imply not fulfilling the miniaturization requirement. With this is mind and from a practical point of view, the NS configuration has the advantage of presenting larger tolerances over the possible b values that the system can present in order to obtain a flat

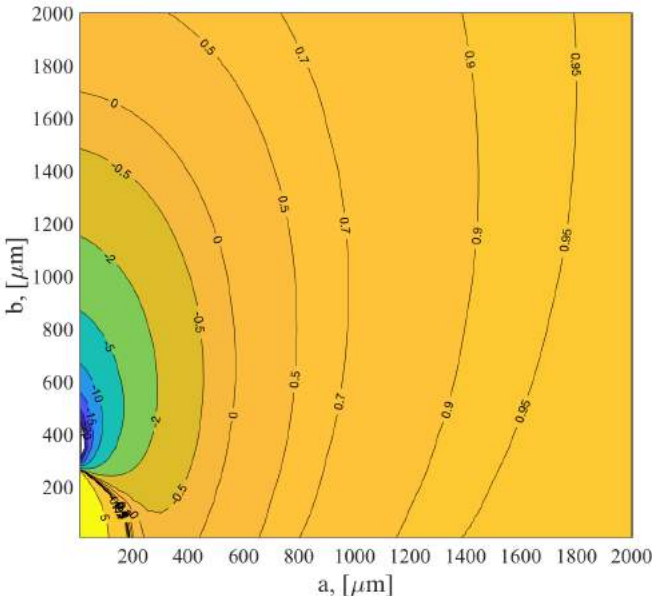

Fig. 9. Contour lines of the k_{eff}/k_0 values for different a and b values associated to the NS configuration.

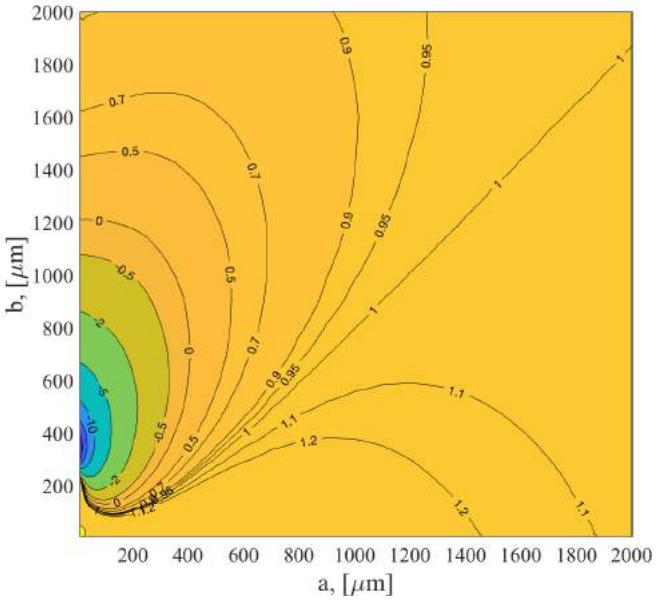

Fig. 10. Contour lines of the k_{eff}/k_0 values for different a and b values associated to the NN configuration..

potential.

5 Experimental results

By using the measuring set-up described in Section 3, impedance measurements are performed while varying the a and b values for the NS magnet configuration. From these measurements, the different resonant frequencies associated to each a and b values are found. Fig. 12 shows the resonant frequencies, impedance magnitudes associated to those resonant frequencies and impedance maximum phases obtained

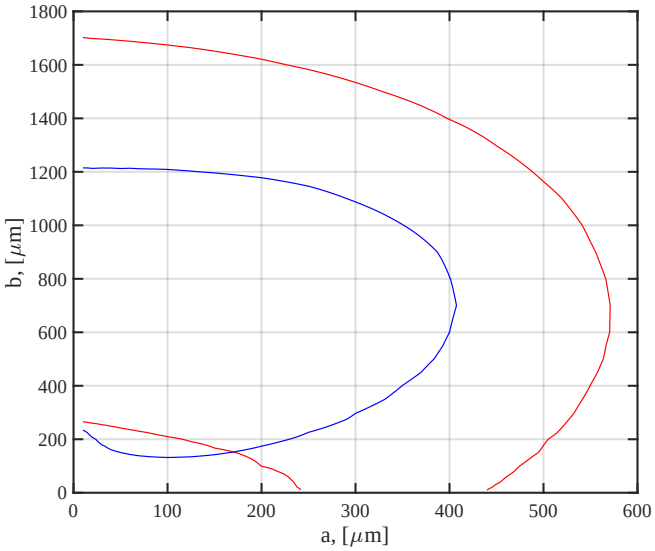

Fig. 11. The contour lines show the magnets separation parameters a and b for which the potential is flat for both the NN (blue) and NS (red) magnet configuration.

for a sweep over a values with constant $b = 420\,\mu\text{m}$. It can be seen that for large values of a the associated values correspond to the linear regime, i.e. the magnetic force is not strong enough at that distance to influence the dynamics of the beam. At a distance of about $a = 3\,\text{mm}$ a small shift in those values occurs. However, it is not until a value of about $a = 2\,\text{mm}$ is reached that a considerable effect takes place. Down until $a = 1\,\text{mm}$ a softening effect takes place and the resonant frequency consistently diminishes. On the other hand, the impedance associated increases. For lower values of a the resonant frequency increases, which clearly demonstrates a hardening effect in that area. The impedance, in contrast, responds by lowering its value in this region, as expected from Section 3.1. These softening and hardening effect observed at these dimensional values are in agreement with what was obtained in Fig. 9. There, at about $b = 420\,\mu\text{m}$ and if a sweep over a is performed from further distances to closer ones, first a softening effect occurs until a flat potential is obtained, as the distance between magnets and beam decreases, a bistable case is obtained, which when measuring the impedance translates to a hardening effect. It is important to note that, in contrast to the contour plot shown in Fig. 9 where all the data set corresponds to zero tip deflection, when performing these measurements if the magnets are close enough the beam will start bending towards either of the magnets. This means that once softening effect is no longer obtained, the results should not be directly compared to the simulation results, where a zero tip deflection was always considered.

Fig. 13 shows both the impedance magnitude and phase versus frequency for $(a, b) = (1000, 420)\,\mu\text{m}$, which corresponds to the dimensional values associated to the lowest resonant frequency shown in Fig. 12, for which a resonant frequency of $158\,\text{Hz}$ is found. Similarly, Fig. 14 shows the impedance

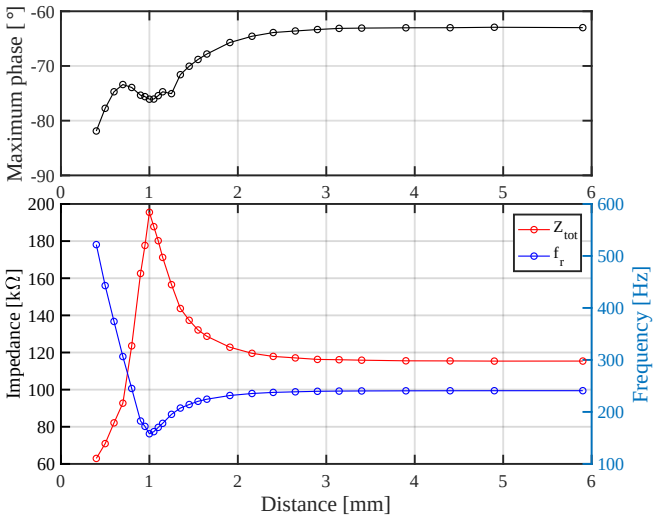

Fig. 12. Plot of the resonant frequency, impedance magnitude at the resonance frequency and maximum phase for a range of a values. All these values correspond to a distance $b = 420\,\mu$m.

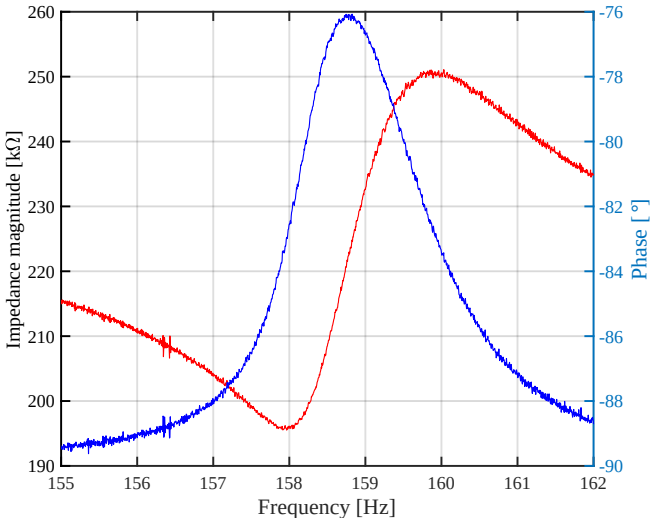

Fig. 13. Impedance magnitude and phase when the beam is under softening effect. The data set corresponds to $(a, b) = (1000, 420)\,\mu$m, which corresponds to the lowest resonant frequency obtained in Fig. 12

magnitude associated to all the data points shown in Fig. 12. From Fig. 14 it is apparent that not only the impedance at the resonant frequency value changes, but the whole spectra shifts. This is due to the electrical side of the system, i.e. Z_{el}, which has in inverse dependency with the frequency, as shown in Eq. 4.

Finally, Fig. 15 shows the relative spring constant values for a range of dimensions that are $a = [400 - 2500]\,\mu$m and $b = [320 - 3140]\,\mu$m. To calculate the relative spring constant values $\frac{f_{\text{eff}}}{f_0} = \frac{k_{\text{eff}}}{k_0}$ is used. This means that by taking each resonant frequency associated to each pair of a and b values and dividing it by the resonant frequency for the linear case the relative spring constant is found. Fig. 15 clearly shows

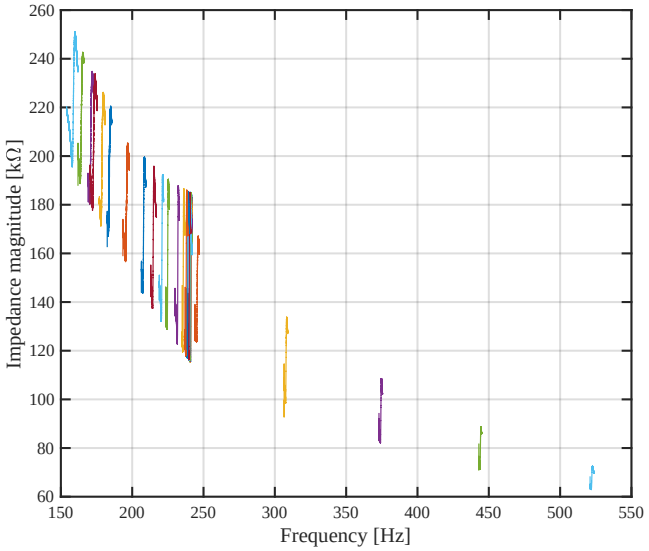

Fig. 14. Impedance magnitudes for all the sweep performed in Fig. 12, that is, for a varying a and $b = 420\,\mu$m.

TABLE II
EXPERIMENTAL RESULTS OBTAINED FOR A NS CONFIGURATION WHEN PERFORMING A SWEEP OVER a AND b VALUES. ONLY THE a VALUES THAT LEAD TO MINIMUM SPRING CONSTANT ARE SHOWN WITH THEIR ASSOCIATED RESONANT FREQUENCY.

$b\,[\mu\text{m}]$	$a_{\text{min}}\,[\mu\text{m}]$	f_{min} [Hz]
3140	450	122.5
2950	550	122.2
2790	750	170
2270	800	129.2
1870	1100	158.9
1170	1100	173.8
910	1100	198
520	1150	177.3
420	1000	158
320	1000	169.4

the two distinct zones that Fig. 9 predicted, i.e. softening and hardening regimes. However, as explained earlier, once a hardening effect occurs the beam bends towards the magnets and therefore it is not possible to constrain the study to zero tip deflection. Besides this, the experimental results are in relative good agreement with what was predicted in the simulation studies. For the sake of completeness, Tab. II shows all the b values for which a sweep over a was performed together with their associated a_{min} that led to the lowest possible resonant frequency value.

6 CONCLUSION

FEM simulations were performed using Comsol Multiphysics 5.2 in order to find optimal dimensional parameters that lead to obtaining BEHs. The model under study consisted of a silicon beam in the millimeter scale to which iron foils were attached at both the bottom and the top surfaces of it, and a pair of external magnets that exert a non-linear force on the beam were added. Static studies were performed to obtain the

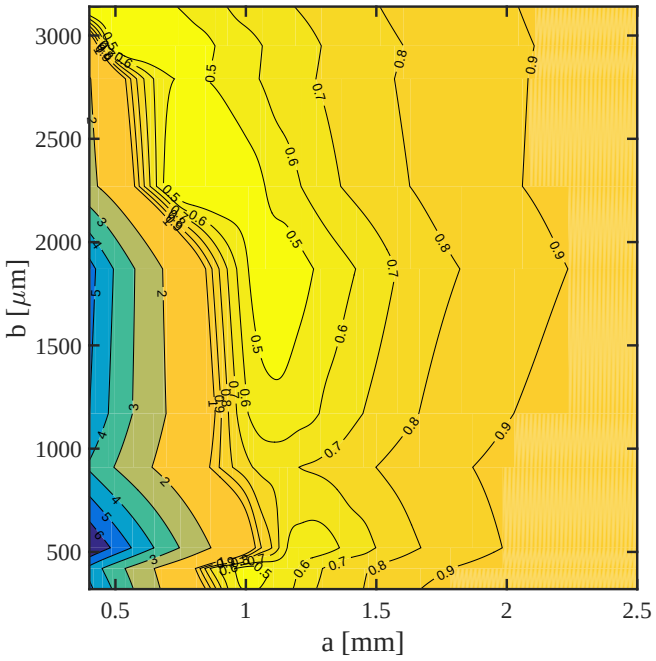

Fig. 15. Contour plot of the relative spring constant values for different a and b values using the NS configuration.

forces associated to the different dimensional configurations. From these forces the energy landscapes were found together with the optimal dimensional parameters that lead to low-frequency broadband energy harvesting. These results showed that the system under study allowed for miniaturization. Impedance measurements were performed for different a and b values and similar results to the ones from the simulations were obtained, where both a softening and hardening effects are observed.

REFERENCES

[1] Y. Tada, "Experimental characteristics of electret generator, using polymer film electrets," *Japanese Journal of Applied Physics*, vol. 31, no. 3R, p. 846, 1992.

[2] S. Roundy, P. K. Wright, and J. Rabaey, "A study of low level vibrations as a power source for wireless sensor nodes," *Computer Communications*, vol. 26, no. 11, pp. 1131–1144, 2003.

[3] S. Boisseau, G. Despesse, T. Ricart, E. Defay, and A. Sylvestre, "Cantilever-based electret energy harvesters," *Smart Materials and Structures*, vol. 20, no. 10, p. 105013, 2011.

[4] M. El-Hami, P. Glynne-Jones, N. White, M. Hill, S. Beeby, E. James, A. Brown, and J. Ross, "Design and fabrication of a new vibration-based electromechanical power generator," *Sensors and Actuators A: Physical*, vol. 92, no. 1, pp. 335–342, 2001.

[5] S. P. Beeby, R. Torah, M. Tudor, P. Glynne-Jones, T. O'Donnell, C. Saha, and S. Roy, "A micro electromagnetic generator for vibration energy harvesting," *Journal of Micromechanics and Microengineering*, vol. 17, no. 7, p. 1257, 2007.

[6] R. Elfrink, T. Kamel, M. Goedbloed, S. Matova, D. Hohlfeld, R. Van Schaijk, and R. Vullers, "Vibration energy harvesting with aluminum nitride-based piezoelectric devices," in *Proceedings of the PowerMEMS Workshop, Sendai*, 2008, pp. 249–52.

[7] A. Erturk and D. J. Inman, "An experimentally validated bimorph cantilever model for piezoelectric energy harvesting from base excitations," *Smart Materials and Structures*, vol. 18, no. 2, p. 025009, 2009.

[8] S. Priya, "Advances in energy harvesting using low profile piezoelectric transducers," *Journal of Electroceramics*, vol. 19, no. 1, pp. 167–184, 2007.

[9] E. Iborra, J. Olivares, M. Clement, L. Vergara, A. Sanz-Hervás, and J. Sangrador, "Piezoelectric properties and residual stress of sputtered AlN thin films for MEMS applications," *Sensors and Actuators A: Physical*, vol. 115, no. 2, pp. 501–507, 2004.

[10] P. Wang, H. Du, S. Shen, M. Zhang, and B. Liu, "Deposition, characterization and optimization of zinc oxide thin film for piezoelectric cantilevers," *Applied Surface Science*, vol. 258, no. 24, pp. 9510–9517, 2012.

[11] D. Zhu, M. J. Tudor, and S. P. Beeby, "Strategies for increasing the operating frequency range of vibration energy harvesters: a review," *Measurement Science and Technology*, vol. 21, no. 2, p. 022001, 2009.

[12] E. S. Leland and P. K. Wright, "Resonance tuning of piezoelectric vibration energy scavenging generators using compressive axial preload," *Smart Materials and Structures*, vol. 15, no. 5, p. 1413, 2006.

[13] C. Eichhorn, F. Goldschmidtboeing, and P. Woias, "A frequency tunable piezoelectric energy converter based on a cantilever beam," *Proceedings of PowerMEMS*, vol. 9, no. 12, pp. 309–312, 2008.

[14] R. B. MacCurdy, T. Reissman, and E. Garcia, "Energy management of multi-component power harvesting systems," in *The 15th International Symposium on: Smart Structures and Materials & Nondestructive Evaluation and Health Monitoring*. International Society for Optics and Photonics, 2008, pp. 692 809–692 809.

[15] M. Ferrari, M. Bau, M. Guizzetti, and V. Ferrari, "A single-magnet nonlinear piezoelectric converter for enhanced energy harvesting from random vibrations," *Sensors and Actuators A: Physical*, vol. 172, no. 1, pp. 287–292, 2011.

[16] M. Ferrari, V. Ferrari, M. Guizzetti, B. Andò, S. Baglio, and C. Trigona, "Improved energy harvesting from wideband vibrations by nonlinear piezoelectric converters," *Sensors and Actuators A: Physical*, vol. 162, no. 2, pp. 425–431, 2010.

[17] F. Cottone, H. Vocca, and L. Gammaitoni, "Nonlinear energy harvesting," *Physical Review Letters*, vol. 102, no. 8, p. 080601, 2009.

[18] R. Ramlan, M. Brennan, B. Mace, and I. Kovacic, "Potential benefits of a non-linear stiffness in an energy harvesting device," *Nonlinear Dynamics*, vol. 59, no. 4, pp. 545–558, 2010.

[19] R. Ramlan, "Effects of non-linear stiffness on performance of an energy harvesting device," Ph.D. dissertation, University of Southampton, 2009.

[20] D. S. Nguyen and E. Halvorsen, "Analysis of vibration energy harvesters utilizing a variety of nonlinear springs," *Proceedings of the PowerMEMS*, vol. 10, pp. 331–334, 2010.

[21] A. Erturk and D. Inman, "Broadband piezoelectric power generation on high-energy orbits of the bistable duffing oscillator with electromechanical coupling," *Journal of Sound and Vibration*, vol. 330, no. 10, pp. 2339–2353, 2011.

[22] S. P. Pellegrini, N. Tolou, M. Schenk, and J. L. Herder, "Bistable vibration energy harvesters: a review," *Journal of Intelligent Material Systems and Structures*, vol. 24, no. 11, pp. 1303–1312, 2012.

[23] P.-h. Wang, S.-w. Shi, and H.-j. Du, "Fabrication and performance of ZnO piezoelectric cantilever for vibration energy harvesting," in *Piezoelectricity, Acoustic Waves, and Device Applications (SPAWDA), 2015 Symposium on*. IEEE, 2015, pp. 147–151.

[24] S.-C. Lin and W.-J. Wu, "Fabrication of PZT MEMS energy harvester based on silicon and stainless-steel substrates utilizing an aerosol deposition method," *Journal of Micromechanics and Microengineering*, vol. 23, no. 12, p. 125028, 2013.

[25] A. Lei and E. V. Thomsen, "Wideband piezomagnetoelastic vibration energy harvesting," in *Journal of Physics: Conference Series*, vol. 557, no. 1. IOP Publishing, 2014, p. 012121.

[26] J. I. Tam and P. Holmes, "Revisiting a magneto-elastic strange attractor," *Journal of Sound and Vibration*, vol. 333, no. 6, pp. 1767–1780, 2014.

[27] G. Sebald, H. Kuwano, D. Guyomar, and B. Ducharne, "Simulation of a duffing oscillator for broadband piezoelectric energy harvesting," *Smart Materials and Structures*, vol. 20, no. 7, p. 075022, 2011.

[28] L. Tang, Y. Yang, and C. K. Soh, "Toward broadband vibration-based energy harvesting," *Journal of Intelligent Material Systems and Structures*, vol. 21, no. 18, pp. 1867–1897, 2010.

[29] *COMSOL Multiphysics 5.2 Users Manual*, COMSOL, Inc., 100 District Avenue Burlington, MA 01803, 2015. [Online]. Available: http://www.comsol.com

[30] E. Halvorsen, L.-C. J. Blystad, S. Husa, and E. Westby, "Simulation of electromechanical systems driven by large random vibrations," in

Perspective Technologies and Methods in MEMS Design, 2007. MEMSTECH 2007. International Conference on. IEEE, 2007, pp. 117–122.

[31] *DinoCapture Users Manual*, AnMo Electronics Corporation, Inc., 17F, No. 97, Sec. 4, ChongHsin Rd., Sanchong Dist., New Taipei City, 241 Taiwan, 2017. [Online]. Available: http://www.dino-lite.com

Increased Mechanical Robustness of Piezoelectric Magnetoelastic Vibrational Energy Harvesters

Increased Mechanical Robustness of Piezoelectric Magnetoelastic Vibrational Energy Harvesters

L. R. Alcala-Jimenez *, T. Passer*, A. Lei*, and E. V. Thomsen*
*Department of Micro and Nanotechnology, Technical University of Denmark, DK-2800 Kgs. Lyngby, Denmark

***Abstract*—This work presents a cantilever based broadband piezoelectric magnetoelastic vibration energy harvester with increased mechanical robustness. The energy harvester is fabricated using KOH etching to define the cantilever and the proof mass is made using micromachined Fe foils which together with a pair of miniature magnets provides the magnetoelastic properties. KOH etching leads to very sharp corners at the anchoring point of the cantilever which makes the cantilever fragile. The mechanical robustness of the energy harvesters is increased using a lithography-free two-step fabrication process which leads to a corner rounding at the anchoring point lowering the stress concentration and increasing the robustness. Both enhanced and non-enhanced beams are excited at increasing frame accelerations. The conventional beams break at frame accelerations of around $3\,\mathrm{g}$ while the enhanced break at almost twice as much, $5.7\,\mathrm{g}$. The devices are characterized electrically by impedance measurements in both their linear and non linear regime. The magnetoelastic behaviour can be adjusted by varying the beam-magnet distance which allows for both spring softening and spring hardening.**

***Keywords*—** MEMS, Energy harvester, Robust, Piezelectric, Magnetoelastic, Ambient vibration.

1 Introduction

The need to power wearable devices, wireless sensor systems, and devices for the Internet of Things (IOT) increases the demand on small-scale power sources. Power source requirements for such systems are physical dimensions in the millimeter-scale range and long lifetime. Conventional batteries imply continuous and sometimes expensive replacement cost. Furthermore, they impose a limit on system miniaturization. This means that a replacement for conventional batteries must be found. Miniaturized cantilever-based vibrational energy harvesters (VEHs) capable of transforming energy from the mechanical domain, i.e. vibrations, into energy in the electrical domain have recently been receiving increasing interest in this field of application. There are three main approaches to harvesting energy from vibrations, which involve the use of either electrostatic [1–3], electromagnetic [4], [5] or piezoelectric [6–10] principles. Among these three different types of VEHs, piezoelectric-based VEHs have attracted much attention because it is feasible to produce them in millimeter-scale whilst having large power densities. In [11–13] a power density of $35.4\,\mathrm{mJ/cm^3}$ is reported for a piezoelectric energy harvester and this value can be compared to results obtained for electrostatic and electromagnetic devices, where power densities of $4\,\mathrm{mJ/cm^3}$ and $24.8\,\mathrm{mJ/cm^3}$ [11] have been reported, respectively.

Most ambient vibrations are characterized by a low frequency range (<$200\,\mathrm{Hz}$) [14] and accelerations are typically below 1 g. In order to tune in to the low frequencies needed, the common approach is to increase the cantilever length and reduce its thickness or increasing the weight of the proof mass often attached to the beam. This leads to very high aspect ratios and therefore to very fragile structures due to stress concentration [15], [16] at the anchoring point. Another method for lowering the operation frequencies has been presented by [17], where a five-step fabrication process is performed. It consists of spray coating resist on the backside of the beam after defining the cantilever, then a lithography process is performed and finally deep holes, with a radius of $25\,\mu\mathrm{m}$ and a depth of $45\,\mu\mathrm{m}$, are etched on the Si hinge. The resulting structure presented a resonant frequency of $802\,\mathrm{Hz}$, this value can be compared to the regular cantilevers, i.e. where no holes were etched on the structure, for which a resonant frequency of $845\,\mathrm{Hz}$ was obtained. Regarding the harvested power, it was increased 18% compared to the standard structures.

Besides the low frequency range of ambient vibrations, most of them do not occur at a specific frequency, but over a wide spectrum of frequencies. Therefore, research has been carried out in the field of broadband energy harvesting, where an external force is typically used to provide a potential energy landscape suitable for broad-band energy harvesting. Depending on the sources of the forces two types of methods can be distinguished: active and passive methods. In the active method the device needs to be continuously either powered or manually modified. Therefore, unless the gained energy is larger than the energy consumed by the powering source, it is of no further interest to investigate this type. On the other hand, a passive method requires to be only intermittently powered or even not powered at all. Magnetoelastic VEHs use an external magnetic setup that interacts with the beam by implementing either a magnet or a ferromagnetic foil on the beam [18–21], as shown in Fig. 1. Adding this magnetic setup will modify the spring constant of the beam according to the distance between the magnets and the beam, a, and the distance between the magnets, b. The spring constant will either become lower or higher depending on whether a softening [22] or hardening [23] effect takes place, respectively. Another passive method is the use of beam stoppers [24] that interact with the beam. This interaction takes place when the beam engages with the stopper and the effective spring constant is therefore changed. Furthermore, by applying stoppers to the energy

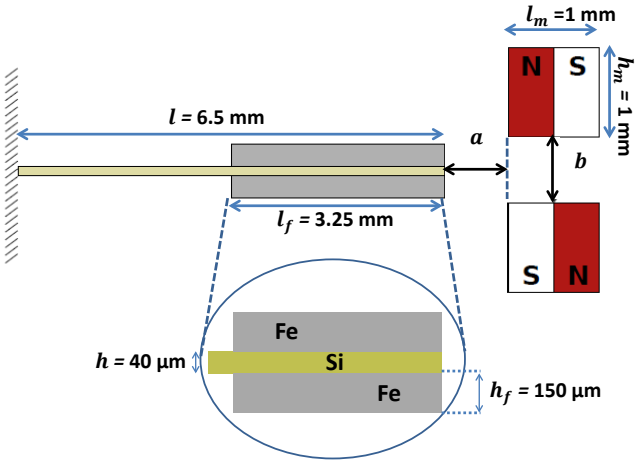

Fig. 1. Side view of the silicon based piezoelectric magnetoeleastic vibrational energy harvester system. The proof mass is realized by gluing pieces of Fe foil to the silicon cantilever.

harvesting system the beam bending is restricted to lower values, therefore they are less prone to fracture.

Typical VEHs use silicon wafers as substrates due to the well established Si micro- and nanofabrication techniques, nevertheless, studies have also been performed using metal substrates instead [25], [26]. This is due to their higher plastic deformation which, compared to the highly brittle material that Si is, clearly displays an advantage in the relative displacement that the beams can undergo. These larger deflections translate to larger strains in the piezoelectric material and, therefore, higher output power. Another advantage of these metal-based structures is that a lower resonant frequency can be achieved even without the use of a seismic mass [25]. However, an important drawback of using metal substrates is the restrictions in micro- and nano-processing techniques that these metals impose.

This study presents a fabrication process for a mechanically robust piezo electric cantilever-based VEH suitable for magnetoelastic energy harvesting. The cantilever is defined in silicon using KOH etching and the increased mechanical robustness is obtained by rounding the sharp KOH etched corner at the anchoring point of the beam. This corner rounding is performed by oxidation using a two-step batch fabrication process that increases the robustness of the beam without compromising beam dimensions. During oxidation the corner is rounded due to a combination of different oxidation rates of the (111) and (100) silicon surfaces and two dimensional diffusion of the oxidant. An AlN thin film is deposited on the beam providing the piezo electric properties and Fe foils are used both as proof mass and to provide magnetoeleastic behaviour.

The article is organized as follows: First, the materials and methods are described and the fabrication process used to fabricate the VEHs is presented. Secondly, the measurement setups for both characterizing the mechanical robustness of the devices and their piezo magnetoelastic behaviour is explained. Then, results and discussions are presented and finally, the article ends with the conclusions.

2 Materials and Methods

2.1 Fabrication of energy harvesters

The main steps of the fabrication process are shown in Fig. 2 and the dimensions of the device are given in Table I. The process begins with a (100) oriented Si substrate having a resistivity of $0.0015\,\Omega$cm, Fig. 2a, which allows the silicon substrate to be used as a bottom electrode for the piezo electric material. The etch mask for KOH etching is a $3000\,$nm thick wet oxide layer which is grown on both sides of the wafer. Then a lithography process is performed followed by a BHF etching of the oxide layer to define the etch mask, Fig. 2b. After this, the beam is made using KOH etching, Fig. 2c, and the oxide layer is removed by etching in BHF, Fig. 2d. Then, the corner rounding step takes place, which consists of growing a $1000\,$nm wet oxide layer at $1100°$C and right afterwards stripping it, as shown in Fig. 2e-f, respectively. After this, the piezo electric material and top and bottom electrodes are deposited by evaporation and sputtering of Pt/AlN/Pt/Ti with thicknesses of $50\,$nm/$400\,$nm/$120\,$nm /$10\,$nm, respectively, Fig. 2g. A lithography process is then performed on that side of the wafer, Fig. 2h, with an opening for the top electrode definition using AZ 4562 resist with a thickness of $10\,\mu$m. The three-stack layer is etched in Aqua Regia at $80°$C, Fig. 2i, with the concentrations shown in Table II. However, the lithography and etching process is performed three times due to the high temperatures that the resist must withstand during the Aqua Regia etchings. Once this is completed, another layer of AZ 4562 resist is spun on the same side of the wafer, Fig. 2j, this time with a thickness of $5\,\mu$m. This serves as masking material for the release of the beams, which is performed by using an STS ICP Advanced Silicon Etcher system, Fig. 2k. After stripping the resist the devices are then ready to be diced out, this is done using a Disco Automatic dicing saw, model DAD321. The normal procedure before dicing is to use electrostatic tape that holds the wafer still while dicing and once it is done this tape is just pealed off. However, due to the fragility of the beams the tape must be pealed off while the wafers are immersed in acetone.

The final step is to attach Fe foils to the beam, Fig. 2l. These foils act both as proof mass, lowering the resonant frequency, and as an integrated part of the magnetoelastic harvesting scheme. It is important that the ferromagnetic foil that is attached to both sides of the beam is as flat as possible, without bending parts, therefore guaranteeing a structurally symmetric foil. The foil is milled in a computer numeric control milling machine from Minitech Machinery Corporation. A methyl methacrylate (PMMA) surface is normally used to hold the substrate while the milling takes place. In order to hold still the foil on the PMMA surface, electrostatic tape is used, as seen in Figure 3, where the blue spots are the residues of the tape once the milling has been completed and the ferromagnetic foil removed. For removing the foil from the electrostatic tape

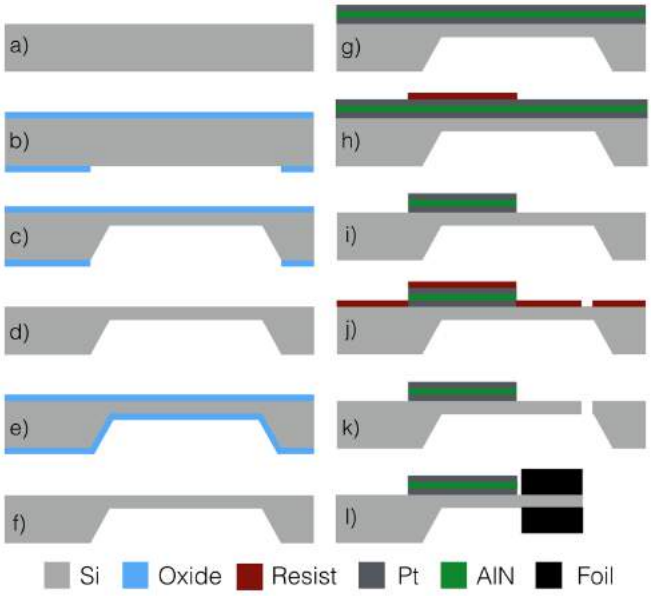

Fig. 2. Main steps of the process flow followed to fabricate the VEHs. a) Si wafer. b) Thermal growth of an oxide layer to serve as masking material. c) KOH etching. d) BHF etch to remove oxide. e) Oxide growth to round corners. f) BHF etch of oxide layer. g) Three-stack deposition of top and bottom electrodes and piezoelectric AlN. h) Lithography process to mask the etching of the three layered stack. i) Aqua regia etch of the three layered stack. j) Lithography process for the beam release. k) Beam release by dry etching. l) Finally, devices are diced and ferromagnetic foil is glued on both sides of the beam.

TABLE I
DIMENSIONAL AND MATERIAL PARAMETERS FOR THE ENERGY HARVESTING SYSTEM.

Device parameter	Value
Beam length (l)	6.5 mm
Beam thickness (h)	40 μm
Beam width	6 mm
Foil length (l_f)	3.25 mm
Foil thickness (h_f)	100 μm
Foil width	6 mm
Magnet length (l_m)	1 mm
Magnet thickness (h_m)	1 mm
Magnet width	5.5 mm
Magnetization	750 A/m
Si Young modulus	150 GPa

the whole substrate is submerged into an acetone bath. After this step, the foil is incorporated to the beam by a pick-and-place operation, i.e. it is glued on both sides of the tip of the beam, Fig. 2l.

2.2 *Measurement setups for characterization*

The characterization of the devices consists of two parts. In the first part, the response of the beams in the mechanical domain is analyzed, i.e. the piezoelectric and electrode layers are not implemented in the beams, only the ferromagnetic foil is included to act as proof mass. The purpose of this part of the analysis is to investigate the mechanical robustness of the devices. In the second part, the piezoelectric and

TABLE II
AQUA REGIA COMPOSITION AND APPROXIMATE ETCH RATES.

Parameter	Value
H_2O	400 ml
HCl	350 ml
HNO_3	50 ml
Etch rate in Pt	$\approx$ 10 nm/min
Etch rate in AlN	$\approx$ 26 nm/min

Fig. 3. Ferromagnetic foil after the milling process. The foil is fixed to a PMMA substrate (white) using electrostatic tape (blue) which allows the foil to be diced in a controlled way.

electrode layers are included on the beams, and the devices are characterized in terms of impedance, i.e. their performance in the electrical domain is analyzed and the magnetoelastic properties of the VEHs are determined.

2.2.1 Mechanical domain: To characterize the beams in mechanical terms the setup shown schematically in Fig. 4 is used. A sinusoidal signal is generated from an Agilent 33220A waveform generator and amplified by a Pioneer VSX-405RDS MKII amplifier, which is directly connected to a B&K Minishaker 4810, which acts as the excitation source for the devices. During vibrational testing the devices are mounted to a sample holder which is screwed to the table of the shaker. The deflection of the beams as function of time is measured by a Micro-Epsilon ILD2300-10 laser triangulation displacement sensor, which is placed above the sample holder. The acceleration of the sample holder for a given harmonic driving signal was previously determined from a deflection-time measurement.

The devices tested are both the enhanced ones, i.e. those that underwent a corner rounding treatment, and the regular beams having a sharp corner at the beam anchoring point. The specific dimensions are the same as the ones listed in Table I. The resonant frequency of the devices was found by sweeping the frequency and measuring the deflection of the beam.

To investigate the mechanical robustness of the devices they were excited at different levels of acceleration and frequency sweeps were performed. The acceleration of the sample holder was increased by changing the magnitude of the signal driving the shaker until the beam under investigation broke. The frequency sweep was performed with a step size of 0.01 Hz to avoid breaking the beams due to a too large step in frequency. In order to perform a statistical analysis of the results, the

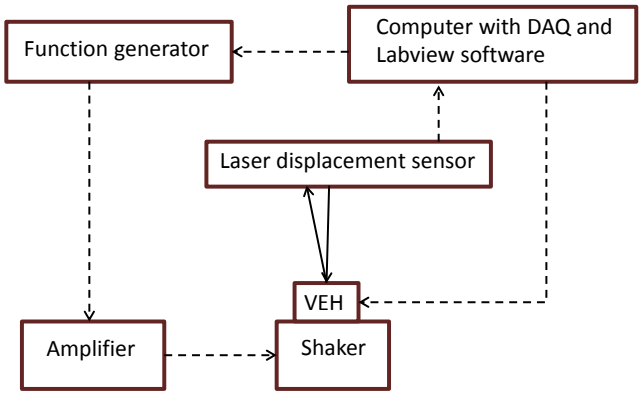

Fig. 4. Schematic of the setup used for characterizing the mechanical properties of the energy harvesters.

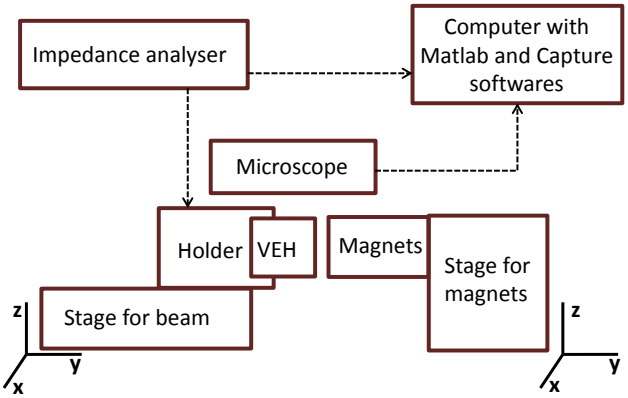

Fig. 5. Schematic of the setup used for characterizing the electrical properties of the devices.

Weibull method [27] was used.

2.2.2 Electrical domain: The electrical characterization of the fabricated devices was performed using impedance measurements. For this purpose an Agilent E4990A Impedance Analyzer was used. The analyzer was connected to an Agilent 4294A impedance probe, Fig. 6, which was connected to the device under investigation. The impedance measurements were performed using a signal amplitude of $50\,\mathrm{mV}$. The top electrode of the beam is in contact with a pogo-pin from the sample holder and a set of other pogo-pins secured it by pressing on the frame of the silicon chip, Fig. 7a. Part of the backside frame structure of the device lies on a metal structure which is connected to the impedance probe. Furthermore, to analyze the non-linear response of the system, a pair of NdFeB magnets are included into the system, Fig. 7b. In order to have a precise control over the positioning of the magnets in the three spatial dimensions, a XYZ 300 TR stage model from Quater Research and Development is used, Fig. 6.

When using the magnetic setup, the distance between the magnets and the beam, a, was measured by a Dino-Lite edge digital microscope model AZ7915MZTL together with

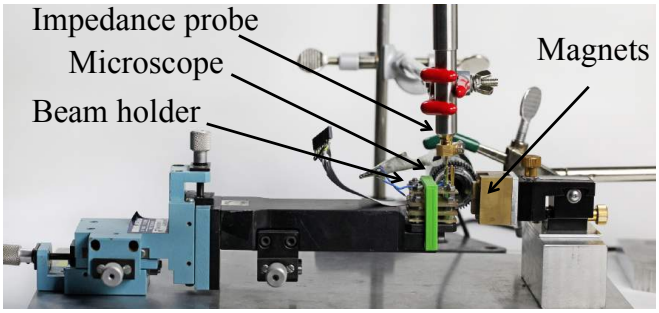

Fig. 6. Setup used for the electrical characterization.

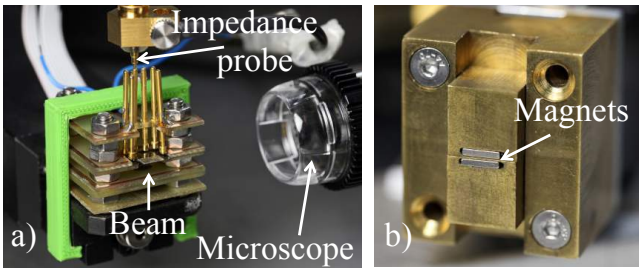

Fig. 7. Part of the setup used for the electrical characterization. a) Beam holder with the pogo-pins holding the beam still and one of them connected to the impedance setup. Also, shown is the microscope used for measuring distances. b) Holder for the magnets with the rectangular magnets located at the center of the fixture.

DinoCapture 2.0 software [28]. For all measurements the distance between the magnets was $b = 520\,\mu\mathrm{m}$.

The impedance measurements were used to determine the resonant frequency of the beam, the effective spring constant, and the capacitance of the piezo electric material.

The effective spring constant of the beam, k_{eff}, was calculated from the resonant frequency of the beam, f_r, determined from the impedance measurements. The spring constant was found using $k_{\mathrm{eff}} = (2\pi f_r)^2 m_{\mathrm{eff}}$, where the value of the effective mass, m_{eff}, was found as described in [29]. The capacitance of the piezo electric layer, C, was calculated from an impedance measurement outside the resonant region of the impedance spectrum using $C = 1/(2\pi f \cdot |Z|)$ where f is the frequency and $|Z|$ is the magnitude of the impedance. The permittivity of the piezo electric layer, ϵ_r, was found from the capacitance using $C = \epsilon_r \epsilon_0 d/A$, where d is the piezoelectric film thickness, A the area of the electrodes, and ϵ_0 is the vacuum permittivity.

3 Results and Discussion

3.1 Corner rounding

The fabrication process for the devices where corner rounding was implemented, was designed using the Silvaco ATHENA [30] process simulator. The simulation takes into account the two dimensional diffusion of the oxidant and the different oxide growth rates on the (111) and (100) silicon surfaces. Furthermore, the simulation takes into account that the linear rate constant is increased due to the high phosphorous

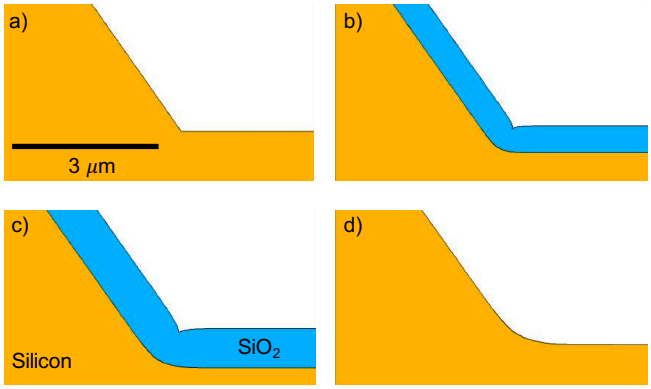

Fig. 8. Results from the corner rounding process simulation. a) As etched, b) After 40 minutes of oxidation, c) After 80 minutes of oxidation, d) After 126 min of oxidation and removal of the oxide.

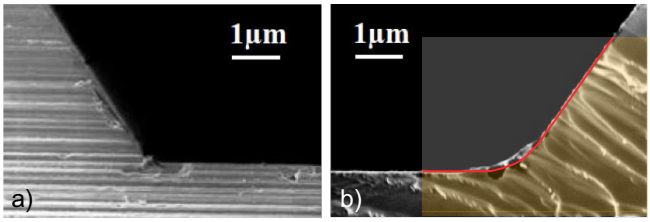

Fig. 9. SEM images of the corner structure of the beam a) before and b) after the oxide growth. The simulation result, Fig. 8d, is shown as the transparent structure overlaid on the SEM image. The solid red line shows the location of the surface of the simulation structure.

doping level of the substrate. The simulation code is included in the appendix. Fig. 8 shows the results from the simulation. Fig. 8a shows the corner of the beam after the KOH etch which is implemented as a geometrical etch in the simulation code. Fig. 8b shows the beam after 40 minutes of oxidation at 1100 °C. At this point the oxide thickness is 619 nm and 764 nm on the (100) and (111) surfaces, respectively. Fig. 8c shows the corner structure after 80 minutes of oxidation and the oxide thicknesses are 876 nm and 1079 nm on the corresponding (100) and (111) surfaces. The total oxidation time is 126 minutes and the final oxide thicknesses on the (100) and (111) surfaces are 1100 nm and 1352 nm, respectively. Finally, Fig. 8d shows the corner structure after the oxide layer has been removed.

Fig. 9 shows SEM images of the corner structure of the beam just after the KOH etch, Fig. 9a, and after the corner rounding has been performed, Fig. 9b. The effectiveness of the corner rounding process is clearly seen as an increased radius of curvature. The radius of curvature after the corner rounding process is 1.8 μm.

Fig. 9b compares the SEM image with the result from the simulation as presented on Fig. 8d. The simulation result is shown as the light structure on top of the SEM image. The solid red line shows the location of the surface of the simulation structure. Therefore, the simulation tool can be used to design a suitable corner rounded structure.

TABLE III
FAILURE BASE ACCELERATIONS FOR BOTH THE REGULAR AND THE ENHANCED DEVICES.

Enhanced		Regular	
f_r [Hz]	acc. [g]	f_r [Hz]	acc. [g]
269.6	3.3	302.4	2.4
283.0	2.4	284.5	3.5
291.9	5.1	302.6	2.0
276.7	7.4	306.2	3.1
264.4	6.1	299.4	3.1
268.6	7.0	296.9	3.8
285.8	5.5	310.9	3.5
281.3	8.3	335.5	2.9
277.7 ± 9.5		304.8 ± 14.6	

TABLE IV
PARAMETERS FOR THE FITTED WEIBULL DISTRIBUTION FUNCTIONS TO THE FAILURE ACCELERATIONS FOR THE REGULAR AND ENHANCED DEVICES.

Parameter	Regular	Enhanced
Shape parameter	6.73	3.49
Scale parameter	3.26	6.29
Mean value [g]	3.0	5.7
Standard deviation [g]	0.5	1.8

3.2 Failure analysis

Table III shows the measured resonant frequencies for enhanced and regular devices and the corresponding base acceleration where the devices failed due to breakage. In all cases, it was observed that the reason for the failure of the devices was that the beam broke at the point where it is attached to the silicon support structure, i.e. at the sharp corner defined by the KOH etch.

The cumulative failure distribution for the regular and enhanced devices, based on the data in Table III, are shown in Fig. 10 together with the fitted Weibull cumulative distribution functions. The characteristics of the fitted Weibull functions are listed in Tab. IV. For the regular devices the shape parameter (Weibull modulus) is $k_r = 6.73$ and the scale parameter is $\lambda_r = 3.26$. For the enhanced devices the corresponding numbers are $k_e = 3.49$ and $\lambda_e = 6.29$, respectively. As both shape parameters are larger than one, the rate of failure increases with acceleration.

Fig. 11 shows a plot of the failure accelerations as function of beam resonant frequencies for the regular and enhanced devices. The mean value of the failure acceleration is 3.0 g and 5.7 g for the regular and enhanced devices, respectively. The mean values are indicated by the dashed lines and the dotted lines correspond to one standard deviation. The data demonstrate that the corner rounding process increases the mechanical robustness of the energy harvesters.

The results found here are in good agreement with the findings of [31] that studied the use of plasma etch induced corner rounding to increase the burst pressure of piezo resistive pressure sensors where KOH etching was used for defining the diaphragm. The burst pressure was increased from around 3 bar to 8 bar when the radius of curvature of the corner was

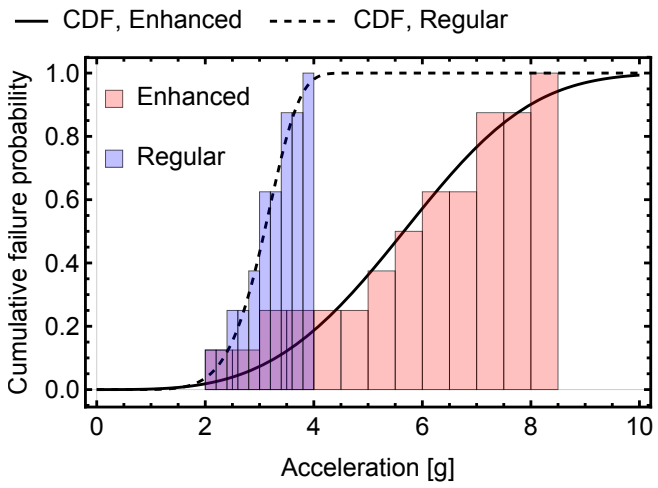

Fig. 10. Cumulative failure distribution for the regular and enhanced devices as function of base acceleration. The solid and dashed lines represents the fitted Weibull cumulative distribution functions (CDF) for the enhanced and regular devices, respectively.

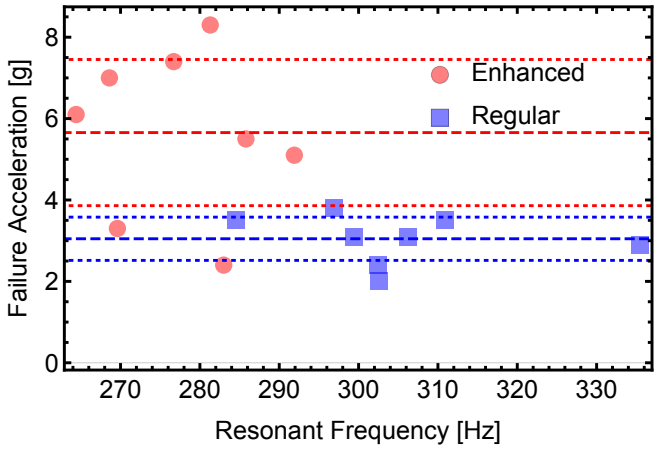

Fig. 11. Failure base acceleration for the enhanced and regular devices as function of beam resonant frequency. The dashed lines are the calculated mean value of the Weibull distributions and the dotted lines represent the corresponding standard deviation. The corner rounding process increases the failure acceleration by almost a factor of two.

etched to obtain a value of 5 μm.

3.3 Electrical domain

Impedance measurements in both the linear regime (without magnets), and the non-linear regime (with magnets implemented into the system) was carried out.

The capacitance of the piezoelectic layer was found before the ferromagnetic foil was mounted on the beam using an impedance measurement in the frequency range from 20 Hz to 1100 Hz and a value of $C = 4.5\,\mathrm{nF}$ was determined. The relative permittivity of the piezoelectric material was calculated to $\epsilon_r = 10.05$, which is in accordance with the value found by Elfrink *et al.* [6].

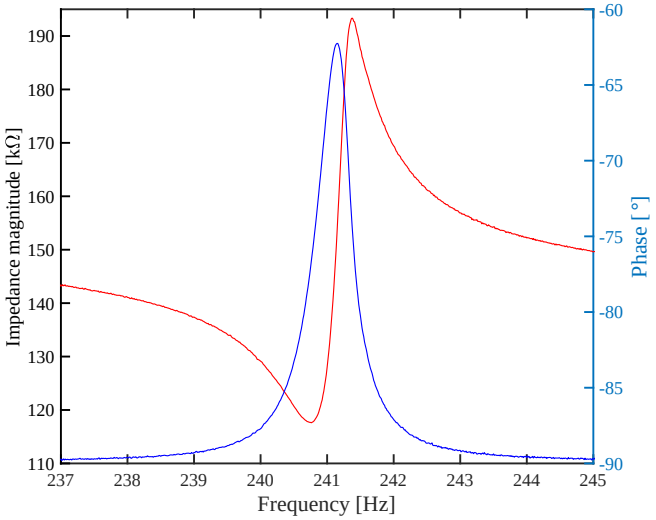

Fig. 12. Impedance measurement of the beam in the linear regime, i.e. with no magnetic force interacting with the beam.

For the linear case, a frequency sweep around the resonant frequency of the beam was performed, as shown in Fig 12, where the impedance magnitude and the phase are plotted on two different y-axes. The results show a resonant frequency, $f_r = 240.6\,\mathrm{Hz}$ and the spring constant was calculated to $k_{\mathrm{eff}} = 98.7\,\mathrm{N/m}$ using an effective mass of $m_{\mathrm{eff}} = 43\,\mathrm{mg}$.

The non-linear response was characterized by using the setup described in Section 2.2.2. Figures 13 and 14 show the impedance measurements obtained for a horizontal distance between the magnets and the beam of $a = 1.15\,\mu\mathrm{m}$ and $a = 500\,\mu\mathrm{m}$, respectively.

In the first case, Fig. 13, the magnetoelastic effect leads to softening of the beam, and the resonant frequency is $f_r = 177.3\,\mathrm{Hz}$ and the effective spring constant is $k_{\mathrm{eff}} = 53.58\,\mathrm{N/m}$, which is 0.54 times the effective spring constant measured in the linear case. As can be seen in Fig. 13, there is some noise in the impedance spectrum compared to Fig. 12 and Fig. 14. The reason is that the larger the softening effect is, the more sensitive the beam becomes to any noise in the surroundings.

In the second case, Fig. 14, a resonant frequency of $f_r = 577.4\,\mathrm{Hz}$ is found, with an associated effective spring constant of $k_{\mathrm{eff}} = 568.3\,\mathrm{N/m}$, which is 5.76 times larger the value found in the linear case showing a significant spring hardening.

Impedance spectra were measured for different distances between the magnets and beam, i.e. for different values of a, ranging from $a = 6\,\mathrm{mm}$ to $a = 400\,\mu\mathrm{m}$. The distance between the magnets was $b = 520\,\mu\mathrm{m}$. The results are shown in Fig. 15, where the resonant frequency of the beam, the impedance magnitude associated to the resonant frequency and the maximum phase are plotted as function of a. It can be seen that for large values of a the associated values correspond to the linear regime, i.e. the magnetic force is not strong enough at that distance to influence the dynamics of the beam. At a distance of about $a = 3\,\mathrm{mm}$ a small

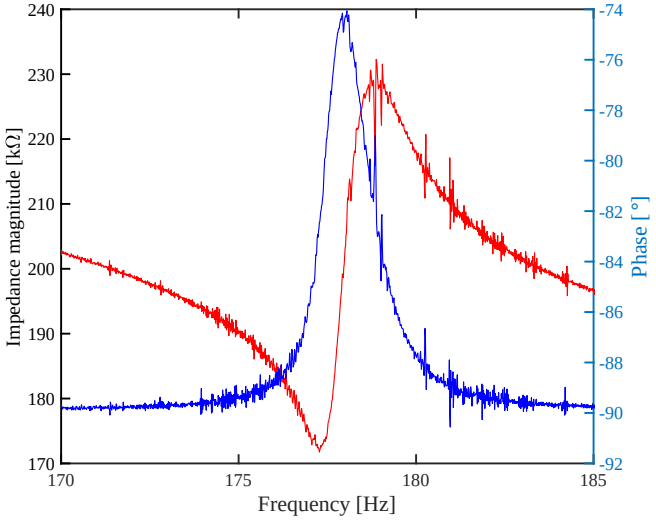

Fig. 13. Impedance measurement around the lowest non-linear resonant frequency due to the softening effect. The magnet-beam distance a is $1.1\,\mathrm{mm}$ and the distance between the magnets is $b = 520\,\mu\mathrm{m}$.

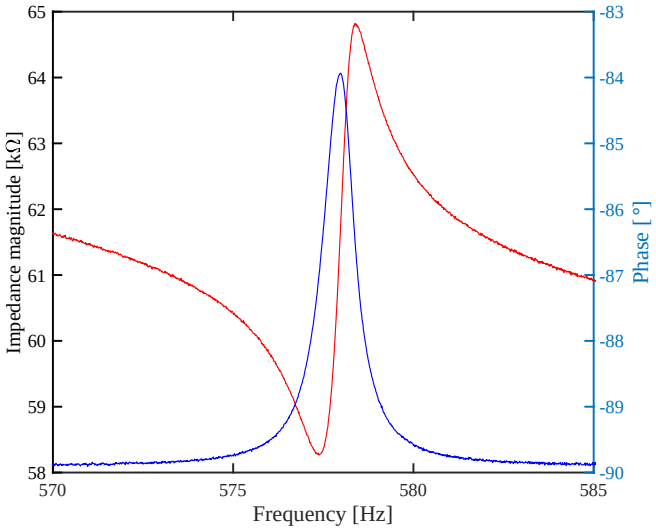

Fig. 14. Impedance measurement around the highest non-linear resonant frequency due to the hardening effect. The magnet-beam distance a is $400\,\mu\mathrm{m}$ and the distance between the magnets is $b = 520\,\mu\mathrm{m}$.

shift in the measured values begins. However, it is not until a value of about $a = 2\,\mathrm{mm}$ is reached that a considerable effect takes place. Down until $a = 1.15\,\mathrm{mm}$ a softening effect takes place and the resonant frequency consistently decreases until $f_r = 177.3\,\mathrm{Hz}$ and the impedance magnitude increases as expected. For lower values of a the resonant frequency increases and the impedance magnitude is lowered, which demonstrates a hardening effect in that region.

These results demonstrate that it is possible to obtain a significant spring softening in a miniature system. The needed distances between the beam and the magnets can be easily obtained in practice. The spring softening obtained will widen the frequency bandwidth where energy harvesting can be

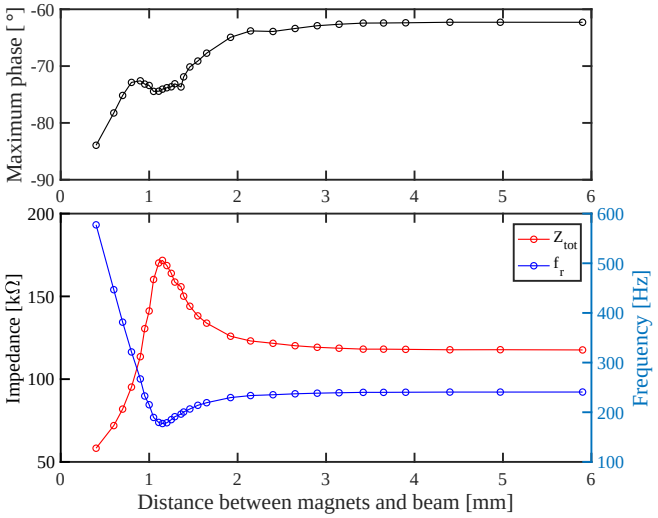

Fig. 15. Plot of the resonant frequency, impedance magnitude at the resonance frequency and maximum phase for a range of a values. The distance between the magnets was $b = 520\,\mu\mathrm{m}$.

performed.

4 Conclusion

In conclusion, a cantilever-based piezoelectric magnetoelastic vibrational energy harvester with increased mechanical robustness has been presented. The energy harvester was fabricated using KOH etching of silicon to define the cantilever and ferromagnetic iron foils were used both as a proof mass and as part of the magnetoelastic design. A two-step lithography-free fabrication process capable of increasing the mechanical robustness of the cantilever was developed. The increased mechanical robustness was obtained by rounding the sharp corner at the anchoring point of the beam, developed during the KOH etch, by oxidation. A $1100\,\mathrm{nm}$ thick wet thermal oxide was grown once the beam had been defined, and the two dimensional diffusion of the oxidant and the different growth rates of the oxide on the (100) and (111) surfaces of the structure led to a corner rounding increasing the radius of curvature to $1.8\mu\mathrm{m}$. The thermal process was simulated with the Silvaco ATHENA process simulation software and the simulation could accurately predict the corner rounding as demonstrated by comparison of the simulated structure with a SEM image of the fabricated device. The corner rounding increased the mechanical robustness of the beam and the enhanced beams withstood a base mean acceleration of $5.7\,\mathrm{g}$ at their resonant frequency, which is almost twice as much as what was observed for the devices without corner rounding where the mean failure base acceleration was $3.0\,\mathrm{g}$.

The devices were also characterized electrically by impedance measurements, which demonstrated the magnetoelastic behaviour of the beam and both spring softening and hardening was observed depending on the distance between the magnets used and the tip of the beam. The lowest resonant frequency achieved was $177\,\mathrm{Hz}$, which occurred at a distance between the tip of the beam and the magnets of $a = 1.15\,\mathrm{mm}$,

a distance that is easily obtained during assembly of the energy harvesting system.

REFERENCES

[1] Y. Tada, "Experimental characteristics of electret generator, using polymer film electrets," *Japanese Journal of Applied Physics*, vol. 31, no. 3R, p. 846, 1992.

[2] S. Roundy, P. K. Wright, and J. Rabaey, "A study of low level vibrations as a power source for wireless sensor nodes," *Computer Communications*, vol. 26, no. 11, pp. 1131–1144, 2003.

[3] S. Boisseau, G. Despesse, T. Ricart, E. Defay, and A. Sylvestre, "Cantilever-based electret energy harvesters," *Smart Materials and Structures*, vol. 20, no. 10, p. 105013, 2011.

[4] M. El-Hami, P. Glynne-Jones, N. White, M. Hill, S. Beeby, E. James, A. Brown, and J. Ross, "Design and fabrication of a new vibration-based electromechanical power generator," *Sensors and Actuators A: Physical*, vol. 92, no. 1, pp. 335–342, 2001.

[5] S. P. Beeby, R. Torah, M. Tudor, P. Glynne-Jones, T. O'Donnell, C. Saha, and S. Roy, "A micro electromagnetic generator for vibration energy harvesting," *Journal of Micromechanics and Microengineering*, vol. 17, no. 7, p. 1257, 2007.

[6] R. Elfrink, T. Kamel, M. Goedbloed, S. Matova, D. Hohlfeld, R. Van Schaijk, and R. Vullers, "Vibration energy harvesting with aluminum nitride-based piezoelectric devices," in *Proceedings of the PowerMEMS Workshop, Sendai*, 2008, pp. 249–52.

[7] A. Erturk and D. J. Inman, "An experimentally validated bimorph cantilever model for piezoelectric energy harvesting from base excitations," *Smart Materials and Structures*, vol. 18, no. 2, p. 025009, 2009.

[8] S. Priya, "Advances in energy harvesting using low profile piezoelectric transducers," *Journal of Electroceramics*, vol. 19, no. 1, pp. 167–184, 2007.

[9] E. Iborra, J. Olivares, M. Clement, L. Vergara, A. Sanz-Hervás, and J. Sangrador, "Piezoelectric properties and residual stress of sputtered AlN thin films for MEMS applications," *Sensors and Actuators A: Physical*, vol. 115, no. 2, pp. 501–507, 2004.

[10] P. Wang, H. Du, S. Shen, M. Zhang, and B. Liu, "Deposition, characterization and optimization of zinc oxide thin film for piezoelectric cantilevers," *Applied Surface Science*, vol. 258, no. 24, pp. 9510–9517, 2012.

[11] S. Roundy, E. S. Leland, J. Baker, E. Carleton, E. Reilly, E. Lai, B. Otis, J. M. Rabaey, P. K. Wright, and V. Sundararajan, "Improving power output for vibration-based energy scavengers," *IEEE Pervasive computing*, vol. 4, no. 1, pp. 28–36, 2005.

[12] P.-h. Wang, S.-w. Shi, and H.-j. Du, "Fabrication and performance of ZnO piezoelectric cantilever for vibration energy harvesting," in *Piezoelectricity, Acoustic Waves, and Device Applications (SPAWDA), 2015 Symposium on*. IEEE, 2015, pp. 147–151.

[13] S.-C. Lin and W.-J. Wu, "Fabrication of PZT MEMS energy harvester based on silicon and stainless-steel substrates utilizing an aerosol deposition method," *Journal of Micromechanics and Microengineering*, vol. 23, no. 12, p. 125028, 2013.

[14] S. Roundy, P. K. Wright, and J. Rabaey, "A study of low level vibrations as a power source for wireless sensor nodes," *Computer Communications*, vol. 26, no. 11, pp. 1131–1144, 2003.

[15] J. Gere and S. Timoshenko, *Mechanics of materials*, ser. General Engineering Series. PWS Pub Co., 1997.

[16] R. Budynas, W. Young, and A. Sadegh, *Roark's Formulas for Stress and Strain, 8th Edition*. McGraw-Hill Education, 2011.

[17] M. T. Todaro, F. Guido, V. Mastronardi, D. Desmaele, G. Epifani, L. Algieri, and M. De Vittorio, "Piezoelectric MEMS vibrational energy harvesters: Advances and outlook," *Microelectronic Engineering*, vol. 183–184, pp. 23–26, 2017.

[18] F. Moon and P. J. Holmes, "A magnetoelastic strange attractor," *Journal of Sound and Vibration*, vol. 65, no. 2, pp. 275–296, 1979.

[19] M. Ferrari, V. Ferrari, M. Guizzetti, B. Andò, S. Baglio, and C. Trigona, "Improved energy harvesting from wideband vibrations by nonlinear piezoelectric converters," *Sensors and Actuators A: Physical*, vol. 162, no. 2, pp. 425–431, 2010.

[20] A. Lei and E. V. Thomsen, "Wideband piezomagnetoelastic vibration energy harvesting," in *Journal of Physics: Conference Series*, vol. 557, no. 1. IOP Publishing, 2014, p. 012121.

[21] J. I. Tam and P. Holmes, "Revisiting a magneto-elastic strange attractor," *Journal of Sound and Vibration*, vol. 333, no. 6, pp. 1767–1780, 2014.

[22] D. S. Nguyen and E. Halvorsen, "Analysis of vibration energy harvesters utilizing a variety of nonlinear springs," *Proceedings of the PowerMEMS*, vol. 10, pp. 331–334, 2010.

[23] R. Ramlan, "Effects of non-linear stiffness on performance of an energy harvesting device," Ph.D. dissertation, University of Southampton, 2009.

[24] M. S. Soliman, E. M. Abdel-Rahman, E. F. El-Saadany, and R. R. Mansour, "A design procedure for wideband micropower generators," *Journal of Microelectromechanical Systems*, vol. 18, no. 6, pp. 1288–1299, 2009.

[25] K. Morimoto, I. Kanno, K. Wasa, and H. Kotera, "High-efficiency piezoelectric energy harvesters of c-axis-oriented epitaxial PZT films transferred onto stainless steel cantilevers," *Sensors and Actuators A: Physical*, vol. 163, no. 1, pp. 428–432, 2010.

[26] S.-C. Lin and W.-J. Wu, "Piezoelectric micro energy harvesters based on stainless-steel substrates," *Smart Materials and Structures*, vol. 22, no. 4, p. 045016, 2013.

[27] W. Weibull, "A statistical distribution function of wide applicability," *Journal of Applied Mechanics*, vol. 18, no. 3, pp. 293–297, 1951.

[28] *DinoCapture Users Manual*, AnMo Electronics Corporation, Inc., 17F, No. 97, Sec. 4, ChongHsin Rd., Sanchong Dist., New Taipei City, 241 Taiwan, 2017. [Online]. Available: http://www.dino-lite.com

[29] A. Erturk and D. J. Inman, *Piezoelectric energy harvesting*. John Wiley & Sons, 2011, pg. 27.

[30] *ATHENA Users Manual*, SILVACO, Inc., 4701 Patrick Henry Drive, Bldg. 2 Santa Clara, CA 95054, 2010. [Online]. Available: http://www.silvaco.com

[31] H. D. Ngo, A. T. Tham, M. Simon, and E. Obermeier, "Corner rounding to strengthen silicon pressure sensors using DRIE," in *2008 IEEE Sensors*, Oct 2008, pp. 1576–1579.

APPENDIX

```
# Corner rounding simulation
go athena

# Define the grid in the y-direction
# (vertical, in units of um)
line y loc=0     spac=0.1
line y loc=10     spac=0.1
line y loc=20    spac=2

# Define the grid in the x-direction
# (horisontal, in units of um)
line x loc=-10   spac=.5
line x loc=-5   spac=0.1
line x loc=5    spac=0.1
line x loc=10    spac=0.5

#
# Define the wafer
# n-type silicon, highly doped
#
init silicon phosphor \
resistivity=0.0015 orientation=100

# KOH etch
etch silicon start x=-3 y=0.00
etch cont x=3 y=8.485
etch done x=10.00 y=8.485

#
# Grow oxide to round corners
#
```

```
# Define a fine grid in the oxide
method grid.ox=0.05

# Oxidixe
diffuse time=126 temp=1100 weto2

# Etch oxide away
strip oxide

# Save structure
structure outfile=corner.str

# Plot structure
tonyplot corner.str

# leave simulator
quit
```

References

[1] *Micro Sensors – World Wide Markets and Economic Impact*, 2006.

[2] Niell Elvin and Alper Erturk. *Advances in energy harvesting methods*. Springer Science & Business Media, 2013.

[3] Shad Roundy, Paul K Wright, and Jan Rabaey. A study of low level vibrations as a power source for wireless sensor nodes. *Computer Communications*, 26(11):1131–1144, 2003.

[4] S. Oshima et al. Vibrational energy harvesting with microelectromechanical system technology. *NTT Technical Review*, •.

[5] Steve P Beeby, RN Torah, MJ Tudor, P Glynne-Jones, T O'donnell, CR Saha, and S Roy. A micro electromagnetic generator for vibration energy harvesting. *Journal of Micromechanics and Microengineering*, 17(7):1257, 2007.

[6] Yasufusa Tada. Experimental characteristics of electret generator, using polymer film electrets. *Japanese Journal of Applied Physics*, 31(3R):846, 1992.

[7] Sébastien Boisseau, Ghislain Despesse, Thibaud Ricart, E Defay, and Alain Sylvestre. Cantilever-based electret energy harvesters. *Smart Materials and Structures*, 20(10):105013, 2011.

[8] Shad Roundy and Paul K Wright. A piezoelectric vibration based generator for wireless electronics. *Smart Materials and structures*, 13(5):1131, 2004.

[9] SM Shahruz. Design of mechanical band-pass filters for energy scavenging. *Journal of Sound and Vibration*, 292(3):987–998, 2006.

[10] Eli S Leland and Paul K Wright. Resonance tuning of piezoelectric vibration energy scavenging generators using compressive axial preload. *Smart Materials and Structures*, 15(5):1413, 2006.

[11] Christoph Eichhorn, Frank Goldschmidtboeing, and Peter Woias. A frequency tunable piezoelectric energy converter based on a cantilever beam. *Proceedings of PowerMEMS*, 9(12):309–312, 2008.

[12] J Loverich, R Geiger, and J Frank. Stiffness nonlinearity as a means for resonance frequency tuning and enhancing mechanical robustness of vibration power harvesters. In *Proc. SPIE*, volume 6928, page 692805, 2008.

[13] In-Ho Kim, Hyung-Jo Jung, Bo Mi Lee, and Seon-Jun Jang. Broadband energy-harvesting using a two degree-of-freedom vibrating body. *Applied Physics Letters*, 98(21):214102, 2011.

[14] Jing-Quan Liu, Hua-Bin Fang, Zheng-Yi Xu, Xin-Hui Mao, Xiu-Cheng Shen, Di Chen, Hang Liao, and Bing-Chu Cai. A MEMS-based piezoelectric power generator array for vibration energy harvesting. *Microelectronics Journal*, 39(5):802–806, 2008.

[15] Samuel C Stanton, Clark C McGehee, and Brian P Mann. Reversible hysteresis for broadband magnetopiezoelastic energy harvesting. *Applied Physics Letters*, 95(17):174103, 2009.

[16] Ji-Tzuoh Lin, Barclay Lee, and Bruce Alphenaar. The magnetic coupling of a piezoelectric cantilever for enhanced energy harvesting efficiency. *Smart Materials and Structures*, 19(4):045012, 2010.

[17] Anders Lei and Erik V Thomsen. Wideband piezomagnetoelastic vibration energy harvesting. In *Journal of Physics: Conference Series*, volume 557, page 012121. IOP Publishing, 2014.

[18] Jee Ian Tam and Philip Holmes. Revisiting a magneto-elastic strange attractor. *Journal of Sound and Vibration*, 333(6):1767–1780, 2014.

[19] Maria Teresa Todaro, Francesco Guido, Vincenzo Mastronardi, Denis Desmaele, Gianmichele Epifani, Luciana Algieri, and Massimo De Vittorio. Piezoelectric MEMS vibrational energy harvesters: Advances and outlook. *Microelectronic Engineering*, 2017.

[20] TM Kamel, R Elfrink, M Renaud, D Hohlfeld, M Goedbloed, C De Nooijer, M Jambunathan, and R Van Schaijk. Modeling and characterization of MEMS-based piezoelectric harvesting devices. *Journal of Micromechanics and Microengineering*, 20(10):105023, 2010.

[21] Shad Roundy. On the effectiveness of vibration-based energy harvesting. *Journal of Intelligent Material Systems and Structures*, 16(10):809–823, 2005.

[22] H Bardaweel, O Al Hattamleh, R Richards, D Bahr, and C Richards. A comparison of piezoelectric materials for MEMS power generation. In *Proceedings of the 6th International Workshop on Micro and Nanotechnology for Power Generation and Energy Conversion Applications, Berkeley, CA, USA*, volume 29, 2006.

[23] Shashank Priya. Advances in energy harvesting using low profile piezoelectric transducers. *Journal of Electroceramics*, 19(1):167–184, 2007.

[24] Dibin Zhu, Michael J Tudor, and Stephen P Beeby. Strategies for increasing the operating frequency range of vibration energy harvesters: a review. *Measurement Science and Technology*, 21(2):022001, 2009.

[25] Sergio P Pellegrini, Nima Tolou, Mark Schenk, and Just L Herder. Bistable vibration energy harvesters: a review. *Journal of Intelligent Material Systems and Structures*, 24(11):1303–1312, 2012.

[26] Jee Ian Tam and Philip Holmes. Revisiting a magneto-elastic strange attractor. *Journal of Sound and Vibration*, 333(6):1767–1780, 2014.

[27] Ethem Erkan Aktakka, Rebecca L Peterson, and Khalil Najafi. Thinned-PZT on SOI process and design optimization for piezoelectric inertial energy harvesting. In *Solid-State Sensors, Actuators and Microsystems Conference (TRANSDUCERS), 2011 16th International*, pages 1649–1652. IEEE, 2011.

[28] Anders Lei, Ruichao Xu, Anders Thyssen, Adam Carsten Stoot, Thomas Lehrmann Christiansen, K Hansen, R Lou-Moeller, Erik Vilain Thomsen, and Karen Birkelund. MEMS-based thick film PZT vibrational energy harvester. In *Micro electro mechanical systems (MEMS), 2011 IEEE 24th international conference on*, pages 125–128. IEEE, 2011.

[29] R Elfrink, TM Kamel, M Goedbloed, S Matova, D Hohlfeld, Y Van Andel, and R Van Schaijk. Vibration energy harvesting with aluminum nitride-based piezoelectric devices. *Journal of Micromechanics and Microengineering*, 19(9):094005, 2009.

[30] Marc-Alexandre Dubois and Paul Muralt. Measurement of the effective transverse piezoelectric coefficient e31, f of AlN and Pb (Zrx, Ti1- x) o3 thin films. *Sensors and Actuators A: Physical*, 77(2):106–112, 1999.

[31] M Renaud, K Karakaya, Tom Sterken, P Fiorini, Christiaan Van Hoof, and Robert Puers. Fabrication, modelling and characterization of MEMS piezoelectric vibration harvesters. *Sensors and Actuators A: Physical*, 145:380–386, 2008.

[32] Marcin Marzencki, Maxime Defosseux, and Skandar Basrour. MEMS vibration energy harvesting devices with passive resonance frequency adaptation capability. *Journal of Microelectromechanical Systems*, 18(6):1444–1453, 2009.

[33] Deepak Bhatia, Himanshu Sharma, RS Meena, and VR Palkar. A novel ZnO piezoelectric microcantilever energy scavenger: Fabrication and characterization. *Sensing and Bio-Sensing Research*, 9:45–52, 2016.

[34] Pei-hong Wang, Shi-wei Shi, and He-jun Du. Fabrication and performance of ZnO piezoelectric cantilever for vibration energy harvesting. In *Piezoelectricity, Acoustic Waves, and Device Applications (SPAWDA), 2015 Symposium on*, pages 147–151. IEEE, 2015.

[35] Peihong Wang, Hejun Du, Shengnan Shen, Mingsheng Zhang, and Bo Liu. Deposition, characterization and optimization of zinc oxide thin film for piezoelectric cantilevers. *Applied Surface Science*, 258(24):9510–9517, 2012.

[36] Xiaoming Wu, Jianhui Lin, Seiki Kato, Kai Zhang, Tianling Ren, and Litian Liu. A frequency adjustable vibration energy harvester. *Proceedings of PowerMEMS*, pages 245–248, 2008.

[37] Zengtao Yang and Jiashi Yang. Connected vibrating piezoelectric bimorph beams as a wide-band piezoelectric power harvester. *Journal of Intelligent Material Systems and Structures*, 20(5):569–574, 2009.

[38] Vinod R Challa, MG Prasad, Yong Shi, and Frank T Fisher. A vibration energy harvesting device with bidirectional resonance frequency tunability. *Smart Materials and Structures*, 17(1):015035, 2008.

[39] Roszaidi Ramlan. *Effects of non-linear stiffness on performance of an energy harvesting device*. PhD thesis, University of Southampton, 2009.

[40] Duy S Nguyen and Einar Halvorsen. Analysis of vibration energy harvesters utilizing a variety of nonlinear springs. *Proceedings of the PowerMEMS*, 10:331–334, 2010.

[41] A Erturk and DJ Inman. Broadband piezoelectric power generation on high-energy orbits of the bistable duffing oscillator with electromechanical coupling. *Journal of Sound and Vibration*, 330(10):2339–2353, 2011.

[42] Samuel C Stanton, Clark C McGehee, and Brian P Mann. Nonlinear dynamics for broadband energy harvesting: Investigation of a bistable piezoelectric inertial generator. *Physica D: Nonlinear Phenomena*, 239(10):640–653, 2010.

[43] Bozidar Marinkovic and Hur Koser. Smart sand—a wide bandwidth vibration energy harvesting platform. *Applied Physics Letters*, 94(10):103505, 2009.

[44] Arman Hajati and Sang-Gook Kim. Ultra-wide bandwidth piezoelectric energy harvesting. *Applied Physics Letters*, 99(8):083105, 2011.

[45] Lars-Cyril Julin Blystad, Einar Halvorsen, and Svein Husa. Piezoelectric MEMS energy harvesting systems driven by harmonic and random vibrations. *IEEE Transactions on Ultrasonics, Ferroelectrics, and Frequency Control*, 57(4), 2010.

[46] Lars-Cyril Julin Blystad and Einar Halvorsen. An energy harvester driven by colored noise. *Smart Materials and Structures*, 20(2):025011, 2011.

[47] Gael Sebald, Hiroki Kuwano, Daniel Guyomar, and Benjamin Ducharne. Simulation of a duffing oscillator for broadband piezoelectric energy harvesting. *Smart Materials and Structures*, 20(7):075022, 2011.

[48] Abdessattar Abdelkefi and Nilma Barsallo. Nonlinear analysis and power improvement of broadband low-frequency piezomagnetoelastic energy harvesters. *Nonlinear Dynamics*, 83(1-2):41–56, 2016.

[49] M Ferrari, M Bau, M Guizzetti, and V Ferrari. A single-magnet nonlinear piezoelectric converter for enhanced energy harvesting from random vibrations. *Sensors and Actuators A: Physical*, 172(1):287–292, 2011.

[50] Alper Erturk and Daniel J Inman. *Piezoelectric energy harvesting*. John Wiley & Sons, 2011.

[51] Lihua Tang, Yaowen Yang, and Chee Kiong Soh. Broadband vibration energy harvesting techniques. In *Advances in Energy Harvesting Methods*, pages 17–61. Springer, 2013.

[52] Deepesh Upadrashta, Yaowen Yang, and Lihua Tang. Material strength consideration in the design optimization of nonlinear energy harvester. *Journal of Intelligent Material Systems and Structures*, 26(15):1980–1994, 2015.

[53] Anders Lei. *Energy Harvesting Using Screen Printed PZT on Silicon*. PhD thesis, DTU, Lynbgy, Denmark, 2013.

[54] Ruichao Xiu. *Energy Harvesting for Microsystems*. PhD thesis, DTU, Lynbgy, Denmark, 2012.

[55] Stephen D Senturia. *Microsystem design*. Springer Science & Business Media, 2007.

[56] Yaowen Yang and Lihua Tang. Equivalent circuit modeling of piezoelectric energy harvesters. *Journal of Intelligent Material Systems and Structures*, 20(18):2223–2235, 2009.

[57] Shuo Cheng, Naigang Wang, and David P Arnold. Modeling of magnetic vibrational energy harvesters using equivalent circuit representations. *Journal of Micromechanics and Microengineering*, 17(11):2328, 2007.

[58] Jamil M Renno, Mohammed F Daqaq, and Daniel J Inman. On the optimal energy harvesting from a vibration source. *Journal of Sound and Sibration*, 320(1):386–405, 2009.

[59] Anders Lei, Ruichao Xu, Louise M Borregaard, Michele Guizzetti, Ole Hansen, and Erik V Thomsen. Impedance based characterization of a high-coupled screen printed PZT thick film unimorph energy harvester. *Journal of Microelectromechanical Systems*, 23(4):842–854, 2014.

[60] Francesco Cottone, Helios Vocca, and L Gammaitoni. Nonlinear energy harvesting. *Physical Review Letters*, 102(8):080601, 2009.

[61] Ian S Grant and William Robert Phillips. *Electromagnetism*. John Wiley & Sons, 2013.

[62] Thomas Passer. Fabrication and characterization of a bistable piezoelectric energy harvester. B.sc. thesis, DTU, Lyngby, Denmark, 2016.

[63] COMSOL, Inc., 100 District Avenue Burlington, MA 01803. *COMSOL Multiphysics 5.2 User's Manual*, 2015.

[64] Mathworks, Inc., 1 Apple Hill Drive Natick, MA 01760-2098. *Matlab User's Manual*, 2017.

[65] AV Dobrynin. Thermoelastic strain and plastic yielding in aluminum nitride on sapphire. *Journal of Applied Physics*, 85(3):1876–1882, 1999.

[66] Gouri Radhakrishnan. Properties of AlN films grown at 350 k by gas-phase excimer laser photolysis. *Journal of Applied Physics*, 78(10):6000–6005, 1995.

[67] Satoru Tanaka, R Scott Kern, James Bentley, and Robert F Davis. Defect formation during hetero-epitaxial growth of aluminum nitride thin films on 6h-silicon carbide by gas-source molecular beam epitaxy. *Japanese Journal of Applied Physics*, 35(3R):1641, 1996.

[68] Paul Muralt. AlN thin film processing and basic properties. In *Piezoelectric MEMS Resonators*, pages 3–37. Springer, 2017.

[69] A Sanz-Hervás, M Clement, E Iborra, L Vergara, J Olivares, and J Sangrador. Degradation of the piezoelectric response of sputtered c-axis AlN thin films with traces of non-(0002) x-ray diffraction peaks. *Applied Physics Letters*, 88(16):161915, 2006.

[70] Nathan Jackson, Rosemary O'Keeffe, Finbarr Waldron, Mike O'Neill, and Alan Mathewson. Influence of aluminum nitride crystal orientation on MEMS energy harvesting device performance. *Journal of Micromechanics and Microengineering*, 23(7):075014, 2013.

[71] Morito Akiyama, Toshihiro Kamohara, Kazuhiko Kano, Akihiko Teshigahara, and Nobuaki Kawahara. Influence of oxygen concentration in sputtering gas on piezoelectric response of aluminum nitride thin films. *Applied Physics Letters*, 93(2):021903, 2008.

[72] L Vergara, M Clement, E Iborra, A Sanz-Hervas, J Garcıa López, Y Morilla, J Sangrador, and MA Respaldiza. Influence of oxygen and argon on the crystal quality and piezoelectric response of AlN sputtered thin films. *Diamond and Related Materials*, 13(4):839–842, 2004.

[73] Raj Jakkaraju, G Henn, C Shearer, M Harris, N Rimmer, and P Rich. Integrated approach to electrode and AlN depositions for bulk acoustic wave (BAW) devices. *Microelectronic Engineering*, 70(2):566–570, 2003.

[74] Jin-Bock Lee, Jun-Phil Jung, Myung-Ho Lee, and Jin-Seok Park. Effects of bottom electrodes on the orientation of AlN films and the frequency responses of resonators in aln-based fbars. *Thin Solid Films*, 447:610–614, 2004.

[75] HP Löbl, M Klee, R Milsom, R Dekker, C Metzmacher, W Brand, and P Lok. Materials for bulk acoustic wave (BAW) resonators and filters. *Journal of the European Ceramic Society*, 21(15):2633–2640, 2001.

[76] A Sanz-Hervas, L Vergara, J Olivares, E Iborra, Y Morilla, J Garcia-Lopez, M Clement, J Sangrador, and MA Respaldiza. Comparative study of c-axis AlN films sputtered on metallic surfaces. *Diamond and Related Materials*, 14(3):1198–1202, 2005.

[77] Cinzia Caliendo and P Massimiliano Latino. Characterization of Pt/AlN/Pt-based structures for high temperature, microwave electroacoustic devices applications. *Thin Solid Films*, 519(19):6326–6329, 2011.

[78] James W Edwards, Rudolph Speiser, and Herrick L Johnston. High temperature structure and thermal expansion of some metals as determined by X-ray diffraction data. i. platinum, tantalum, niobium, and molybdenum. *Journal of Applied Physics*, 22(4):424–428, 1951.

[79] FS Ohuchi and PE Russell. AlN thin films with controlled crystallographic orientations and their microstructure. *Journal of Vacuum Science & Technology A: Vacuum, Surfaces, and Films*, 5(4):1630–1634, 1987.

[80] A Ababneh, U Schmid, J Hernando, JL Sánchez-Rojas, and H Seidel. The influence of sputter deposition parameters on piezoelectric and mechanical properties of AlN thin films. *Materials Science and Engineering: B*, 172(3):253–258, 2010.

[81] H Cheng, Yong Sun, JX Zhang, YB Zhang, S Yuan, and P Hing. AlN films deposited under various nitrogen concentrations by rf reactive sputtering. *Journal of Crystal Growth*, 254(1):46–54, 2003.

[82] Marc-Alexandre Dubois and Paul Muralt. Properties of aluminum nitride thin films for piezoelectric transducers and microwave filter applications. *Applied Physics Letters*, 74(20):3032–3034, 1999.

[83] Jeppe Olsen and Jonas Jauho. Fabrication and characterization of a bistable piezoelectric energy harvester. B.sc. thesis, DTU, Lyngby, Denmark, 2012.

[84] Keiji Morimoto, Isaku Kanno, Kiyotaka Wasa, and Hidetoshi Kotera. High-efficiency piezoelectric energy harvesters of c-axis-oriented epitaxial PZT films transferred onto stainless steel cantilevers. *Sensors and Actuators A: Physical*, 163(1):428–432, 2010.

[85] Shun-Chiu Lin and Wen-Jong Wu. Piezoelectric micro energy harvesters based on stainless-steel substrates. *Smart Materials and Structures*, 22(4):045016, 2013.

[86] H. D. Ngo, A. T. Tham, M. Simon, and E. Obermeier. Corner rounding to strengthen silicon pressure sensors using DRIE. In *2008 IEEE Sensors*, pages 1576–1579, Oct 2008.

[87] SILVACO, Inc., 4701 Patrick Henry Drive, Bldg. 2 Santa Clara, CA 95054. *ATHENA User's Manual*, 2010.

[88] Da Chen, Dong Xu, Jingjing Wang, Bo Zhao, and Yafei Zhang. Dry etching of AlN films using the plasma generated by fluoride. *Vacuum*, 83(2):282–285, 2008.

[89] S Saravanan, E Berenschot, G Krijnen, and M Elwenspoek. A novel surface micromachining process to fabricate AlN unimorph suspensions and its application for rf resonators. *Sensors and Actuators A: Physical*, 130:340–345, 2006.

[90] Kazuo Sato, Mitsuhiro Shikida, Takashi Yamashiro, Kazuo Asaumi, Yasuroh Iriye, and Masaharu Yamamoto. Anisotropic etching rates of single-crystal silicon for TMAH water solution as a function of crystallographic orientation. *Sensors and Actuators A: Physical*, 73(1):131–137, 1999.

[91] AnMo Electronics Corporation, Inc., 17F, No. 97, Sec. 4, ChongHsin Rd., Sanchong Dist., New Taipei City, 241 Taiwan. *DinoCapture User's Manual*, 2017.

[92] National Instruments, Corp., 11500 Mopac Expwy Austin, TX 78759-3504. *Labview User's Manual*, 2014.

[93] ZX Bi, YD Zheng, R Zhang, SL Gu, XQ Xiu, LL Zhou, B Shen, DJ Chen, and Y Shi. Dielectric properties of AlN film on Si substrate. *Journal of Materials Science: Materials in Electronics*, 15(5):317–320, 2004.

[94] Sadao Adachi. *Properties of semiconductor alloys: group-IV, III-V and II-VI semiconductors*, volume 28. John Wiley & Sons, 2009.